NASA TECHNICAL NOTE

NASA TN D-3940

NASA TN D-3940

LOW-SPEED WIND-TUNNEL INVESTIGATION OF TENSION-STRUCTURE PARAWINGS

by Rodger L. Naeseth and Paul G. Fournier

Langley Research Center

Langley Station, Hampton, Va.

NATIONAL AERONAUTICS AND SPACE ADMINISTRATION • WASHINGTON, D. C. • JUNE 1967

NASA TN D-3940

LOW-SPEED WIND-TUNNEL INVESTIGATION OF TENSION-STRUCTURE PARAWINGS

By Rodger L. Naeseth and Paul G. Fournier

Langley Research Center
Langley Station, Hampton, Va.

NATIONAL AERONAUTICS AND SPACE ADMINISTRATION

For sale by the Clearinghouse for Federal Scientific and Technical Information
Springfield, Virginia 22151 – CFSTI price $3.00

LOW-SPEED WIND-TUNNEL INVESTIGATION OF TENSION-STRUCTURE PARAWINGS

By Rodger L. Naeseth and Paul G. Fournier
Langley Research Center

SUMMARY

Low-speed wind-tunnel studies were made to obtain the static aerodynamic characteristics of numerous tension-structure parawings. These all-flexible parawings were made of nonporous fabric and were attached to a mounting bar by means of multiple suspension lines.

Planform variations investigated included sweep angles of 40°, 45°, and 50°, different amounts and shapes of cuts which removed the apex of the wing, and variations in the shape of the flat-pattern leading edge. Also studied were the effects of adding stiffness to the keel by the use of flexible battens or by the use of a ram-inflated fabric tube on the keel. The basic wing configuration selected for detailed study had 45° leading-edge sweep of the flat pattern and 1/8 keel length of the apex removed. Longitudinal- and lateral-control information and line-tension data were obtained on the basic wing for a very limited range of wing angles of attack. Tests of the basic wing were also made with an apparatus which supported the canopy so that angles of attack up to 90° could be investigated. Some limited sideslip data were also obtained for the basic wing with this apparatus.

The maximum lift-drag ratio obtained for the basic all-flexible wing was about 2.4 and the maximum lift coefficient obtained was about 1.0. The longitudinal-stability characteristics indicated that the basic wing could be trimmed and had positive static stability over the angle-of-attack range from conditions of maximum lift-drag ratio up to stall. Static longitudinal instability was indicated for a range of angles of attack above wing stall. Of all the configurations investigated, only the stiffened-keel models showed substantially higher lift-drag ratios than the basic wing and these models provided maximum lift-drag ratios of approximately 3.2.

INTRODUCTION

The National Aeronautics and Space Administration is continuing the investigation of parawings in order to develop more fully the tension-structure-wing concept of reference 1. Parawings have lifting surfaces with flexible membranes of relatively large

curvature so that the lift may be sustained with a minimum of bending and compression load in any part of the structure. Performance can generally be improved, however, by the judicious addition of local stiffening. Parawing stiffening can be located in the membranes, either concentrated as in sail battens or spread more evenly through the membrane, but stiffening is generally found only in the frame to which the membrane is attached. Application of the concept leads to light and rugged wings. The nonstiffened version has modest lift-drag ratios and can be packed like a parachute. The stiffened version has higher lift-drag ratios, is lightweight, and may have a folding rigid structure or an inflatable structure. Past work (refs. 2, 3, and 4) has indicated the aerodynamic characteristics of parawings with both rigid and inflatable structural members. The inflatable type has the advantage of compact packaging.

Designs based on the fairly wide range of wing efficiency shown in references 2 to 4 and others have been developed or proposed for many applications. However, the inevitable complications involved in carefully sequenced deployments of some of these wing designs and the fact that some applications require only moderate values of lift-drag ratio have led to renewed interest in the all-flexible tension-structure parawing. An all-flexible parawing configuration was first flown in small sizes as a kite and a glider in 1948. Recently, intensive development work on the all-flexible parawing has been done. This work includes the wind-tunnel work of this paper and more than 50 manned deployments and flights (ref. 5). The manned flights were initiated by the U.S. Army parachute team and the John F. Kennedy Center for Special Warfare at Fort Bragg, North Carolina, who were favorably impressed by its simplicity, dependability, stability, performance, and control. A more recent series of flight tests is discussed in reference 6.

Recent wind-tunnel work on the all-flexible parawing has concentrated on 2-foot-long (0.6096-m) models and 5-foot-long (1.5240-m) models based on the previous rigid leading-edge and keel models with leading-edge sweep angle of 45°. The wings were made of acrylic-coated rip-stop nylon and were made capable of gliding flight by proper rigging of multiple suspension lines. This report presents primarily the results of wind-tunnel tests of 5-foot-long (1.5240-m) models made to measure the aerodynamic characteristics of all-flexible parawings and to investigate other possible planforms and modifications to a 45° swept planform. Subsequent tests of a combination of a 7.833-foot (2.388-m) wing and a lifting body are reported in reference 7.

The basic model investigated was derived from a pointed wing which had leading edges and keel of equal length, 45° sweep of the canopy flat pattern, and the nose cut off at 1/8 keel length aft of the theoretical leading-edge apex. Planform variations tested included leading-edge flat-pattern sweep angles of 40°, 45°, and 50°; nose cuts of 0, 1/8, 1/4, and 3/8 keel length; and variations of leading-edge line attachment and leading-edge curvature. The use of flow control slots in the canopy was investigated. The effect of

line length and line stretch on the aerodynamic characteristics of the wing was also investigated and the effect of roll and pitch control on the attitude of the model in the tunnel was measured. In the area of minimum-structure wings, the characteristics of wings with flexible keel battens and with ram-inflated stiffeners were obtained.

The tests were made at dynamic pressures ranging from 0.50 lb/sq ft (23.9 N/sq m) to as high as 3.00 lb/sq ft (143.6 N/sq m) and angles of attack from the lowest angle at which the nose tended to collapse to about 60°. These tests were made with the model tethered to a mounting bar by multiple suspension lines. To obtain the stability characteristics of the basic model for a wide range of angles of attack and a limited range of angles of sideslip, tests were made with an apparatus which supported the model at the confluence of the suspension lines and at the canopy so that a range of angles of attack from 24° to 90° could be investigated for other than trimmed conditions. Tests were made in the 17-foot (5.18-m) test section of the Langley 300-MPH 7- by 10-foot tunnel.

SYMBOLS

The data presented in this report are referred to the axis system shown in figure 1. Inasmuch as there was no well-defined reference line on the wing for use in defining wing angle of attack, the angle of the seventh line back on the keel with respect to the vertical was generally taken as the angle of attack. The reference area used in determining the coefficients was the area of the wing-canopy flat pattern, and the reference length was the keel length, except in the cut-off-nose series for which all coefficients were based on the pointed-wing geometry. All dimensions are presented in nondimensional form obtained by dividing the measured lengths by the theoretical keel length of the wing.

A aspect ratio, $\frac{b^2}{S}$

b span of inflated wing canopy, feet (m)

b_o span of wing flat pattern, feet (m)

C_A axial-force coefficient, $\frac{\text{Axial force}}{qS}$

C_D drag coefficient, $\frac{\text{Drag}}{qS}$

C_L lift coefficient, $\frac{\text{Lift}}{qS}$

$C_{L,max}$ maximum observed lift coefficient

C_m pitching-moment coefficient, $\frac{\text{Pitching moment}}{qSc}$

C_N normal-force coefficient, $\frac{\text{Normal force}}{qS}$

C_n yawing-moment coefficient, $\frac{\text{Yawing moment}}{qSb_o}$

C_{n_β} yawing-moment parameter, $\frac{\Delta C_n}{\Delta \beta}$, per degree

C_T tension coefficient, $\frac{\text{Line tension}}{qS}$

C_Y side-force coefficient, $\frac{\text{Side force}}{qS}$

C_{Y_β} side-force parameter, $\frac{\Delta C_Y}{\Delta \beta}$, per degree

C_l rolling-moment coefficient, $\frac{\text{Rolling moment}}{qSb_o}$

C_{l_β} rolling-moment parameter, $\frac{\Delta C_l}{\Delta \beta}$, per degree

c length of keel of wing, l_k, minus length of nose cut off, feet (m)

d_1, d_2, h_1, h_2, y displacements of control lines from center of moments (see fig. 4), inches (cm)

L/D lift-drag ratio, $\frac{C_L}{C_D}$

$(L/D)_{max}$ maximum observed lift-drag ratio

q free-stream dynamic pressure, lb/sq ft (N/sq m)

S area of wing-canopy flat pattern, square feet (sq m)

x,l linear dimensions, inches (cm)

x/l_k nondimensional distance to line attachment point from apex along wing leading edge or wing keel

l_k length of keel of theoretical wing-canopy flat pattern measured from theoretical apex to the trailing edge at the plane of symmetry, inches (cm)

l/l_k nondimensional length of keel and leading-edge suspension lines measured from wing leading edge to top of clamping block, line length/l_k

α angle of keel line number 7 measured from normal to wind stream when viewed from side, positive for rearward displacement of line. (For some models, keel line number 7 was not convenient to use; thus an alternate line is indicated on geometric drawing accompanying data.), degrees

α_B angle between normal to wind stream and balance axes for constrained-model tests, degrees

β sideslip angle, degrees

$\Delta\alpha = \alpha - \alpha_B$

$\Delta l/l_k$ incremental nondimensional length of a line

θ angle from vertical of any line projected in plane of symmetry, degrees

Λ_o angle of sweepback of leading edge of wing-canopy flat pattern, degrees

ϕ angle from vertical line to any leading-edge line projected into a plane normal to the relative wind, degrees

ϕ_w wing roll angle defined as angle between keel lines and vertical when viewed from rear, positive for right wing down, degrees

Subscripts:

k keel

le leading edge

DESCRIPTION OF MODELS

Basic Configurations

Preliminary exploratory work to determine rigging requirements for steady glide was done with models having various planform shapes and having a keel length of 2 feet (60.96 cm). Most of this work was done by hand-launching models in still air. These preliminary tests indicated a problem with the apex of a pointed wing. The apex was found to turn to the side and stay or if unloaded slightly was pulled down by the weight and drag of the nose lines. The problems of nose collapse could be greatly alleviated by removing the part of the apex that tended to fold back in flight. A basic wing configuration that had 45° flat-pattern sweep, leading edges and keel of equal length for the theoretical planform, and a straight nose cut perpendicular to the keel which removed the forward one-eighth of the keel length was selected from these small model tests. This configuration is referred to as the basic model. A sketch detailing the construction of the basic wing is presented in figure 2, where all dimensions are given in terms of the theoretical keel length. Photographs of the basic wing in the tunnel are given in figure 3. All wind-tunnel data for the basic planform were obtained for models with a theoretical keel length of 5 feet (1.5240 m). A triangular-planform wing with 3-foot (0.9144-m) keel was also tested.

Most of the test wings were constructed of rip-stop parachute nylon with an acrylic coating applied to make the fabric nonporous. The weight of the canopy material was approximately 1.1 ounces/square yard (37.2 g/sq m). Sewing was avoided and all joints were made with an elastic adhesive because it was believed that this joint contributed less local stiffness. The joint overlap was 0.0083 l_k. The weave of the fabric was oriented so that the fill was parallel to the trailing edge and, therefore, the keel and leading edges were cut on the bias. No seams or reinforcements were made to the leading and trailing edges and fraying of the fabric edges was avoided by cutting the material with a hot iron.

Line attachments to the wing were made by tying off a loop of nylon rope and fraying the loose ends of the rope to form a fan patch which was attached to the upper surface of the wing with an elastic adhesive, as shown in figure 2. The suspension lines for the wings were nylon cord of about 1/16-inch (1.6-mm) diameter, except in two instances when 1/32-inch (0.8-mm) steel cable was used. The nondimensional line lengths and line locations used in rigging the various models are summarized in table I. The lines were held at the confluence point in a clamp as shown in figure 4. Dimensions pertinent to the location of the line attachments of figure 4 are given in table II for each data figure. A complete basic canopy weighed 0.34 pound (0.154 kg) and a set of nylon lines weighed about 0.26 pound (0.118 kg).

Modified Configurations

Wing-planform variations studied in the wind-tunnel tests are shown in figure 5. A detailed drawing of each wing is given just prior to the associated aerodynamic data. The descriptions of the modified wings are concerned only with factors which were different from the basic wing.

Wing-sweep series.- Wings with leading-edge sweep angles of 40°, 45°, and 50° were investigated in wind-tunnel tests. Sketches of the swept-wing series are included in figure 5(a).

Curved-planform series.- The geometry was derived from the basic wing but had 1.25 l_k arcs at the leading edge and either straight or 1.00 l_k arcs at the trailing edges. The lines were evenly spaced along leading edge and keel. The straight-trailing-edge model was tested with 1/8 l_k nose cut off and with 0- and $7\frac{1}{2}$-percent boltrope in the trailing edge. Sketches of these planforms are given in figure 5(a).

Cut-off-nose series.- In this series of tests a $\Lambda_o = 45°$ model was tested with pointed nose and with nose cut off in straight cuts at 1/8 l_k, 1/4 l_k, and 3/8 l_k from the theoretical planform apex (fig. 5(a)). A 0.010- by 0.750-inch (0.025- by 1.905-cm) mylar batten which was crimped down the center and taped to the keel from the nose to the 0.45 l_k keel point was used for the pointed-wing tests. In addition to the straight cuts, circular-arc cuts were made at these locations with the intention of removing material which appeared to be luffing and carrying little load. Single- and double-radius cuts were made as shown in figure 5(a). Lines had to be added for the single curved cuts at the point the curved cut intersected the leading edge.

Slotted-wing model.- A 5-foot-long (1.5240-m) wing was constructed of the same fabric used for the basic wing but had a canopy with five overlapping panels which were joined only at the overlap at the keel and leading edges. The suspension lines to the leading edges were continuous from the clamping block to one leading edge, through a pocket in the leading edge of the panel, through the opposite wing panel, and back to the clamping block. These lines were made 7 percent shorter than the flat pattern of each leading edge and were stitched to the keel and at the points where they pass through the leading edge (7-percent boltrope shortening). Nylon loops for line attachment were attached to the bottom surface of the wing by stitching the free ends to the wing. A boltrope was also installed in a pocket in the wing trailing edge, and the boltrope shortening was 5 percent of the flat-pattern length. A sketch of the slotted wing is presented in figure 5(a).

Parabolic-suspension models.- An investigation was made of one means of transferring loads from the canopy material to the lines. A 500-pound (2224.1-N) tape was sewed to the canopy material between lines in a parabolic pattern. (See fig. 5(a).) Tests

were made with the tape sewed on a basic wing and with the material enclosed by the tapes cut out.

Keel-batten models.- A series of pointed wings with leading-edge sweep angles of 40°, 45°, and 50° was tested. A 0.010- by 0.750-inch (0.025- by 1.905-cm) mylar batten which was crimped down the center and taped to the keel of each wing (fig. 5(b)) was necessary to overcome the problems associated with nose collapse, as discussed at the beginning of this section. A triangular wing of $\Lambda_o = 45^{\circ}$, straight trailing edge, and a 3-foot (0.9144-m) keel length was also tested. (See fig. 5(b).)

Inflatable keel models.- One method of local stiffening is the ram-air-inflated type. A basic 45° swept model was given keel stiffness by sewing on a 12-inch (0.3048-m) strip centered on keel which could be inflated to form a tube (fig. 5(b)). Ram air was supplied through a smaller cloth tube with the forward-facing open end tied to a keel shroud line at a point below the canopy. The front end of the keel stiffening tube was closed by a cloth hemisphere. Tests were also made with the hemisphere and ram-air tube removed to form a ram-air-inflated model with a nose inlet.

EXPERIMENTAL PROCEDURE

Static wind-tunnel tests were conducted in the 17-foot (5.18-m) test section of the Langley 300-MPH 7- by 10-foot tunnel. Most of the results were obtained for a range of dynamic pressure from 0.5 to 2.0 lb/sq ft (23.9 to 95.8 N/sq m). The Reynolds number based on 5-foot-long (1.5240-m) models was 1.2×10^6 at $q = 2.0$ lb/sq ft (95.8 N/sq m).

Pretest Check of Rigging

Valuable information on the proper relationships of the various line lengths for steady-glide conditions was obtained in the early exploratory free-glide tests of small models. A technique which was also found to be particularly useful in obtaining the proper rigging was to lay the wing on the floor with the top surface down and apply a steady upward pull. If the wing was properly rigged, it would immediately inflate and transfer some of the vertical motion into horizontal motion.

Tethered Method of Testing

The model could not be tested in the tunnel with the one-point suspension system used in preliminary free-gliding-flight tests because the model diverged when tethered to the tunnel strut. Modifications had to be made to the point suspension, therefore, in order to obtain tunnel data. The attachment points of the rear keel and tip lines were moved aft to stabilize the model in pitch attitude, and the attachment points of the tip

lines were moved outboard to stabilize the model in roll attitude. Sketches of the wind-tunnel line-attachment configurations at the balance are shown in figure 4. Dimensions pertinent to the offset of the line attachments from a one-point-payload suspension system are given in table II for each data figure. Tests made in this manner will be referred to as tethered tests. Tests were made through a dynamic-pressure range for angles of attack limited at the low end of the range (highest L/D) by the angle at which the nose just started to tuck under and at the high end of the range by angles at which instability occurs. The aft-keel line and/or tip lines were used to set the angle of attack, and a differential deflection of the tip lines was used to set roll attitude. These attachment arrangements were not fully satisfactory for all wings or for the full desired angle-of-attack range; however, they provided very good attitude stability for the low angles at which the best lift-drag ratios were obtained. Longitudinal and lateral oscillations prevented obtaining data at angles of attack in excess of about 65° with the line attachments used. This rigging-mount data would be only directly applicable to a payload on which the lines could be similarly attached.

Data were obtained by means of a six-component strain-gage balance, which was mounted to a single-support strut attached to the tunnel floor or to a sting which gave the same balance location in the tunnel.

The lines of each model were held by a single clamp. A clamp was provided for each model to facilitate transfer of the complete model to the tunnel for test. The clamp was made up of six 1/8-inch (0.318-cm) laminations consisting of four inner pieces of wood to provide three separate clamping spaces for the leading-edge and keel line groups and two steel outer pieces for strength.

Constrained Method of Testing

The second method of testing was used in order to obtain data through a large angle-of-attack range with the control-line lengths fixed. A support frame, shown in the sketch and photographs of figure 6, was used as a means of moving the canopy off of its trim position in pitch and sideslip as required. All lines were attached at the confluence point. To measure the forces and moments, balances were used at the confluence point, at the lateral guide bars, and on a pin which extended through a hole in the canopy (fig. 6(a)). This pin was a loose fit in the canopy so that the restraint was effective only in the roll and pitch directions. By using a balance at each point of attachment to the model, the frame tare was largely eliminated. The frame was mounted on a sting arrangement which moved through angles of attack from 22° to 88° in three overlapping ranges. Tests were made at sideslip angles of 0° and $\pm 4^{\circ}$.

The model tested on the support was a basic wing; however, to eliminate line-length variations throughout the tests, 1/32-inch (0.8-mm) steel lines were fitted to the

model. The procedure in the tunnel was somewhat different for the constrained tests than for the tethered tests. After attachment of the model to the support apparatus, the wing was carefully draped on the balance so that weight tares could be obtained throughout the angle range. This procedure obviously cannot be carried out as precisely for a flexible model as for a rigid model; however, the data are believed to be essentially free of model-weight effects. Tests were made with various adjustments to the lines to obtain a range of trim angle of attack. These adjustments were made by observing the pin projecting through the canopy and by noting a change in the moment as indicated by a change in direction of the force exerted on the canopy by the pin.

Angle-of-Attack Measurements

Angles of attack were obtained from visual measurements of the angle of the seventh keel line with respect to the vertical on most of the wings. The angle-of-attack reference for the rigid-frame apparatus was the balance axis (fig. 6(a)). The small angle between this reference and the seventh keel line is plotted with the aerodynamic data.

Line-Tension Measurements and Analysis

Measurement of line tension was considered necessary from the standpoint of determining corrections to account for line stretch in designing the rigging for a gliding configuration. Also, from line tensions along with line directions, some canopy loading characteristics could be calculated.

Line-tension measurements were made with a hand-held tensiometer developed during these tests. (See fig. 7.) This type of gage was used to obviate the difficulties associated with building, installing, and calibrating the wide range of individual gages needed for the approximately 25 lines of each model. The tensiometer had a wide range of sensitivity which was necessary to measure forces from very light to 5 pounds (22.24 N) and the output was compatible with the data readout system. Measurements were made at dynamic pressures of 1.0 and 2.0 lb/sq ft (47.9 and 95.8 N/sq m) at which speed it was safe to enter the tunnel.

Nylon lines chosen for the flight tests because of their strength and resistance to wear and shock were used in the wind-tunnel tests. The stretch characteristics of the line, however, gave rise to problems in the measurement of the line lengths. Prestretching the lines and measuring line lengths with a constant small load reduced the difficulties. A brief experiment indicated that the prestretched nylon line used stretched 0.0037 inch per inch per pound (8.32×10^{-4} cm per cm per N) for loads up to about 10 pounds (44.48 N).

Automatic 70-mm cameras were used to record the canopy shape and line angles from top, side, and rear locations. This film was read with a cathetometer to obtain line angles and locations to be used in resolving tensions into lift and drag forces and pitching moments.

Corrections to Data

The tunnel-wall corrections have not been applied to most of the data but were found to be relatively small for a 5-foot-long (1.5240-m) model in the 17-foot (5.18-m) test section. Jet-boundary corrections to angle of attack and drag coefficient and blocking corrections to dynamic pressure, as determined from references 8 and 9, have been applied to constrained-model test results.

PRESENTATION OF DATA

The present test results were obtained in an investigation of a considerable number of similar models. In order to avoid possible confusion in matching results with configurations, the data obtained for each model is preceded by a detailed drawing and photographs of the model. Details of the line lengths and attachment locations are given in tables I and II and figure 4. The data consist of longitudinal aerodynamic characteristics over a dynamic-pressure range, one or more figures showing line lengths and rigging variations, and for many of the models, line-tension data at one or more angles of attack and line angles. Note that some of the test techniques and equipment were developed as the work progressed and therefore all the measurements for the various models were not obtained.

In the present test results on flexible models, the usual sources of error accompanying tests of conventional rigid wind-tunnel models are present. In addition to these possible uncertainties, tunnel time available and the skill of the test engineer in working with the many possible riggings that can be obtained with approximately 25 lines enters into the determination of whether one wing configuration can be considered better than another.

To relate the details of the wing geometry and test results, a summary of the models, results (L/D and $C_{L,max}$), and figures in which they appear is given in table III. A measurement of the span of some wings b/l_k is also included in the table. The data and test results are presented in the following figures:

	Figure
Planform variables:	
Wing-sweep series –	
$\Lambda_o = 40^o$	8 to 10

DISCUSSION

Planform Variables

Effect of flat-pattern sweep.- Variations in wing flat-pattern sweep angle of $\pm 5^{\circ}$ from the basic wing were investigated. Force data for these wings showing the effect of angle of attack are presented in figures 9, 12, 15, and 18, and a comparison showing the effect of flat-pattern sweep angle is given in figure 21. These results show that both the 40° and 45° swept wings provided lift-drag ratios of about 2.4, whereas the 50° swept wing gave a value of about 2.1. The angle of attack at which the nose began to deform, the lower limit of the test, was less for the 40° and 45° swept wings than for the 50° swept wing. The wings, as will be shown, operate above theoretical $(L/D)_{max}$; thus, wings which reach low angles of attack, and hence low C_L, show the best L/D.

Effect of nose planform.- Early flight tests indicated a tendency for the nose to collapse when the planform extended to the apex. Because the $1/8\, l_k$ cut off made to alleviate the problem (basic model) was arbitrary, a series of curved and straight cuts were made on a $\Lambda_o = 45^{\circ}$ pointed model to investigate briefly the effect of nose planform (figs. 23 to 34). Several items, some of which have been previously mentioned, must be considered in analysis of the data. The coefficients are based on the geometry of the pointed model; the line attachments are at different locations than on the basic wing; and extra lines were necessary for the single-radius cuts.

The pointed planform was rigged and tested with the batten installed. After this test, the wings were cut and tested with the least amount of change in this rigging needed to obtain a fairly good flying model. (See fig. 25.) Other than for the pointed planform on which the rigging was experimentally worked out, some of the planforms could possibly have been improved by spending much more time on each rigging.

Observations of the models in the tunnel and the data of figures 24, 27, 30, and 33 lead to these conclusions. The pointed-nose model with the keel batten could be tested at a low angle of attack and gave a relatively high lift-drag ratio. The straight-cut planforms $1/8\, l_k$, $1/4\, l_k$, and $3/8\, l_k$ did not differ a great deal in lift-drag ratio. The $3/8\, l_k$

cut model had a smooth appearance (fig. 23(b)) but had a fore-and-aft oscillation of the tips. Based on the planform area of this model, the lift coefficient would be about the same as that of the pointed model. The curved cuts, especially the single curves (for example, fig. 29) formed hard-to-manage pointed areas of fabric at the most forward suspension-line attachment. The small area produced small forces at low angles of attack with the result that the points were pulled down by the line weight and drag. Therefore, these configurations generally had to be rigged to higher angles of attack and lower L/D values than were obtained with the straight cuts.

Effect of leading-edge planform.- The problem of transferring loads from the wing canopy to the multiple suspension lines was of interest because a lightweight canopy and the smoothest aerodynamic shape were desired. A possible method of line attachment and reinforcement of the leading edge and keel is shown in figure 35. A reinforcing tape (500-pound (2224.1-N) parachute line) was sewed to the canopy material of a basic wing in a parabolic pattern between the line-attachment points. These data are presented in figures 36 and 37. The model was also tested with about one-half of the depth of the material enclosed by the reinforcement cut out, cut A, and with all the material cut out, cut B (figs. 38 to 42). The data are based on the uncut area. The parabolic suspension patches appeared to distribute the load over the canopy as is indicated by the less distorted canopy of the model with parabolic suspension patches (compare the model of fig. 38(b) with the basic model of fig. 3). A slight eyebrow appearance of the material between the parabolic suspension patches at the leading edge indicated transfer of the local loads to the suspension patch. One effect on the force data is the smooth appearance of the data of figure 36 as compared with the basic data of figures 12 and 15; however, the maximum lift-drag ratio values were about the same.

The removal of the material outlined by the parabolic-suspension patches had an effect on the appearance and the aerodynamic characteristics of the model. A comparison of the basic parabolic-suspension-patch model and cut-B model of figure 38(b) for similar test conditions indicates a deeper parabolic form between lines and a somewhat different stress pattern in the canopy for the cut-B model. The more curved keel of the cut-B model is shown in the photographs and in the plane of keel rigging (figs. 38(b), 40, and 42). As shown in figure 39, removal of the material increased the minimum angle at which the model could be rigged and caused a loss in lift-drag ratio. If the depth of the cuts had been graduated from the nose to the wing tip or if some material had been added at each leading-edge suspension line instead of cutting deeply, better performance might have been shown. In designing for deployment loads, it is believed that some reinforcements for carrying the line loads into the keel and leading edges would be necessary.

A more rounded planform was of interest from several viewpoints. A wing with curved leading edges and trailing edges being more like a parachute could have better deployment characteristics and perhaps more even line-load distributions. A curved

trailing edge might eliminate the flap-like appearance of the trailing edge in the vicinity of the keel (fig. 3(b)) and a curved leading edge might improve the model characteristics by straightening the leading-edge curve in flight (fig. 3(c)). The results of tests of curved planforms are given in figures 43 to 54. (The angle of attack was measured on the sixth line aft of the nose of these models.)

Details of the curved leading-edge and trailing-edge models are given in figure 43(a) and in the photographs of figure 43(b). The wing leading edge in flight was nearly straight as expected (fig. 43(b), rear view) and the keel appeared less sharply curved down at the aft end. (See front three-quarter view of fig. 43(b).) However, the curved trailing edge did not appear to be carrying load well as indicated by the upward reflex of the trailing edge in the photograph. The maximum lift-drag ratio was 2.2 (fig. 44). The tension coefficients (fig. 45) show higher loads on the forward keel and a somewhat more even load distribution than for the basic model (fig. 16(a)).

A curved-leading-edge model with a straight trailing edge (fig. 46) was also tested and gave results similar to those obtained for the model with the curved trailing edge. These models were the only ones without stiffening in the nose that could be tested without cutting off the apex. This behavior is attributed to the low sweep angle of the leading edge at the apex. A careful examination of figure 43(b), front three-quarter view, however, shows some collapse occurred at the apex. Therefore, a model with 1/8 l_k nose cut off was tested (fig. 51). The model with and without trailing-edge boltrope had about the same $(L/D)_{max}$ as the other models in this series. Boltrope used in the trailing edge appeared to allow the aft-keel line to be lengthened somewhat (figs. 53 and 54) with the relatively smooth line-load distribution resulting, as shown in figure 53.

Slotted wing.- A 45° swept, slotted wing was formed by overlapping panels of fabric which were joined only at the leading edges and keel (figs. 55 to 57). The leading edge of each panel was placed under the trailing edge of the next forward panel in an arrangement similar to slotted flaps. The rigging for this model (fig. 57) was considerably different than that for the basic model (fig. 16). The maximum lift-drag ratio for the slotted-wing model was considerably less than that for the basic wing; the minimum angle of attack and the minimum lift coefficient were relatively high. The difference in the angle of attack is partially due to the fact that the reference line for angle of attack was located at 0.667 l_k, somewhat more aft than the 0.645 l_k location on the basic wing. Boltrope was necessary to shape the panels properly, especially in the trailing edge. Figure 55(b) suggests that more shaping of the panels, more overlap, and more ties connecting the panels are needed. The results from the one slotted wing (fig. 56) indicate that slots may be a useful device because a large lift coefficient could be developed by the wing. The slots also may possibly be arranged for alleviation of deployment loads. Although the lift-drag ratio was not high, with more extensive work it may be improved.

Effect of Rigging Changes on Basic Wing

Modulation of lift and lift-drag ratios.- Results are presented in figure 14, which is a crossplot of figure 12, to indicate the extent that C_L, α, and L/D have been varied in tunnel tests by rigging changes for the basic model. For these tests, only the lengths of the wing-tip and keel trailing-edge lines were varied, as indicated in the top part of the figure. The initial angle of attack and rigging condition selected was the condition for maximum lift-drag ratio which occurred just before the nose started to tuck under. The control-line lengths were shortened from this condition to provide two increases in angle of attack. The angle-of-attack range was from about 26° to 45°. The lift-drag ratios varied from 2.4 to 1.2 for the angle-of-attack and dynamic-pressure ranges investigated. The maximum angle of attack was limited in the tunnel tests to angles for which the model was longitudinally and laterally stable in the tunnel. Experience with static tunnel tests and free-glide tests of the same wing has indicated that the infinite-mass payload constraint in the tunnel tests may impose somewhat more severe or possibly different stability problems than the free-flight condition in which the payload can respond to disturbances.

A point-mounted model with stable static stability characteristics should maintain a trim position in pitch. However, for a weightless canopy, the model could take any roll-angle position and at this position the lateral-directional parameters should tend to keep a perfectly trimmed model alined in the tunnel, but the roll parameter would tend to move it to different roll angles in response to disturbances. The weightless canopy was specified because canopy weight favorably located can give a small righting moment to keep the model vertical or properly oriented about the balance system of axes. Of course, this weight moment decreases in relation to aerodynamic moments as the dynamic pressure is increased. Marginal static stability and oscillatory problems, including those involving the changing of the shape of the canopy, can make it difficult to obtain good tunnel data, and therefore, data were obtained only for stable conditions.

The control lines were displaced from the confluence point for most tests. This arrangement provided data directly applicable to a payload shape on which the lines could be located the same as in the tunnel tests and the pitching-moment coefficient could be trimmed out. Line stretch and the effect of canopy weight must be considered in applying these results. The canopy weight contributes a more negative moment in gliding flight than in tests in a horizontal tunnel. Generally, as discussed previously, the lines had to be spread laterally to keep the roll orientation of the model vertical; however, after careful trimming, one test was made with the lines essentially at a point (figs. 58 to 60). The data are compared (fig. 59) with a model having rear lines moved aft. The point confluence test shows similar data with slightly lower lift-drag ratios and smaller values of pitching moment. The fact that the lines were not clamped at a point because of the physical size of 23 lines may be the cause of the pitching-moment coefficient shown.

Roll control.- Free-flight tests of the basic wing have indicated that directional control could be simply obtained by shortening the wing-tip line to the wing on the inside of the desired turn. Since the parawing responded to a downward deflection of the tip in the opposite direction to a flap-type aileron control, it appears that line shortening does not operate as a flap-type control. It is believed therefore that control by wing-tip lines of the all-flexible parawing was achieved partly by changes in canopy shape and partly by shifts in the center of gravity. Also note that in applying control differentially, the amount of up-going control-line motion is limited to the point the trailing-edge flaps free and the next line ahead becomes the loaded line.

Some measure of the effect of tip-line roll control was obtained in the tunnel by progressively shortening the line at one tip or differentially applying control. The tunnel data from these tests are presented in figure 61 in terms of wing roll angle as a function of the line-length reduction from the initial trim position of 0^{o} roll. The sketch in figure 61 shows a rear view of the model on the support strut and the spread attachment for the tip lines. The tip lines were spread to allow steady-state roll angles to be obtained as previously discussed. The results presented in figure 61 show that the control produced a roll angle in the tunnel which was linear with line-length reduction for angles up to about 40^{o} and that the result was the same with differential control as with shortening of only one line. Very little sideslip was observed during the tests, even for the highest roll angles reached.

These static data indicate that the tip lines when displaced laterally on the mounting bar can stabilize the model at various roll positions in the tunnel. From the aforementioned, the usefulness of the tip lines as controls may be inferred; however, there is need for more tests before free-flight turn characteristics can be computed.

Effects of dynamic pressure and line stretch.- The force data of figures 9, 12, and 18 show an appreciable variation with test dynamic pressure. Part of this variation was due to stretch in the nylon lines and canopy, which generally resulted in a reduction in angle of attack since the aft lines are most heavily loaded. The test results presented in figure 62 show a comparison of data obtained with steel cables and with nylon lines. At dynamic pressures above 1.0 lb/sq ft (47.9 N/sq m), there was very little variation of lift coefficient or angle of attack with dynamic pressure for the model with the steel cables. In general, the lift coefficient and angle of attack were slightly lower with the steel cables and the lift-drag ratios obtained with the steel cables were slightly higher than those obtained with the nylon lines. A higher lift-drag ratio would be expected with the steel cables inasmuch as the diameter of the cables was one-half the diameter of the nylon lines. The total frontal area of the nylon was about 100 square inches (0.065 sq m).

Effect of keel-line shortening.- A controlled change of effective wing area is a possible method of modulating lift if the changes produced by angle-of-attack variation are

not considered great enough to do so. One method proposed for changing the effective area of the wing was keel-line shortening, in which the upper surfaces of the fabric on each side of the keel are made to come together by shortening the keel lines (figs. 65 to 69). As shown in figure 69, the keel was pulled from the basic position above the leading edges to a position below the leading edges. The desired changes in geometry were not obtained because the nose area tended to come together but the large aft area where the greatest reduction in area was desired showed very little change in area. The results of force measurements (fig. 65) indicate some loss in lift (about 10 percent) for the smallest shortening of the keel lines; however, an approximately equal rise above the basic level of lift coefficient was indicated for keel-line length 2. Apparently, some shortening of the keel lines from the original rigging caused an increase in maximum lift coefficient with little or no change in lift-drag ratio.

Effect of keel-payload distance.- The basic keel-payload distance was chosen from parachute practice as a nominal $1.25\,l_k$. This distance is of more significance in regard to a gliding wing than in regard to a parachute because the drag of the lines decreases the gliding efficiency, the vertical center-of-gravity position affects stability, and the angle of the lines at the canopy affects projected area and span. To investigate the effects of reducing the keel-payload distance on the characteristics of a basic model, distances of $1.25\,l_k$, $1.00\,l_k$, and $0.75\,l_k$ were investigated (figs. 70 and 71).

The data of figure 70 indicate an increase in lift-drag ratio when the keel-payload distance was reduced from $1.25\,l_k$ to $1.00\,l_k$ and a reduction when the distance was reduced from $1.25\,l_k$ to $0.75\,l_k$. Apparently, some reduction of keel-payload distance may be of advantage from consideration of lift-drag ratios. This conclusion is believed valid even though a higher L/D value is shown for a keel-payload distance of $1.25\,l_k$ in figure 12 than is shown in figure 70 for a keel-payload distance of $1.00\,l_k$ because the general rigging of the two models is significantly different. (See figs. 13 and 71 for rigging designs.) Examination of the line lengths plotted on figure 71 indicates that the reduction of keel-payload distance from $1.25\,l_k$ to $1.00\,l_k$ was made with relatively little change in the shape of the keel and leading edges, but that the further decrease to $0.75\,l_k$ was more drastic and required many rigging changes to make the test model inflate properly in the tunnel.

Local Stiffness Experiments

Keel-batten stiffening.- The use of a mylar keel stiffener made testing of the sweep series of models with pointed noses possible. Sketches of the wings are given in figure 72. A triangular wing with 0^o trailing-edge sweep was included. The stiffener used was bent to a V-shaped cross section so that in addition to compressive strength, it provided considerable bending stiffness. The data are plotted in figures 73 and 76 and

summarized in figure 81. Data were not obtained over the complete dynamic-pressure range for all models because the compressive loads caused the taped-on stiffener to buckle or to come loose at the high loads. From observations in the tunnel, the triangular wing appeared to have the lowest compressive loads in the keel and also showed about the best lift-drag ratio, 3.22. Results of tests of a short stiffener, 0.325 l_k, on a modified pointed wing (figs. 78 to 80) indicated a somewhat lower lift-drag ratio than was obtained with the pointed wings.

The use of stiffeners complicates packing design and may cause an operational problem as it did in the tunnel. A nonstiffened apex which folded under could be restored by a pull on the control line, whereas a model with a stiffened apex required careful manipulation to restore it to flying condition.

Ram-air-inflated keel stiffener.- The objections to adding structure to the wings are largely overcome if a ram-air-inflated stiffener is used. Ram-air inlets located at the front of a vehicle are capable of yielding full ram pressure, but this location of the inlets usually results in a poorly streamlined front end and, hence, a high drag which reduces the performance gain which might have been realized from the addition of the stiffening. A method of inflating a keel stiffener tube by means of a fabric tube located aft on the keel is shown in figure 82 and a nose inlet model is shown in figure 86. The inlets for both models were made of fabric and were found easy to inflate and test in the tunnel. The results (figs. 83 and 87) show that the maximum lift-drag ratio was about the same, 3.15, at low dynamic pressures, but the rear-inlet model showed higher lift-drag ratios over most of the range of dynamic pressures. Lift coefficients were lower for the inflated-keel models than those of the basic wing and the possible variation of lift coefficient was about the same as that obtained with the basic wing (compare fig. 15 with fig. 83). The operating difficulties which limited the low end of the angle range did not originate with the inflatable part of the model but with the leading edge of the wing which tended to collapse at low angles of attack. Experience with the wings indicated that although all the gains anticipated from use of the designs were not realized, a basis for further profitable experiment was established.

The rigging for these wings was different than that for the basic wings, as may be seen by comparing figures 16 and 84. The rather straight-line character of the keel well below the leading edge was much different from the rigging of the basic wing. Although the tension coefficients on these figures are not directly comparable because of the difference in angle of attack, the higher loads in the forward part of the inflated keel and the low loads of the forward leading-edge lines may be noted.

Experimental and Estimated Drag

A comparison of experimental and estimated drag coefficients and lift-drag ratios is given in figure 90. Estimates of skin friction and line-drag increments were assumed to be invariant with lift coefficient. The drag due to lift was assumed to be that given by full leading-edge suction $\Delta C_D = C_L^2/\pi A$, where the aspect ratio was obtained by use of the model span measured during the tests of the basic wing and the flat pattern area. Measurements of the wing span were made from photographs of the models in the tunnel. Estimated lift-drag ratios were obtained from the estimated total-drag coefficients and are shown in the upper part of the figure.

The level of the experimental lift-drag ratios for a given lift coefficient appears reasonable when compared with the estimated curve, which may be considered as an upper boundary for the aspect ratio and minimum drag used. The highest experimental lift-drag ratios indicated by the faired data were much lower than the maximum estimated values because the wings could not be flown at the lower lift coefficients. If the wing had flown at these lower values, the ratios may have given values approaching the higher theoretical values shown. The lowest lift coefficient and the highest lift-drag ratio were indicated in the tunnel by a slight unsteadiness of the wing nose. Attempts to lower the angle of attack further resulted in nose collapse and high drag. The considerable variation in wing twist angle across the span must be considered. In reference 2, the wings with a large twist-angle variation showed lower maximum lift-drag ratios and the maximum occurred at higher lift coefficients than those indicated for the untwisted wings. The aforementioned theory for lift due to drag was the basis for interest in increasing the span to improve the lift-drag ratios. As shown in figure 91, the curved leading edge had increased span, but an improvement in L/D was not indicated. Differences in twist and camber in comparison with those of the basic wing probably counteracted the favorable effect of increased span.

Three test points for the pointed wings with full keel battens and curves for the inflated keel wings are given in figure 90. These wings showed a somewhat higher maximum lift-drag ratio at a lower lift coefficient than the basic wing did.

Line-Tension Coefficients and Wing Geometry

The critical-design line loads for a deployable wing will, of course, be expected during deployment; however, the distribution of line tension for steady-state flight is important for proper rigging. The line-tension data may be used to determine rigging geometry with respect to line grouping for payload attachments other than that of the present tests. The tension data may also be used to account for line stretch when determining rigging for lines of different elastic properties. A combination of measured line angles and tension data can be used to determine the center of load and direction of the

resultant force. The tensiometer used in the tests was not available until later in the investigation so that tension data are not presented for all configurations. The data for the basic wing are given in figure 16 and are typical for the wings reported. (The figures are faired to make it easier to locate the points; however, the points are discrete and the curve is not to be used as a variation of C_T with distance.) The highest loadings for both the keel lines and the leading-edge lines were at the 60-percent location and at the most rearward lines. Increasing the angle of attack by shortening the aft lines generally increased the tension coefficients in the rear lines (fig. 16). The results for dynamic pressures of 1.0 and 2.0 lb/sq ft (47.9 and 95.8 N/sq m) have a similar appearance, the higher dynamic pressure showing slightly lower lift coefficients at the somewhat lower angles of attack indicated. This difference in angle of attack resulted from increased stretch in the aft lines as dynamic pressure increased. The data indicate that the use of fairly elastic lines, such as nylon parachute lines, gives rise to rigging problems not encountered on a conventional parachute because the line tension varies appreciably from line to line on the parawing. This unequal tension distribution (a 10 to 1 ratio is not unusual) causes unequal stretch in the elastic lines and has to be properly accounted for in rigging. A good knowledge of the deployment loads would be a prerequisite for establishing detailed procedure for designing the rigging. The elongation constant given in the section entitled "Experimental Procedure" can be used with the tension data to give an approximate line-length correction for a particular test point.

A diagram of the attachment lines of the basic $\Lambda_O = 45^O$ parawing under load was constructed by use of the line lengths and angles measured in the investigation. These results are plotted in figures 92(a) to 92(d). The figures represent the shape of the keel and the shape of the leading edge projected on the plane of symmetry. The geometric data was used to resolve the line-tension coefficients into incremental lift and drag values for each line. The wing lift-drag ratio is given on each figure. As indicated on the figure, a center of load was obtained from the incremental values. The summation of the lift and drag increments was used to calculate the direction of the resultant force which is also indicated on the figures.

Other than general experimental errors, an error in the location of the apex-line vectors is involved. This error came about because these lines were lightly loaded and hence noticeably curved. The line angle was measured at the canopy to give the correct resolution of forces at the canopy; however, this line angle gave a more forward location of the end of the vector when plotted from the confluence point. On the other hand, the fact that these lines were lightly loaded tends to compensate for this error and to reduce the total error in computed results. For example, as computed from the balance data, the lift-drag ratio corresponding to figure 92(a) would be 2.31 compared with the value 2.42 shown in the figure. The resultant vector (balance data) would act through $0.038\ x/l_K$ aft of the confluence point.

The appearance of the keel and leading edges projected on the plane of symmetry determined from line-angle and line-length data is distorted, as compared with a keel and leading-edge profile drawn from measurements taken on a model in the tunnel (fig. 93). A higher, elongated nose section is shown for the profiles constructed from the line geometry. (Compare fig. 92 with fig. 93.)

Constrained-Model Tests

The results of the tests of the basic parawing constrained by a frame (fig. 6) are presented for a large angle-of-attack range in figures 94 to 100. Because of lack of experience in correlating static tunnel results for constrained models with flight characteristics and because of the difficulties encountered in testing flexible wings, conclusions drawn from analysis of these early data are tentative.

Static longitudinal characteristics.- The longitudinal aerodynamic characteristics of the $1/8\, l_k$ nose cut off, $\Lambda_o = 45^o$ parawing with steel cables are given in figure 94 for three dynamic pressures. The line lengths used are the same as those presented in figure 60 except the aft-keel lines were extended to trim the model to the lowest angle of attack. The results, particularly in the low-angle range, indicate that the effects of line stretch are eliminated by using the steel cables and that at $q = 1.0$ lb/sq ft (47.9 N/sq m) the data are representative of the model characteristics. When examining these results, consideration must be given to changes in shape of the model as the angle of attack is increased. Ranges of angles of attack and descriptions of the characteristics of the model are given in figure 94(a). At the lowest angle of attack (highest L/D), the model was generally steady except for a slight movement of the fabric along the cut-off line of the nose. As the angle of attack was increased, the coefficients indicated a linear range up to the angle of attack for maximum lift coefficient. The lift coefficient at $(L/D)_{max}$ was 0.85 and the maximum lift coefficient was 1.00. Most of the angle-of-attack range shown in the figures was above the angle of attack for maximum lift coefficient. Near maximum lift ($\alpha \approx 30^o$), the part of the wing from the nose to the balance pin which extended through the canopy tended to compress with a resulting loss of nose area which caused a positive pitching-moment change and a sharp decrease in lift coefficient. These effects were largely due to the effect of the pin on the model. The change in moment can also be deduced from the C_A curve of figure 94(c) because, with a very low center-of-moment location, the axial components of the line tensions have a large effect in determining the pitching moment. At an angle of attack of about 48^o, a severe oscillation was observed. The forward half of the wing was unsteady at angles of attack around 48^o but was fully extended and taut at the high end of the range, as indicated in the figure for $\alpha \approx 57^o$. The pitching moments became more negative as the angle of attack was increased from $\alpha \approx 48^o$ to $\alpha \approx 57^o$ because of the nose loads. The model became

steady at higher angles of attack ($\alpha \approx 75^{\circ}$). It is difficult to assess the effects of the constraint on these data; however, the effects were least near trim.

A gap in the data at $\alpha \approx 55^{\circ}$ in figure 94 and the figures to follow was due to mechanical restrictions at the ends of the angle-of-attack range. A few tests were run with an angle-of-attack range which overlapped the usual ranges (fig. 95) to show that the data are continuous here.

Longitudinal control by means of the aft-keel line, tip lines, or all three lines has been applied to parawings. Static tunnel data were obtained for the first two methods above and, in addition, the use of the most forward line on the leading edge as a control was investigated. Longitudinal characteristics for aft-keel-line control are shown in figure 96. Shortening the rear-keel control line shifted the pitching moments in a positive direction throughout the angle-of-attack range. A statically stable trim range of about 6° is indicated at the lower angles of attack. The L/D modulation occurred from about 2.3 to 1.8. Although a second stable range is indicated at medium angles of attack, the previous discussion of tunnel-model instability in this range indicates that trimmed flight here is questionable.

In figures 97 to 99, results are shown for combined changes in the leading-edge lines nearest the nose and at the wing tips. Shortening the nose lines provided a negative increment in pitching moment at high angles of attack. Observation of the model indicated that this control also was very effective in removing the compression of the nose previously discussed (fig. 94). A light pull on these lines completely inflated the nose area and generally eliminated many of the oscillations in the range of angles of attack between 35° and 45°. The comparatively smooth variation of lift coefficient with angle of attack indicates that the model retained an inflated shape through the angle-of-attack range.

Although identical control positions are not presented, comparison of figures 97 to 99 indicates that shortening the tip lines is similar to shortening the aft-keel line in that a positive pitching-moment increment results. The combination of shortened leading-edge lines (fig. 99) extends the stable trim range.

Static lateral-stability parameters.- The lateral-stability parameters (fig. 100) indicate decreasing directional stability and effective dihedral $-C_{l_\beta}$ with increased angle of attack until approximately zero values are shown at an angle of attack of about 45°. This angle coincides with the beginning of the range of severe oscillations in the tunnel. For angles of attack between 60° and 90° both the effective-dihedral and side-force parameters were about zero, and positive directional stability was indicated at the highest angles of attack.

The static lateral-stability derivatives were measured in order to obtain some indication of the nature of these derivatives for an all-flexible parawing. Care must be taken in interpreting the significance of these derivatives in terms of past experience on conventional aircraft. It is believed that much more information is needed to assess properly the static stability characteristics of all-flexible parawings.

SUMMARY OF RESULTS

The results of a low-speed wind-tunnel investigation of the effect of canopy-planform variables, rigging changes, and the addition of local stiffness on the stability and performance of a nonstiffened tension-structure parawing may be summarized as follows:

1. Most models with an unstiffened pointed nose could not be rigged for testing.

2. A wing with 45° swept planform was rigged to fly with the nose cut off as much as 3/8 keel length; however, the basic 1/8 keel length cut was sufficient to alleviate problems of nose collapse. Curved nose cuts showed no advantage.

3. Nonstiffened wings with 1/8 keel length nose cut off and three sweep angles were tested. Both the 40° and 45° swept wings provided lift-drag ratios of about 2.4, the highest for any nonstiffened configuration tested, and the 50° swept wing gave a value of 2.1.

4. A variety of detailed changes in leading-edge and trailing-edge shape, keel-payload distance, and trailing-edge boltrope were investigated and it was determined that there was considerable latitude in varying some design details without appreciably affecting the performance obtained with the basic wing.

5. The results indicated that changes in the lengths of the wing-tip lines and/or the aft-keel line gave longitudinal and lateral control. Shortening the nose lines was found to be very effective in reshaping a collapsed nose area at moderate and high angles of attack.

6. Static longitudinal-stability results obtained from pitch tests with the model constrained by a frame indicated that the minimum lift coefficient (low angle of attack) at which the basic model canopy would inflate properly was about 0.85 and that maximum lift coefficient was 1.00. Static stability and trim were shown in this angle-of-attack range below wing stall.

7. The highest values of lift-drag ratio observed for the various wings tested fell slightly below the theoretical estimates.

8. The use of either flexible keel battens or inflatable keel stiffeners made testing possible at lower lift coefficients than could be reached with the fully flexible wings and gave lift-drag ratios as high as 3.22.

9. Line-tension coefficients measured indicated a considerable variation in tension of the suspension lines at the various line locations which must be properly handled in designing the wing rigging.

Langley Research Center,
National Aeronautics and Space Administration,
Langley Station, Hampton, Va., January 9, 1967,
126-13-01-58-23.

REFERENCES

1. Rogallo, Frances M.: Paraglider Recovery Systems. Presented at IAS Meeting on Man's Progress in the Conquest of Space (St. Louis, Mo.), Apr. 30 – May 1-2, 1962.
2. Polhamus, Edward C.; and Naeseth, Rodger L.: Experimental and Theoretical Studies of the Effects of Camber and Twist on the Aerodynamic Characteristics of Parawings Having Nominal Aspect Ratios of 3 and 6. NASA TN D-972, 1963.
3. Naeseth, Rodger L.; and Gainer, Thomas G.: Low-Speed Investigation of the Effects of Wing Sweep on the Aerodynamic Characteristics of Parawings Having Equal-Length Leading Edges and Keel. NASA TN D-1957, 1963.
4. Croom, Delwin R.; Naeseth, Rodger L.; and Sleeman, William C., Jr.: Effect of Canopy Shape on Low-Speed Aerodynamic Characteristics of a 55° Swept Parawing With Large-Diameter Leading Edges. NASA TN D-2551, 1964.
5. Makulowich, Michael: Project "Flexwing." Sky Diver, Vol. VIII, no. 5, May 1966, pp. 18-19.
6. Hamilton, J. Scott: Flight of the Parawing. Parachutist, Vol. 7, no. 9, Sept. 1966, pp. 5-9.
7. Bugg, Frank M.; and Sleeman, William C., Jr.: Low-Speed Tests of an All-Flexible Parawing for Landing a Lifting-Body Spacecraft. NASA TN D-4010, 1967.
8. Gillis, Clarence L.; Polhamus, Edward C.; and Gray, Joseph L., Jr.: Charts for Determining Jet-Boundary Corrections for Complete Models in 7- by 10-Foot Closed Rectangular Wind Tunnels. NACA WR L-123, 1945. (Formerly NACA ARR L5G31.)
9. Herriot, John G.: Blockage Corrections for Three-Dimensional-Flow Closed-Throat Wind Tunnels, With Consideration of the Effect of Compressibility. NACA Rept. 995, 1950. (Supersedes NACA RM A7B28.)

TABLE I.- LINE LOCATIONS AND LENGTHS

Keel		Leading edge	
x/l_k	l/l_k	x/l_k	l/l_k
Figure 10; rigging A			
0.125	1.352	0.177	1.354
.208	1.335	.333	1.286
.292	1.333	.500	1.249
.375	1.327	.667	1.197
.459	1.313	.833	1.138
.542	1.298	1.000	.945
.645	1.273		
.750	1.270		
.833	1.242		
.917	1.183		
1.000	1.046		
Figure 10; rigging B			
0.125	1.352	0.177	1.354
.208	1.335	.333	1.286
.292	1.333	.500	1.249
.375	1.327	.667	1.197
.459	1.313	.833	1.138
.542	1.298	1.000	.922
.645	1.273		
.750	1.271		
.833	1.242		
.917	1.183		
1.000	1.033		
Figure 13; rigging A			
0.125	1.354	0.177	1.363
.208	1.350	.333	1.298
.292	1.342	.500	1.254
.375	1.335	.667	1.198
.459	1.317	.833	1.146
.542	1.298	1.000	.965
.645	1.281		
.750	1.263		
.833	1.238		
.917	1.200		
1.000	1.079		
Figure 13; rigging B			
0.125	1.354	0.177	1.363
.208	1.350	.333	1.298
.292	1.342	.500	1.254
.375	1.335	.667	1.198
.459	1.317	.833	1.146
.542	1.298	1.000	.947
.646	1.281		
.750	1.263		
.833	1.238		
.917	1.200		
1.000	1.054		
Figure 13; rigging C			
0.125	1.354	0.177	1.363
.208	1.350	.333	1.298
.292	1.342	.500	1.254
.375	1.335	.667	1.198
.459	1.317	.833	1.146
.542	1.298	1.000	.930
.645	1.281		
.750	1.263		
.833	1.238		
.917	1.200		
1.000	1.054		
Figure 16(a); rigging A			
0.125	1.354	0.177	1.370
.208	1.350	.333	1.301
.292	1.342	.500	1.252
.375	1.335	.667	1.194
.459	1.317	.833	1.142
.542	1.298	1.000	.971
.645	1.281		
.750	1.263		
.833	1.238		
.917	1.200		
1.000	1.088		
Figure 16(b); rigging B			
0.125	1.354	0.177	1.370
.208	1.350	.333	1.301
.292	1.342	.500	1.252
.375	1.335	.667	1.194
.459	1.317	.833	1.142
.542	1.298	1.000	.954
.645	1.281		
.750	1.263		
.833	1.238		
.917	1.200		
1.000	1.065		
Figure 16(c); rigging C			
0.125	1.354	0.177	1.370
.208	1.350	.333	1.301
.292	1.342	.500	1.252
.375	1.335	.667	1.194
.459	1.317	.833	1.142
.542	1.298	1.000	.958
.645	1.281		
.750	1.263		
.833	1.238		
.917	1.200		
1.000	1.060		
Figure 19; rigging A			
0.125	1.330	0.177	1.322
.208	1.322	.333	1.278
.292	1.318	.500	1.247
.375	1.292	.667	1.182
.459	1.282	.833	1.145
.542	1.272	1.000	.963
.645	1.269		
.750	1.272		
.833	1.248		
.917	1.246		
1.000	1.129		
Figure 19; rigging B			
0.125	1.330	0.177	1.322
.208	1.322	.333	1.277
.292	1.318	.500	1.247
.375	1.292	.667	1.182
.459	1.282	.833	1.145
.542	1.272	1.000	.985
.645	1.269		
.750	1.272		
.833	1.248		
.917	1.246		
1.000	1.063		
Figure 19; rigging C			
0.125	1.330	0.177	1.322
.208	1.322	.333	1.277
.292	1.318	.500	1.247
.375	1.292	.667	1.182
.459	1.282	.833	1.145
.542	1.272	1.000	.943
.645	1.269		
.750	1.272		
.833	1.248		
.917	1.246		
1.000	1.092		
Figure 22; $\Lambda_o = 40^o$			
0.125	1.352	0.177	1.354
.208	1.335	.333	1.286
.292	1.333	.500	1.249
.375	1.327	.667	1.197
.459	1.313	.833	1.138
.542	1.298	1.000	.945
.645	1.273		
.750	1.270		
.833	1.242		
.917	1.183		
1.000	1.046		
Figure 22; $\Lambda_o = 45^o$			
0.125	1.354	0.177	1.363
.208	1.350	.333	1.298
.292	1.342	.500	1.254
.375	1.335	.667	1.198
.459	1.317	.833	1.146
.542	1.298	1.000	.965
.645	1.281		
.750	1.263		
.833	1.238		
.917	1.200		
1.000	1.079		
Figure 22; $\Lambda_o = 50^o$			
0.125	1.330	0.177	1.322
.208	1.322	.333	1.278
.292	1.318	.500	1.247
.375	1.292	.667	1.182
.459	1.282	.833	1.145
.542	1.272	1.000	.963
.645	1.269		
.750	1.272		
.833	1.248		
.917	1.246		
1.000	1.129		
Figure 25; pointed with batten			
0	1.379	0.177	1.347
.125	1.360	.353	1.303
.250	1.352	.530	1.261
.375	1.333	.687	1.197
.458	1.310	.843	1.138
.542	1.310	1.000	.993
.625	1.306		
.720	1.300		
.813	1.275		
.905	1.233		
1.000	1.125		
Figure 25; 1/8 l_k cut			
0.125	1.350	0.177	1.349
.250	1.358	.353	1.304
.375	1.350	.530	1.260
.458	1.325	.687	1.195
.542	1.306	.843	1.139
.625	1.285	1.000	.960
.720	1.269		
.813	1.242		
.905	1.204		
1.000	1.083		
Figure 25; with batten			
0.125	1.350	0.177	1.349
.250	1.358	.353	1.304
.375	1.350	.530	1.260
.458	1.325	.687	1.195
.542	1.306	.843	1.139
.625	1.285	1.000	.960
.720	1.269		
.813	1.242		
.905	1.204		
1.000	1.053		
Figure 25; 1/4 l_k cut			
0.250	1.358	0.353	1.304
.375	1.350	.530	1.260
.458	1.325	.687	1.195
.542	1.306	.843	1.139
.625	1.285	1.000	.960
.720	1.269		
.813	1.242		
.905	1.204		
1.000	1.053		
Figure 25; 3/8 l_k cut			
0.375	1.200	0.530	1.281
.458	1.235	.687	1.200
.542	1.252	.843	1.146
.625	1.263	1.000	.957
.720	1.256		
.813	1.242		
.905	1.206		
1.000	1.079		
Figure 28			
0.125	1.350	0.177	1.349
.250	1.358	.353	1.304
.375	1.350	.530	1.260
.458	1.325	.687	1.195
.542	1.306	.843	1.139
.625	1.285	1.000	.960
.720	1.269		
.813	1.242		
.905	1.204		
1.000	1.053		
Figure 31; straight			
0.250	1.358	0.353	1.304
.375	1.350	.530	1.260
.458	1.325	.687	1.195
.542	1.306	.843	1.139
.625	1.285	1.000	.960
.720	1.269		
.813	1.242		
.905	1.204		
1.000	1.053		
Figure 31; double radius			
0.250	1.294	0.353	1.307
.375	1.323	.530	1.267
.458	1.331	.687	1.200
.542	1.310	.843	1.142
.625	1.294	1.000	.971
.720	1.277		
.813	1.252		
.905	1.223		
1.000	1.067		
Figure 31; single radius			
0.250	1.358	0.250	1.349
.375	1.350	.353	1.304
.458	1.325	.530	1.260
.542	1.306	.687	1.195
.625	1.285	.843	1.139
.720	1.269	1.000	.960
.813	1.242		
.905	1.204		
1.000	1.053		
Figure 34; straight			
0.375	1.200	0.530	1.281
.458	1.235	.687	1.200
.542	1.252	.843	1.146
.625	1.263	1.000	.957
.720	1.256		
.813	1.242		
.905	1.206		
1.000	1.079		
Figure 34; single radius			
0.375	1.350	0.375	1.307
.458	1.325	.530	1.267
.542	1.306	.687	1.200
.625	1.285	.843	1.142
.720	1.269	1.000	.971
.813	1.242		
.905	1.204		
1.000	1.083		
Figure 37(a); rigging A			
0.125	1.354	0.177	1.370
.208	1.350	.333	1.301
.292	1.342	.500	1.252
.375	1.335	.667	1.194
.459	1.317	.833	1.142
.542	1.298	1.000	.953
.645	1.281		
.750	1.263		
.833	1.238		
.917	1.200		
1.000	1.069		
Figure 37(b); rigging B			
0.125	1.354	0.177	1.370
.208	1.350	.333	1.301
.292	1.342	.500	1.252
.375	1.335	.667	1.194
.459	1.317	.833	1.142
.542	1.298	1.000	.941
.645	1.281		
.750	1.263		
.833	1.238		
.917	1.200		
1.000	1.054		
Figure 37(c); rigging C			
0.125	1.354	0.177	1.370
.208	1.350	.333	1.301
.292	1.342	.500	1.252
.375	1.335	.667	1.194
.459	1.317	.833	1.142
.542	1.298	1.000	.943
.645	1.281		
.750	1.263		
.833	1.238		
.917	1.200		
1.000	1.045		
Figure 40			
0.125	1.354	0.177	1.370
.208	1.350	.333	1.301
.292	1.342	.500	1.252
.375	1.335	.667	1.194
.459	1.317	.833	1.142
.542	1.298	1.000	.971
.645	1.281		
.750	1.263		
.833	1.238		
.917	1.200		
1.000	1.083		
Figure 41			
0.125	1.340	0.177	1.380
.208	1.346	.333	1.308
.292	1.338	.500	1.255
.375	1.331	.667	1.200
.459	1.310	.833	1.150
.542	1.292	1.000	.965
.645	1.279		
.750	1.263		
.833	1.238		
.917	1.198		
1.000	1.069		
Figure 42			
0.125	1.389	0.177	1.390
.208	1.385	.333	1.307
.292	1.363	.500	1.238
.375	1.362	.667	1.188
.459	1.352	.833	1.135
.542	1.340	1.000	.972
.645	1.315		
.750	1.288		
.833	1.248		
.917	1.208		
1.000	1.085		
Figure 45			
0	1.325	0.129	1.331
.125	1.333	.259	1.264
.250	1.317	.389	1.211
.375	1.283	.518	1.163
.500	1.244	.647	1.121
.625	1.219	.771	1.084
.750	1.174	.905	1.067
.875	1.131	1.034	.965
1.000	.974		
Figure 48			
0	1.317	0.129	1.302
.125	1.315	.259	1.244
.250	1.296	.389	1.177
.375	1.258	.518	1.139
.500	1.227	.647	1.102
.625	1.196	.771	1.091
.750	1.156	.905	1.056
.875	1.100	1.034	.937
1.000	.958		
Figure 49			
0	1.317	0.129	1.302
.125	1.315	.259	1.244
.250	1.296	.389	1.177
.375	1.258	.518	1.139
.500	1.227	.647	1.102
.625	1.196	.771	1.091
.750	1.156	.905	1.056
.875	1.100	1.034	.922
1.000	.935		
Figure 50			
0	1.317	0.129	1.302
.125	1.315	.259	1.244
.250	1.296	.389	1.177
.375	1.258	.518	1.139
.500	1.227	.647	1.102
.625	1.196	.771	1.091
.750	1.156	.905	1.056
.875	1.095	1.034	.918
1.000	.908		
Figure 53			
0.125	1.285	0.259	1.258
.250	1.294	.389	1.193
.375	1.265	.518	1.146
.500	1.225	.647	1.103
.625	1.200	.771	1.077
.750	1.163	.905	1.052
.875	1.133	1.034	.990
1.000	1.033		

TABLE I.- LINE LOCATIONS AND LENGTHS – Continued

Keel		Leading edge	
x/l_k	l/l_k	x/l_k	l/l_k
Figure 54			
0.125	1.296	0.259	1.265
.250	1.302	.389	1.199
.375	1.273	.518	1.150
.500	1.233	.647	1.109
.625	1.208	.771	1.078
.750	1.171	.905	1.057
.875	1.113	1.034	.998
1.000	.992		
Figure 57; rigging A			
0.167	1.363	0.167	1.342
.333	1.354	.333	1.308
.500	1.333	.500	1.267
.667	1.304	.667	1.198
.833	1.233	.833	1.119
1.000	1.035	1.000	.921
Figure 57; rigging B			
0.167	1.363	0.167	1.342
.333	1.354	.333	1.308
.500	1.333	.500	1.267
.667	1.304	.667	1.198
.833	1.233	.833	1.119
1.000	1.022	1.000	.908
Figure 57; rigging C			
0.167	1.363	0.167	1.342
.333	1.354	.333	1.308
.500	1.333	.500	1.267
.667	1.304	.667	1.198
.833	1.233	.833	1.119
1.000	1.004	1.000	.888

Keel		Leading edge	
x/l_k	l/l_k	x/l_k	l/l_k
Figure 60; one point			
0.125	1.354	0.177	1.370
.208	1.350	.333	1.301
.292	1.342	.500	1.252
.375	1.335	.667	1.194
.459	1.317	.833	1.142
.542	1.298	1.000	.971
.645	1.281		
.750	1.263		
.833	1.238		
.917	1.200		
1.000	1.088		
Figure 60; spread			
0.125	1.354	0.177	1.370
.208	1.350	.333	1.301
.292	1.342	.500	1.252
.375	1.335	.667	1.194
.459	1.317	.833	1.142
.542	1.298	1.000	1.037
.645	1.281		
.750	1.263		
.833	1.238		
.917	1.200		
1.000	1.104		
Figure 63			
0.125	1.312	0.177	1.344
.208	1.323	.333	1.302
.292	1.317	.500	1.238
.375	1.313	.667	1.186
.459	1.300	.833	1.127
.542	1.281	1.000	.977
.645	1.267		
.750	1.248		
.833	1.221		
.917	1.185		
1.000	1.079		
Figure 64; nylon			
0.125	1.312	0.177	1.344
.208	1.323	.333	1.302
.292	1.317	.500	1.238
.375	1.313	.667	1.186
.459	1.300	.833	1.127
.542	1.281	1.000	.977
.645	1.267		
.750	1.248		
.833	1.221		
.917	1.185		
1.000	1.079		

Keel		Leading edge	
x/l_k	l/l_k	x/l_k	l/l_k
Figure 64; steel			
0.125	1.354	0.177	1.363
.208	1.350	.333	1.298
.292	1.342	.500	1.254
.375	1.335	.667	1.198
.459	1.317	.833	1.146
.542	1.298	1.000	.965
.645	1.281		
.750	1.263		
.833	1.238		
.917	1.200		
1.000	1.079		
Figure 66			
0.125	1.354	0.177	1.370
.208	1.340	.333	1.301
.292	1.332	.500	1.252
.375	1.316	.667	1.194
.459	1.298	.833	1.142
.542	1.269	1.000	.988
.645	1.253		
.750	1.224		
.833	1.190		
.917	1.143		
1.000	1.065		
Figure 67			
0.125	1.316	0.177	1.370
.208	1.313	.333	1.301
.292	1.323	.500	1.252
.375	1.297	.667	1.194
.459	1.278	.833	1.142
.542	1.241	1.000	.994
.645	1.224		
.750	1.186		
.833	1.142		
.917	1.104		
1.000	1.019		
Figure 68			
0.125	1.278	0.177	1.370
.208	1.283	.333	1.301
.292	1.294	.500	1.252
.375	1.269	.667	1.194
.459	1.250	.833	1.142
.542	1.212	1.000	.975
.645	1.195		
.750	1.157		
.833	1.113		
.917	1.067		
1.000	.975		

Keel		Leading edge	
x/l_k	l/l_k	x/l_k	l/l_k
Figure 69; basic			
0.125	1.354	0.177	1.370
.208	1.350	.333	1.301
.292	1.342	.500	1.252
.375	1.335	.667	1.194
.459	1.317	.833	1.142
.542	1.298	1.000	.971
.645	1.281		
.750	1.263		
.833	1.238		
.917	1.200		
1.000	1.088		
Figure 69; length 1			
0.125	1.354	0.177	1.370
.208	1.340	.333	1.301
.292	1.332	.500	1.252
.375	1.316	.667	1.194
.459	1.298	.833	1.142
.542	1.269	1.000	.988
.645	1.253		
.750	1.224		
.833	1.190		
.917	1.143		
1.000	1.065		
Figure 69; length 2			
0.125	1.316	0.177	1.370
.208	1.313	.333	1.301
.292	1.323	.500	1.252
.375	1.297	.667	1.194
.459	1.278	.833	1.142
.542	1.241	1.000	.994
.645	1.224		
.750	1.186		
.833	1.142		
.917	1.104		
1.000	1.019		
Figure 69; length 3			
0.125	1.278	0.177	1.370
.208	1.283	.333	1.301
.292	1.294	.500	1.252
.375	1.269	.667	1.194
.459	1.250	.833	1.142
.542	1.212	1.000	.975
.645	1.195		
.750	1.157		
.833	1.113		
.917	1.067		
1.000	.975		

Keel		Leading edge	
x/l_k	l/l_k	x/l_k	l/l_k
Figure 71; 1.25 l_k			
0.125	1.331	0.177	1.333
.208	1.335	.333	1.288
.292	1.335	.500	1.250
.375	1.319	.667	1.183
.459	1.300	.833	1.133
.542	1.292	1.000	.958
.645	1.288		
.750	1.288		
.833	1.263		
.917	1.202		
1.000	1.096		
Figure 71; 1.00 l_k			
0.125	1.062	0.177	1.080
.208	1.062	.333	1.032
.292	1.060	.500	.968
.375	1.042	.667	.917
.459	1.034	.833	.865
.542	1.025	1.000	.672
.645	1.008		
.750	.991		
.833	.986		
.917	.937		
1.000	.800		
Figure 71; 0.75 l_k			
0.125	0.814	0.177	0.829
.208	.841	.333	.832
.292	.850	.500	.795
.375	.835	.667	.745
.459	.816	.833	.681
.542	.807	1.000	.506
.645	.795		
.750	.769		
.833	.735		
.917	.696		
1.000	.553		
Figure 74; $\Lambda_o = 40^o$			
0	1.371	0.177	1.334
.083	1.344	.333	1.294
.125	1.356	.500	1.256
.208	1.329	.667	1.191
.292	1.300	.833	1.138
.375	1.283	1.000	.913
.459	1.292		
.542	1.279		
.645	1.288		
.750	1.281		
.833	1.279		
.917	1.258		
1.000	1.188		

TABLE I.- LINE LOCATIONS AND LENGTHS – Concluded

Keel		Leading edge		Keel		Leading edge		Keel		Leading edge		Keel		Leading edge		Keel		Leading edge	
x/l_k	l/l_k	x/l_k	l/l_k	x/l_k	l/l_k	x/l_k	l/l_k	x/l_k	l/l_k	x/l_k	l/l_k	x/l_k	l/l_k	x/l_k	l/l_k	x/l_k	l/l_k	x/l_k	l/l_k
Figure 74; $\Lambda_o = 45^o$				Figure 80; rigging A				Figure 80; rigging E				Figure 85; rigging C				Figure 89; rigging A			
0	1.375	0.177	1.333	0.125	1.346	0.177	1.321	0.125	1.275	0.177	1.241	0.125	1.279	0.177	1.331	0.125	1.273	0.177	1.339
.083	1.363	.333	1.291	.208	1.317	.333	1.274	.208	1.317	.333	1.274	.208	1.277	.333	1.367	.208	1.285	.333	1.338
.125	1.350	.500	1.255	.292	1.313	.500	1.234	.292	1.313	.500	1.234	.292	1.267	.500	1.308	.292	1.290	.500	1.300
.208	1.330	.667	1.188	.375	1.310	.667	1.183	.375	1.310	.667	1.182	.375	1.275	.667	1.237	.375	1.298	.667	1.228
.292	1.300	.833	1.138	.459	1.317	.833	1.136	.459	1.317	.883	1.136	.459	1.275	.833	1.171	.459	1.300	.833	1.146
.375	1.317	1.000	.931	.542	1.310	1.000	.960	.542	1.310	1.000	.938	.542	1.271	1.000	.996	.542	1.300	1.000	.995
.459	1.302			.645	1.302			.645	1.302			.645	1.271			.645	1.300		
.542	1.292			.750	1.298			.750	1.298			.750	1.271			.750	1.296		
.645	1.283			.833	1.263			.833	1.263			.833	1.238			.833	1.273		
.750	1.273			.917	1.221			.917	1.221			.917	1.217			.917	1.248		
.833	1.258			1.000	1.085			1.000	.967			1.000	1.158			1.000	1.183		
.917	1.248																		
1.000	1.163																		
Figure 74; $\Lambda_o = 50^o$				Figure 80; rigging B				Figure 84				Figure 85; rigging D				Figure 89; rigging B			
0	1.383	0.177	1.356	0.125	1.346	0.177	1.321	0.125	1.279	0.177	1.331	0.125	1.279	0.177	1.331	0.125	1.279	0.177	1.331
.083	1.363	.333	1.303	.208	1.317	.333	1.274	.208	1.277	.333	1.367	.208	1.277	.333	1.367	.208	1.277	.333	1.367
.125	1.360	.500	1.263	.292	1.313	.500	1.234	.292	1.267	.500	1.308	.292	1.267	.500	1.308	.292	1.267	.500	1.308
.208	1.348	.667	1.194	.375	1.310	.667	1.182	.375	1.275	.667	1.237	.375	1.275	.667	1.237	.375	1.275	.667	1.237
.292	1.313	.833	1.146	.459	1.317	.883	1.136	.459	1.275	.833	1.171	.459	1.275	.833	1.171	.459	1.275	.833	1.171
.375	1.309	1.000	.975	.542	1.310	1.000	.942	.542	1.271	1.000	1.023	.542	1.271	1.000	.963	.542	1.271	1.000	.968
.459	1.300			.645	1.302			.645	1.271			.645	1.271			.645	1.271		
.542	1.294			.750	1.298			.750	1.271			.750	1.271			.750	1.271		
.645	1.296			.833	1.263			.833	1.238			.833	1.238			.833	1.238		
.750	1.300			.917	1.221			.917	1.217			.917	1.217			.917	1.217		
.833	1.298			1.000	1.067			1.000	1.167			1.000	1.150			1.000	1.183		
.917	1.304																		
1.000	1.206																		
Figure 74; triangle				Figure 80; rigging C				Figure 85; rigging A				Figure 85; rigging E				Figure 89; rigging C			
0	1.169	0.250	1.158	0.125	1.346	0.177	1.321	0.125	1.279	0.177	1.331	0.125	1.279	0.177	1.331	0.125	1.279	0.177	1.331
.194	1.158	.444	1.146	.208	1.317	.333	1.274	.208	1.277	.333	1.367	.208	1.277	.333	1.367	.208	1.277	.333	1.367
.333	1.146	.639	1.121	.292	1.313	.500	1.234	.292	1.267	.500	1.308	.292	1.267	.500	1.308	.292	1.267	.500	1.308
.472	1.138	.833	1.092	.375	1.310	.667	1.182	.375	1.275	.667	1.237	.375	1.275	.667	1.237	.375	1.275	.667	1.237
.611	1.144	1.028	1.042	.459	1.317	.883	1.136	.459	1.275	.833	1.171	.459	1.275	.833	1.171	.459	1.275	.833	1.170
.750	1.146	1.222	.967	.542	1.310	1.000	.960	.542	1.271	1.000	1.023	.542	1.271	1.000	.929	.542	1.271	1.000	.934
.889	1.146	1.413	.802	.645	1.302			.645	1.271			.645	1.271			.645	1.271		
1.000	1.083			.750	1.298			.750	1.271			.750	1.271			.750	1.271		
				.833	1.263			.833	1.238			.833	1.238			.833	1.238		
				.917	1.221			.917	1.217			.917	1.217			.917	1.217		
				1.000	1.042			1.000	1.167			1.000	1.150			1.000	1.167		
Figure 77; rigging A				Figure 80; rigging D				Figure 85; rigging B				Figure 88				Figure 89; rigging D			
0	1.169	0.250	1.158	0.125	1.346	0.177	1.321	0.125	1.279	0.177	1.331	0.125	1.273	0.177	1.339	0.125	1.279	0.177	1.331
.194	1.158	.444	1.146	.208	1.317	.333	1.274	.208	1.277	.333	1.367	.208	1.285	.333	1.338	.208	1.277	.333	1.368
.333	1.146	.639	1.121	.292	1.313	.500	1.234	.292	1.267	.500	1.308	.292	1.290	.500	1.300	.292	1.267	.500	1.308
.472	1.138	.833	1.092	.375	1.310	.667	1.182	.375	1.275	.667	1.237	.375	1.298	.667	1.228	.375	1.275	.667	1.237
.611	1.144	1.028	1.042	.459	1.317	.883	1.136	.459	1.275	.833	1.171	.459	1.300	.833	1.146	.459	1.275	.833	1.170
.750	1.146	1.222	.967	.542	1.310	1.000	.933	.542	1.271	1.000	1.023	.542	1.300	1.000	.995	.542	1.271	1.000	.901
.889	1.146	1.413	.802	.645	1.302			.645	1.271			.645	1.300			.645	1.271		
1.000	1.083			.750	1.298			.750	1.271			.750	1.296			.750	1.271		
				.833	1.263			.833	1.238			.833	1.273			.833	1.238		
				.917	1.221			.917	1.217			.917	1.248			.917	1.217		
				1.000	1.019			1.000	1.167			1.000	1.183			1.000	1.167		
Figure 77; rigging B																			
0	1.169	0.250	1.158																
.194	1.158	.444	1.146																
.333	1.146	.639	1.121																
.472	1.138	.833	1.092																
.611	1.144	1.028	1.042																
.750	1.146	1.222	.967																
.889	1.146	1.413	.777																
1.000	1.058																		

TABLE II.- DIMENSIONS OF PARAWING LINE ATTACHMENTS

[Symbols are defined in fig. 4]

Figure	h_1/l_k	h_2/l_k	d_1/l_k	d_2/l_k	y/l_k	Notes
10	0.0090	0.0147	0.1375	0.1460	0.0670	
13	.0090	.0147	.1375	.1460	.0670	
16	.0290	.0350	.1375	.1460	.0670	
19	.0090	.0147	.1375	.1460	.0670	
22	.0090	.0147	.1375	.1460	.0670	
25	.0090	.0147	.1375	.1460	.0670	
28	.0090	.0147	.1375	.1460	.0670	
31	.0090	.0147	.1375	.1460	.0670	
34	.0090	.0147	.1375	.1460	.0670	
37	.0290	.0350	.1375	.1460	.0670	
40 to 42	.0290	.0350	.1375	.1460	.0670	
45	.0290	.0350	.1375	.1460	.0670	
48 to 50	.0290	.0350	.1375	.1460	.0670	
53,54	.0290	.0350	.1375	.1460	.0670	
57	.0090	.0147	.1375	.1460	.0670	
60	.0290	.0350	.1375	.1460	.0670	
60	.0000	.0167	.0000	.0000	.0333	Point confluence
63,64	.0290	.0350	.1375	.1460	.0670	Steel lines
64	.0090	.0147	.1375	.1460	.0670	Nylon lines
66 to 69	.0290	.0350	.1375	.1460	.0670	
71	.0090	.0147	.1125	.1460	.0670	Payload distance 1.25 l_k
71	.0155	.0155	.1000	.2000	.0730	Payload distance 1.00 l_k
71	.0155	.0155	.0960	.1500	.0540	Payload distance 0.75 l_k
74	.0090	.0147	.1375	.1460	.0670	
77	.0090	.0147	.1375	.1460	.0670	
80	.0090	.0147	.1375	.1460	.0670	
84,85	.0290	.0350	.1375	.1460	.0670	
88,89	.0290	.0350	.1375	.1460	.0670	

TABLE III.- SUMMARY OF MODELS AND RESULTS

Planform	Geometry figure	Λ_o, deg	Nose detail	Leading-edge planform	Stiffness at keel	Notes	$C_m, C_L, C_D, L/D, \alpha$ against q figure	l/l_k against x/l_k figure	Parameter	Maximum L/D	C_L at $(L/D)_{max}$	Maximum C_L	b/l_k q = 1.0 lb/sq ft (47.9 N/sq m)
	8	40	1/8 l_k cut	Straight			9	10	α	2.47	0.93	1.06	
	11 11	45 45	1/8 l_k cut 1/8 l_k cut	Straight Straight			12 15	13 *16(a),(b),(c)	α α	2.42 2.33	0.98 1.05	1.11 1.20	0.829 at α = 27.50°
	17	50	1/8 l_k cut	Straight			18	19	α	2.08	0.99	1.21	
	20 20 20	40 45 50	1/8 l_k cut 1/8 l_k cut 1/8 l_k cut	Straight Straight Straight			21 21 21	22 22 22	Λ_o Λ_o Λ_o	2.47 2.43 2.08	0.93 1.00 1.04	0.95 1.02 1.04	
	23 23 23 23 23	45 45 45 45 45	Pointed 1/8 l_k cut 1/8 l_k cut 1/4 l_k cut 3/8 l_k cut	Straight Straight Straight Straight Straight	0.450 l_k batten .150 l_k batten	Partial batten Partial batten	24 24 24 24 24	25 25 25 25 25	Nose cut, batten Nose cut, batten Nose cut, batten Nose cut, batten Nose cut, batten	2.85 2.49 2.27 2.36 2.23	0.81 1.00 .95 .89 .69	0.82 1.05 .99 .90 .69	
	26 26	45 45	1/8 l_k cut 1/8 l_k cut	Straight Straight		Straight cut Double radius cut	27 27	28 28	Nose cut Nose cut	2.27 2.15	0.96 .99	1.11 1.05	
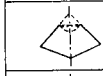	29 29 29	45 45 45	1/4 l_k cut 1/4 l_k cut 1/4 l_k cut	Straight Straight Straight		Straight cut Double radius cut Single radius cut	30 30 30	31 31 31	Nose cut Nose cut Nose cut	2.37 2.15 1.98	0.90 .91 .98	0.91 .94 1.02	
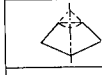	32 32	45 45	3/8 l_k cut 3/8 l_k cut	Straight Straight		Straight cut Single radius cut	33 33	34 34	Nose cut Nose cut	2.43 1.54	0.69 .69	0.69 .69	
	35 38 38	45 45 45	1/4 l_k cut 1/4 l_k cut 1/4 l_k cut	Straight 1/2 parabolic cuts Full parabolic cuts		Parabolic suspension patches Parabolic suspension patches Parabolic suspension patches	36 39 39	*37(a),(b),(c) *40 to 42 *40 to 42	α Leading-edge planform Leading-edge planform	2.48 2.23 2.28	0.94 .96 .91	1.06 1.00 .96	0.794 at α = 26.50° .793 at α = 27.25°
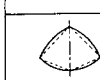	43	45	Pointed	Curved		Curved trailing edge	44	*45	α	2.18	1.05	1.06	0.871 at α = 29.00°

	46	45	Pointed	Curved			47	*48 to 50	α	2.27	1.07	1.22	0.896 at α = 29.30°
 Boltrope	51 51	45 45	1/8 l_k cut 1/8 l_k cut	Curved Curved		No boltrope 7.5-percent boltrope	52 52	53,54 53,54	Boltrope Boltrope	2.21 2.25	0.94 .97	0.96 .97	0.938 at α = 27.90° .918 at α = 28.30°
	55	45	1/6 l_k cut	Straight		Slotted wing	56	57	α	1.91	1.15	1.29	
	58 58 58 58 58 58 58 58 58 58	45 45 45 45 45 45 45 45 45 45	1/8 l_k cut 1/8 l_k cut 1/8 l_k cut 1/8 l_k cut 1/8 l_k cut 1/8 l_k cut 1/8 l_k cut 1/8 l_k cut 1/8 l_k cut 1/8 l_k cut	Straight Straight Straight Straight Straight Straight Straight Straight Straight Straight		Rear lines spread One-point line attachment 1/32-in. steel 90 lb-test nylon Basic length Length 1 Length 2 Length 3 1.25 l_k 1.00 l_k .75 l_k	59 59 62 62 65 65 65 65 70 70 70	60 60 *63,64 *63,64 66 to 69 66 to 69 66 to 69 66 to 69 71 71 71	Confluence point Confluence point Line material Line material Keel line length Keel line length Keel line length Keel line length Line length Line length Line length	2.34 2.22 2.60 2.23 2.34 2.35 2.21 1.88 2.18 2.29 1.98	1.04 1.05 .97 1.00 1.04 .95 1.09 1.15 1.01 .96 .96	1.06 1.11 1.01 1.02 1.06 .98 1.10 1.15 1.07 1.00 1.03	0.829 at α = 27.50° .825 at α = 25.75° .829 at α = 27.50° .829 at α = 27.50° .857 at α = 26.50° .868 at α = 26.95° .839 at α = 31.50°
 Keel batten	72 72 72	40 45 50	Pointed Pointed Pointed	Straight Straight Straight	Full batten Full batten Full batten		73 73 73	74 74 74	Λ_o, planform Λ_o, planform Λ_o, planform	3.20 3.07 3.10	0.74 .83 .70	0.79 .83 .70	
	72 75	45 45	Pointed Pointed	Straight Straight	Full batten Full batten	Triangular planform Triangular planform	73 76	74 77	Λ_o, planform α	3.22 3.22	0.87 .87	0.89 .94	
	78	45	Pointed	Straight	0.325 l_k batten	Pointed from 1/8 l_k nose cut	79	80	α	2.68	0.89	1.15	
	82	45	1/10 l_k cut	Straight	Aft inflated		83	*84,85	α	3.15	0.66	0.85	0.827 at α = 22.35°
	86	45	1/10 l_k cut	Straight	Nose inflated		87	*88,89	α	3.18	0.68	0.81	0.853 at α = 24.40°
	58 58	45 45	1/8 l_k cut 1/8 l_k cut	Straight Straight		Constrained model Constrained model	**94 to 99 ***100	60 60					

*Also θ, ϕ, C_T.

**C_m, C_L, C_D, L/D, C_A, C_N.

***C_{l_β}, C_{n_β}, C_{Y_β}.

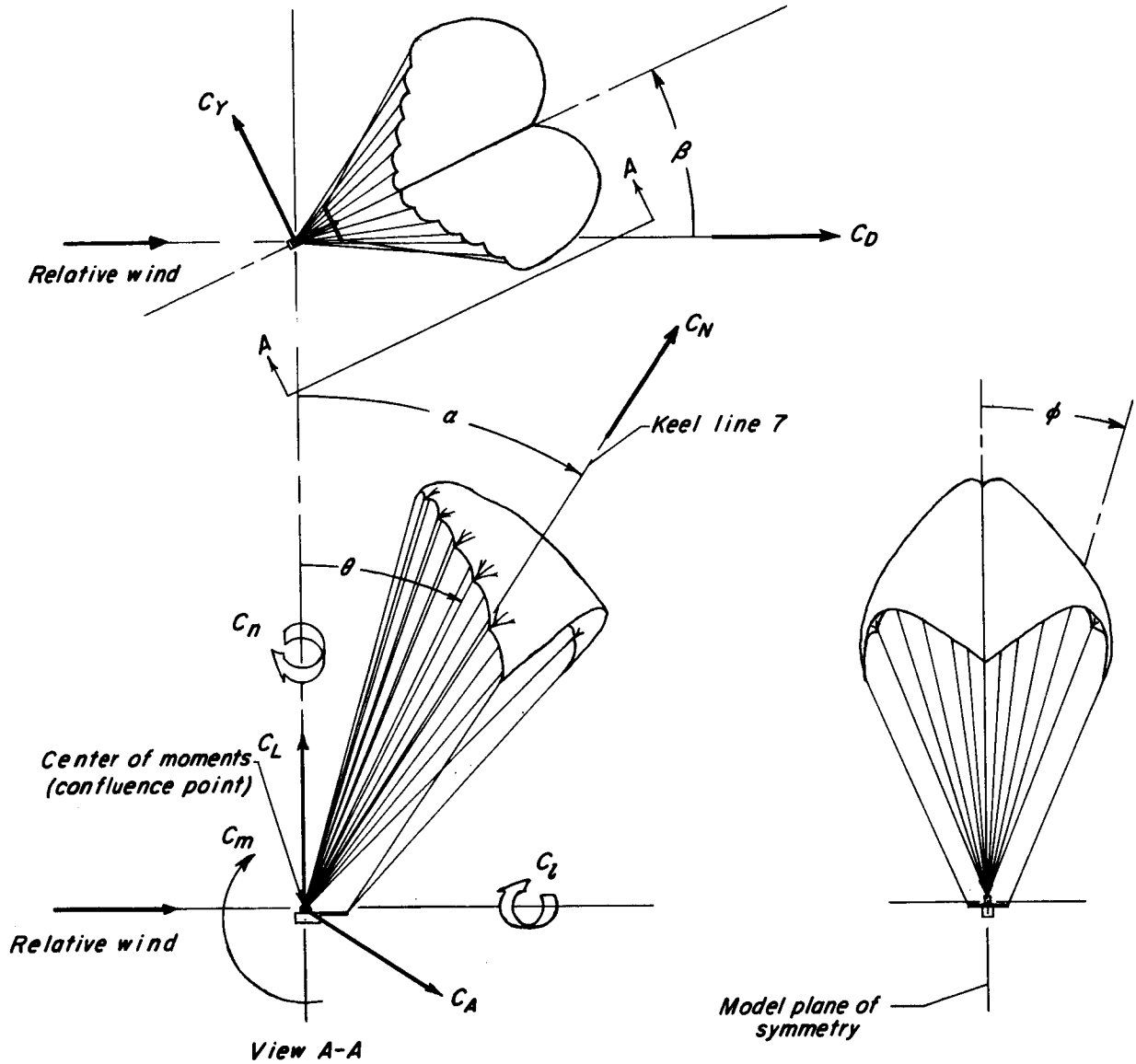

Figure 1.- System of axes. Positive directions of forces, moments, and angles used in presentation of the data are shown by arrows.

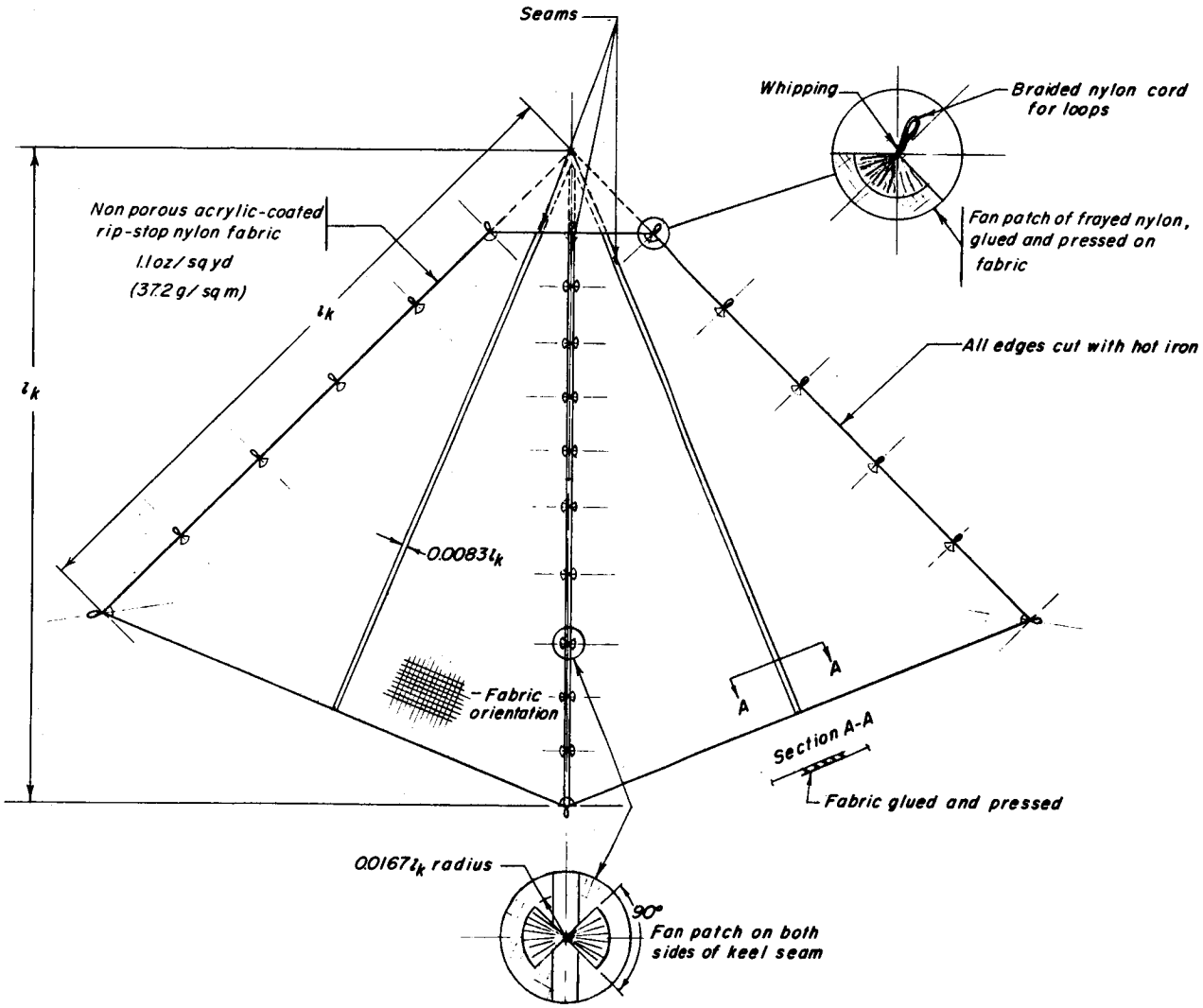

Figure 2.- Construction details of an all-flexible parawing shown for the basic model ($\Lambda_0 = 45^0$; 1/8 l_k nose cut off).

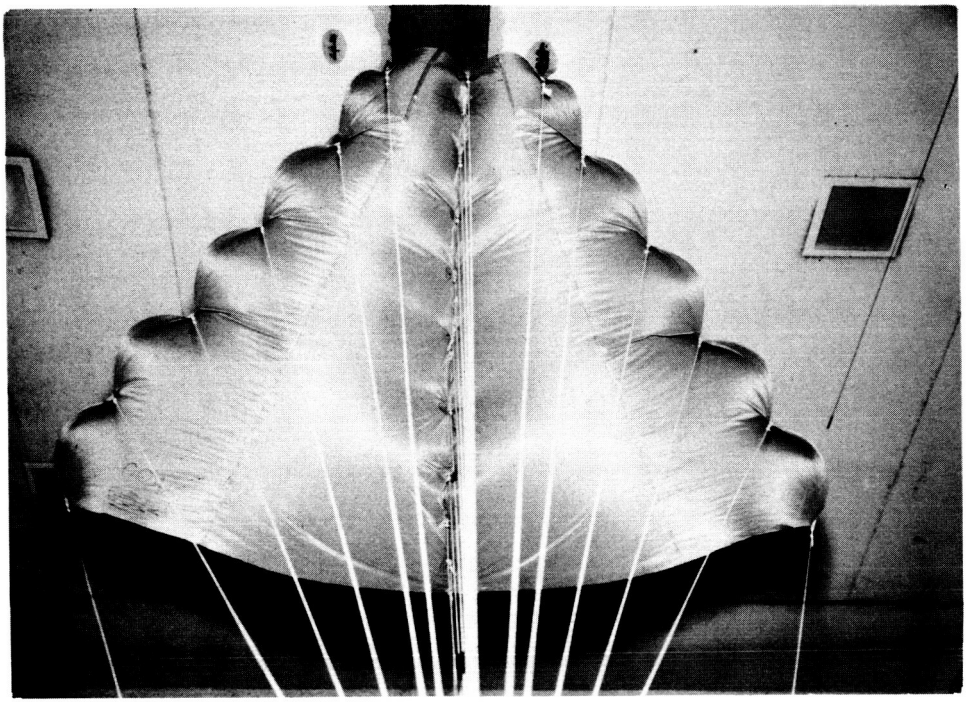

(a) Plan view. L-65-2355

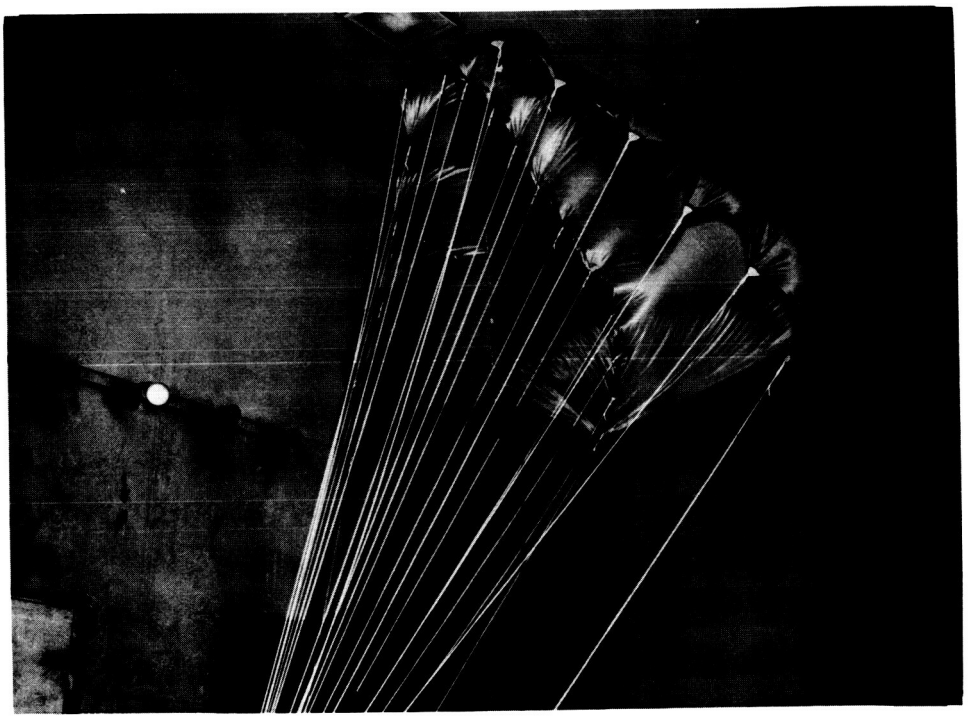

(b) Three-quarter front view. L-65-2356

Figure 3.- Photograph of the basic $\Lambda_0 = 45^0$ parawing model. Tethered test method.

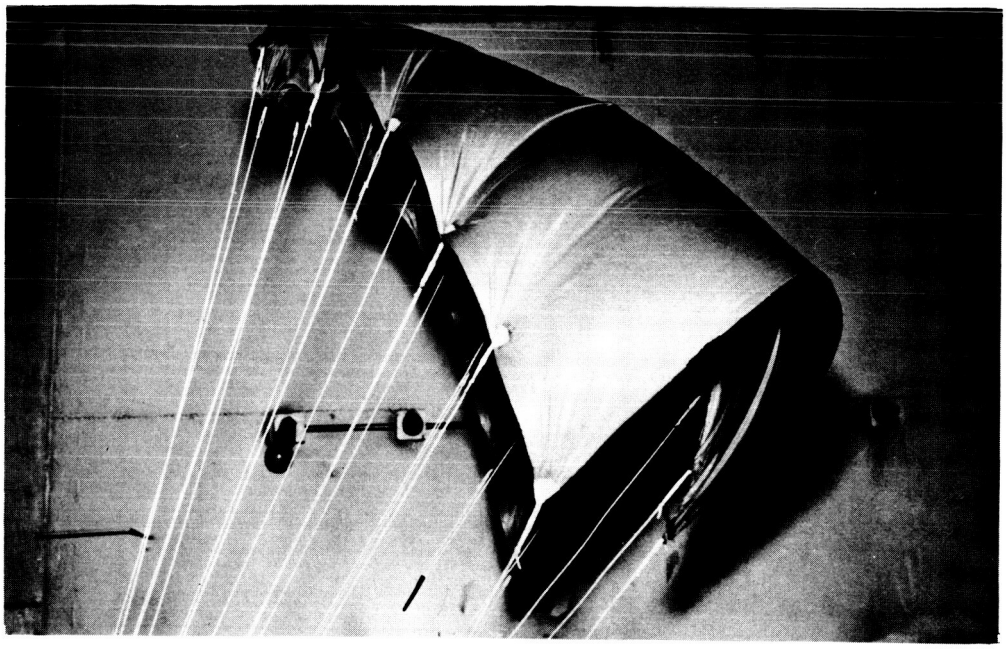

(c) Side view. L-65-2354

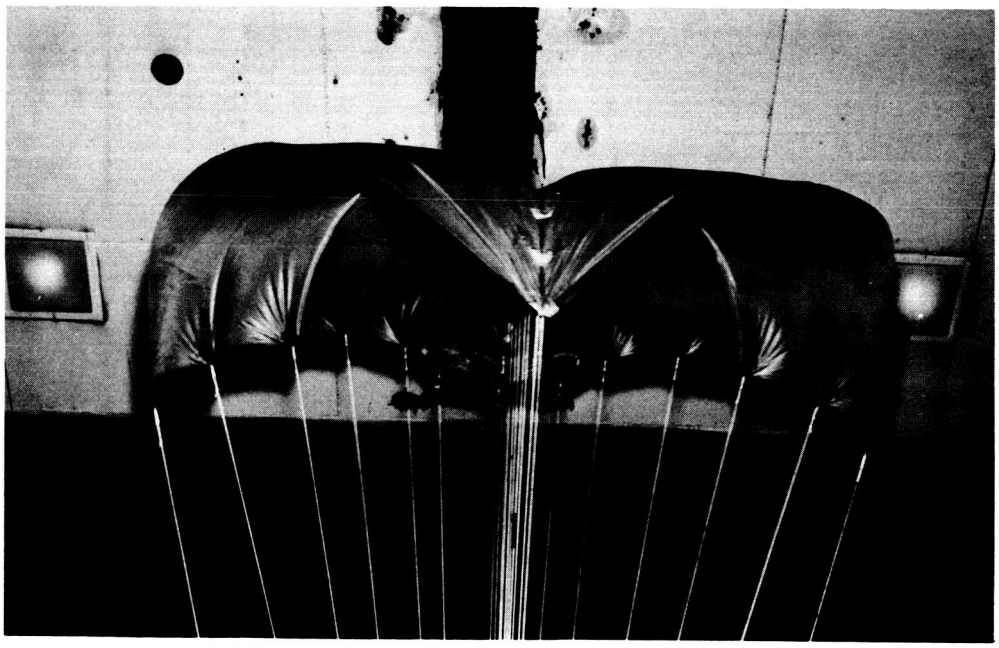

(d) Rear view. L-65-2360

Figure 3.- Concluded.

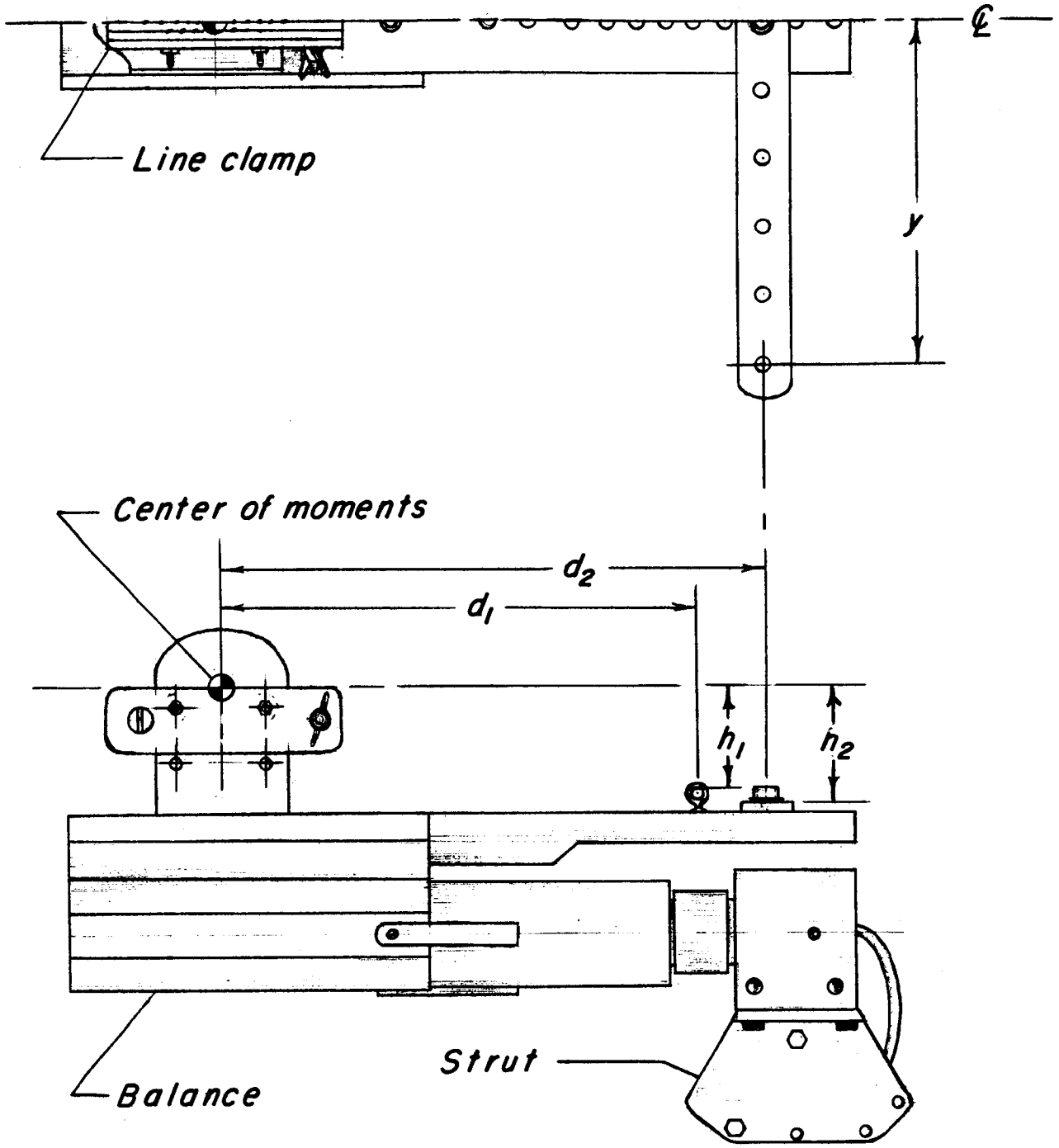

Figure 4.- Parawing line attachments to the balance used for the tethered method of testing. Dimensions are given in table II.

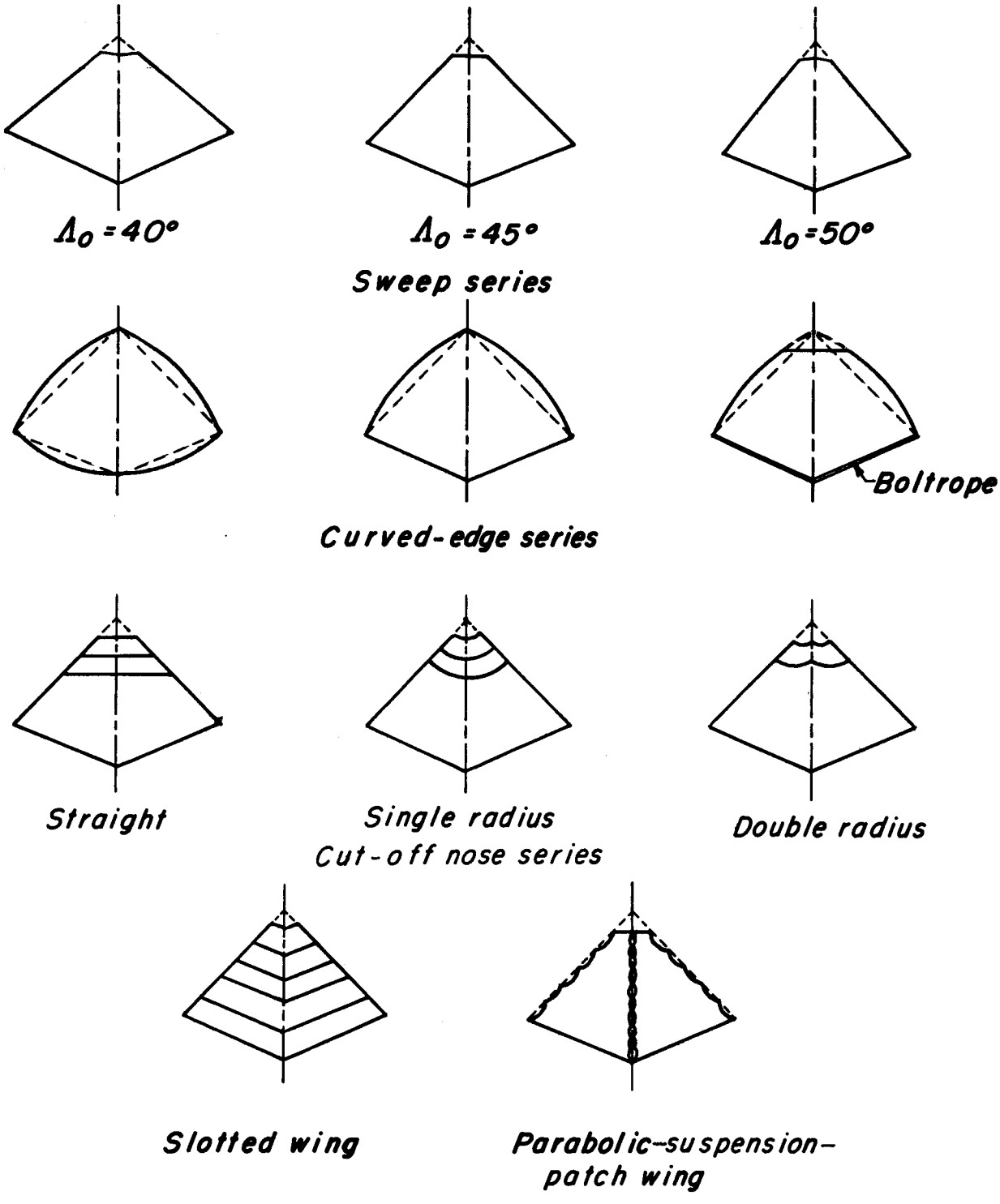

(a) All-flexible models.

Figure 5.- Test models.

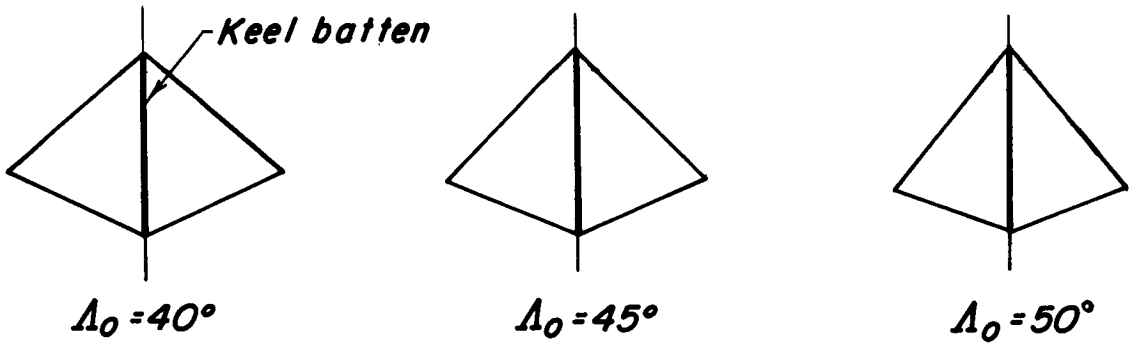

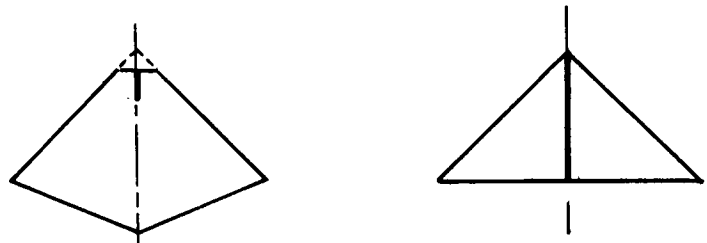

Keel–batten models

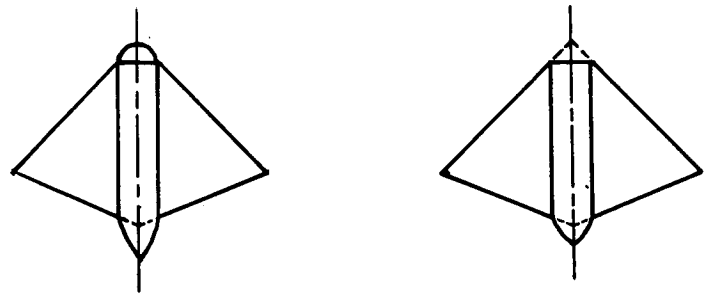

Inflatable–keel models

(b) Models with local stiffness.

Figure 5.- Concluded.

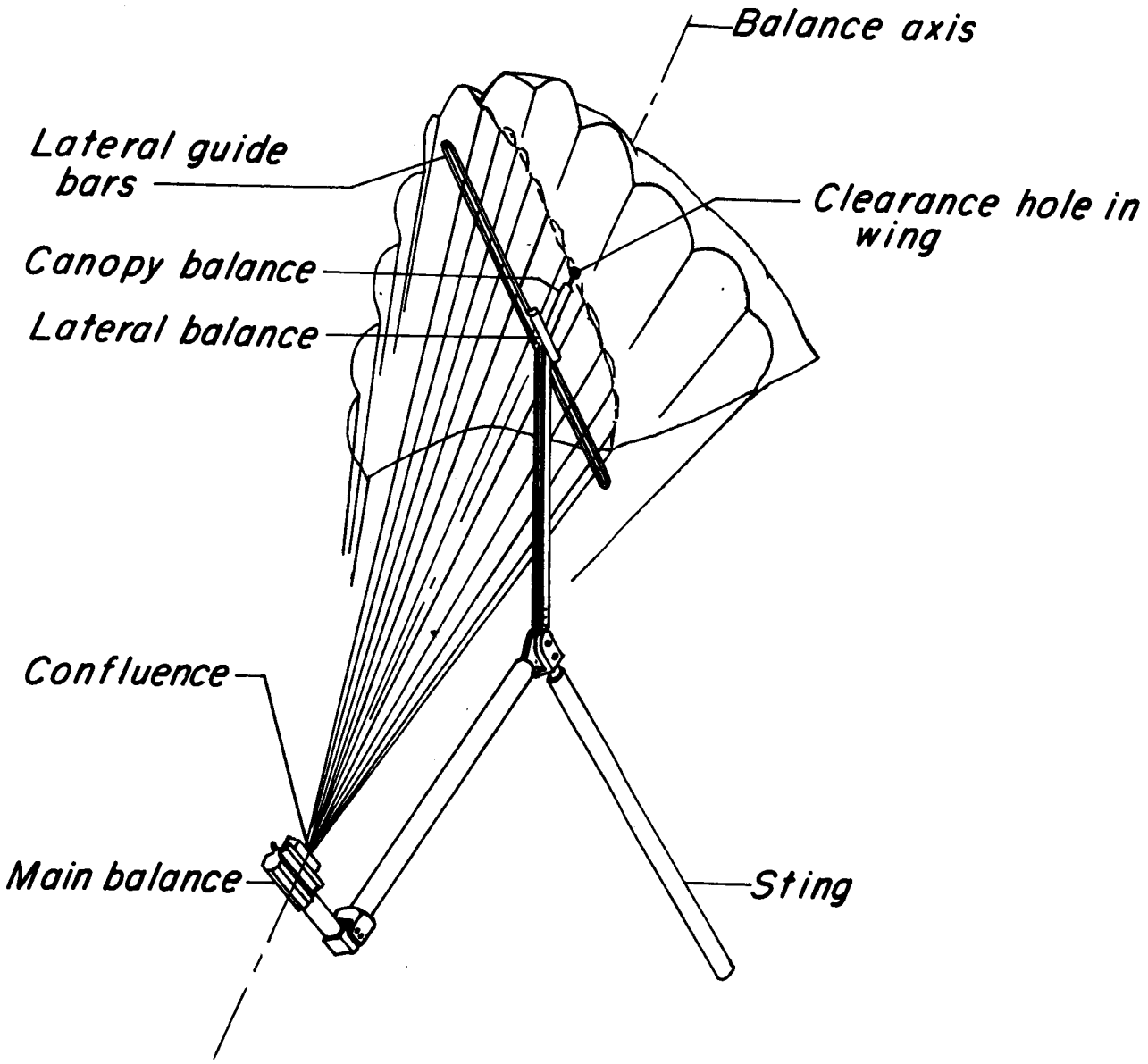

(a) Sketch of apparatus.

Figure 6.- Apparatus used for the constrained method of force testing.

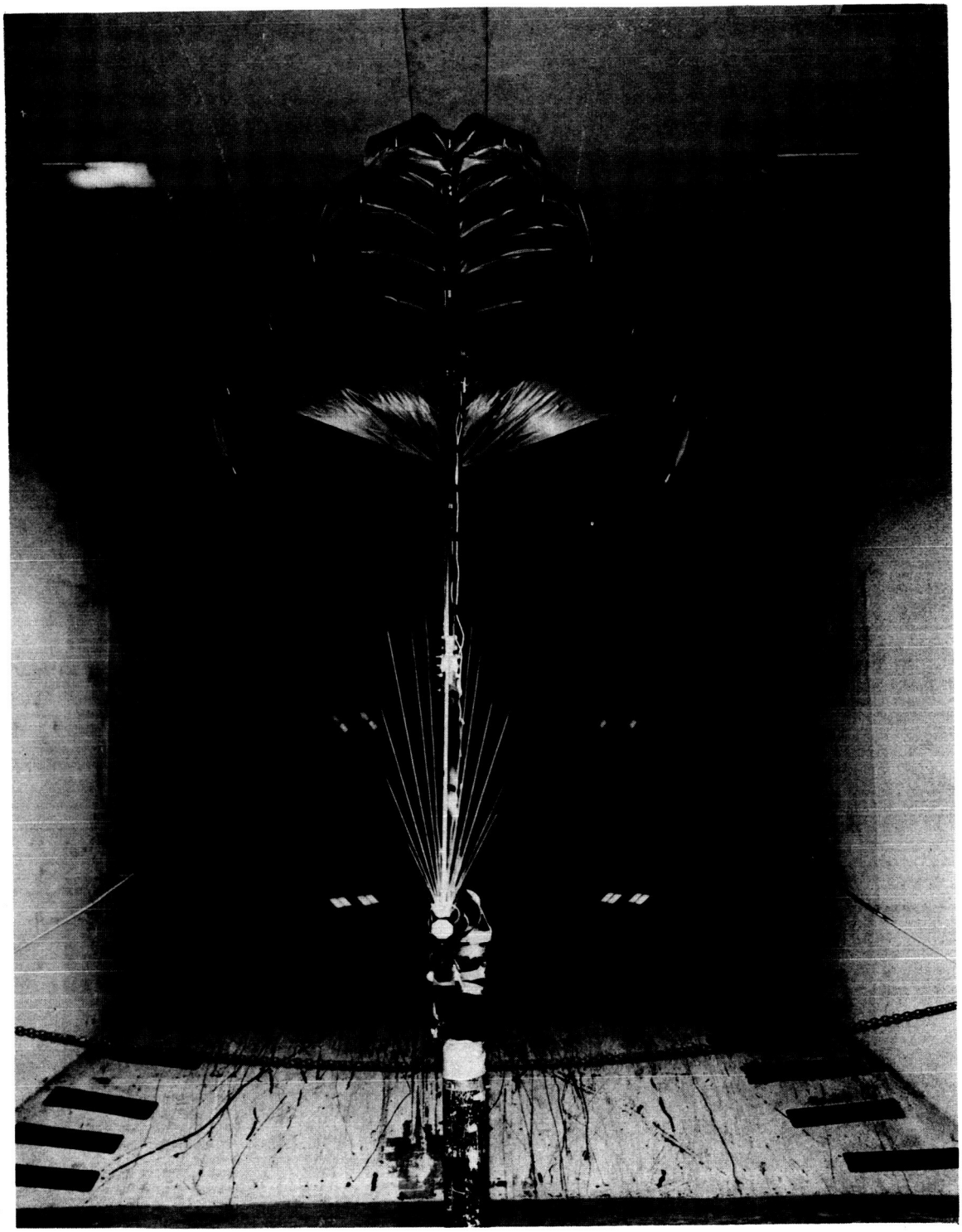

(b) Front view.

L-66-2782

Figure 6.- Continued.

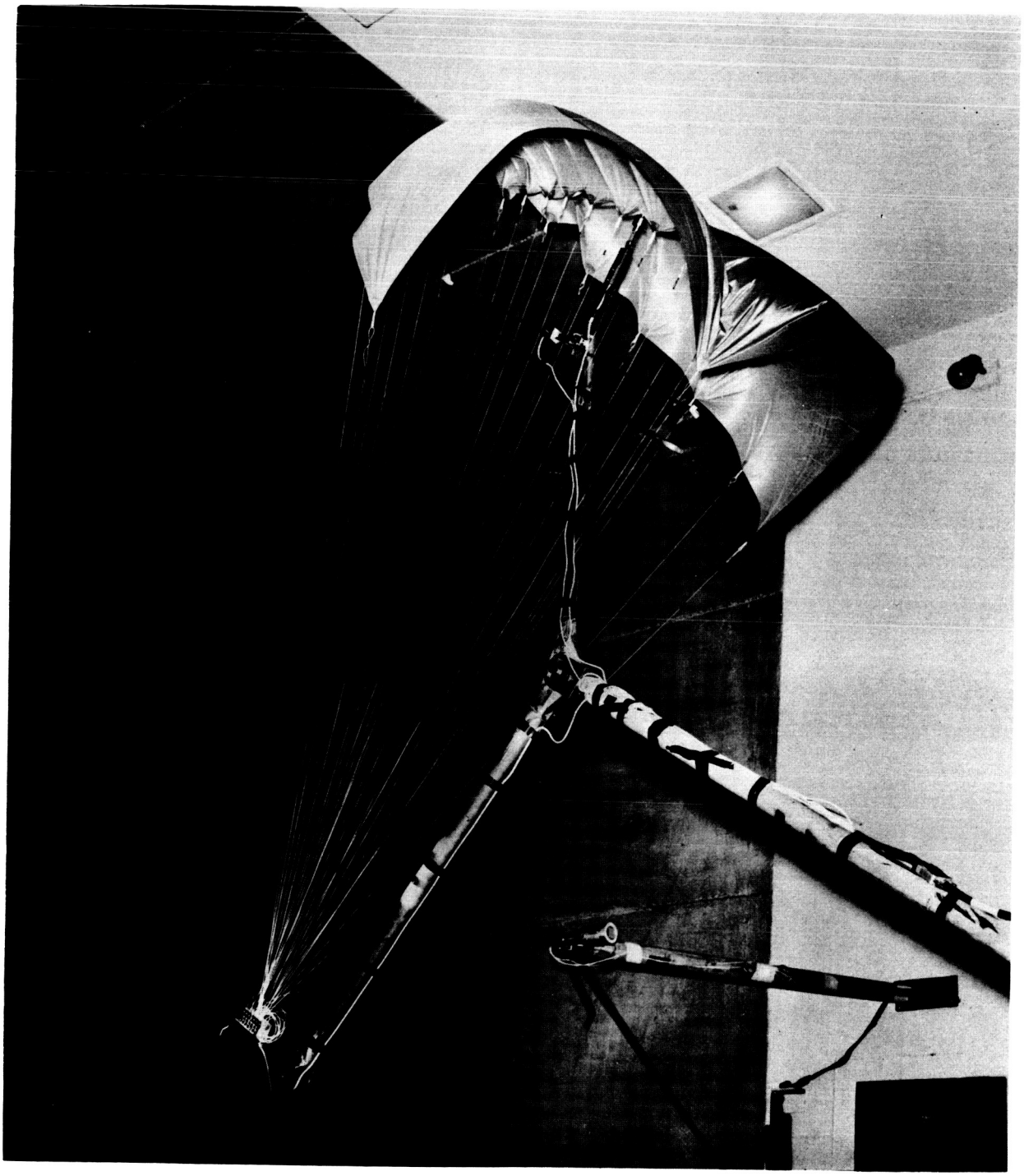

(c) Rear-quarter view. L-66-2783

Figure 6.- Concluded.

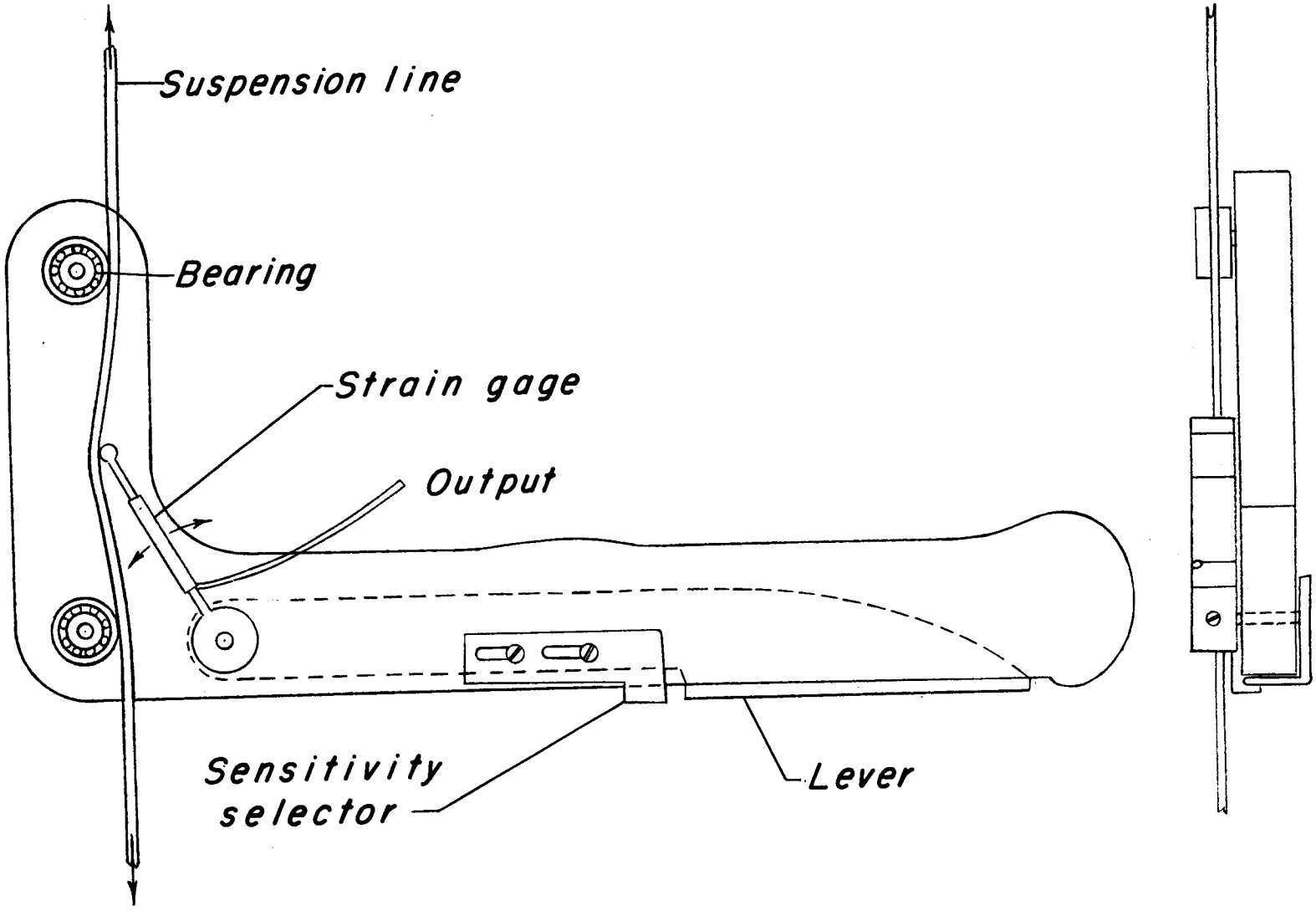

Figure 7.- Tension-measuring device.

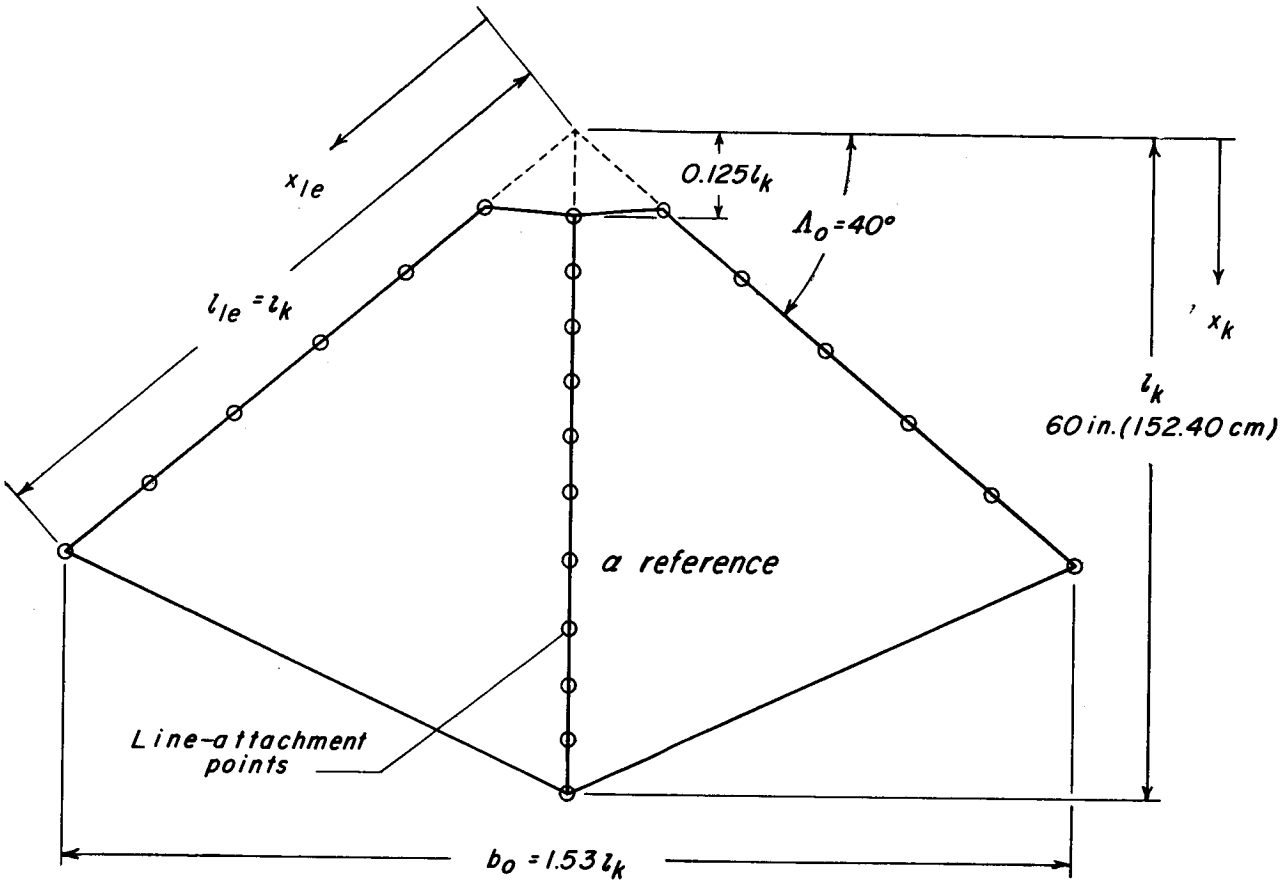

Keel	x/l_k Leading edge
.125	.177
.208	.333
.292	.500
.375	.677
.459	.833
.542	1.000
.645	
.750	
.833	
.917	
1.000	

Line-attachment location

Figure 8.- Details of the flat pattern of a parawing with $\Lambda_0 = 40^0$ and 1/8 l_k nose cut off.

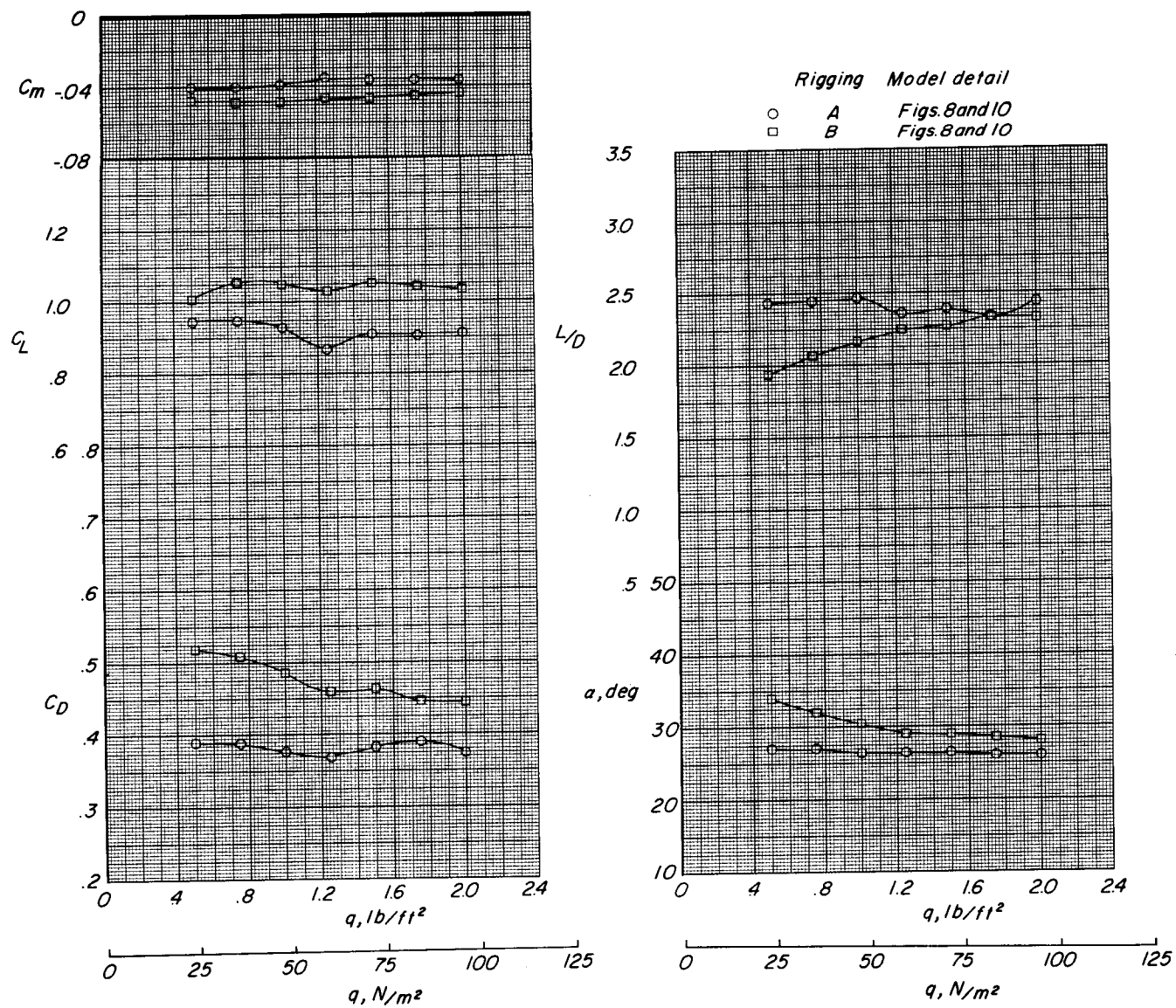

Figure 9.- Effect of changes in rigging on the variation of the wing longitudinal aerodynamic characteristics with dynamic pressure for a parawing with $\Lambda_0 = 40^0$ and 1/8 l_k nose cut off.

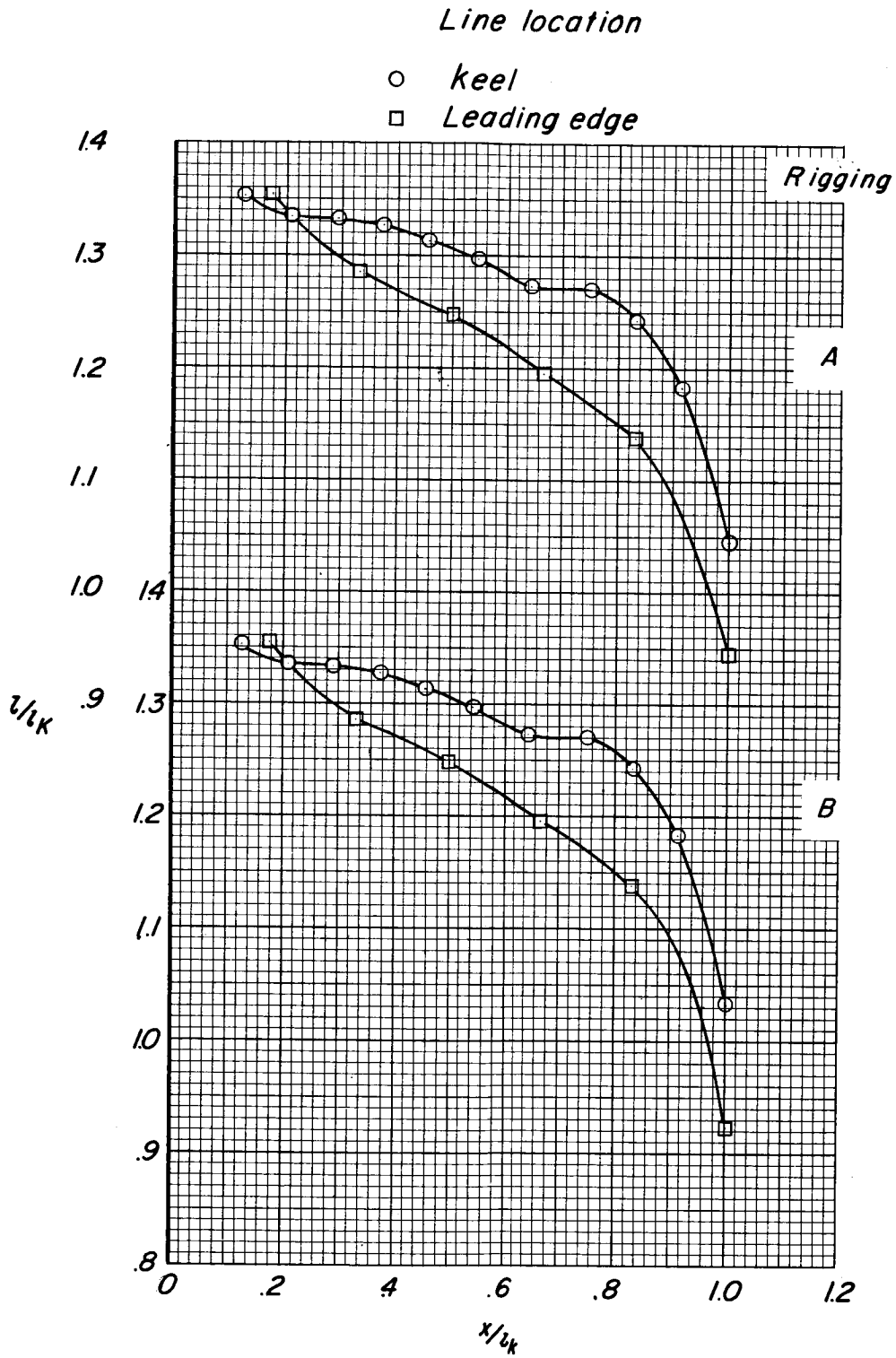

Figure 10.- Line lengths of a parawing with $\Lambda_0 = 40^0$ and $1/8\ l_k$ nose cut off.

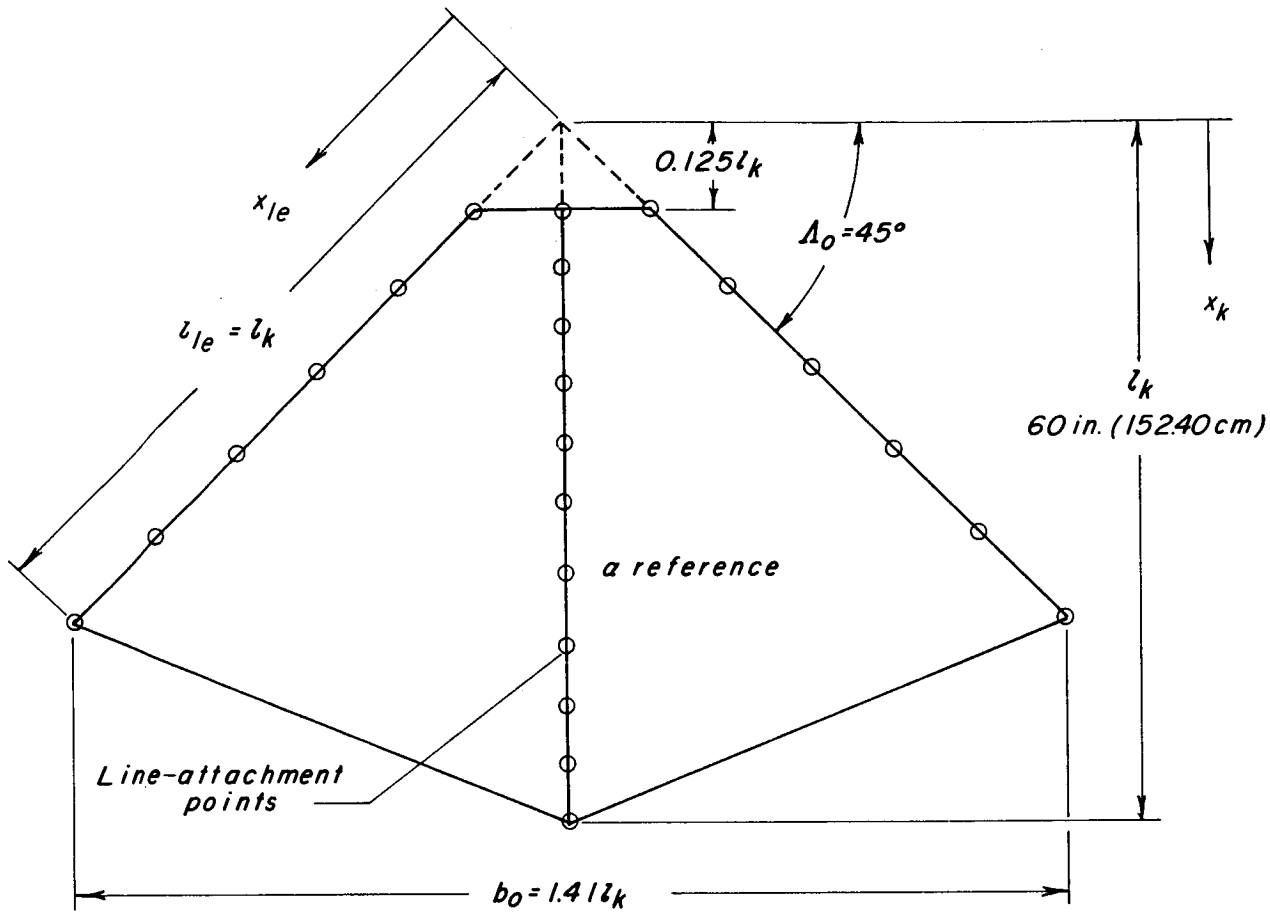

x/l_k	
Keel	Leading edge
.125	.177
.208	.333
.292	.500
.375	.667
.459	.833
.542	1.000
.645	
.750	
.833	
.917	
1.000	

Line-attachment location

(a) Flat-pattern details.

Figure 11.- Model of a parawing with $\Lambda_o = 45^0$ and 1/8 l_k nose cut off.

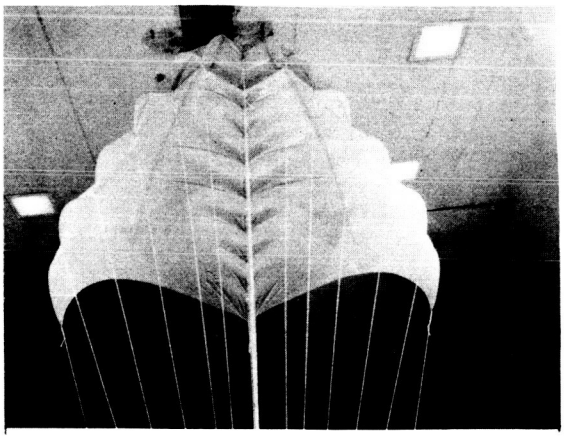

Front view

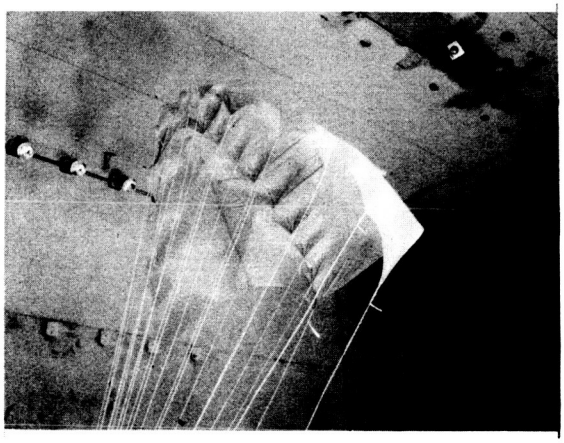

Front three-quarter view

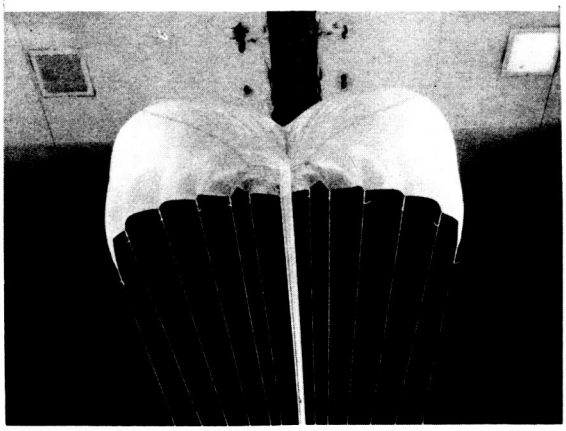

Rear view

(b) Photographs of model. L-67-940

Figure 11.- Concluded.

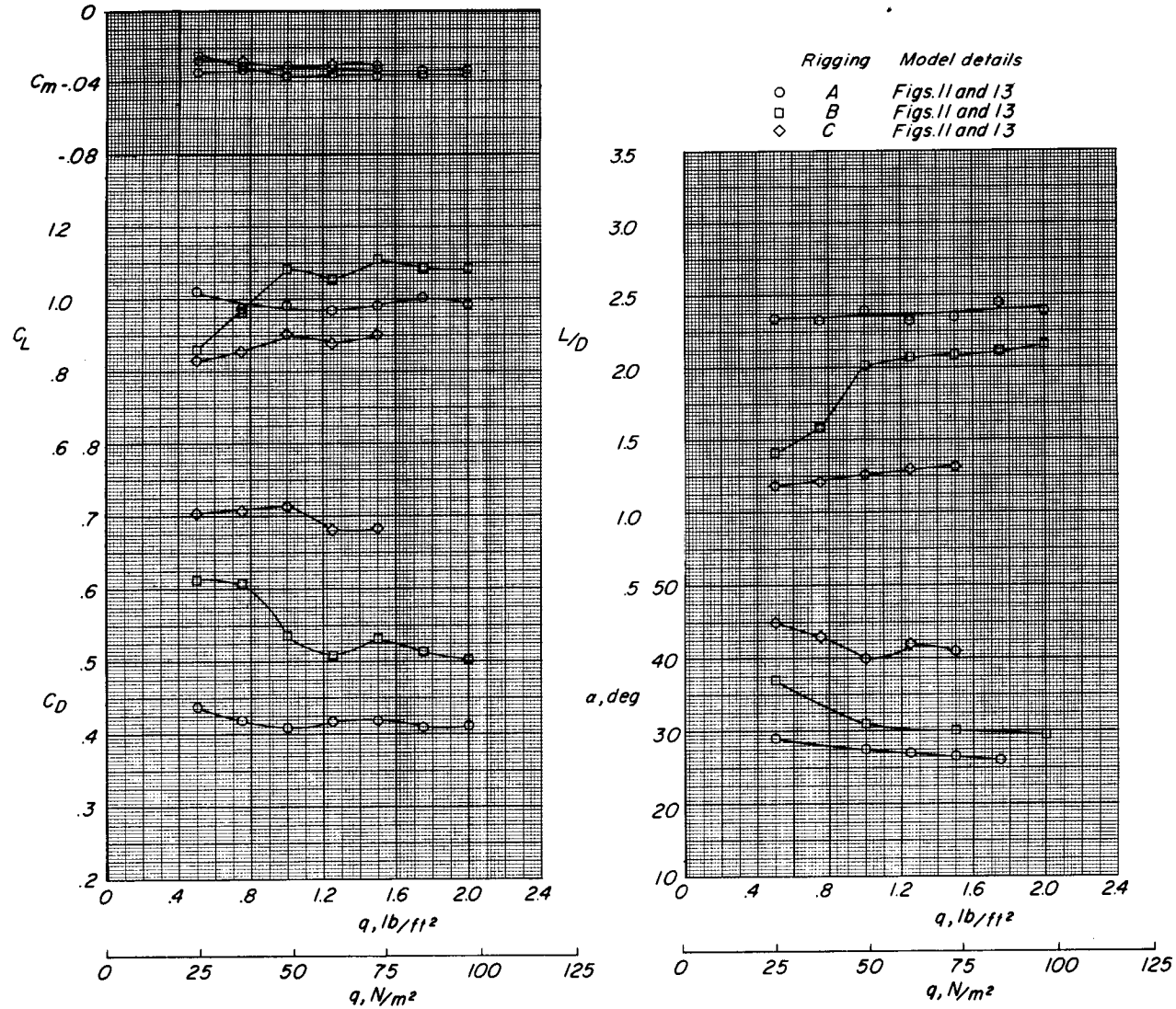

Figure 12.- Effect of changes in rigging on the variation of the wing longitudinal aerodynamic characteristics with dynamic pressure for a parawing with $\Lambda_0 = 45^0$ and 1/8 l_k nose cut off.

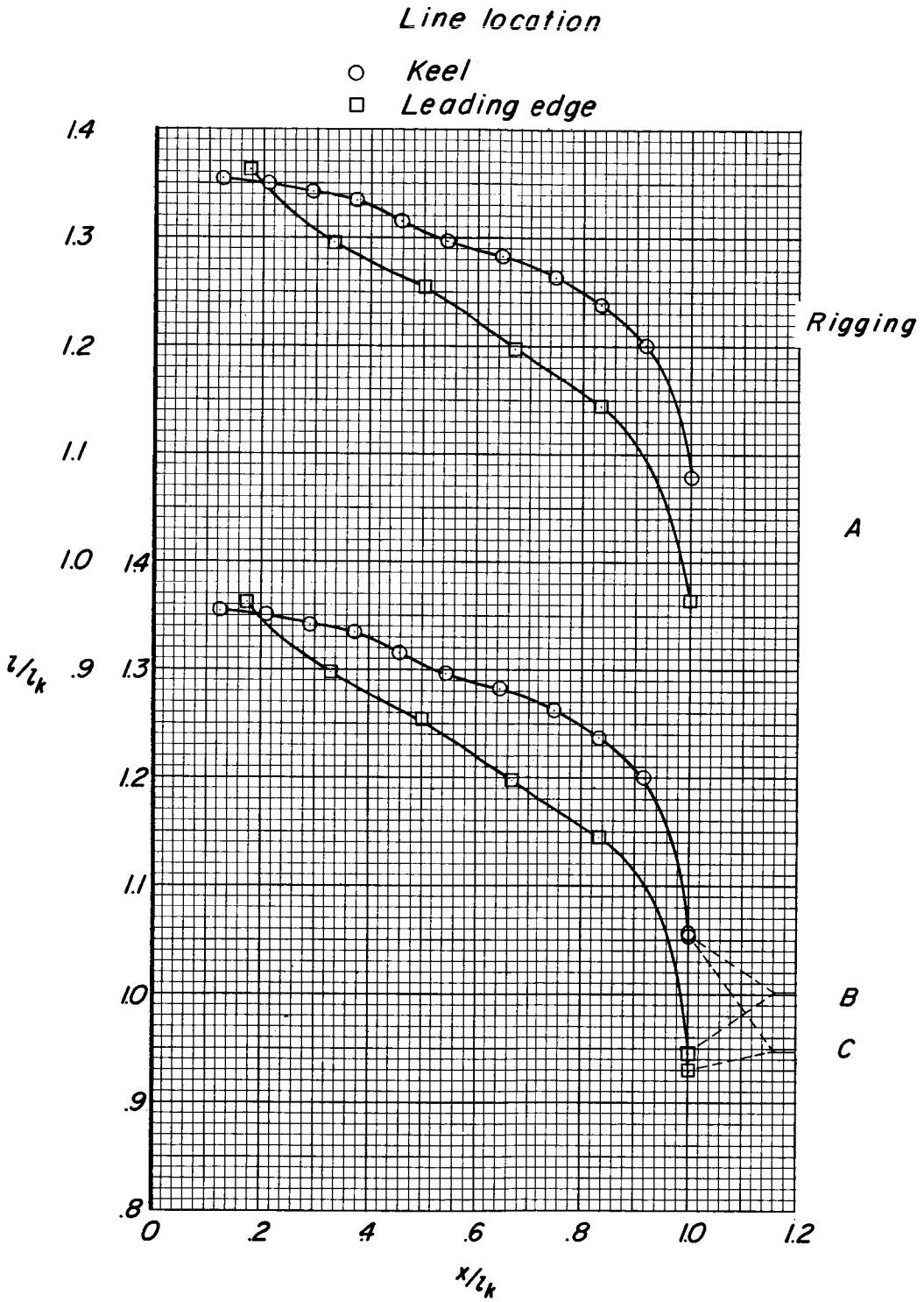

Figure 13.- Line lengths of a parawing with $\Lambda_0 = 45^0$ and 1/8 l_k nose cut off.

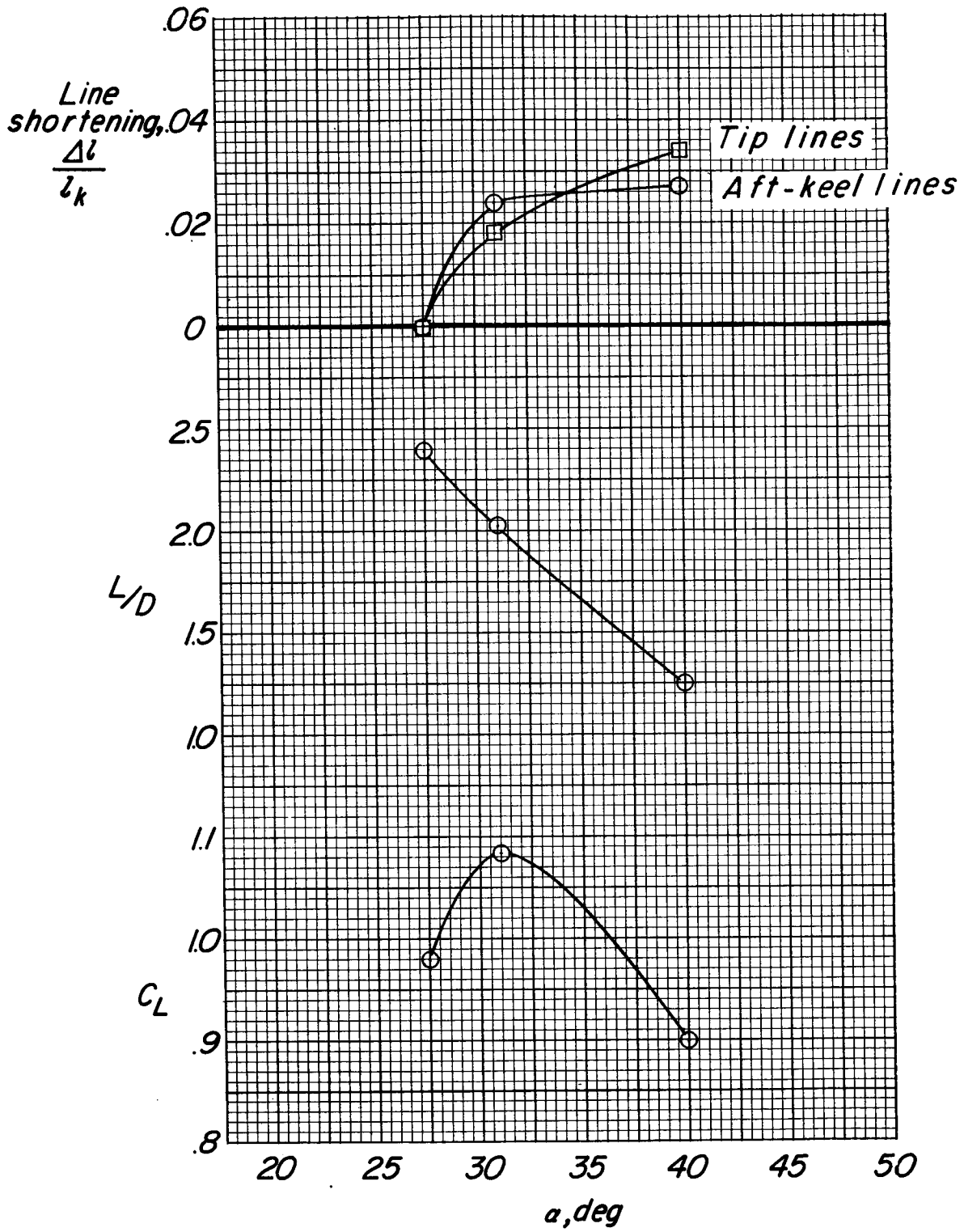

Figure 14.- Modulation of C_L and L/D by rigging changes on a parawing with $\Lambda_0 = 45^0$ and 1/8 l_k nose cut off.

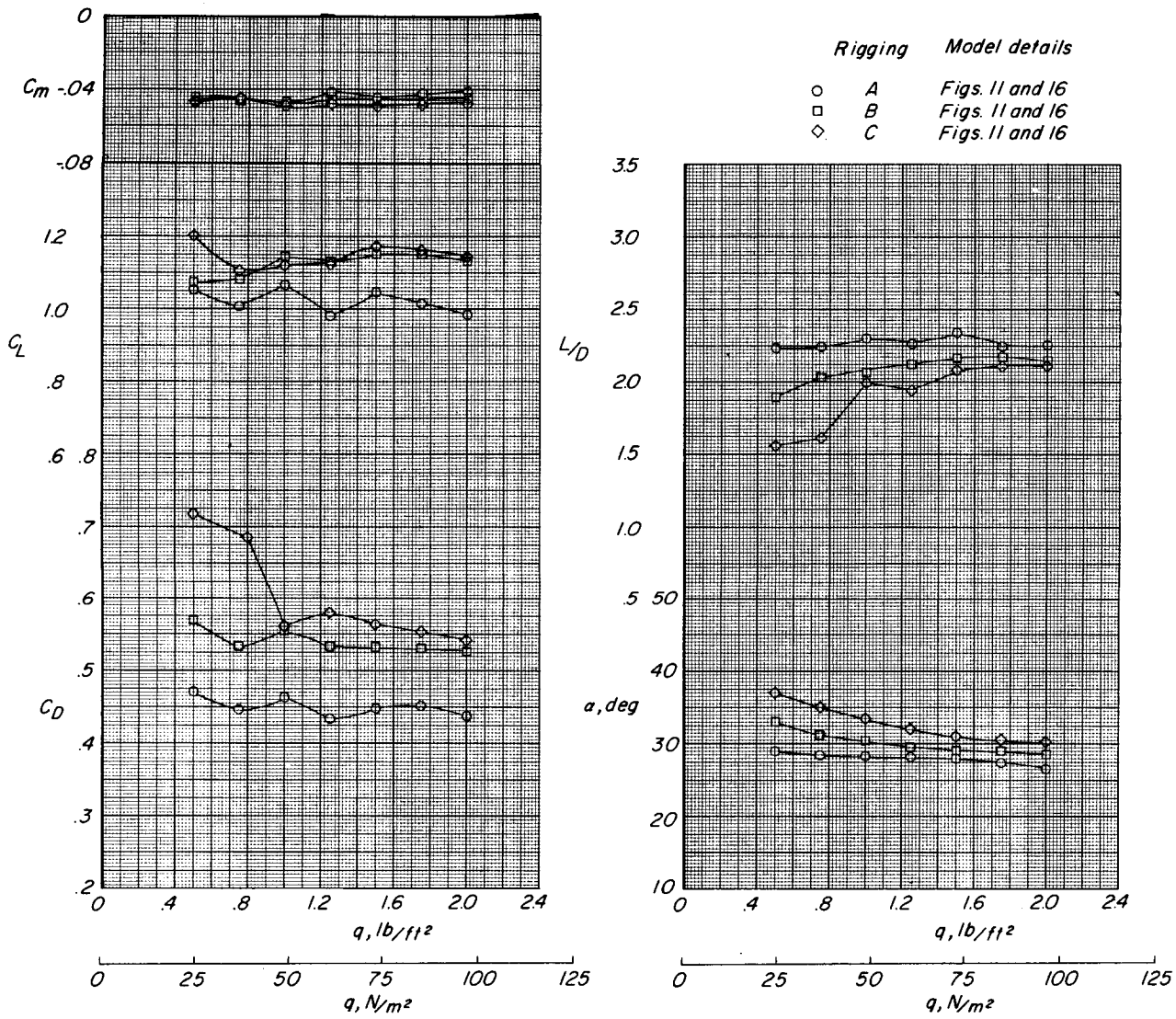

Figure 15.- Effect of changes in rigging on the variation of the wing longitudinal aerodynamic characteristics with dynamic pressure for a parawing with $\Lambda_0 = 45^0$ and 1/8 ℓ_k nose cut off.

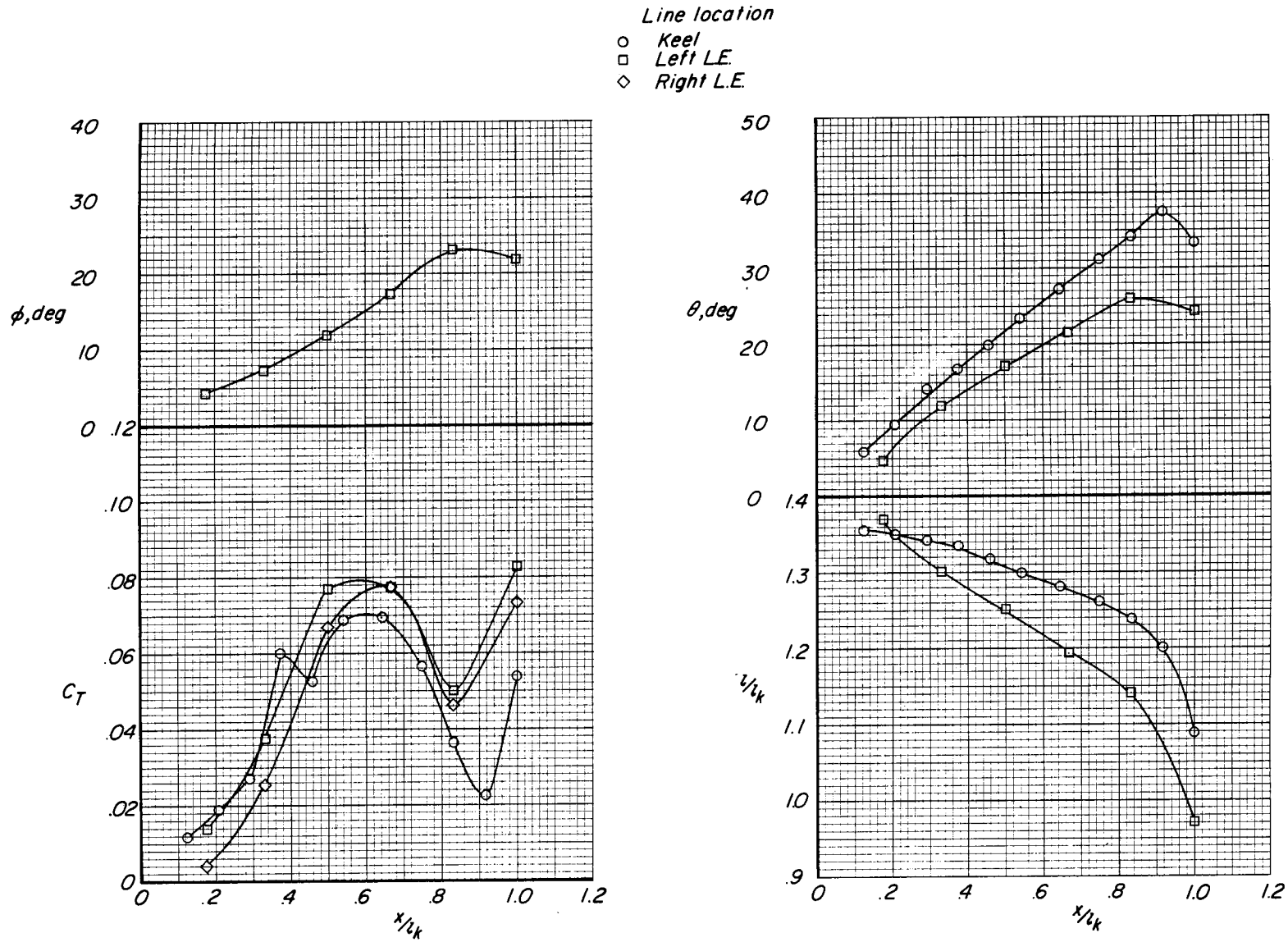

(a) Rigging A; q = 1.0.

Figure 16.- Tension coefficients, line angles, and line lengths for a parawing with $\Lambda_0 = 45^0$ and 1/8 l_k nose cut off.

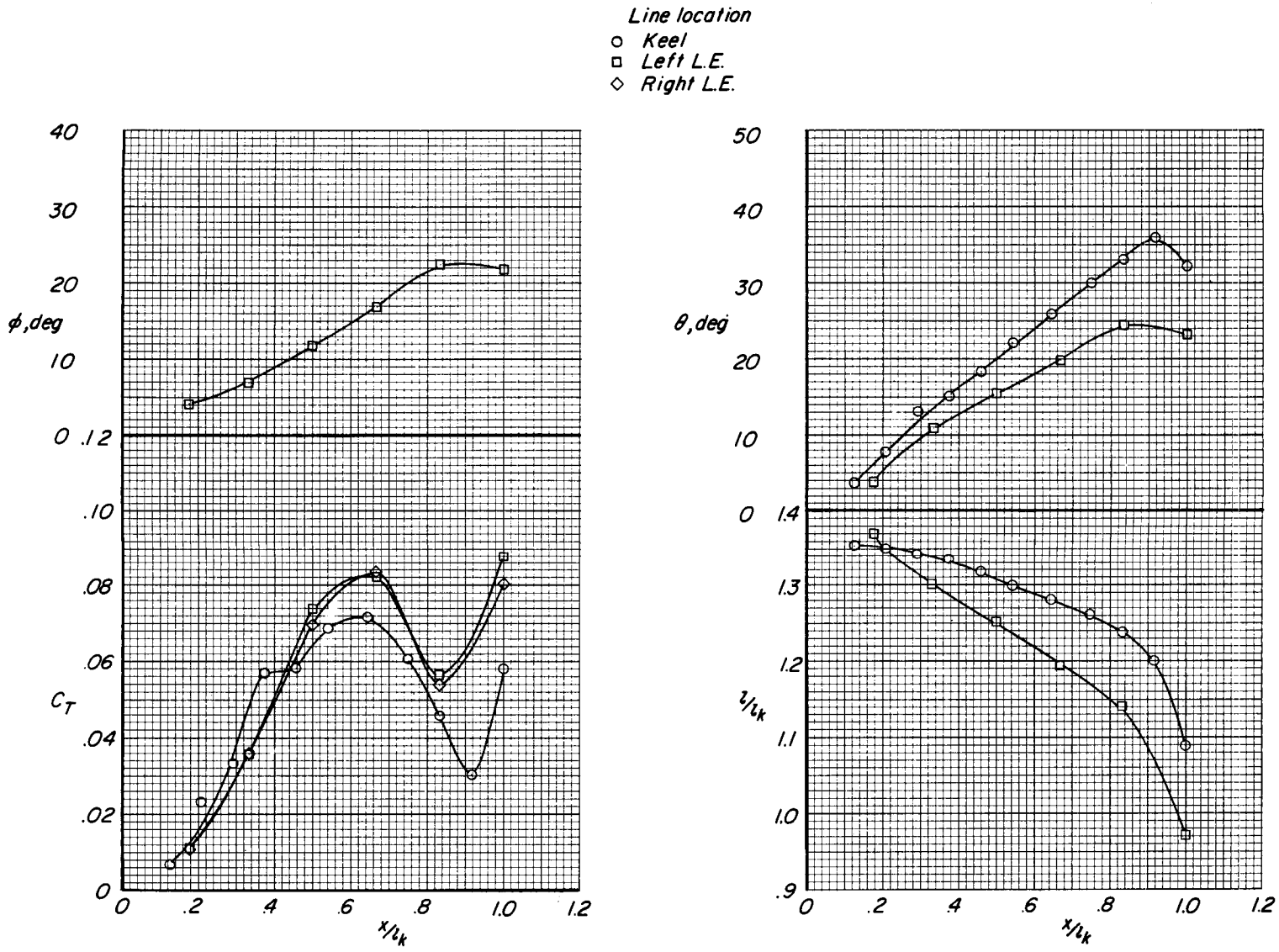

(a) Rigging A; q = 2.0 – Concluded.

Figure 16.- Continued.

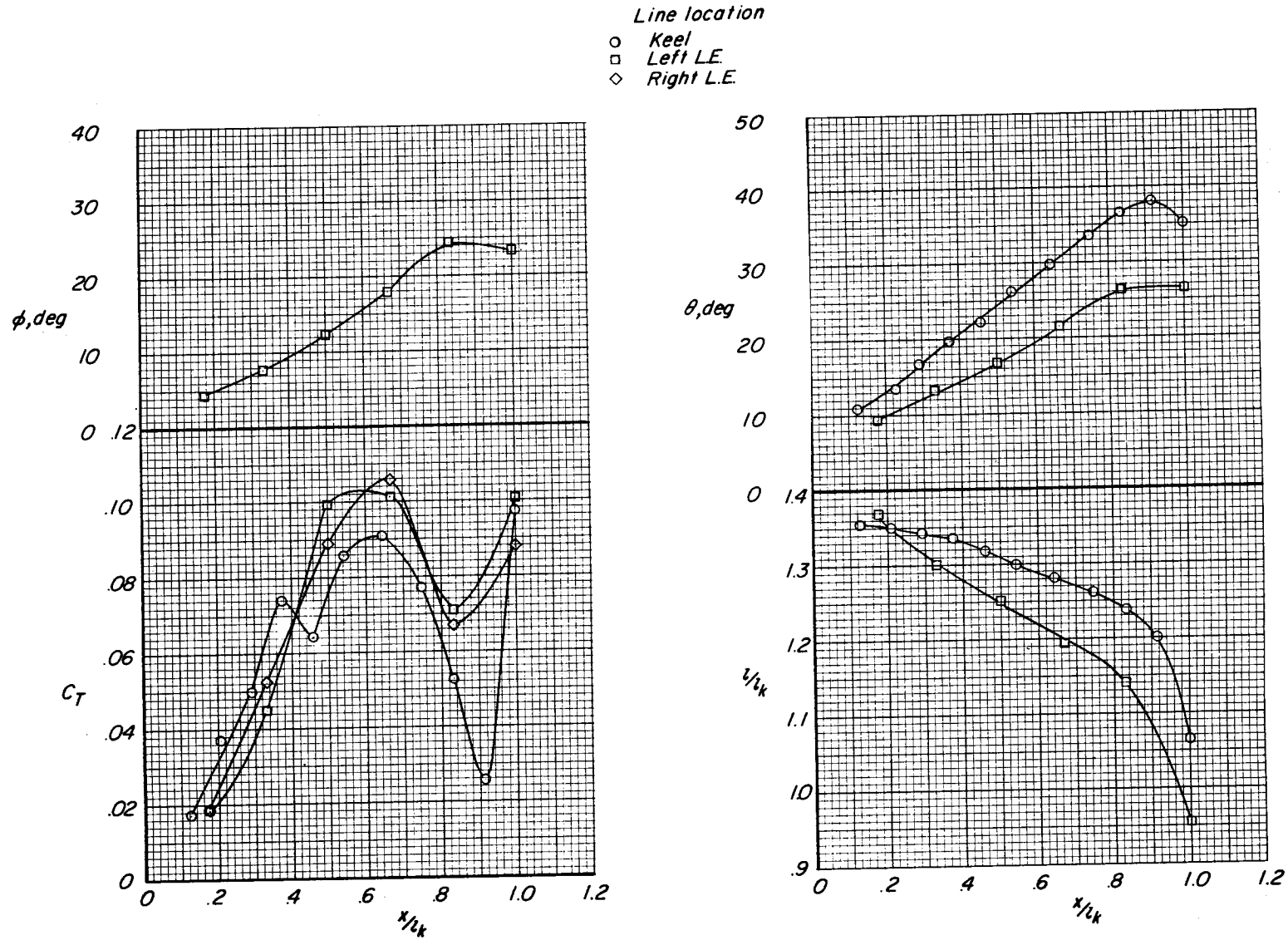

(b) Rigging B; q = 1.0.

Figure 16.- Continued.

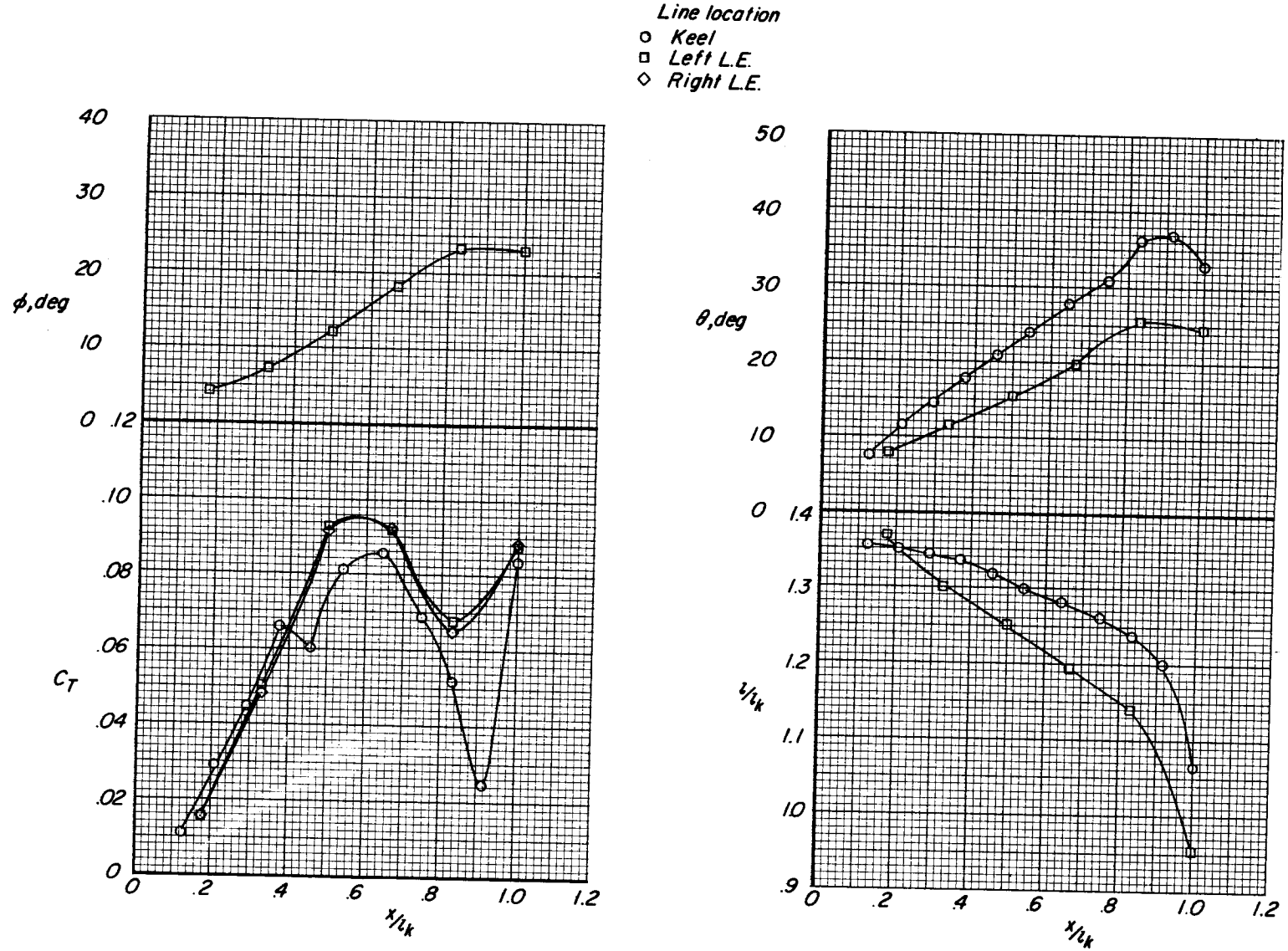

(b) Rigging B; q = 2.0 – Concluded.

Figure 16.- Continued.

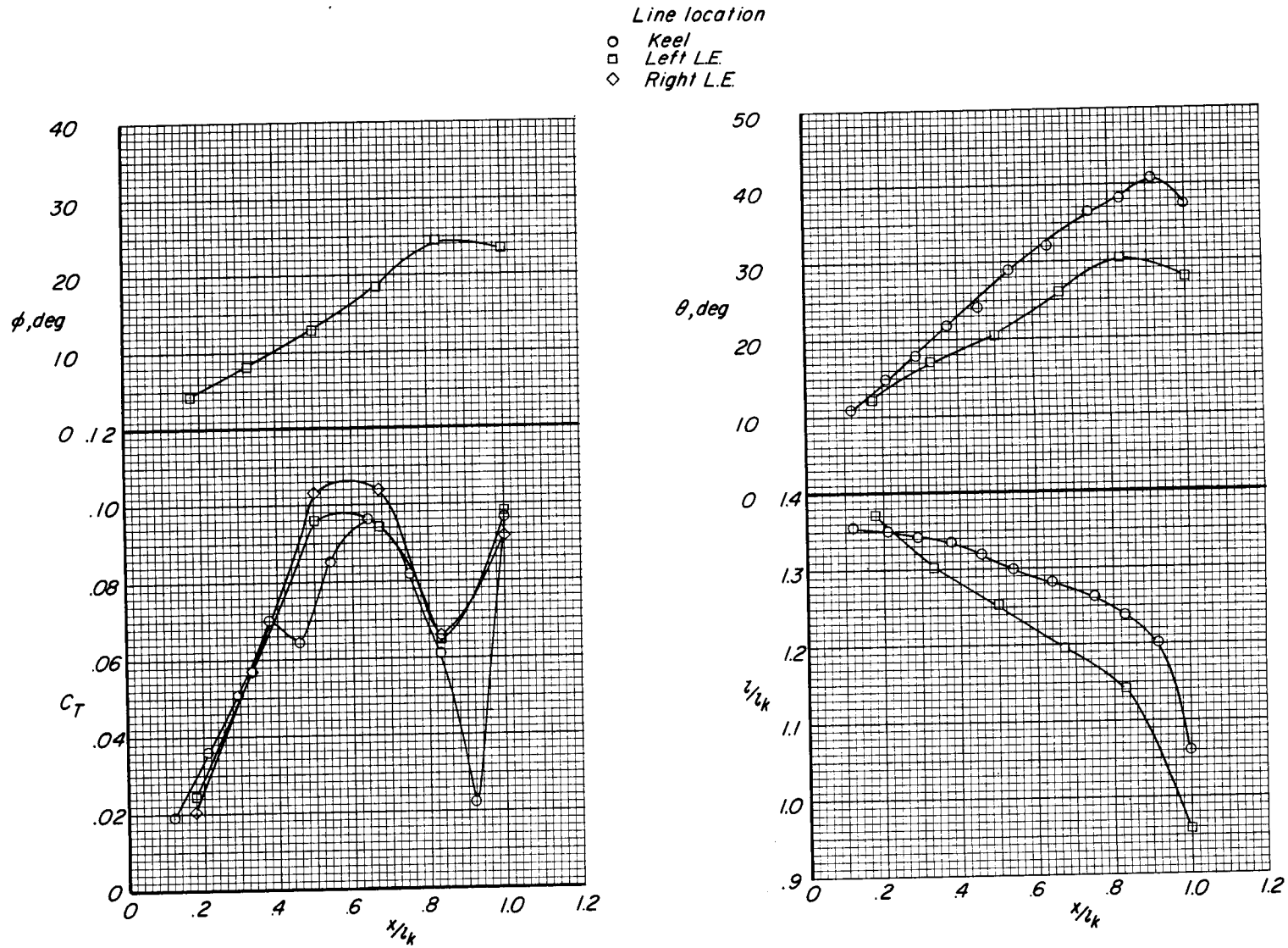

(c) Rigging C; q = 1.0.

Figure 16.- Continued.

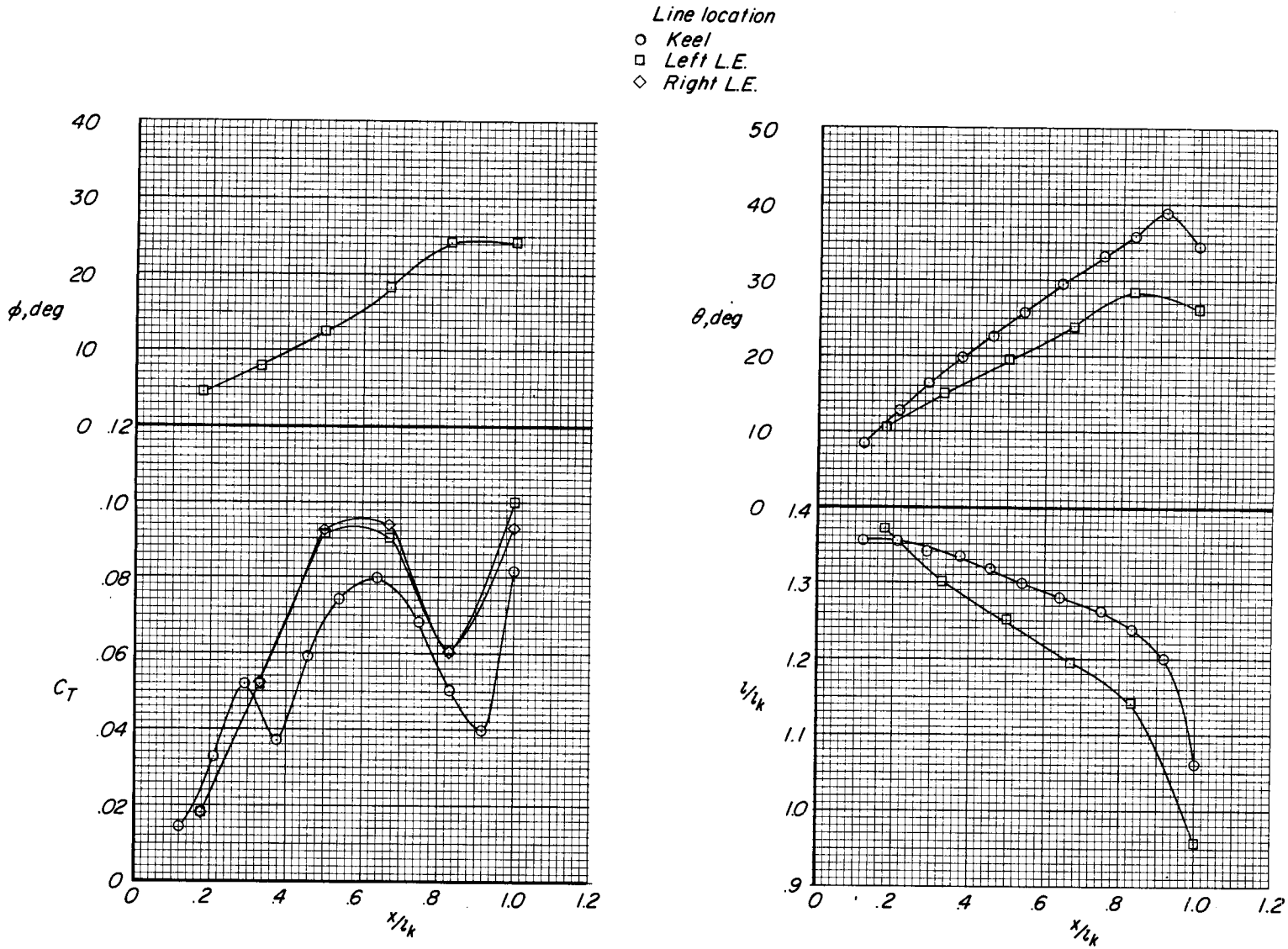

(c) Rigging C; q = 2.0 – Concluded.

Figure 16.- Concluded.

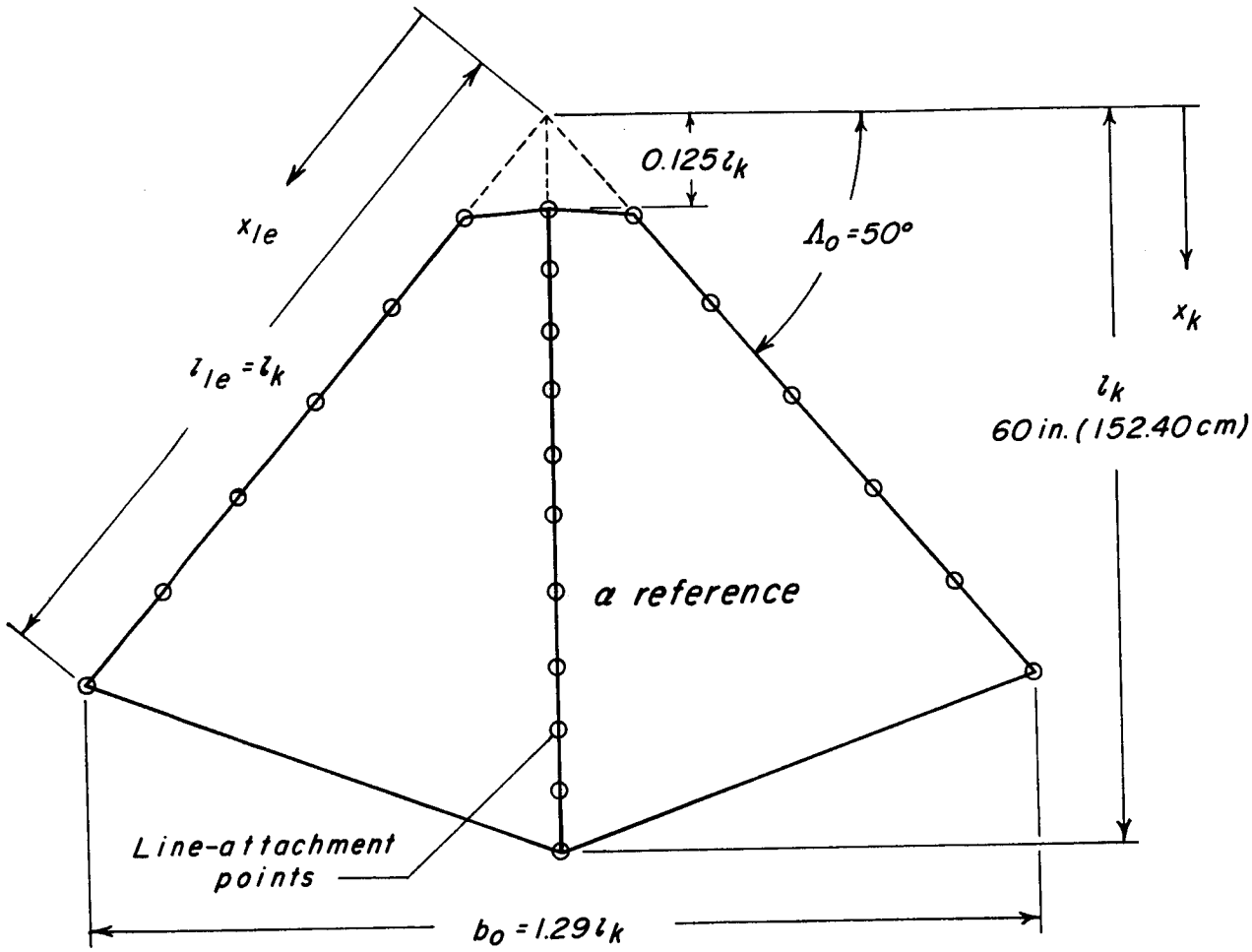

x/l_k	
Keel	Leading edge
.125	.177
.208	.333
.292	.500
.375	.667
.459	.833
.542	1.000
.645	
.750	
.833	
.917	
1.000	

Line-attachment location

Figure 17.- Details of the flat pattern of a parawing with $\Lambda_o = 50^o$ and 1/8 l_k nose cut off.

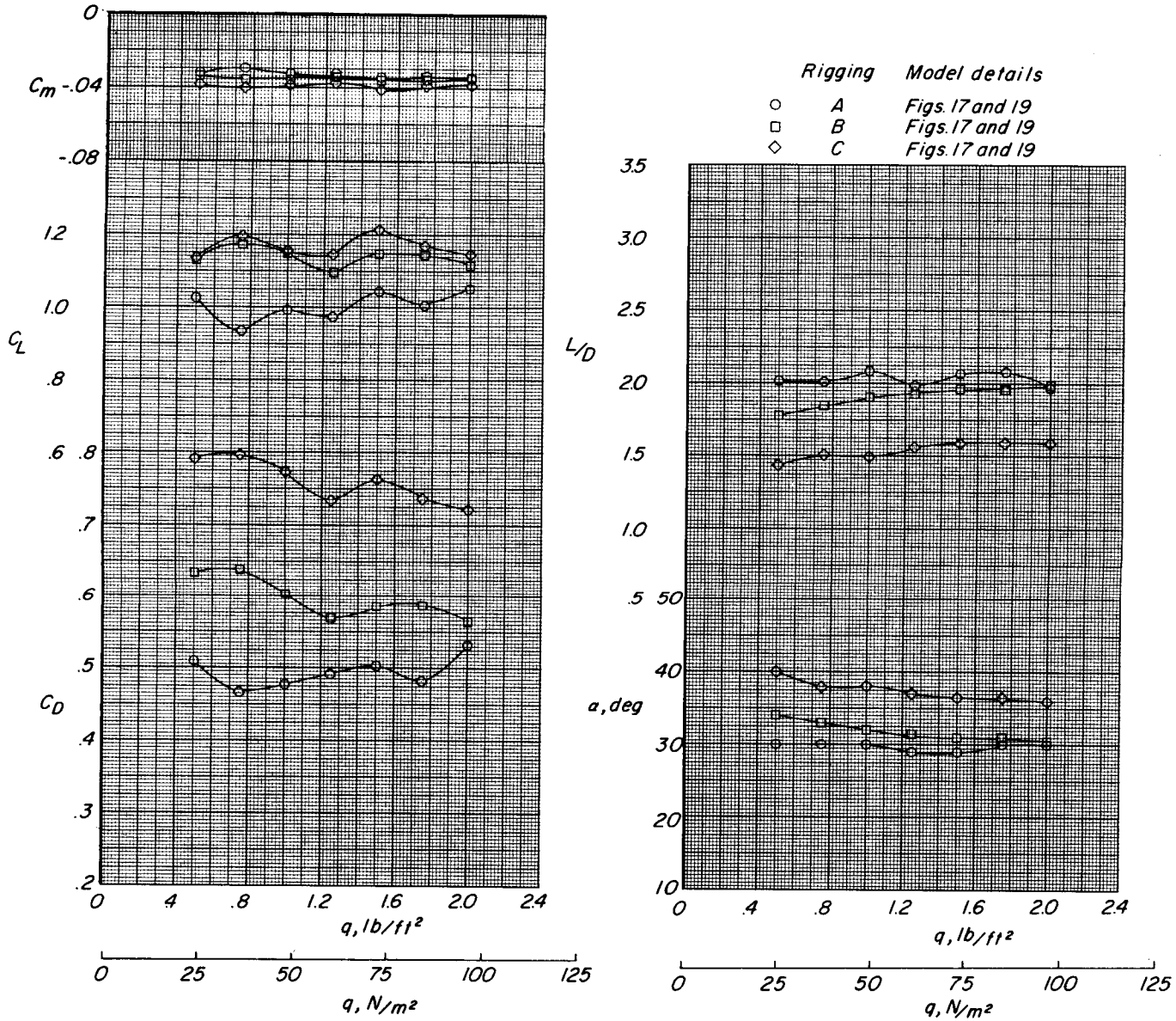

Figure 18.- Effect of changes in rigging on the variation of the wing longitudinal aerodynamic characteristics with dynamic pressure for a parawing with $\Lambda_0 = 50^0$ and 1/8 l_k nose cut off.

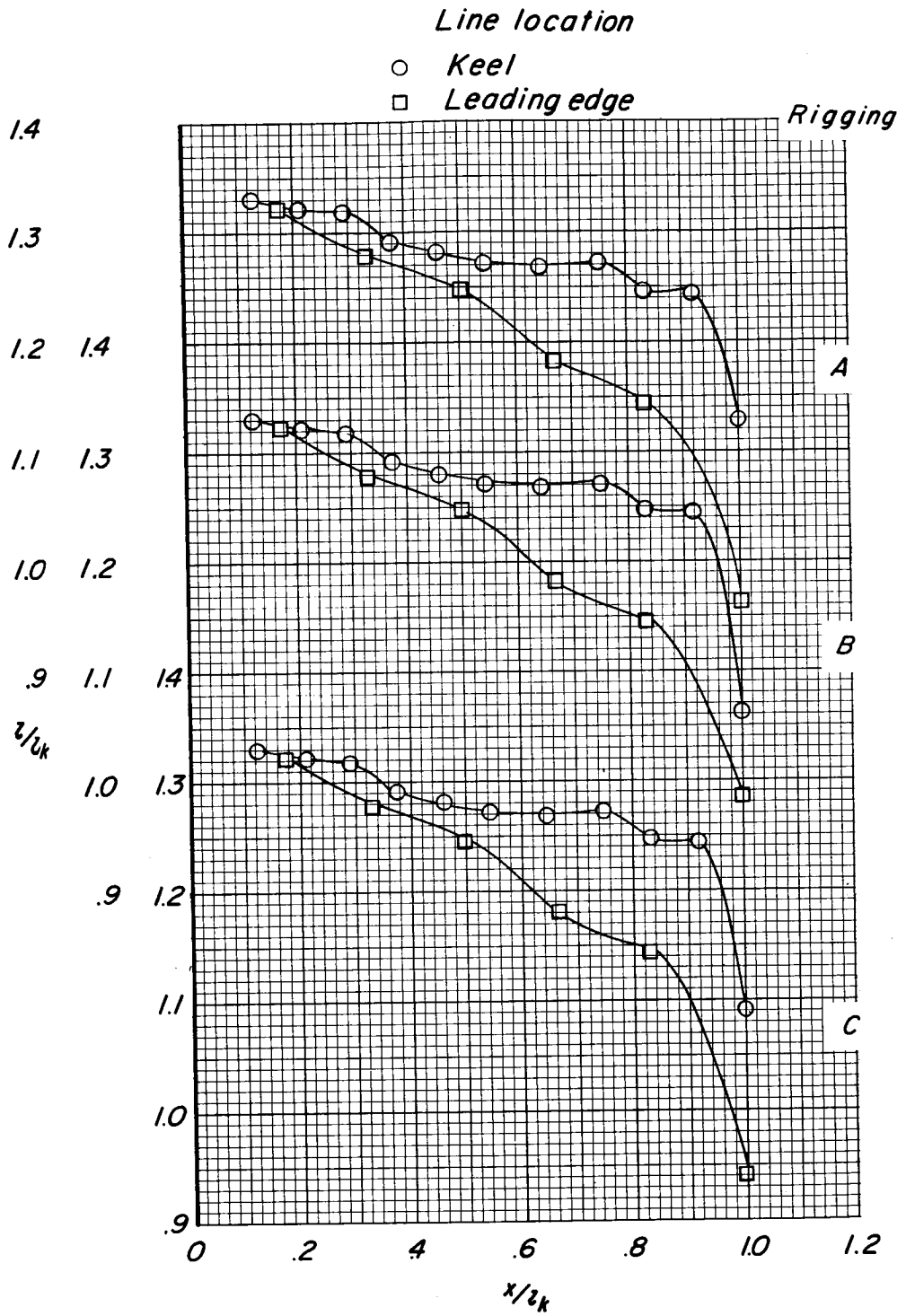

Figure 19.- Line lengths of a parawing with $\Lambda_0 = 50^0$ and 1/8 ℓ_k nose cut off. The scales from left to right are to be read with the curves from top to bottom.

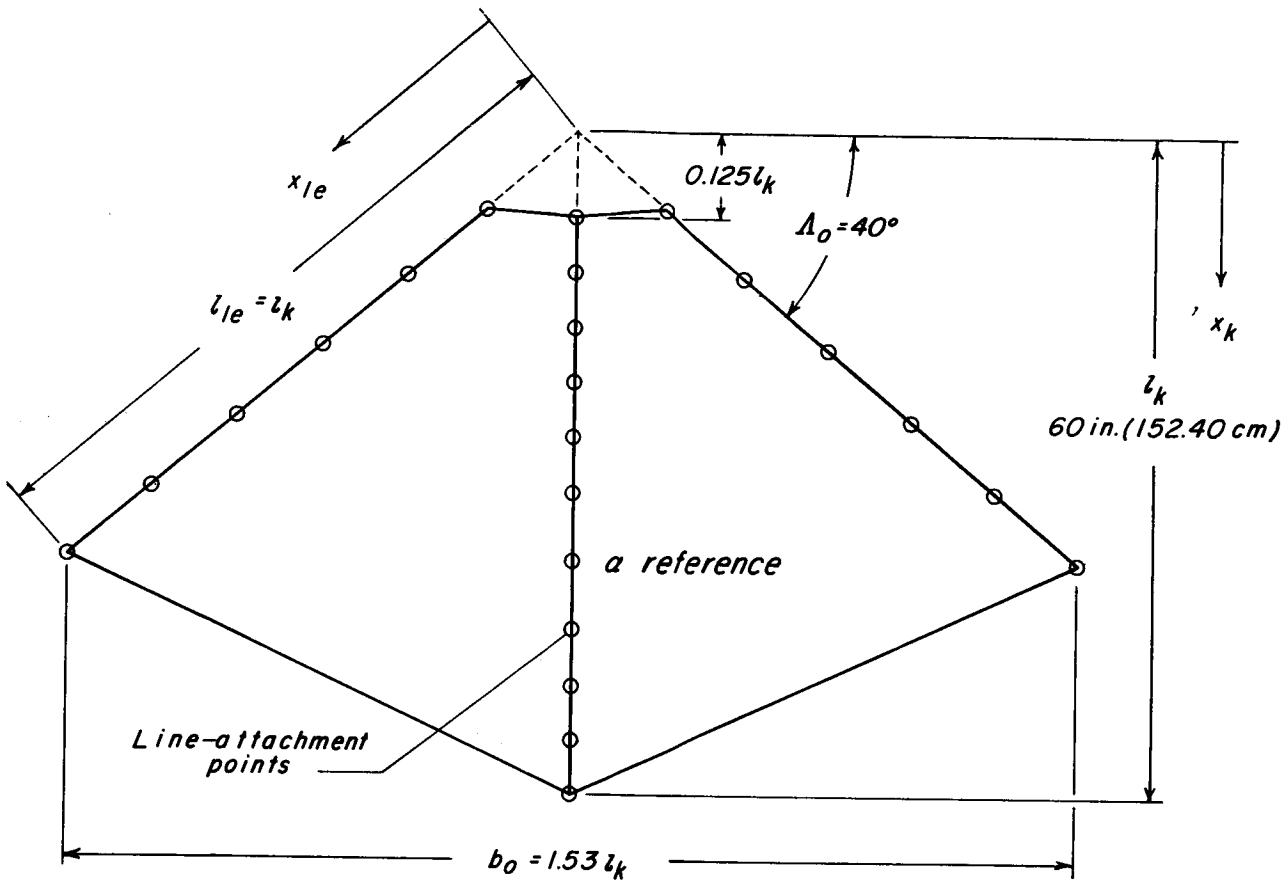

x/l_k	
Keel	Leading edge
.125	.177
.208	.333
.292	.500
.375	.677
.459	.833
.542	1.000
.645	
.750	
.833	
.917	
1.000	

Line-attachment location

(a) $\Lambda_0 = 40°$.

Figure 20.- Details of the flat pattern of a series of parawings with 1/8 l_k nose cut off and varying leading-edge sweep.

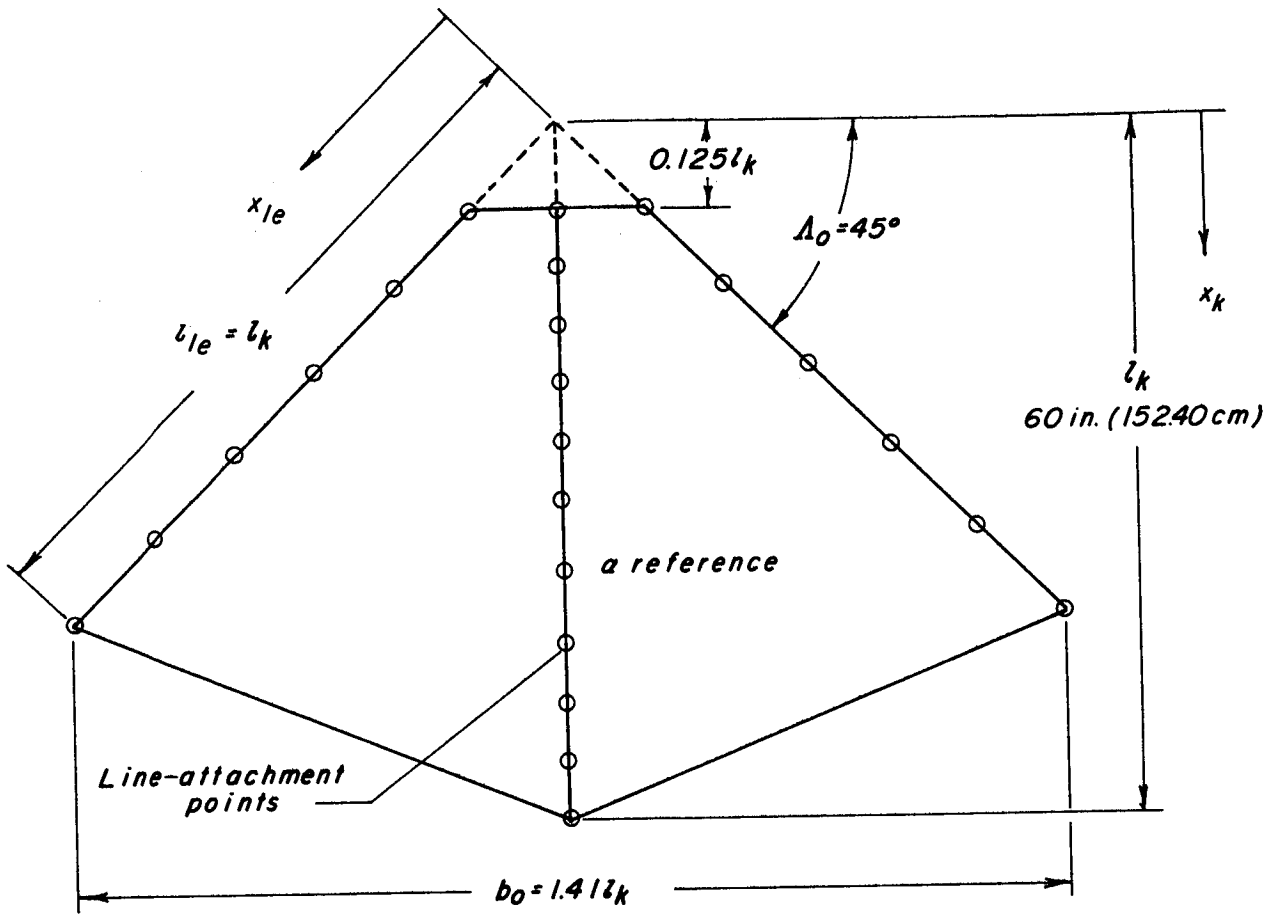

x/l_k	
Keel	Leading edge
.125	.177
.208	.333
.292	.500
.375	.667
.459	.833
.542	1.000
.645	
.750	
.833	
.917	
1.000	

Line-attachment location

(b) $\Lambda_o = 45^o$.

Figure 20.- Continued.

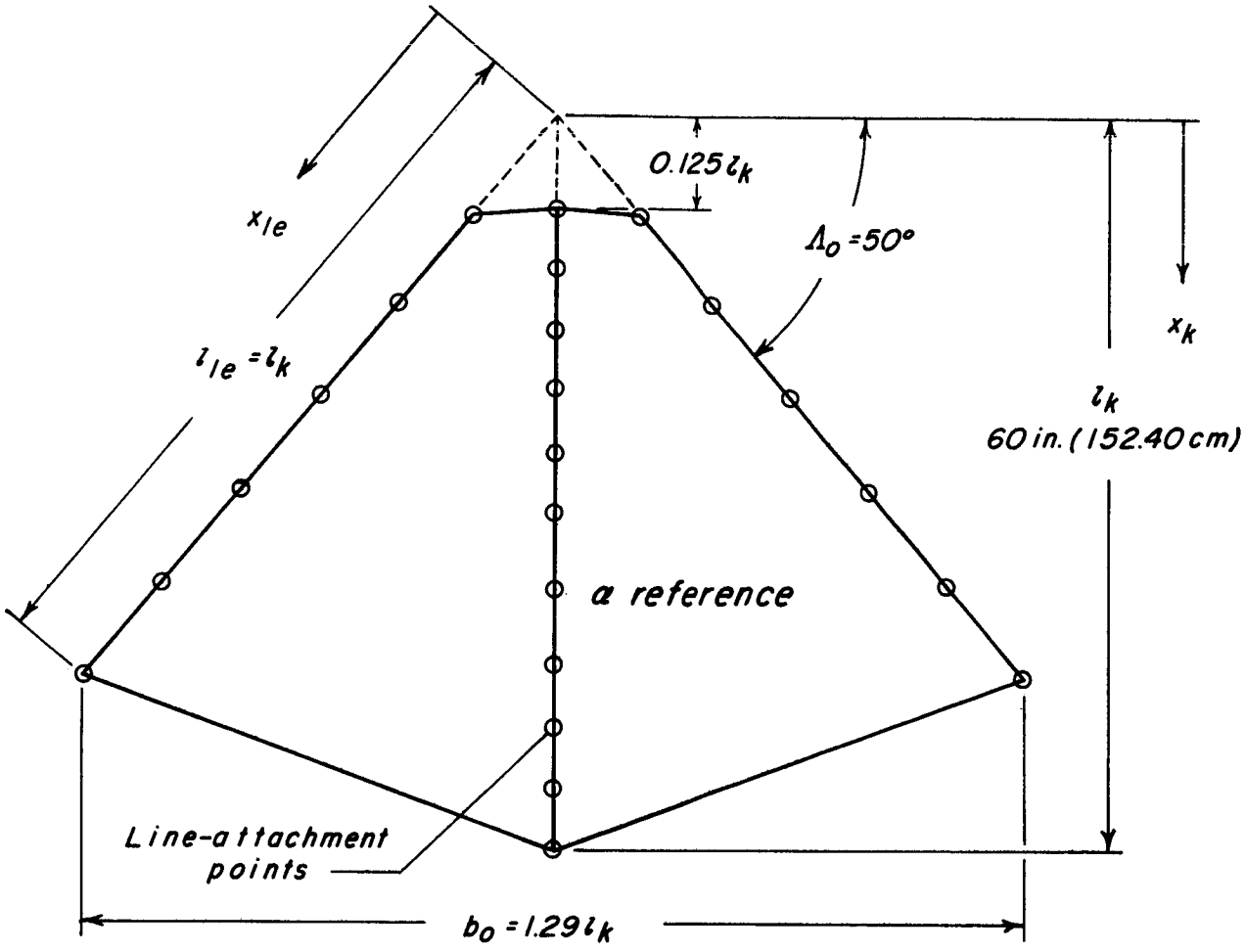

x/l_k	
Keel	Leading edge
.125	.177
.208	.333
.292	.500
.375	.667
.459	.833
.542	1.000
.645	
.750	
.833	
.917	
1.000	

Line-attachment location

(c) $\Lambda_0 = 50°$.

Figure 20.- Concluded.

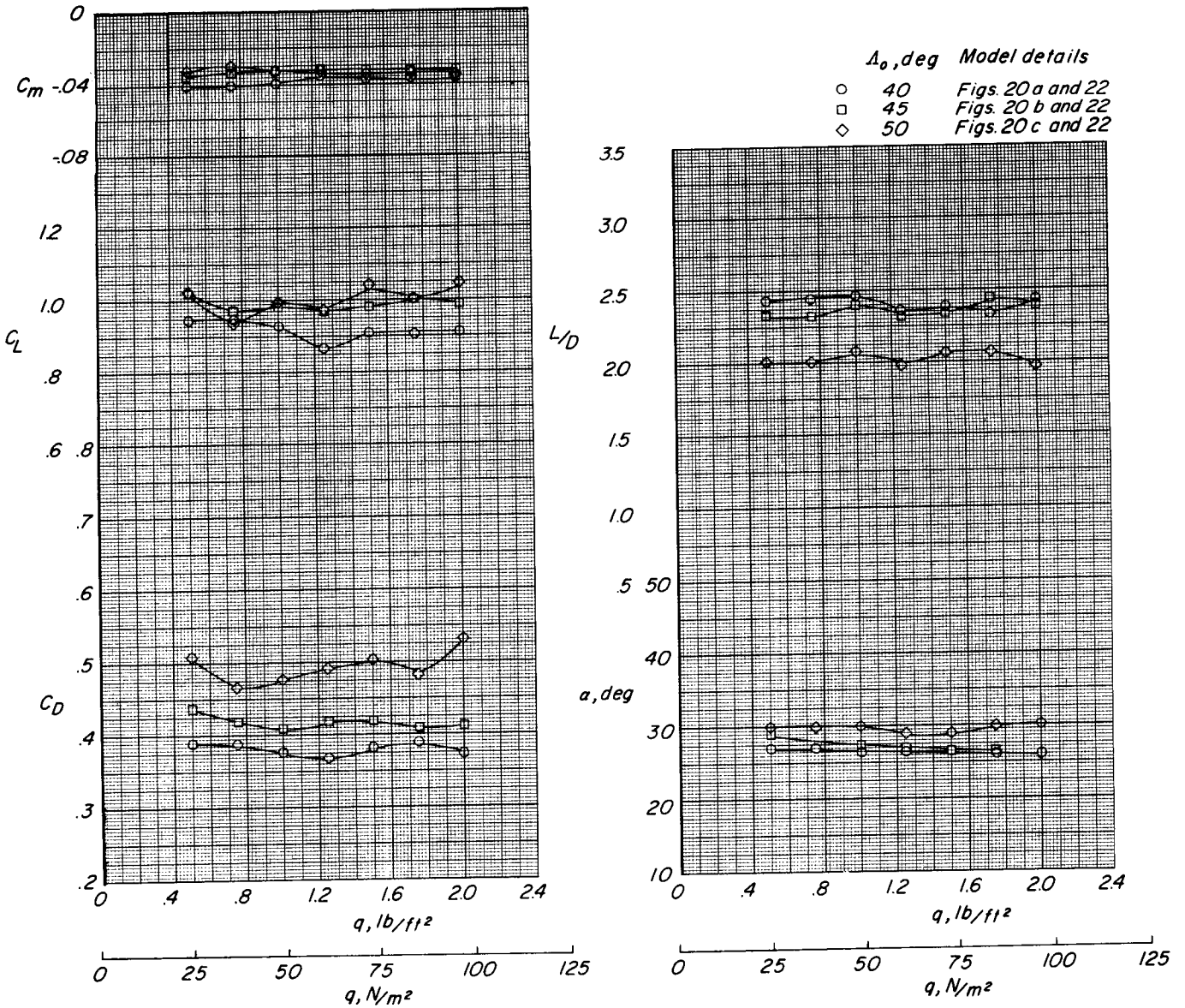

Figure 21.- Variation of the longitudinal aerodynamic characteristics with dynamic pressure for parawings with 1/8 ℓ_k nose cut off and leading-edge sweep angles of 40°, 45°, and 50°.

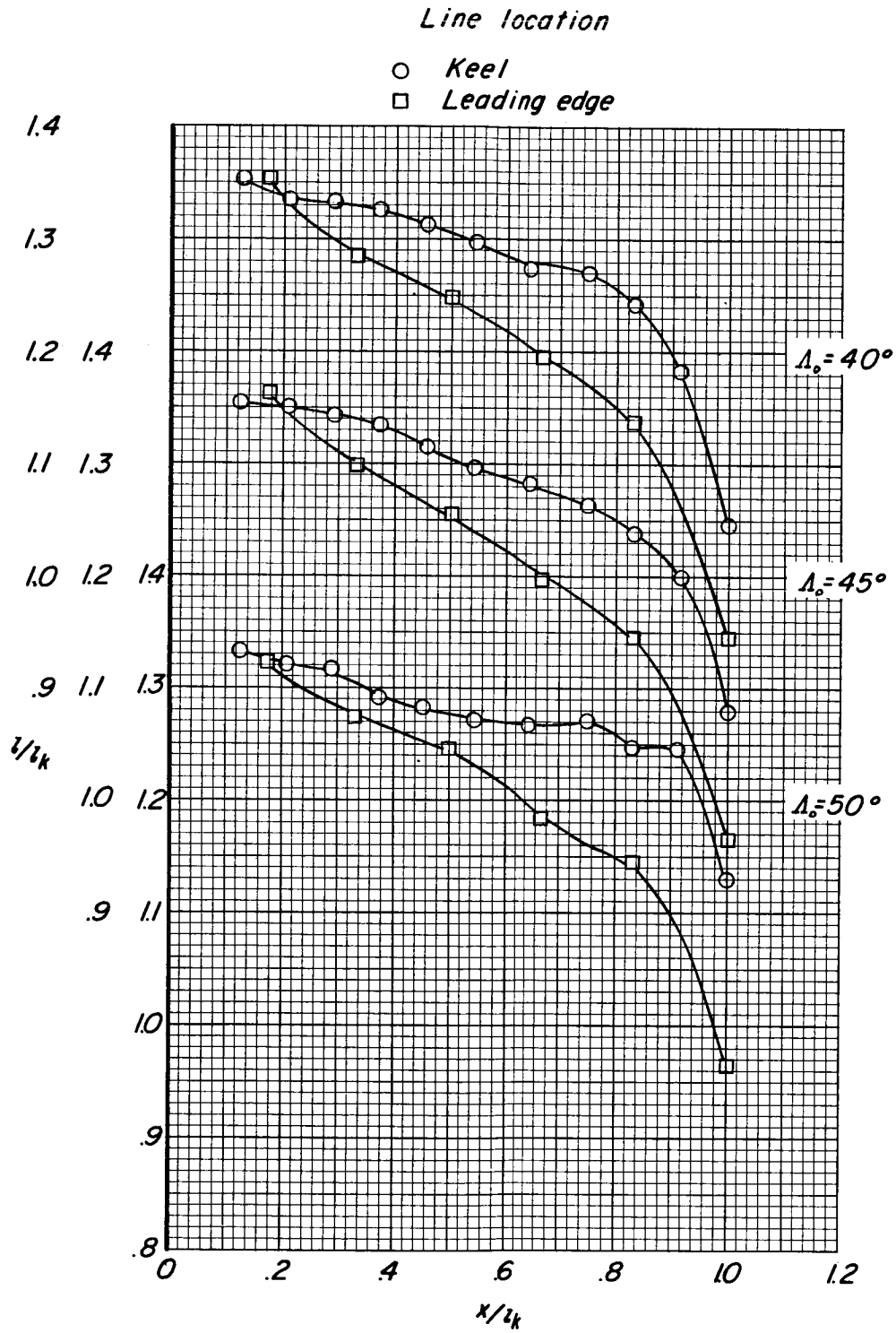

Figure 22.- Line lengths for a series of parawings with 1/8 l_k nose cut off and leading-edge sweep angles of 40°, 45°, and 50°. The scales from left to right are to be read with the curves from top to bottom.

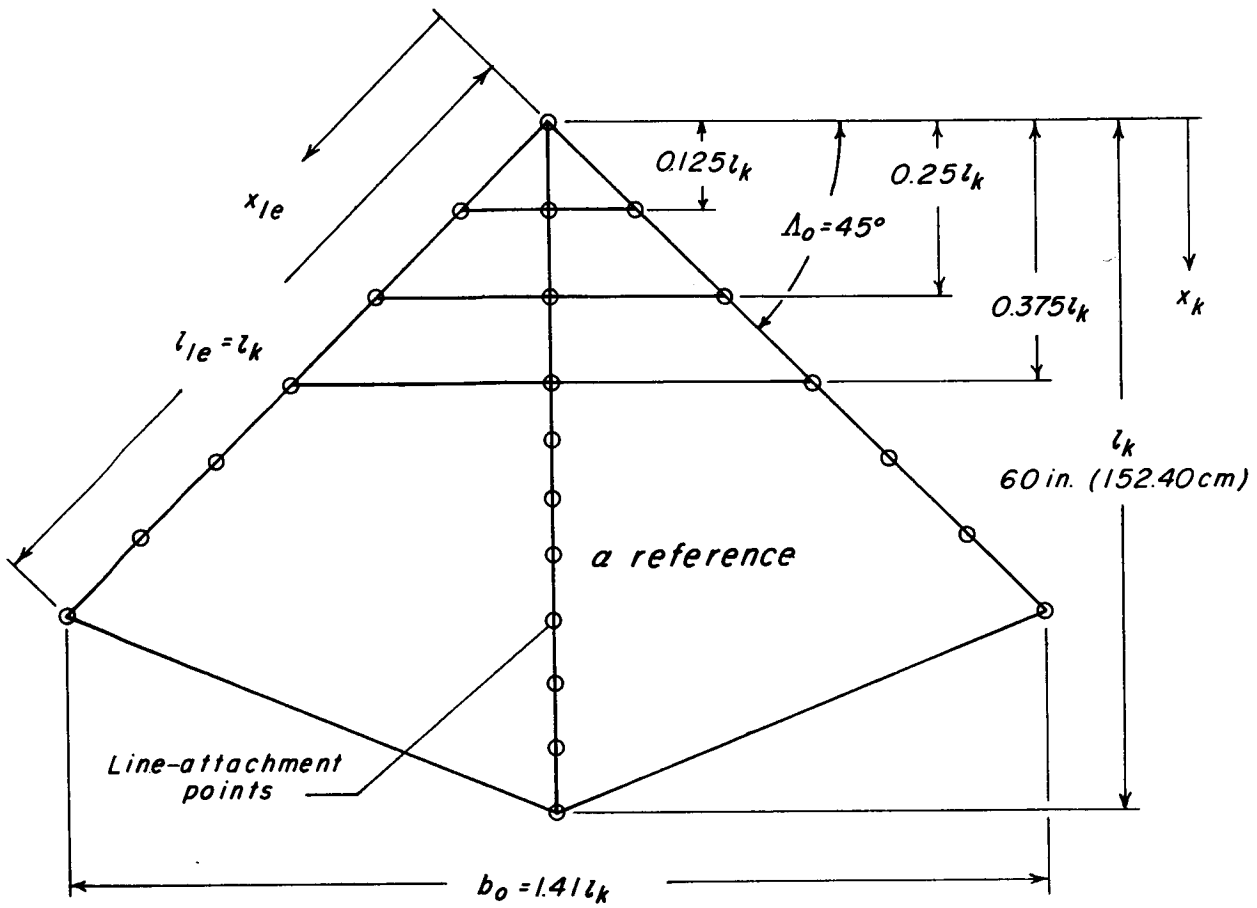

x/l_k	
keel	Leading edge
0	0
.125	.177
.250	.353
.375	.530
.458	.687
.542	.843
.625	1.000
.720	
.813	
.905	
1.000	

Line-attachment location

(a) Flat-pattern details.

Figure 23.- Model of a parawing with $\Lambda_o = 45^0$ and 0 l_k, 1/8 l_k, 1/4 l_k, or 3/8 l_k nose cut off. A mylar batten which extended from apex to $x/l_k = 0.45$ keel location was used for tests with pointed nose.

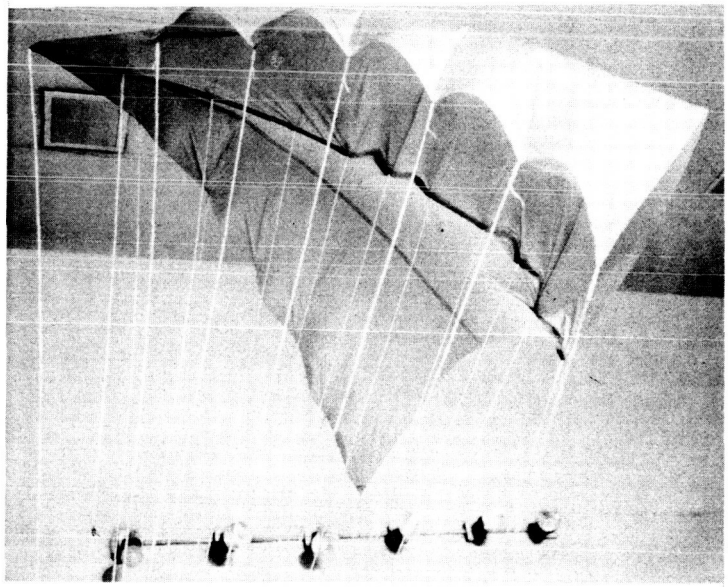

Pointed model with partial keel batten

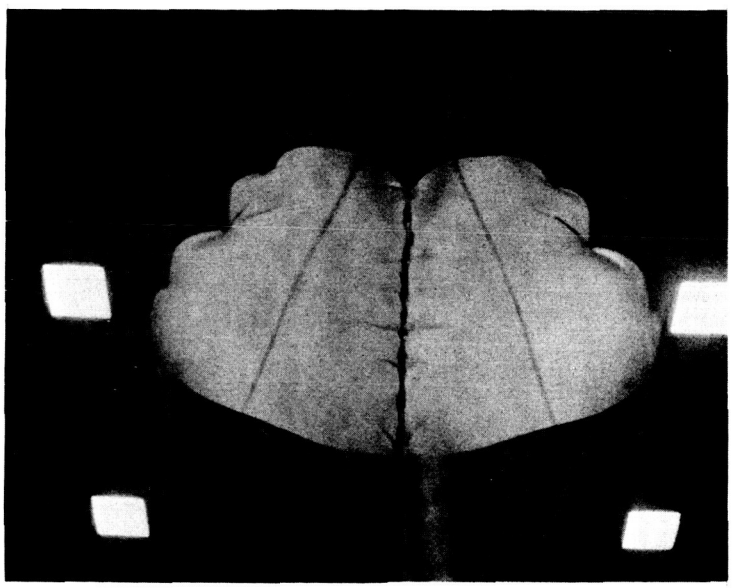

$3/8\ l_k$ nose cut off; front view

(b) Photographs of models. L-67-941

Figure 23.- Concluded.

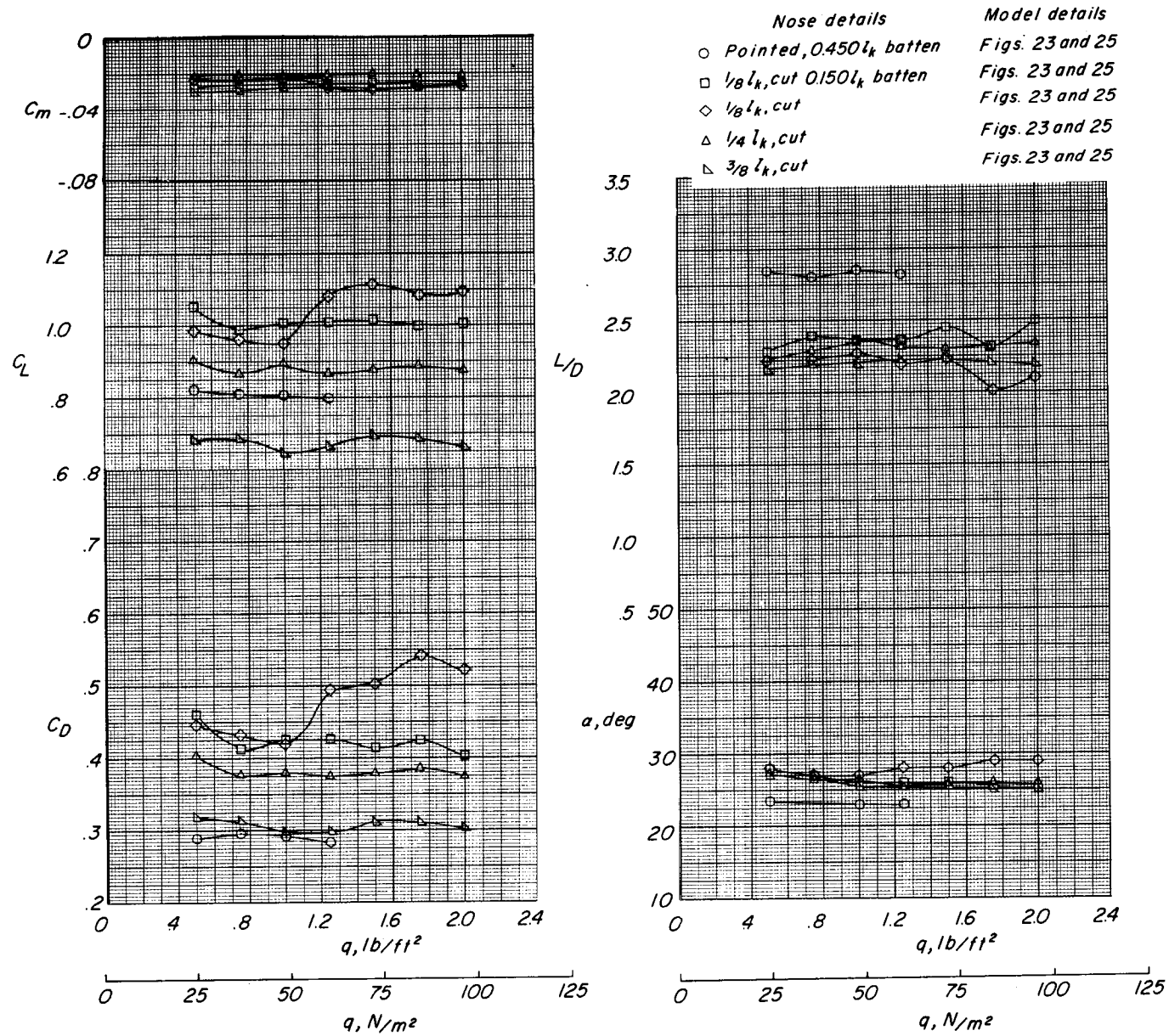

Figure 24.- Effect of changes in nose cut on the variation of the longitudinal aerodynamic characteristics with dynamic pressure for a series of parawings with $\Lambda_0 = 45^0$. Coefficients are based on pointed-nose geometry.

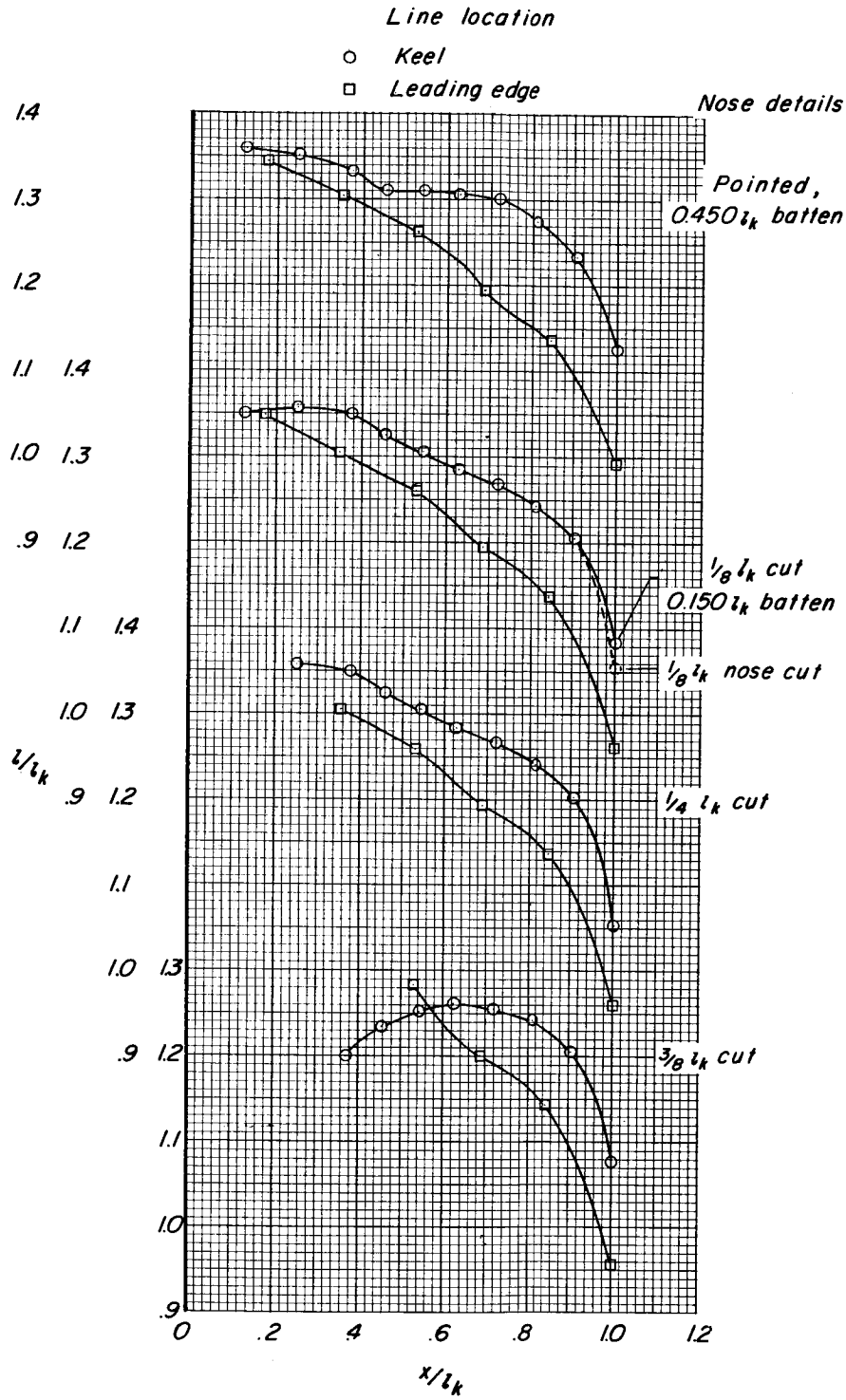

Figure 25.- Line lengths of a series of parawings with $\Lambda_0 = 45^0$ and 0 l_k, 1/8 l_k, 1/4 l_k, and 3/8 l_k nose cut off. The scales from left to right are to be read with the curves from top to bottom.

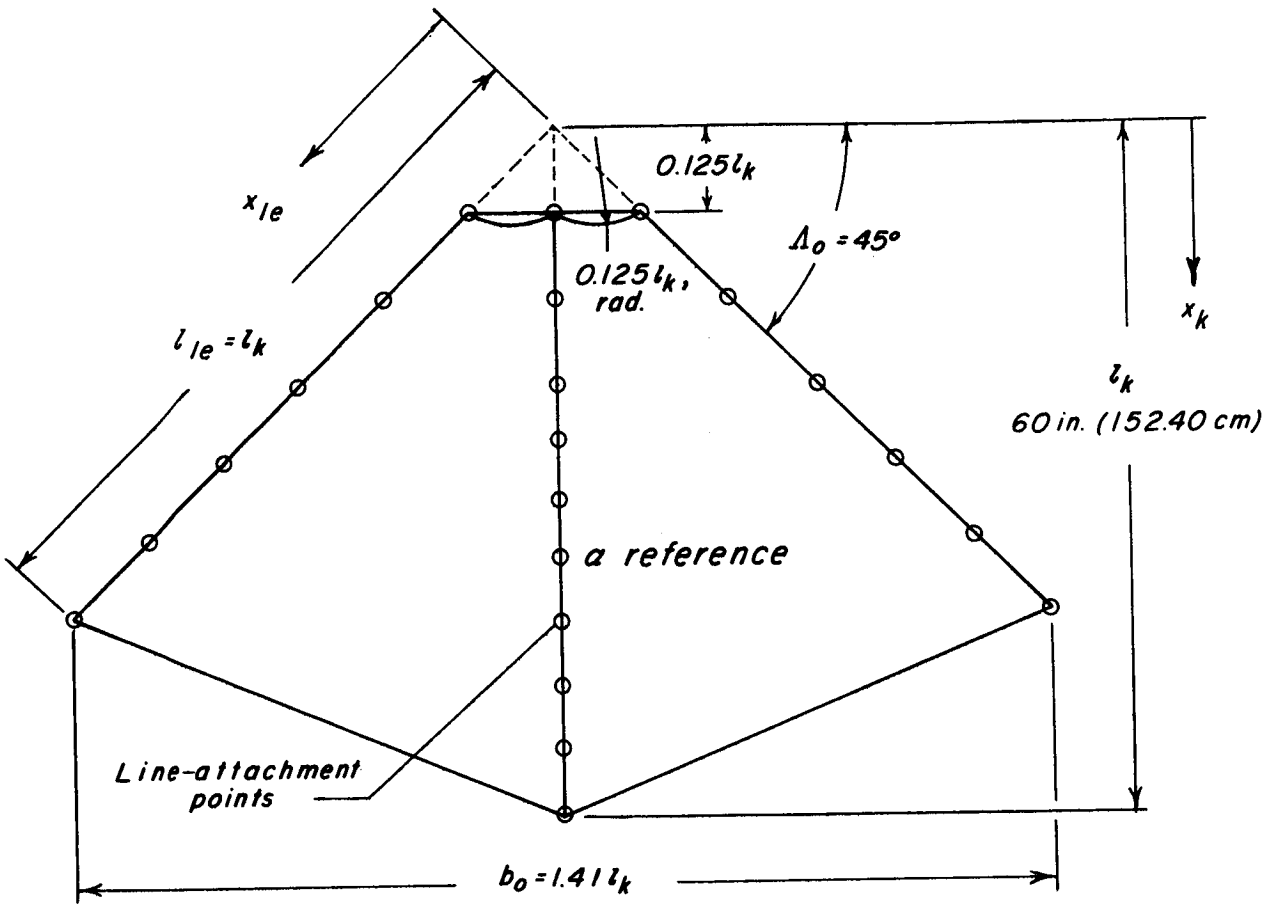

x/l_k	
Keel	Leading edge
.125	.177
.250	.353
.375	.530
.458	.687
.542	.843
.625	1.000
.720	
.813	
.905	
1.000	

Line-attachment location

Figure 26.- Details of the flat pattern of a parawing with either a 1/8 l_k straight nose cut or 1/8 l_k double-radius nose cut.

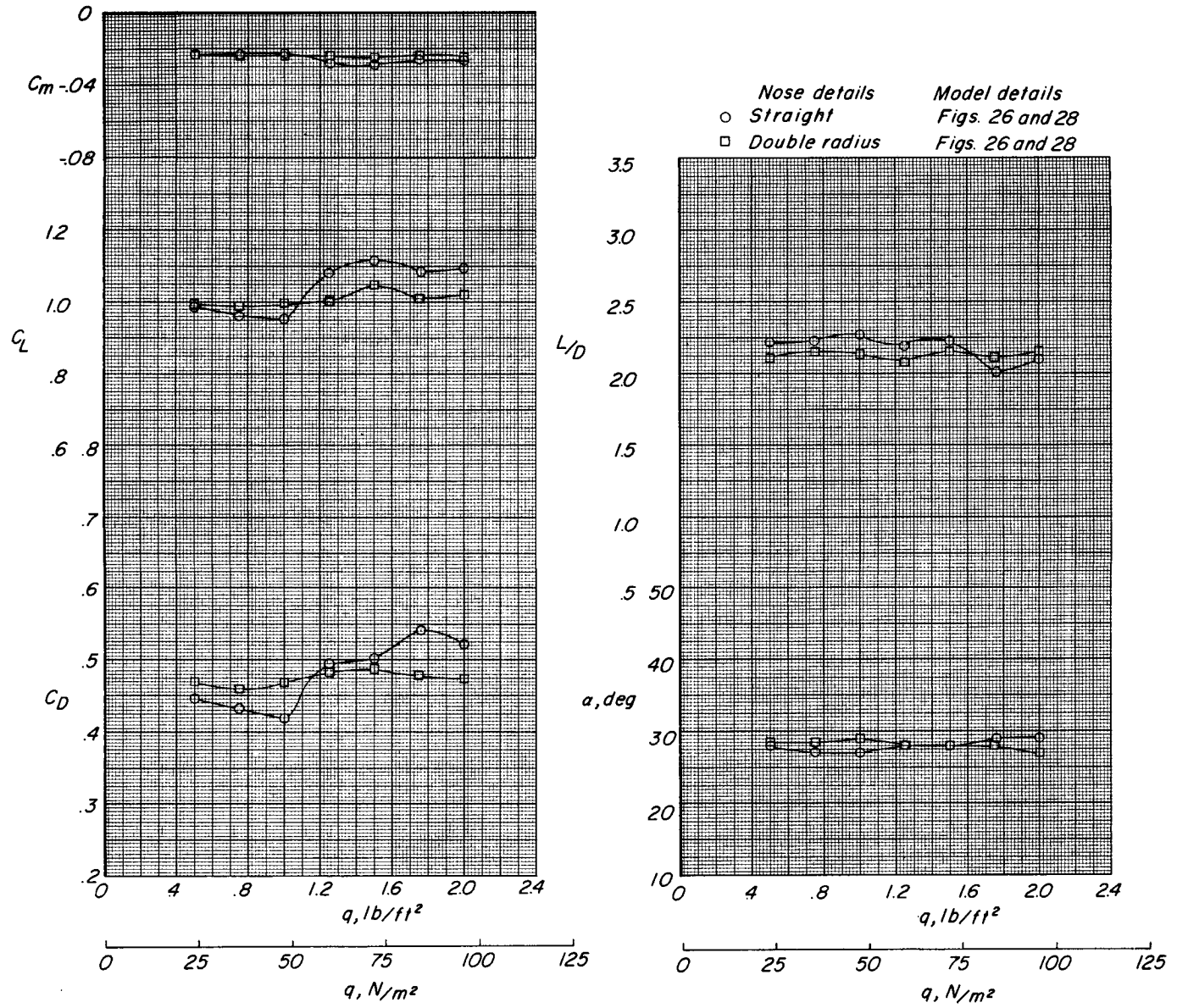

Figure 27.- Variation on the longitudinal aerodynamic characteristics with dynamic pressure for a parawing with $\Lambda_0 = 45^0$ and either a 1/8 ℓ_k straight nose cut or 1/8 ℓ_k double-radius nose cut. Coefficients are based on pointed-nose geometry.

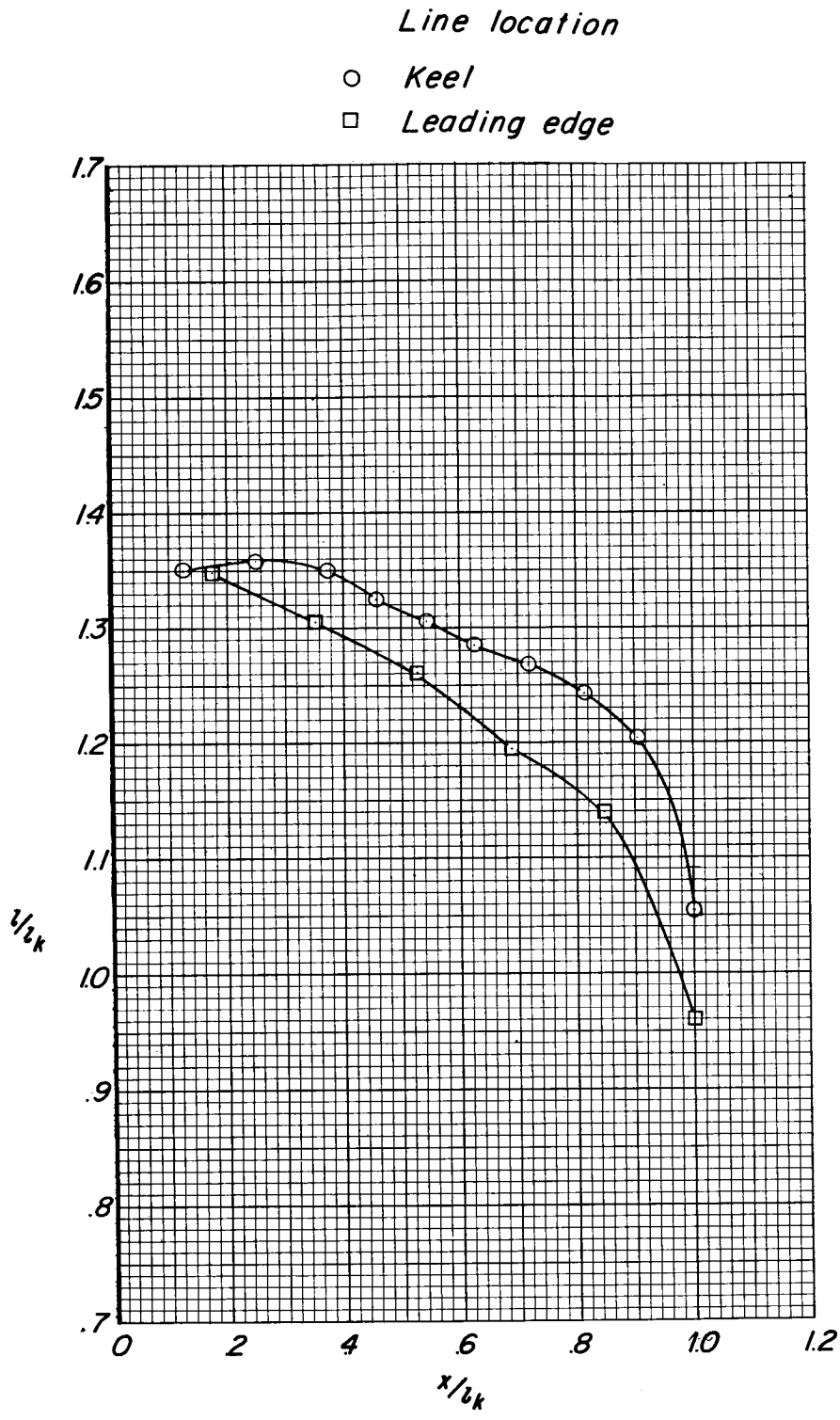

Figure 28.- Line lengths of a parawing with either a 1/8 l_k straight nose cut or 1/8 l_k double-radius nose cut.

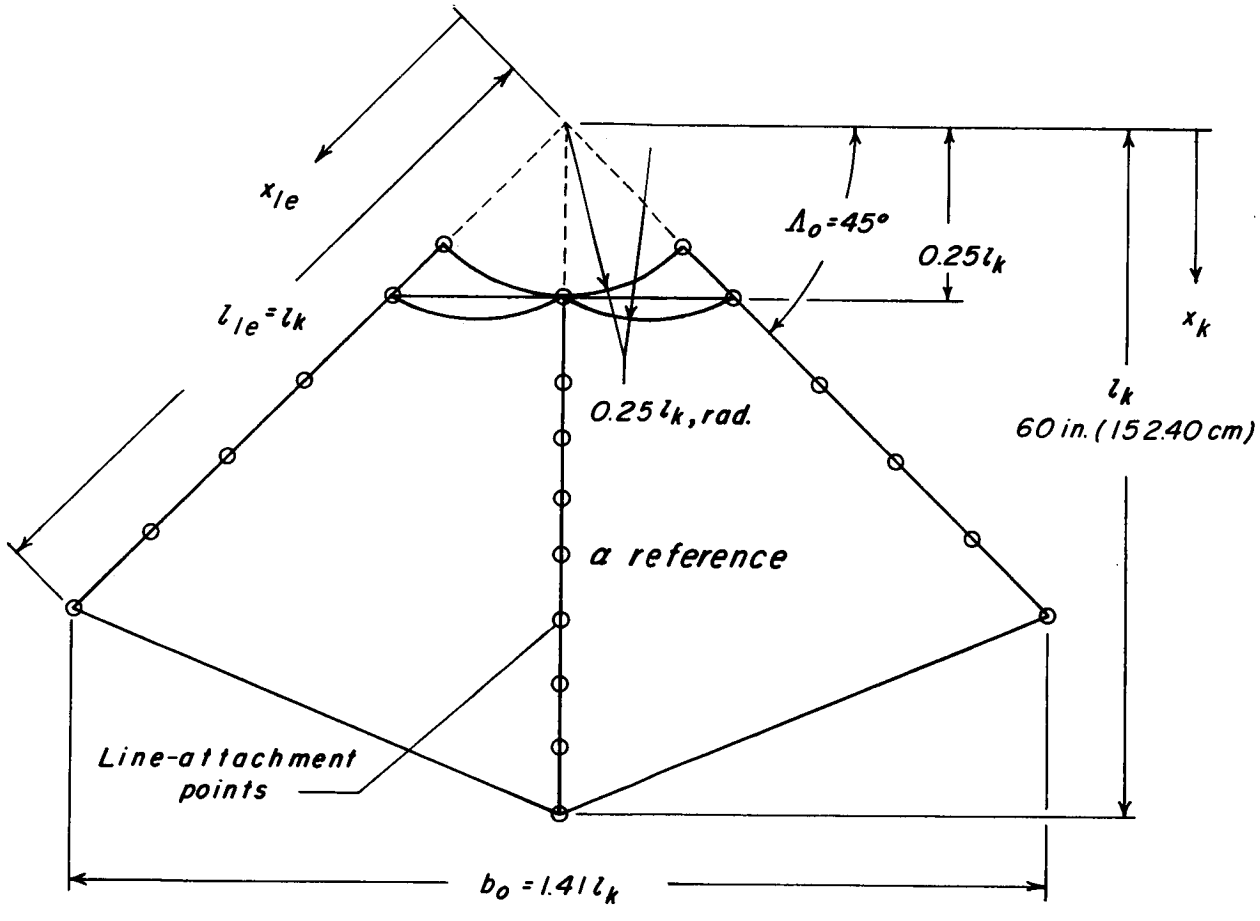

x/l_k	
Keel	Leading edge
.250	.250
.375	.353
.458	.530
.542	.687
.625	.843
.720	1.000
.813	
.905	
1.000	

Line-attachment location

Figure 29.- Details of the flat pattern of a parawing with 1/4 l_k nose cut off in straight, double-radius, or single-radius cuts.

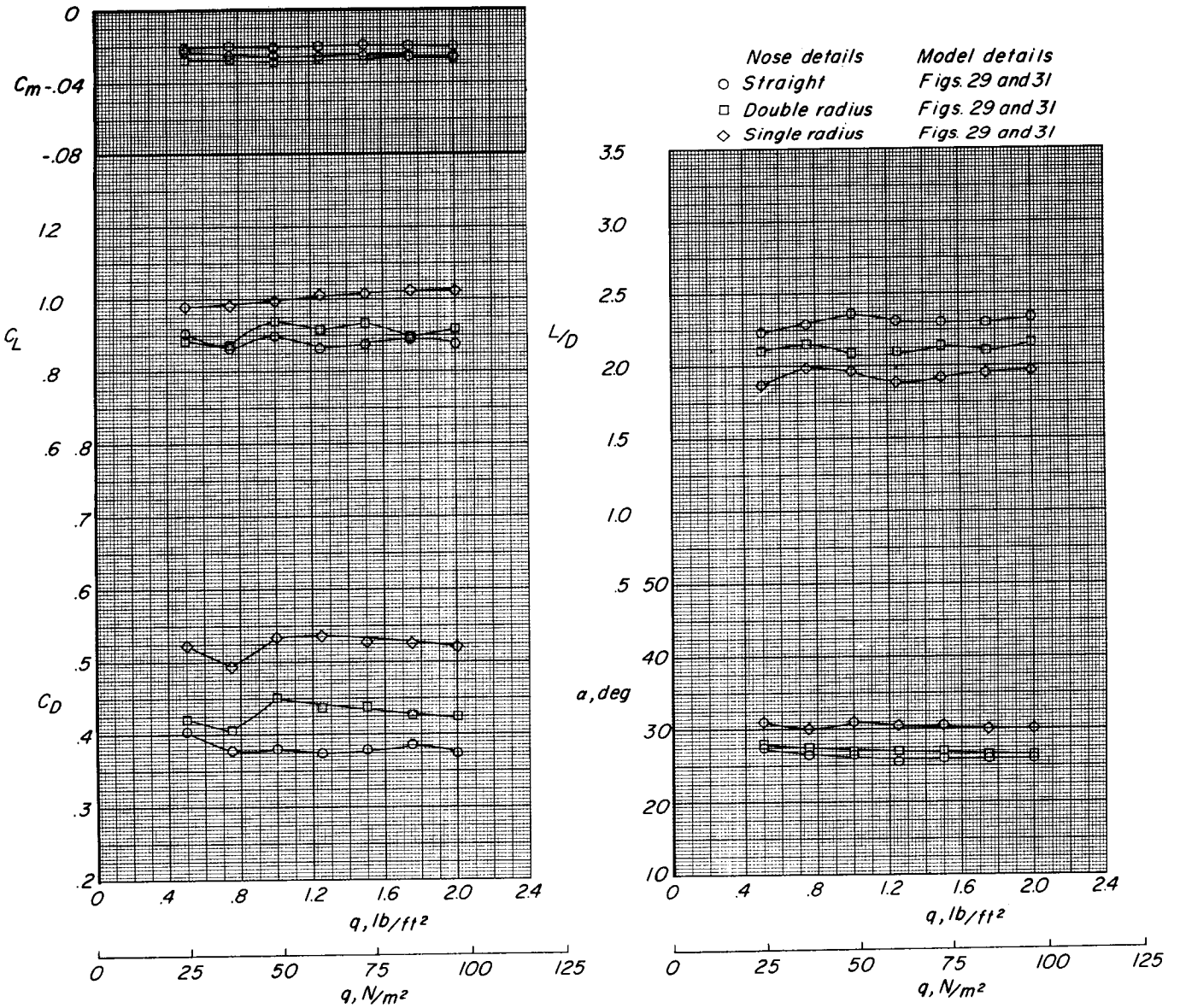

Figure 30.- Variation of the longitudinal aerodynamic characteristics with dynamic pressure for a parawing with $\Lambda_0 = 45^0$ and 1/4 ℓ_k nose cut off in straight, double-radius, or single-radius cuts. Coefficients are based on pointed-nose geometry.

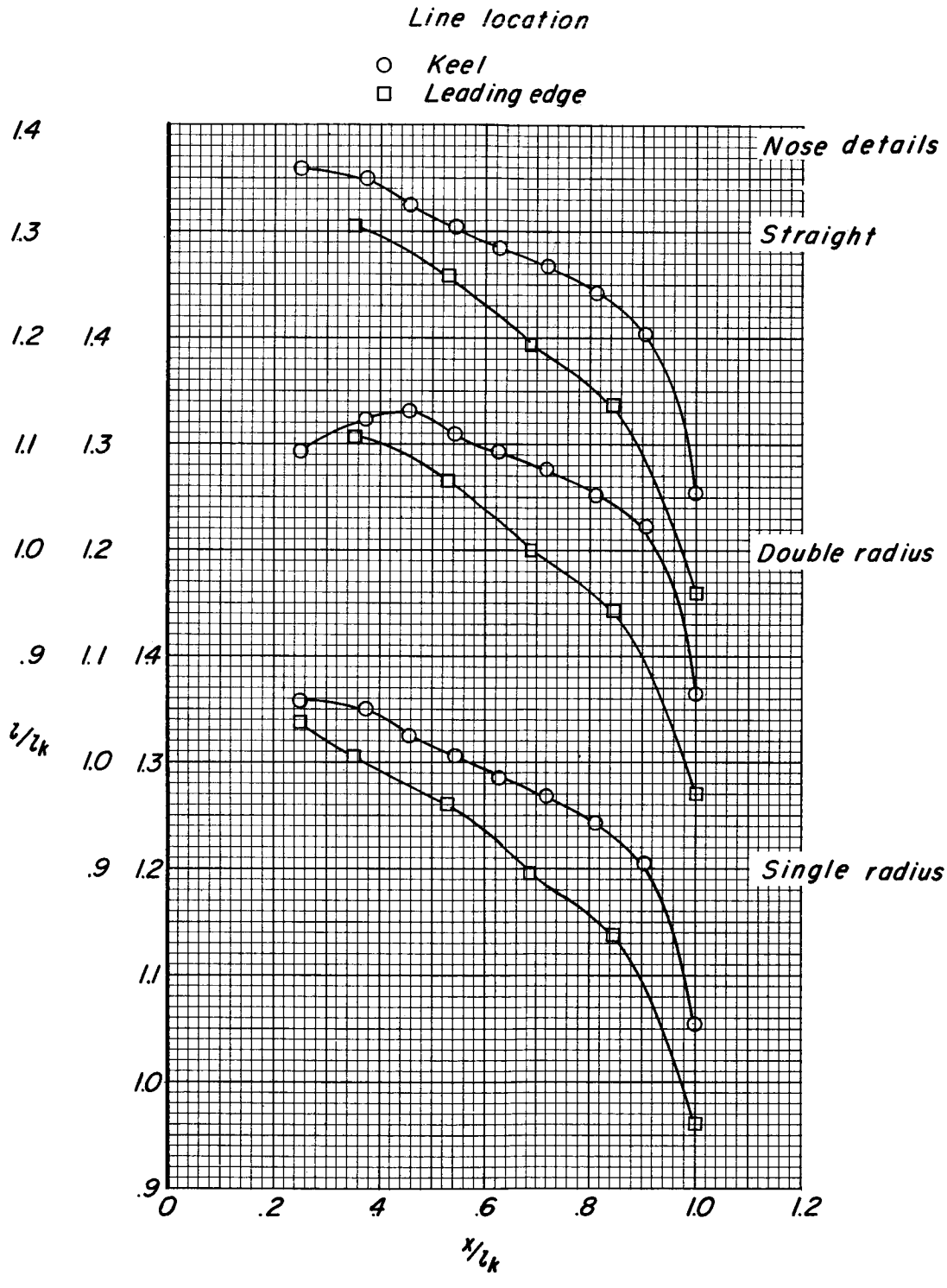

Figure 31.- Line lengths of a parawing with 1/4 l_k nose cut off in straight, double-radius, or single-radius cuts. The scales from left to right are to be read with the curves from top to bottom.

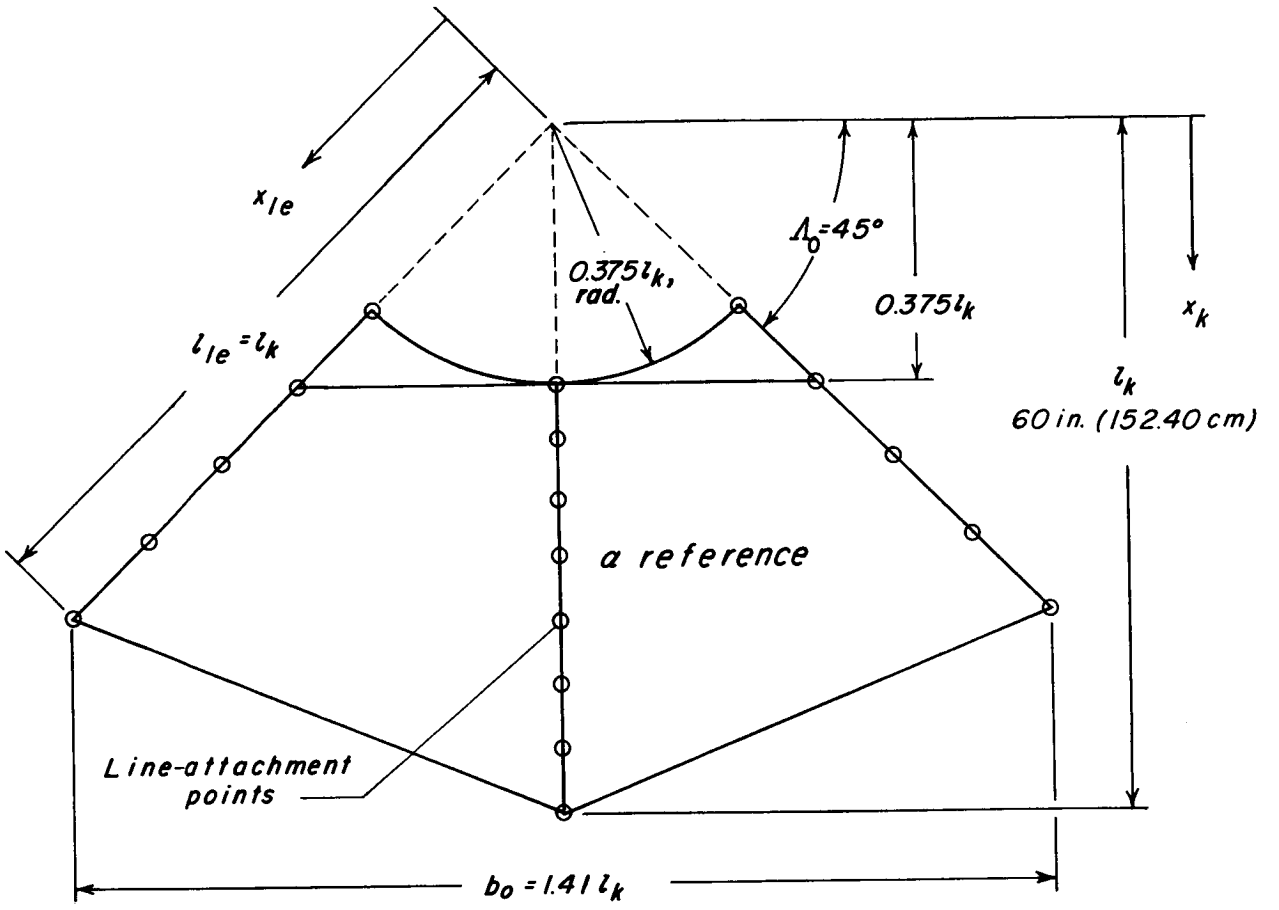

x/l_k	
Keel	Leading edge
.375	.375
.458	.530
.542	.687
.625	.843
.720	1.000
.813	
.905	
1.000	

Line-attachment location

Figure 32.- Details of the flat pattern of a parawing with 3/8 l_k nose cut off in either straight or single-radius cuts.

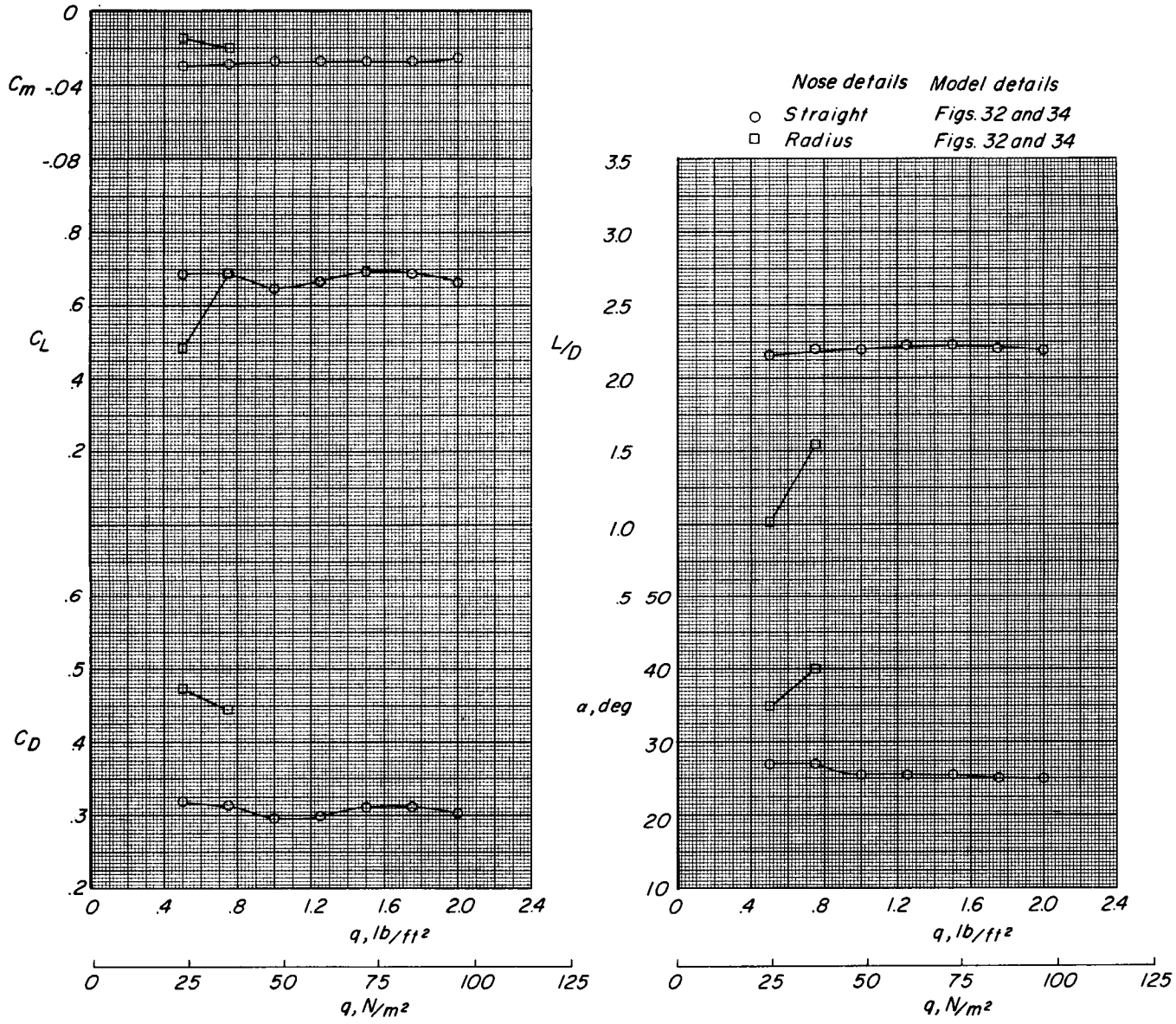

Figure 33.- Variation of the longitudinal aerodynamic characteristics with dynamic pressure for a parawing with $\Lambda_0 = 45^0$ and 3/8 l_k nose cut off in either straight or single-radius cuts. Coefficients are based on pointed-nose geometry.

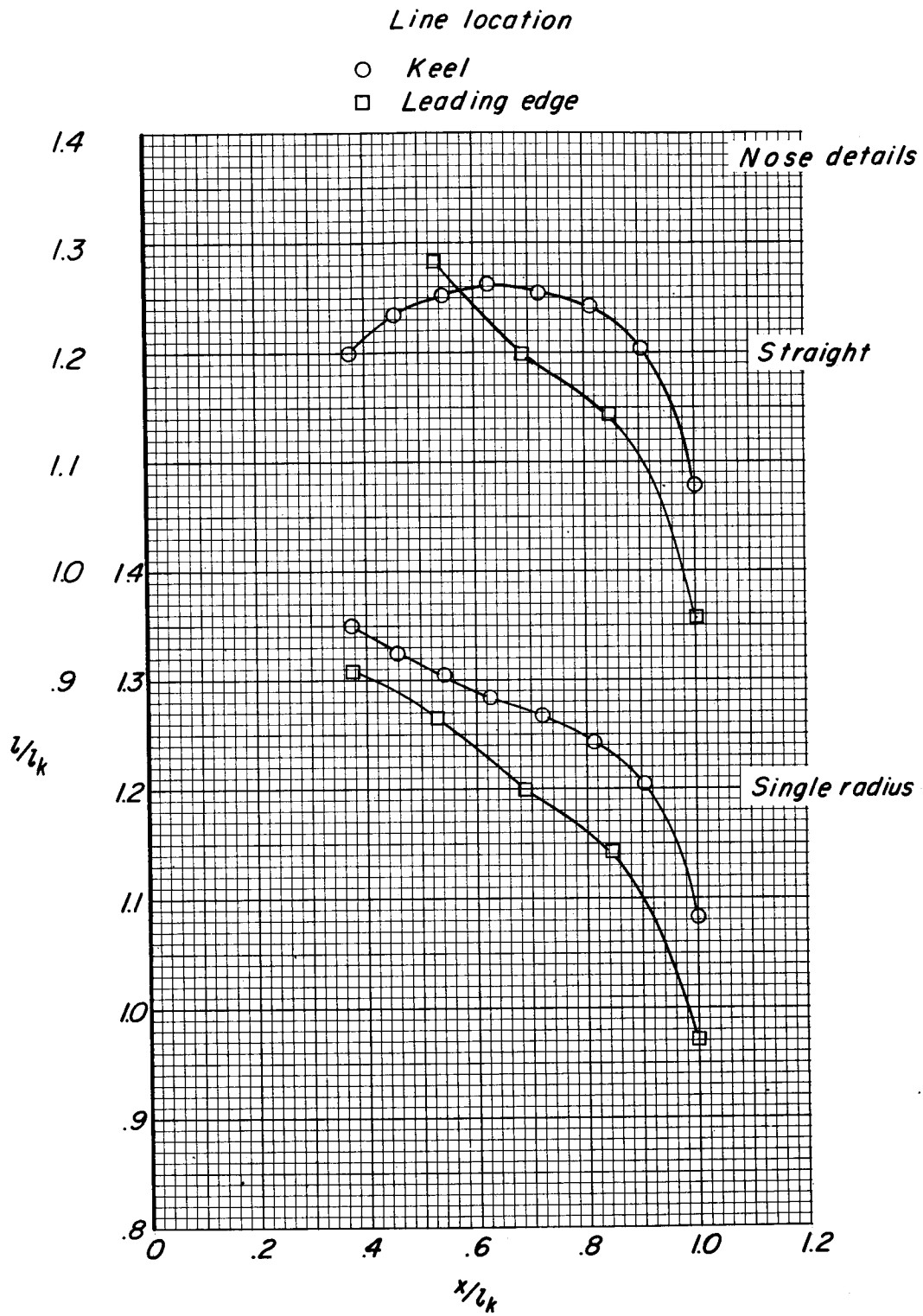

Figure 34.- Line lengths of a parawing with 3/8 l_k nose cut off in either straight or single-radius cuts.

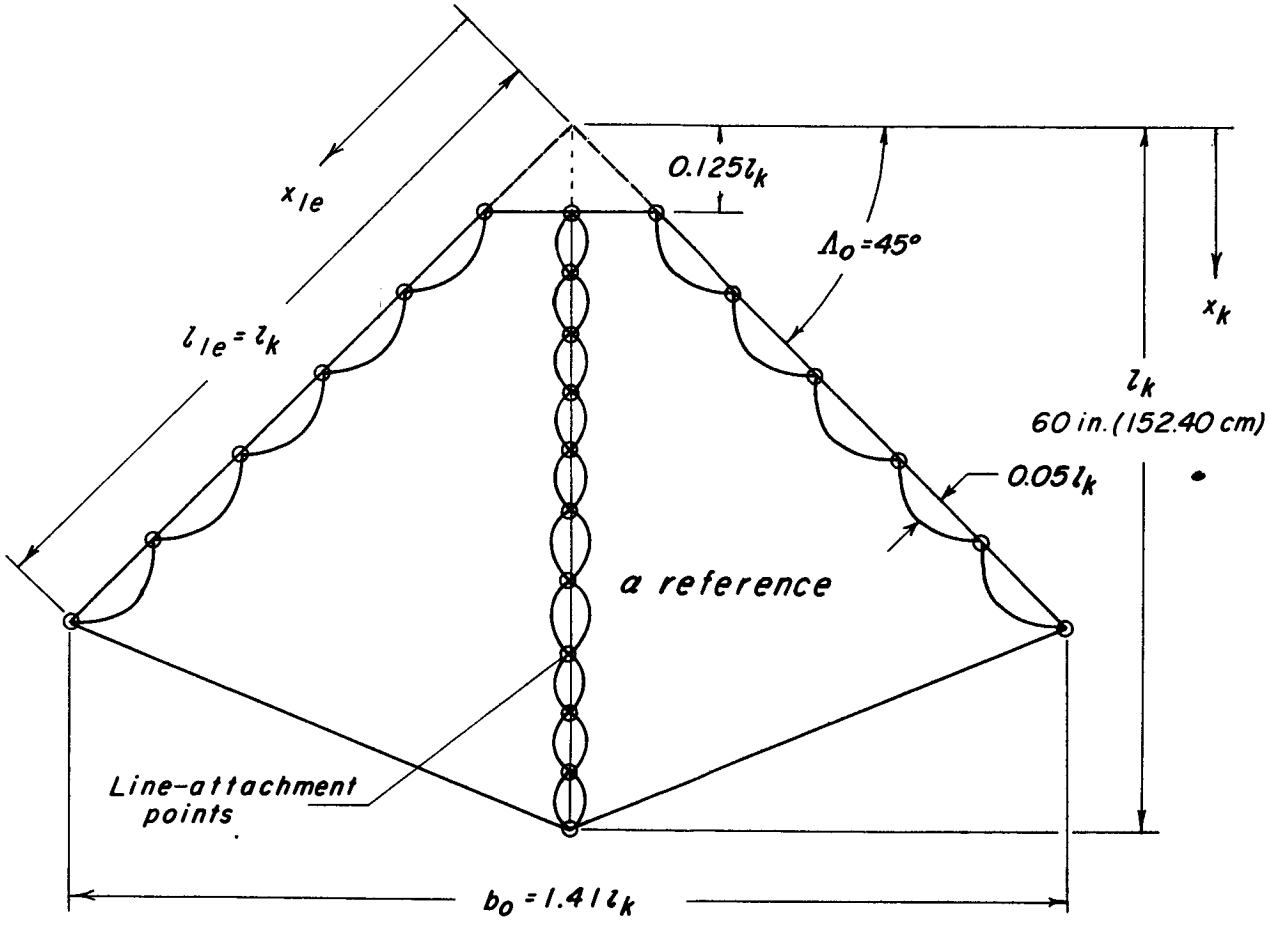

x/l_k	
Keel	Leading edge
.125	.177
.208	.333
.292	.500
.375	.667
.459	.833
.542	1.000
.645	
.750	
.833	
.917	
1.000	

Line-attachment location

Figure 35.- Details of the flat pattern of a parawing with $\Lambda_0 = 45^0$, $1/8\ l_k$ nose cut off, and parabolic suspension patches on the leading edges and keel.

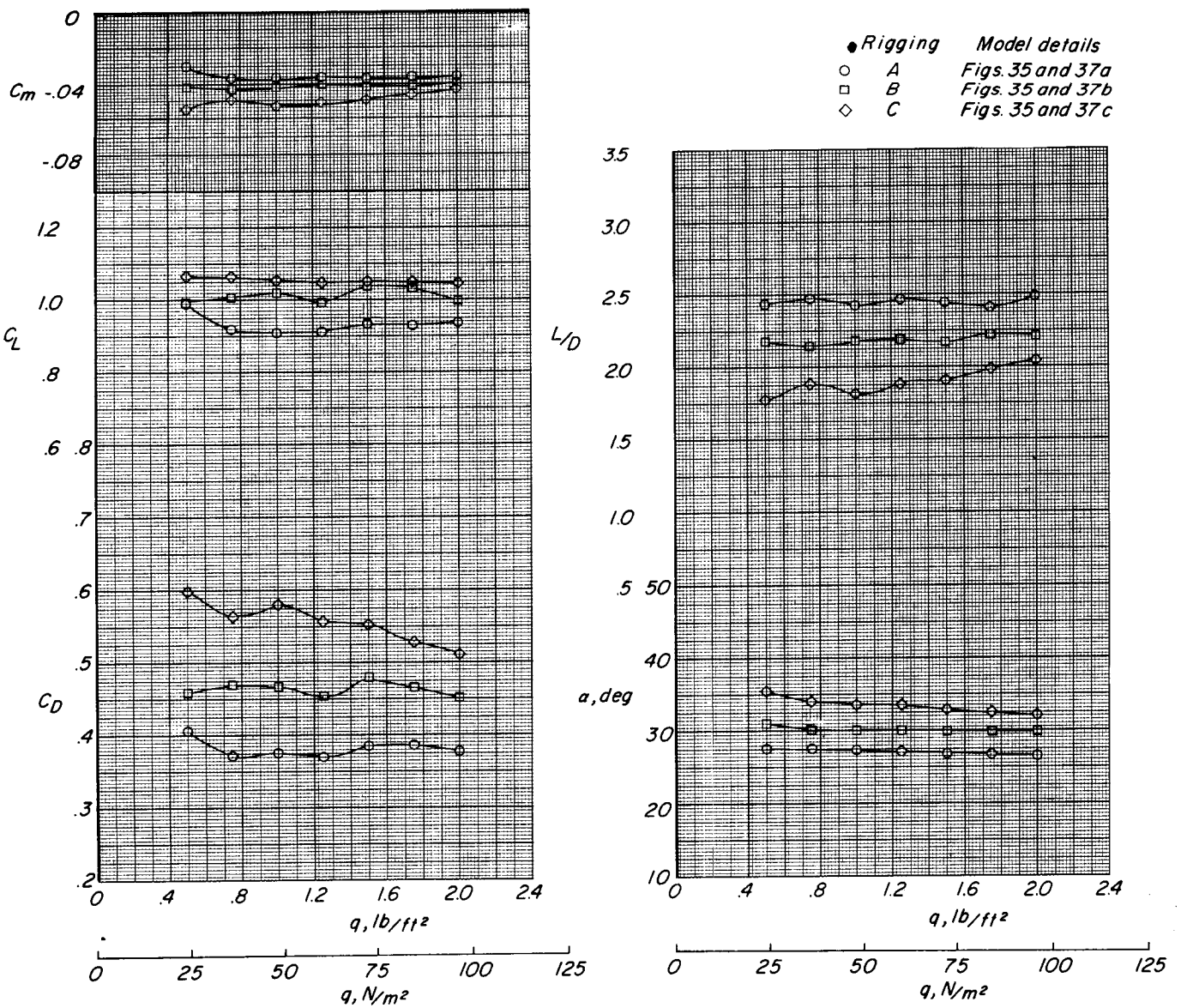

Figure 36.- Effect of changes in rigging on the variation of the wing longitudinal aerodynamic characteristics with dynamic pressure for a parawing with $\Lambda_0 = 45^0$, 1/8 l_k nose cut off, and parabolic suspension patches on the leading edges and keel.

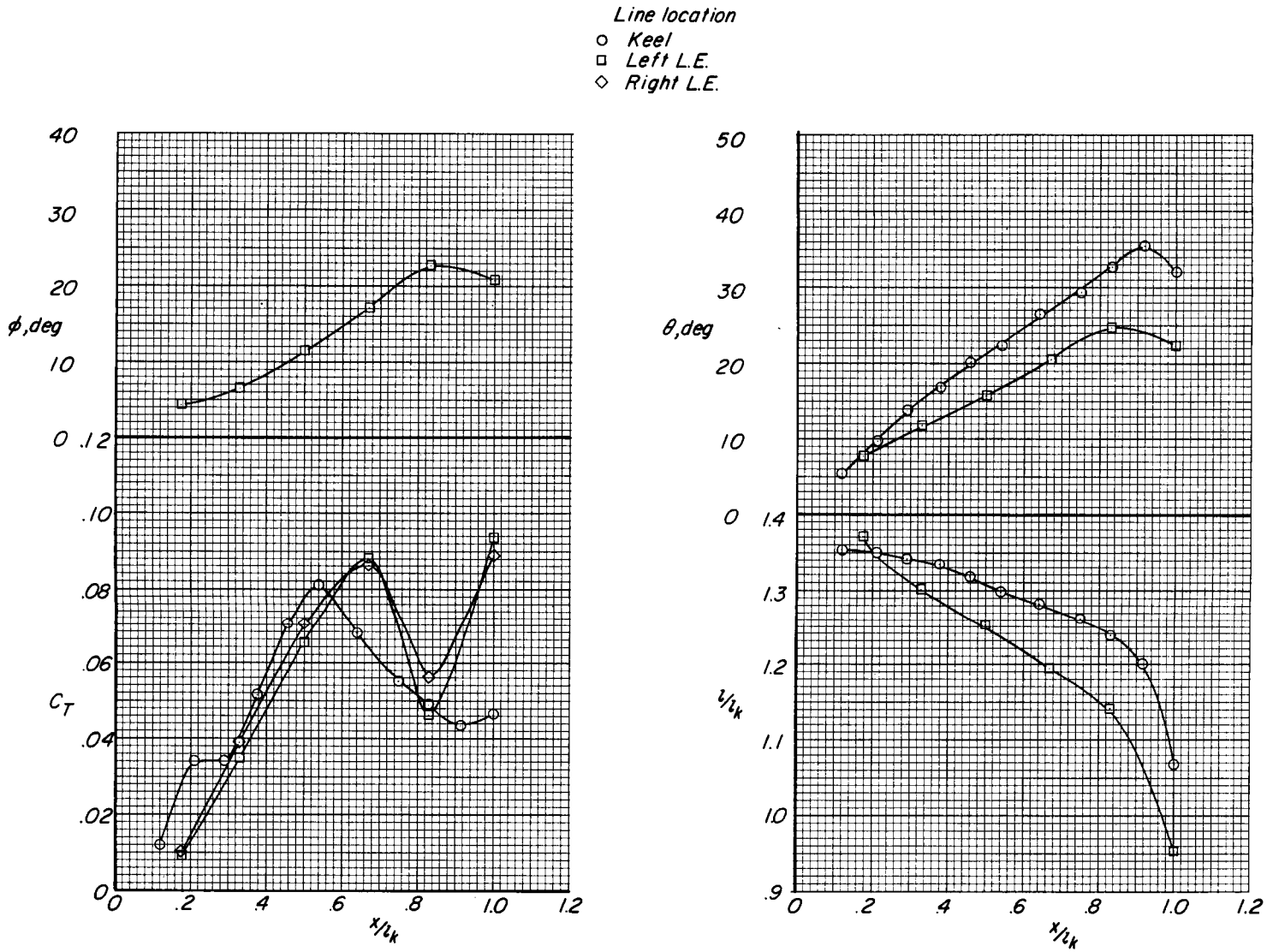

(a) Rigging A; q = 1.0.

Figure 37.- Tension coefficients, line angles, and line lengths for a parawing with $\Lambda_0 = 45^0$, 1/8 l_k nose cut off, and parabolic suspension patches on the leading edges and keel.

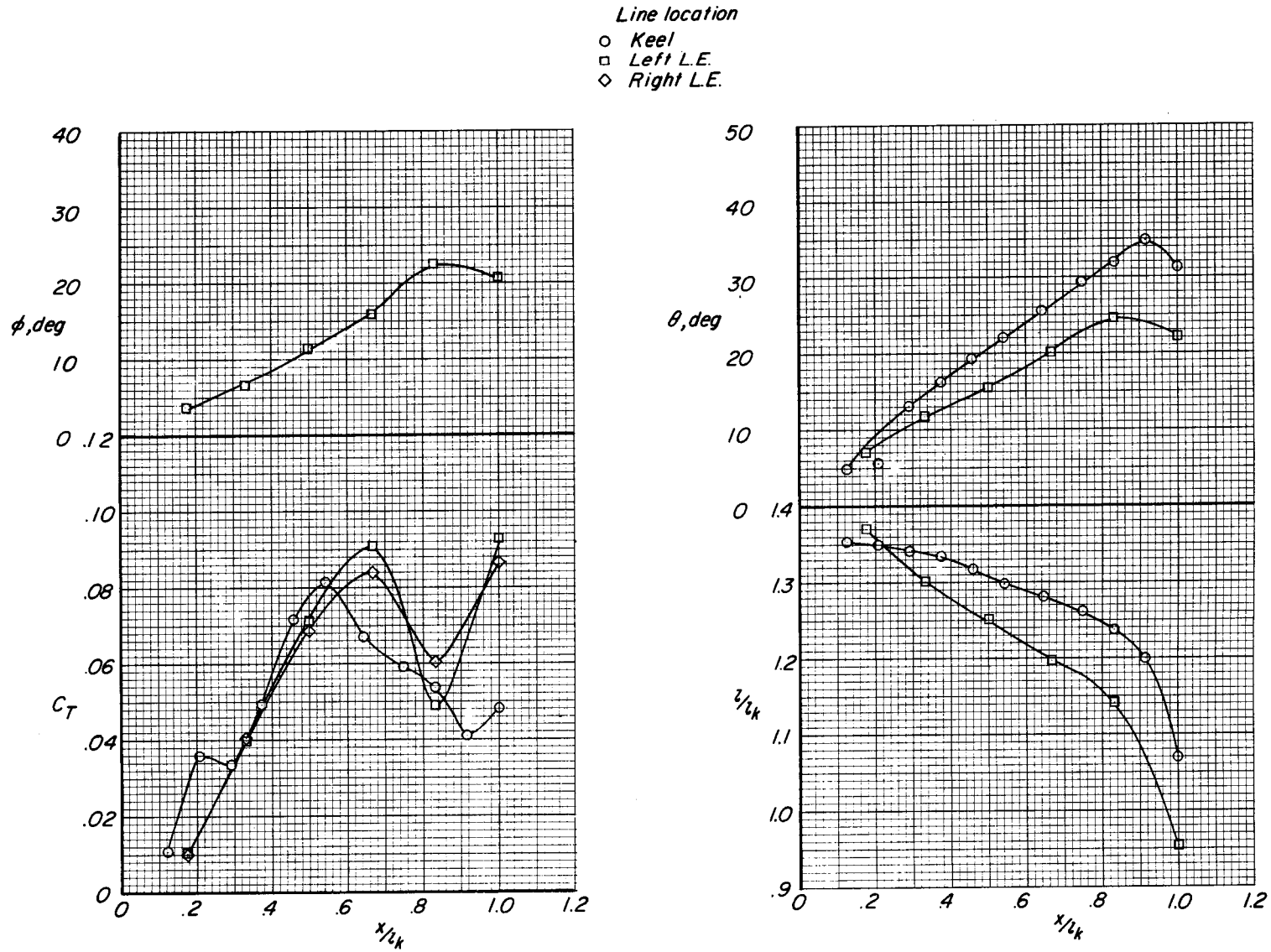

(a) Rigging A; q = 1.5 – Concluded.

Figure 37.- Continued.

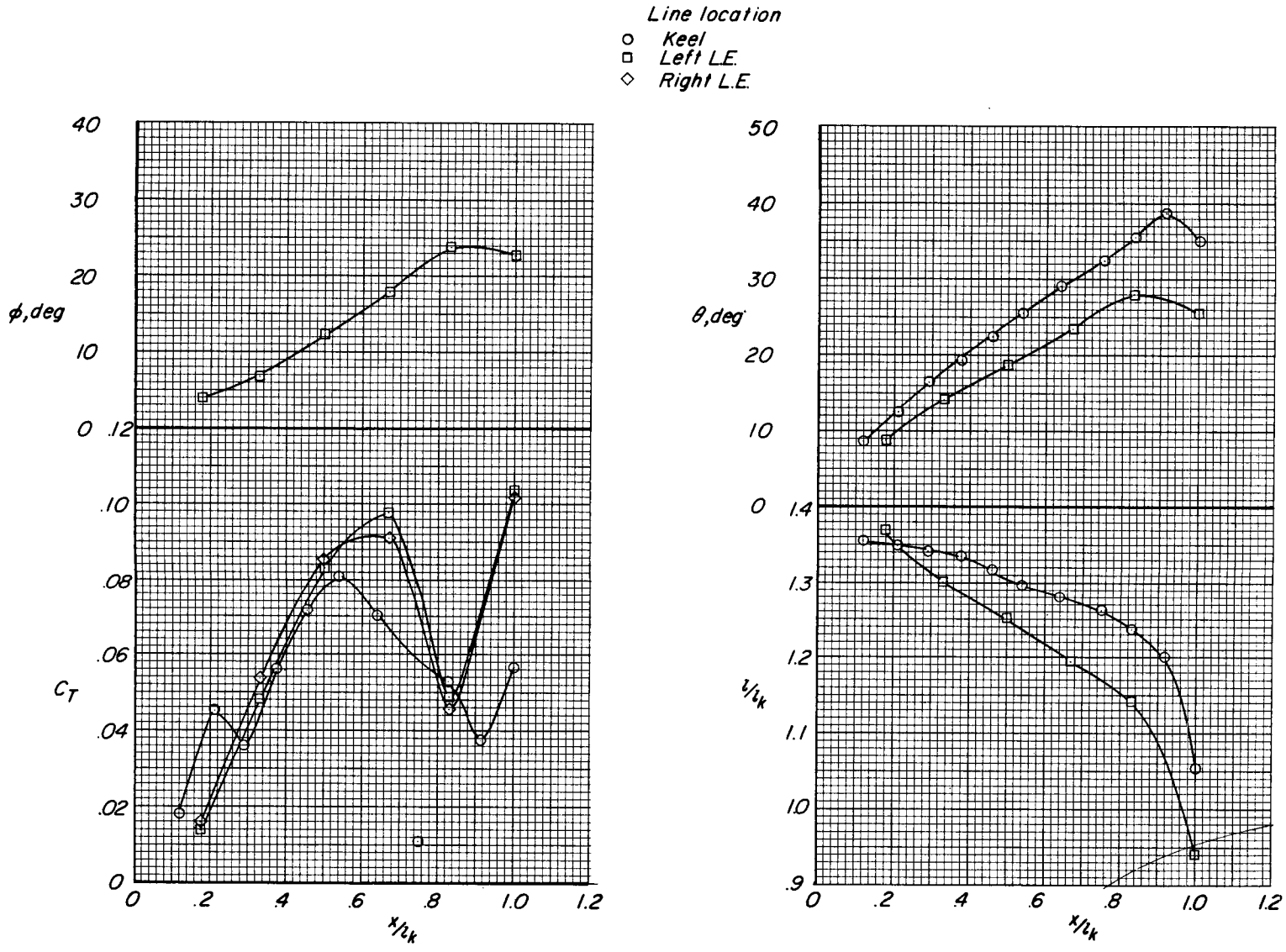

(b) Rigging B; q = 1.0.

Figure 37.- Continued.

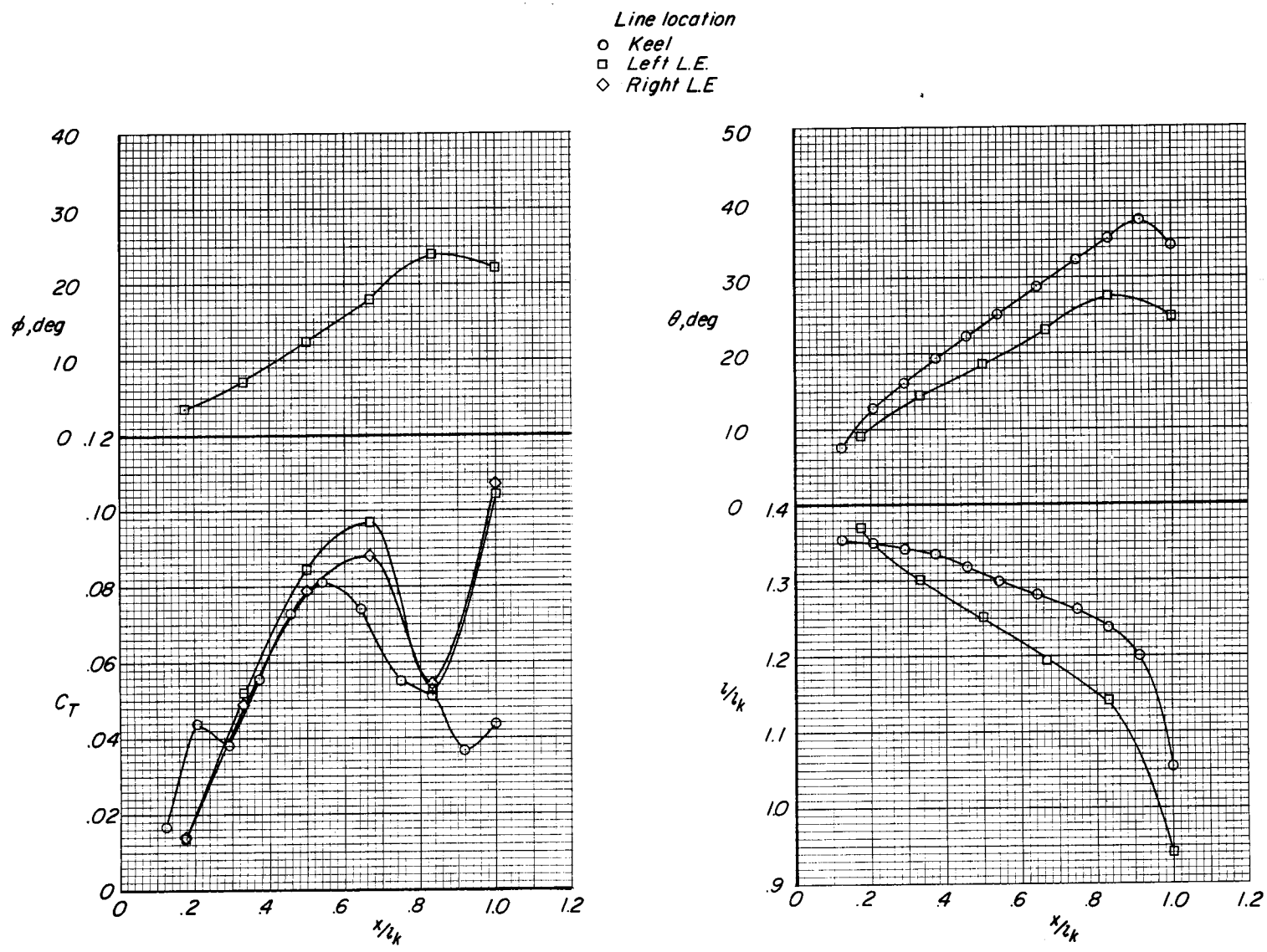

(b) Rigging B; q = 1.5 – Concluded.

Figure 37.- Continued.

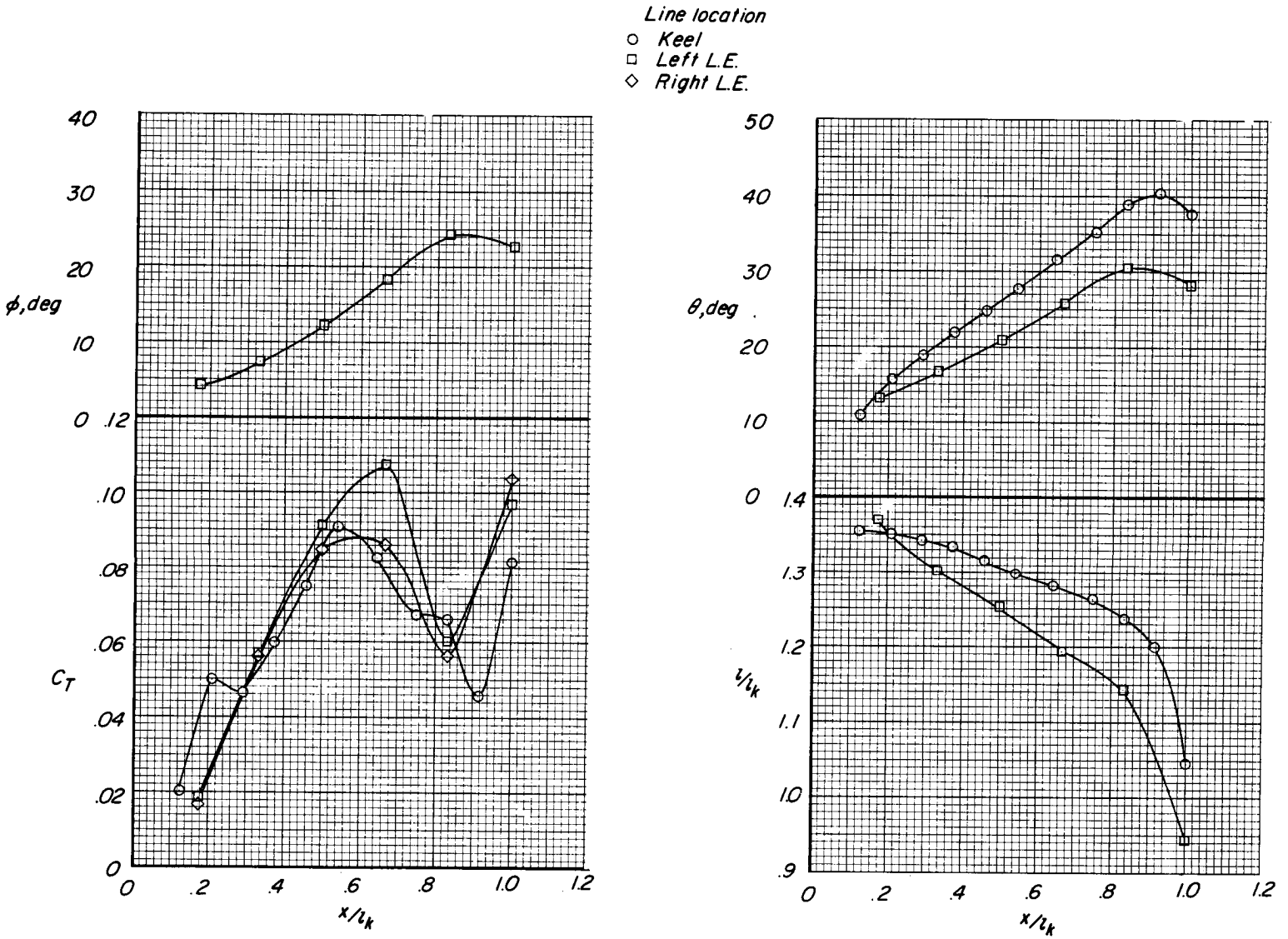

(c) Rigging C; q = 1.0.

Figure 37.- Continued.

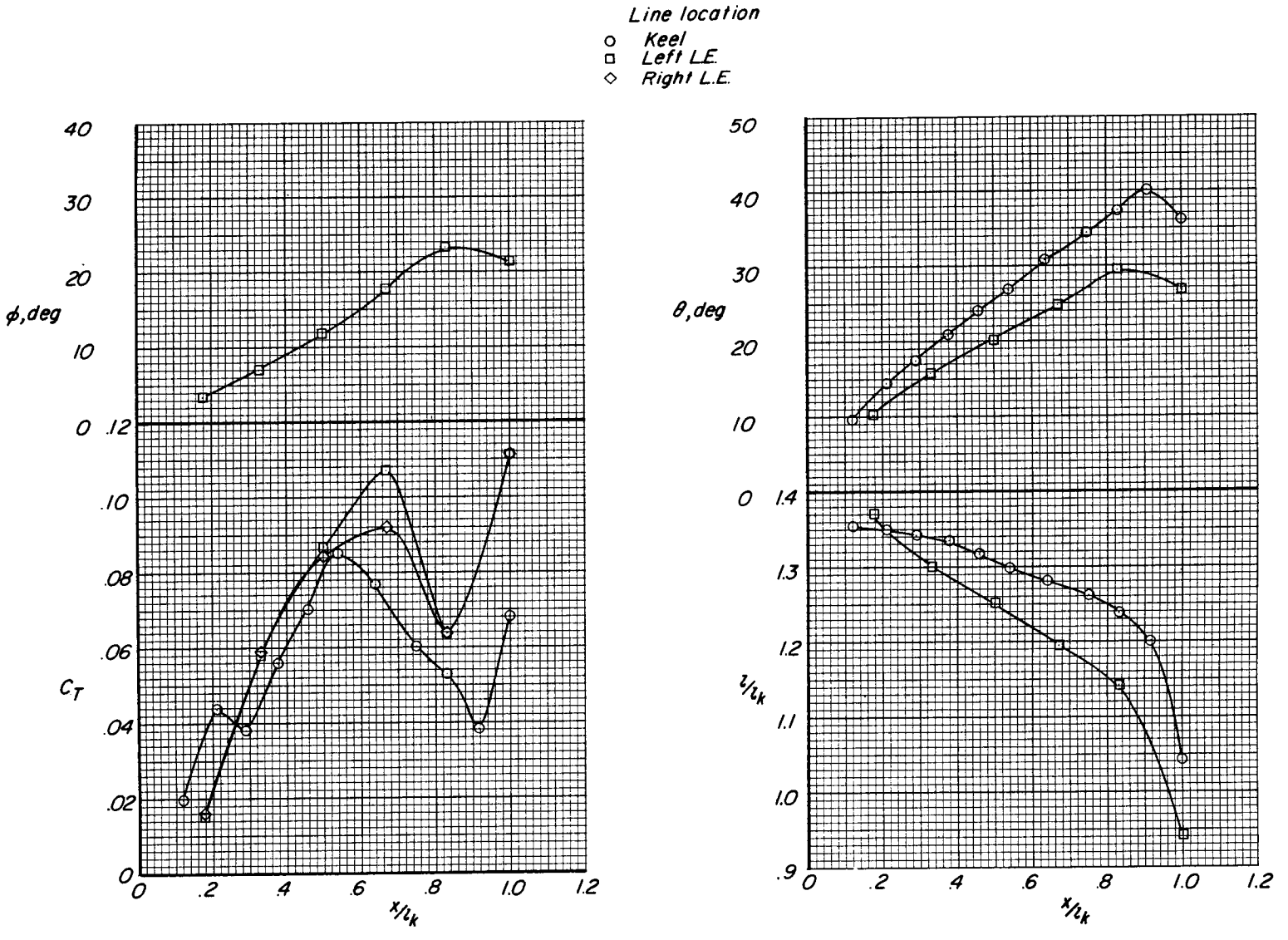

(c) Rigging C; q = 1.5 – Continued.

Figure 37.- Continued.

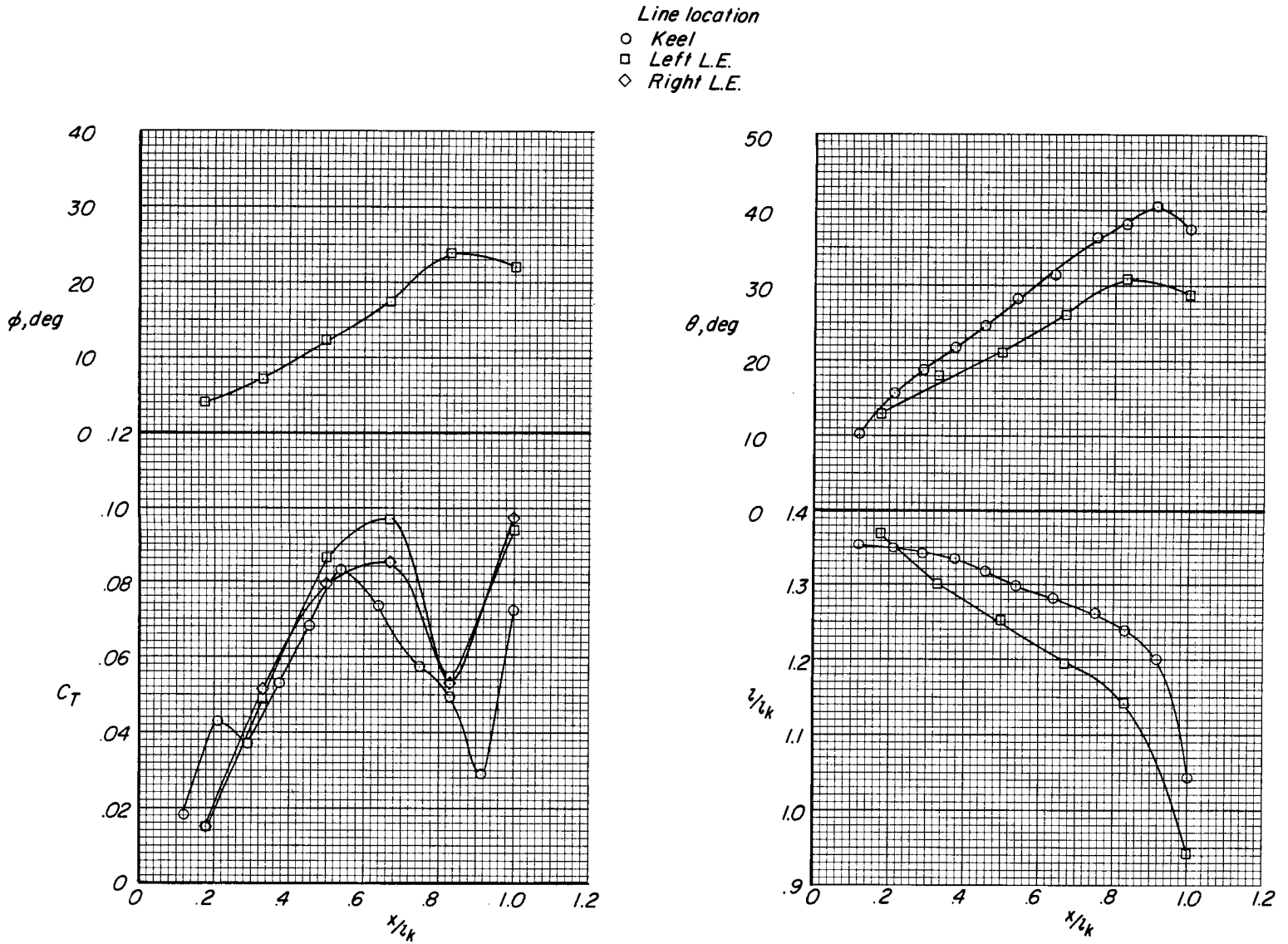

(c) Rigging C; q = 2.0 – Concluded.

Figure 37.- Concluded.

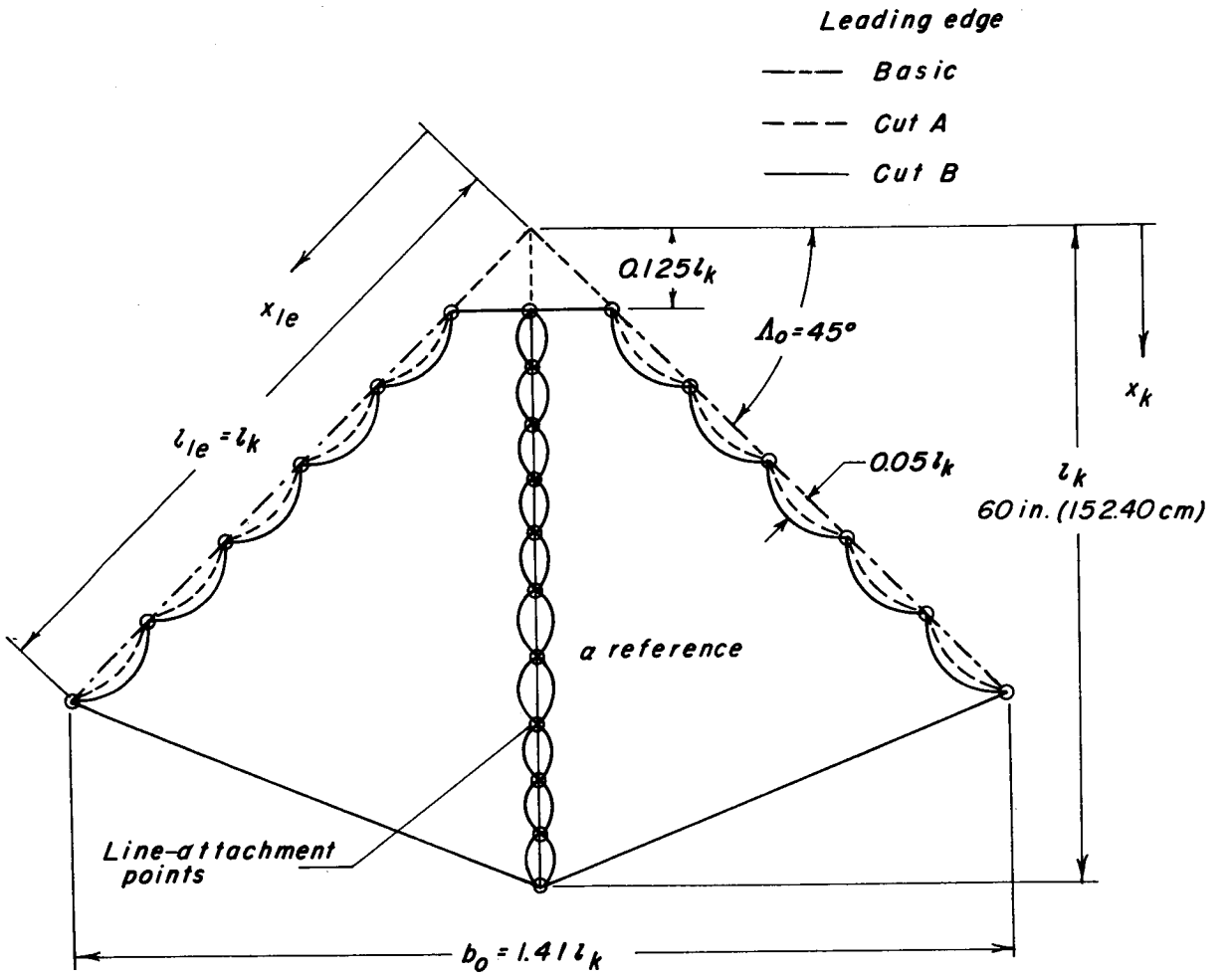

x/l_k	
Keel	Leading edge
.125	.177
.208	.333
.292	.500
.375	.667
.459	.833
.542	1.000
.645	
.750	
.833	
.917	
1.000	

Line-attachment location

(a) Flat-pattern details.

Figure 38.- Model of a parawing with $\Lambda_0 = 45^0$, 1/8 l_k nose cut off, and parabolic suspension patches on the leading edges and keel.

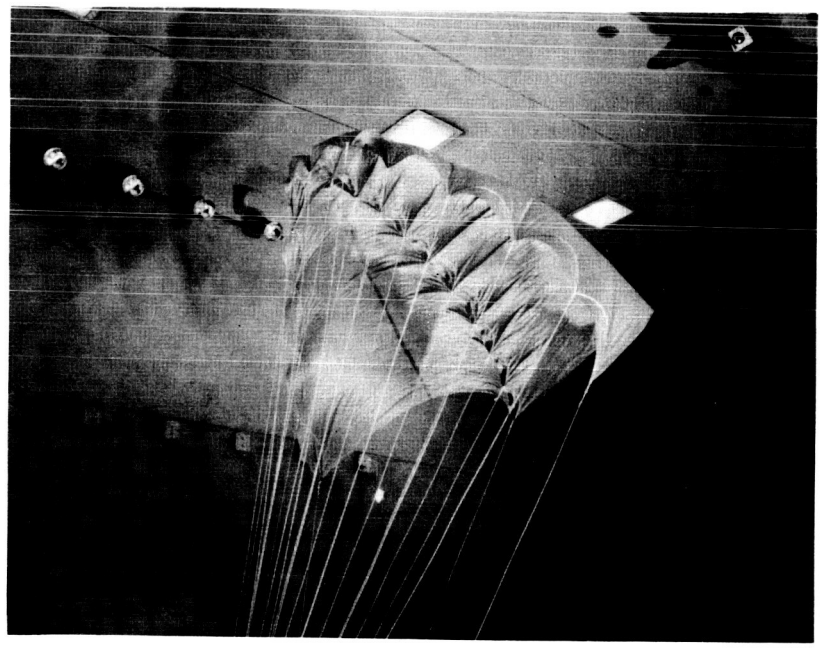

Basic leading-edge model

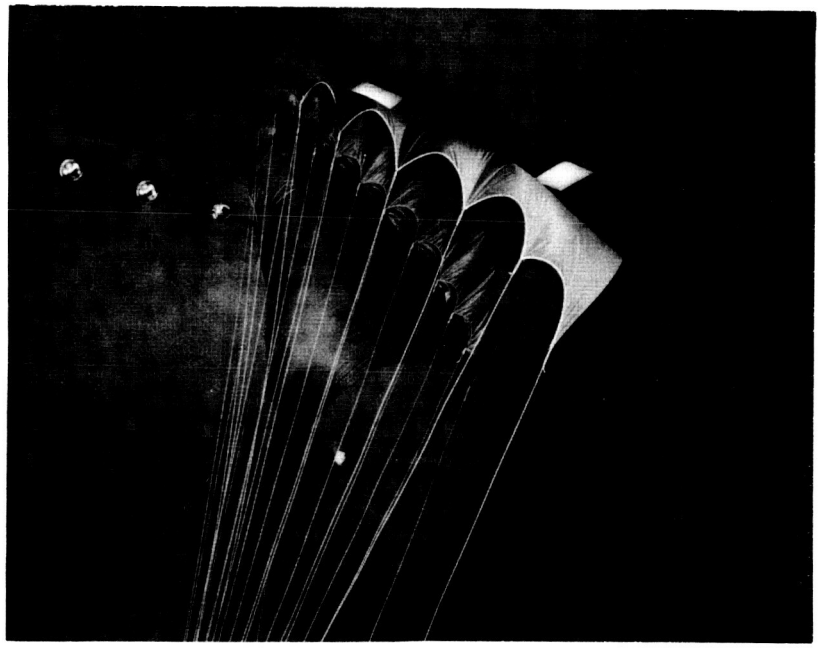

Cut-B model

(b) Photographs of models with parabolic suspension patches. L-67-942

Figure 38.- Concluded.

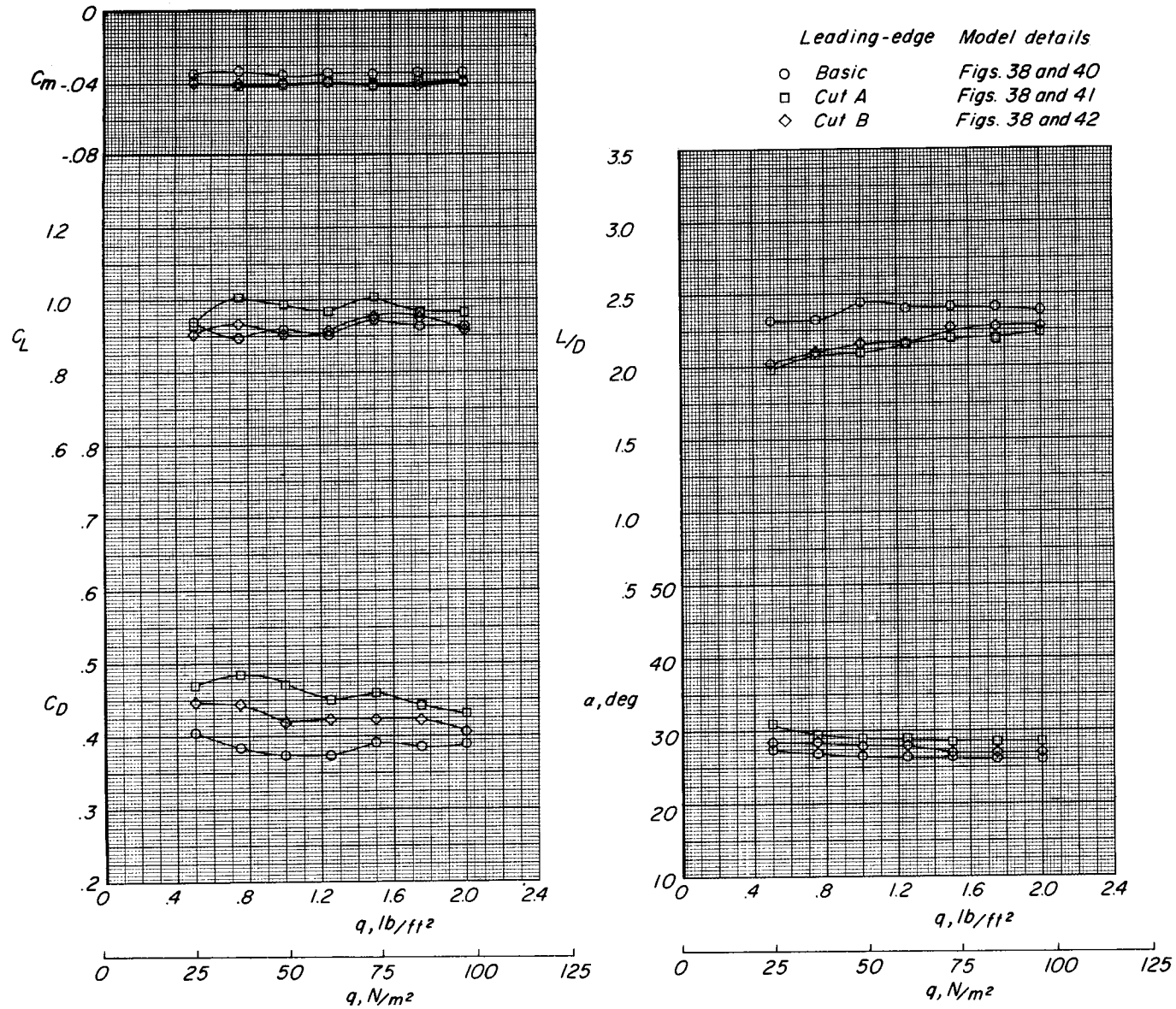

Figure 39.- Effect of fabric removal between leading-edge parabolic suspension patches on the variation of the longitudinal aerodynamic characteristics with dynamic pressure for a parawing with $\Lambda_0 = 45^0$ and 1/8 ℓ_k nose cut off.

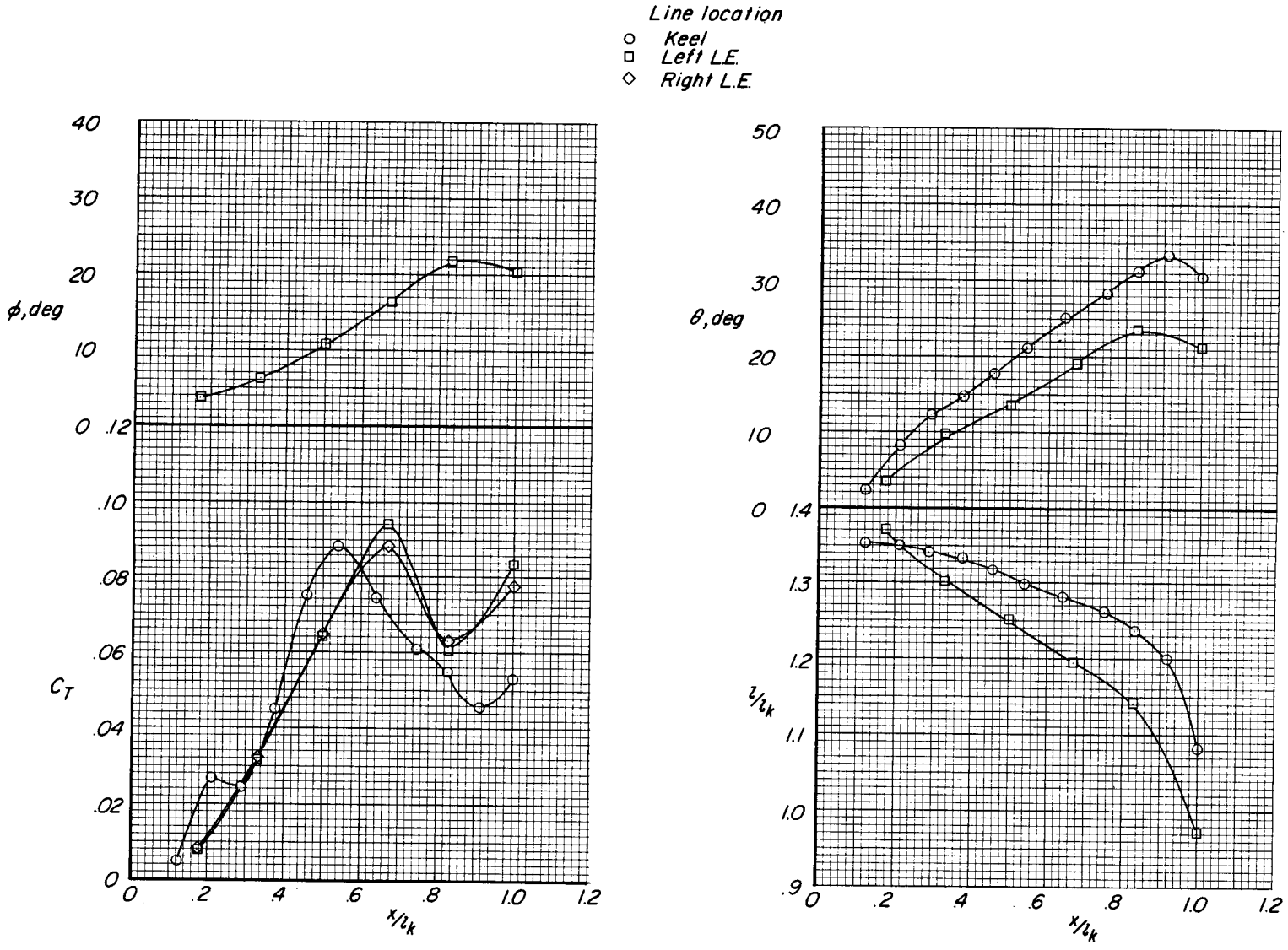

(a) q = 1.0.

Figure 40.- Tension coefficients, line angles, and line lengths for a parawing with $\Lambda_0 = 45^0$, 1/8 l_k nose cut off, basic straight leading edges, and parabolic suspension patches.

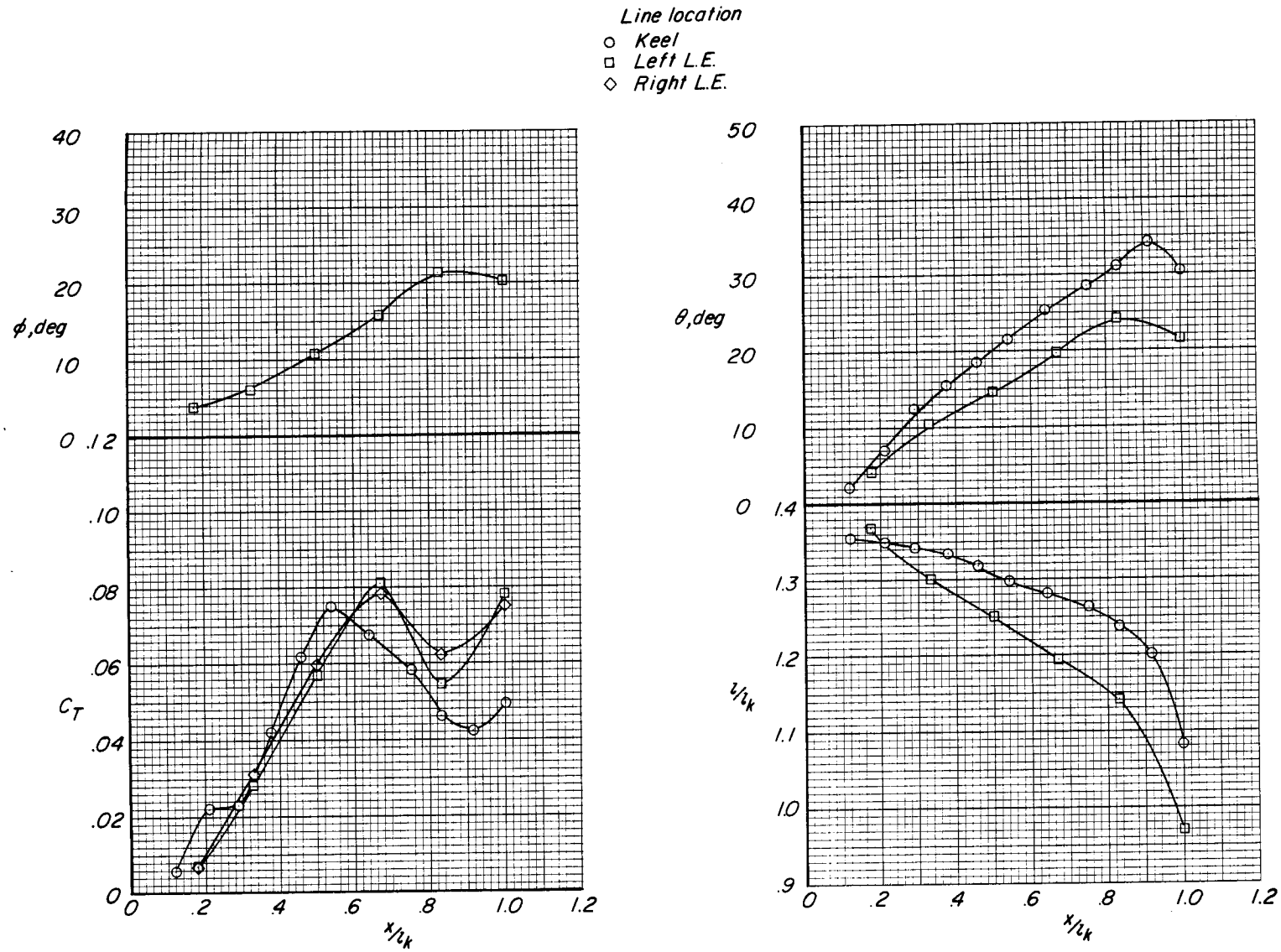

(b) q = 2.0.

Figure 40.- Concluded.

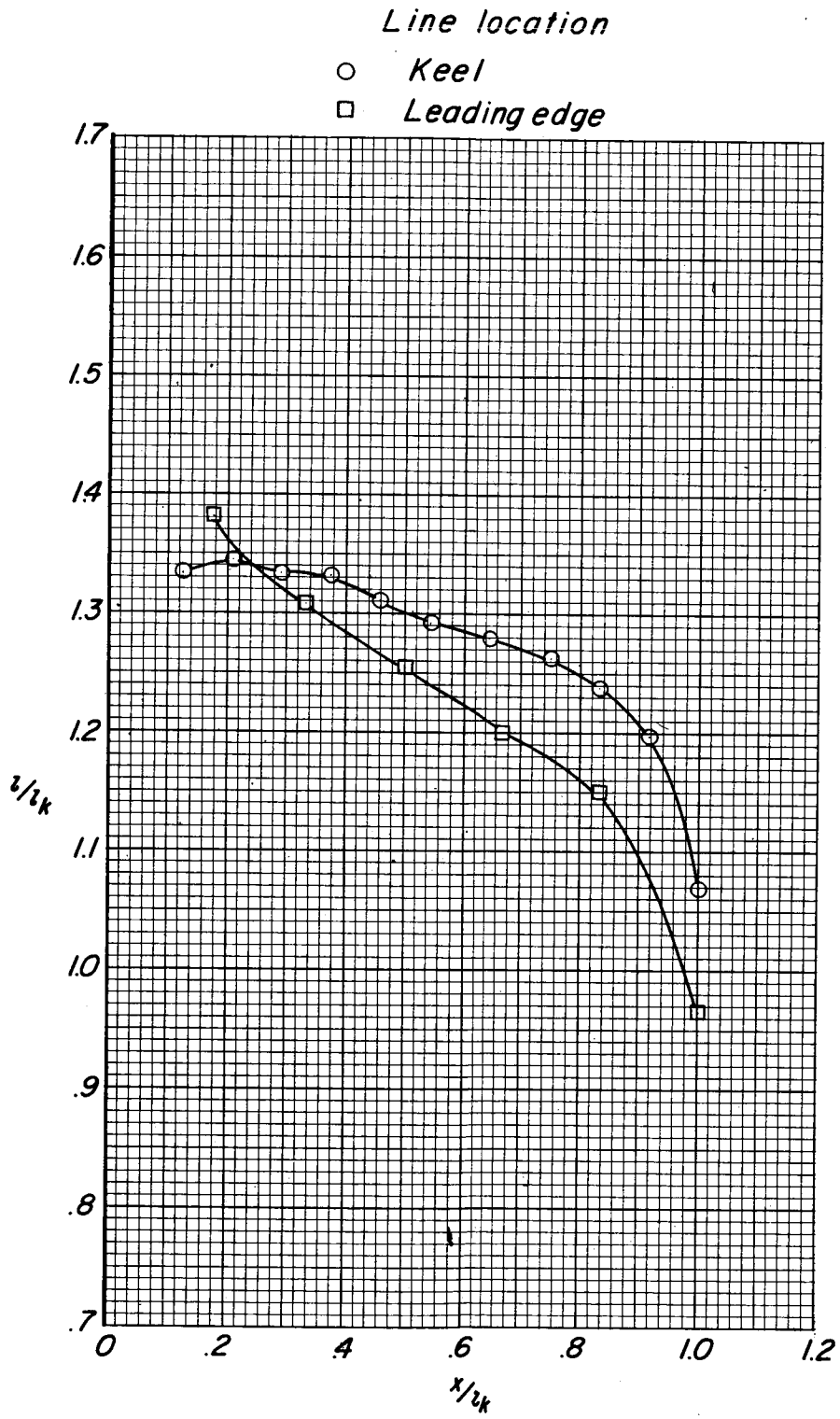

Figure 41.- Line lengths for a parawing with $\Lambda_0 = 45^0$, 1/8 l_k nose cut off, and parabolic suspension patches with fabric (cut A) on leading edges.

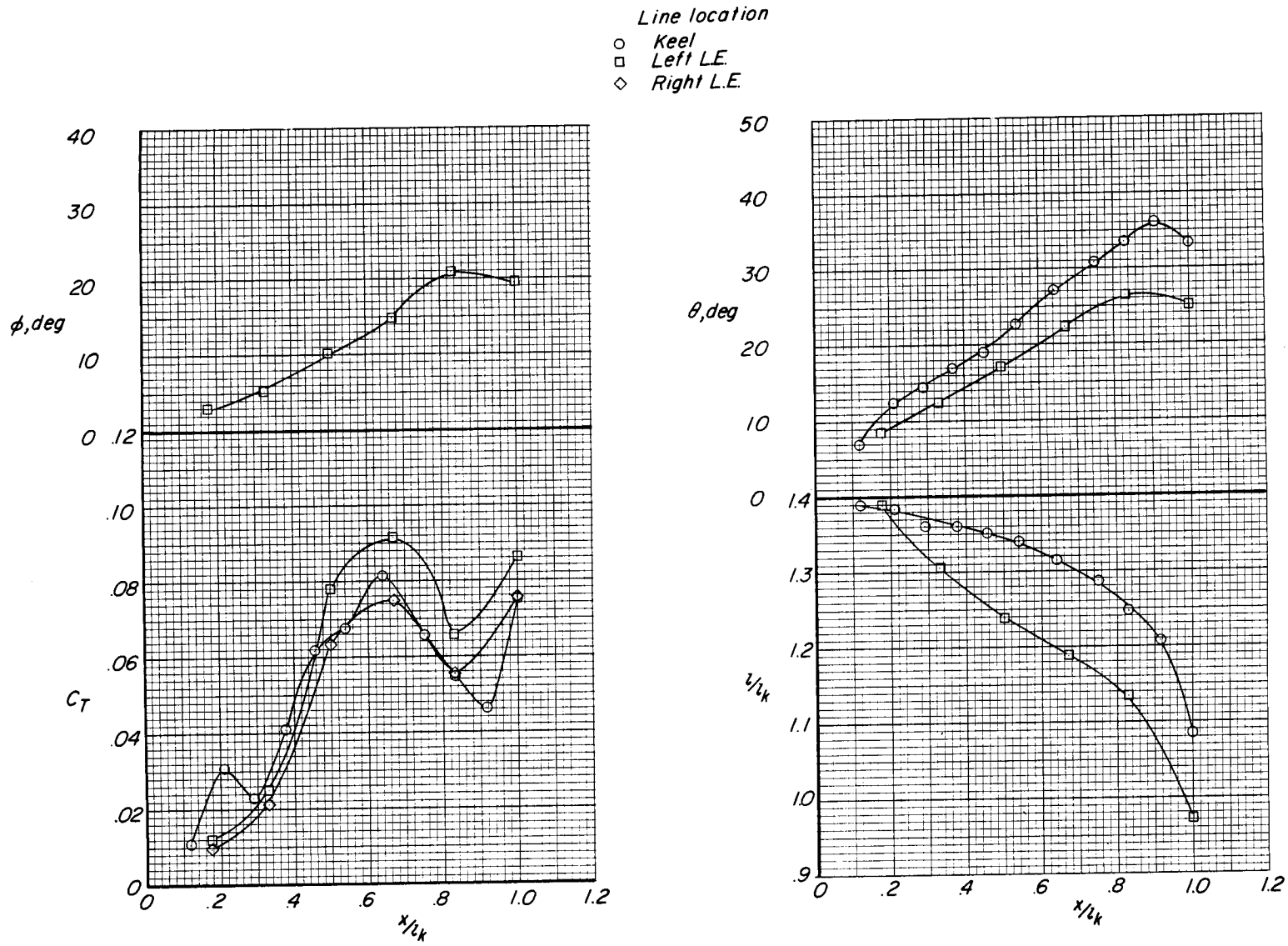

(a) q = 1.0.

Figure 42.- Tension coefficients, line angles, and line lengths for a parawing with $\Lambda_0 = 45^0$, 1/8 l_k nose cut off, and parabolic suspension patches with fabric (cut B) on leading edges.

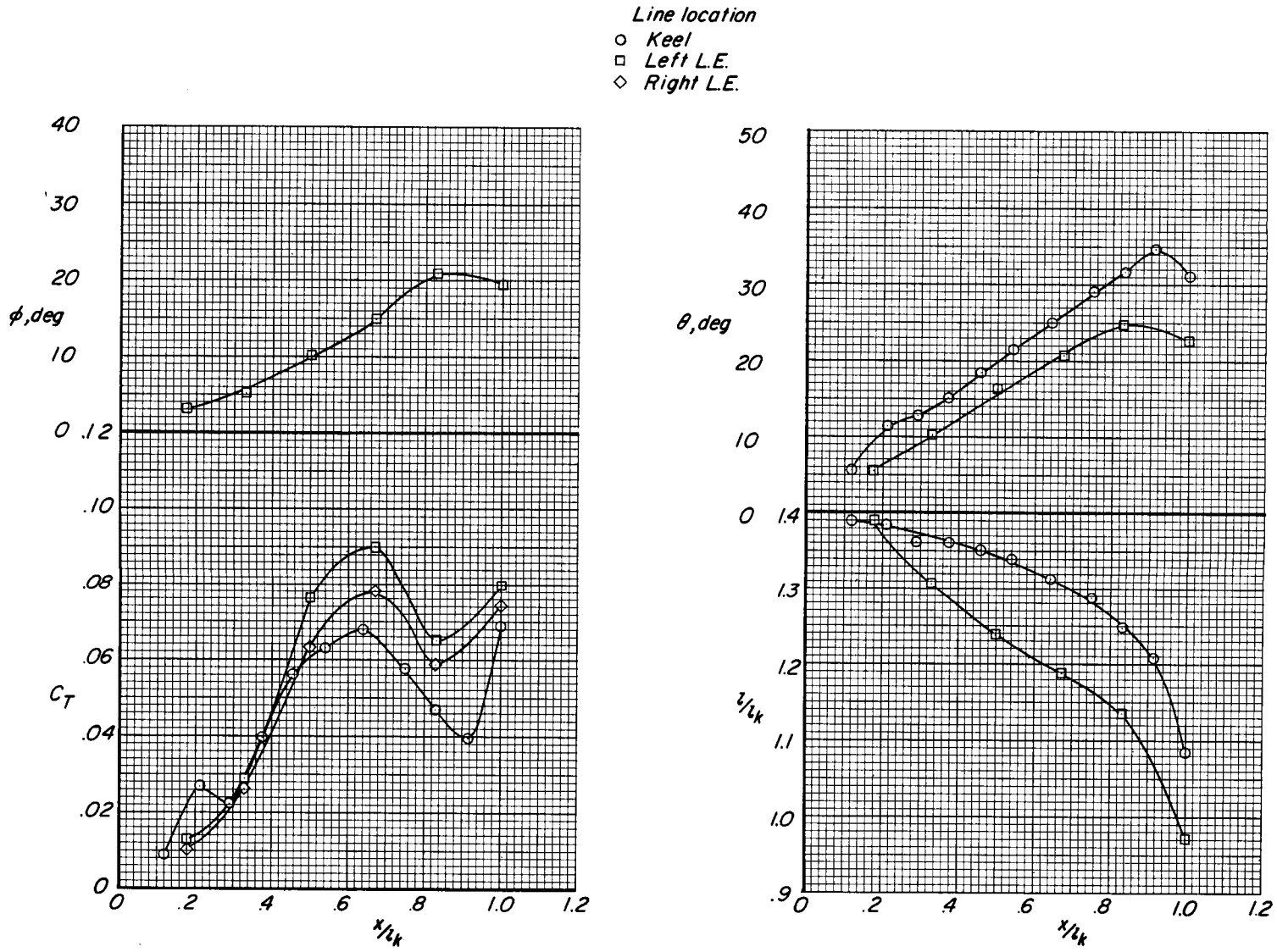

(b) q = 2.0.

Figure 42.- Concluded.

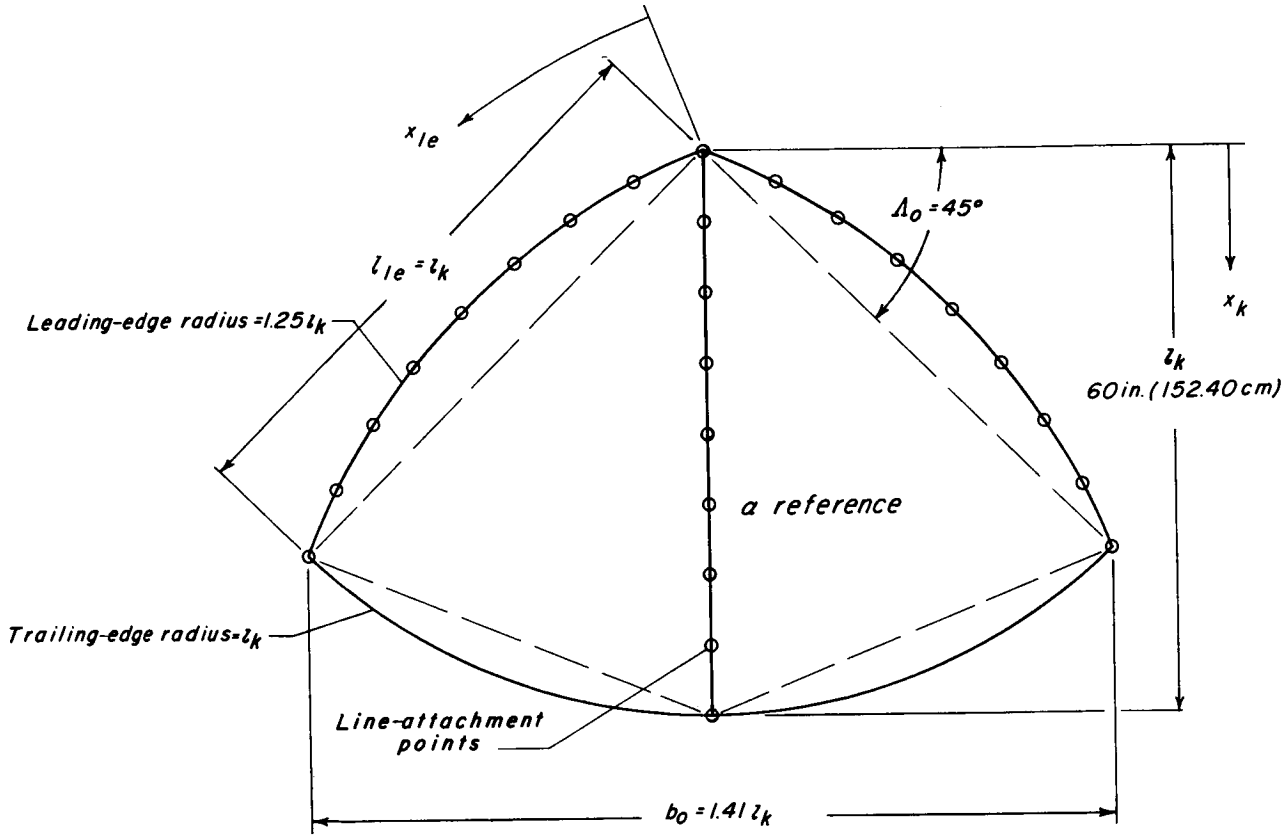

x/l_k	
Keel	Leading edge
0	0
.125	.129
.250	.259
.375	.389
.500	.518
.625	.647
.750	.776
.875	.905
1.000	1.034

Line-attachment location

(a) Flat-pattern details.

Figure 43.- Model of a parawing with a curved leading-edge and trailing-edge planform and theoretical $\Lambda_0 = 45^0$.

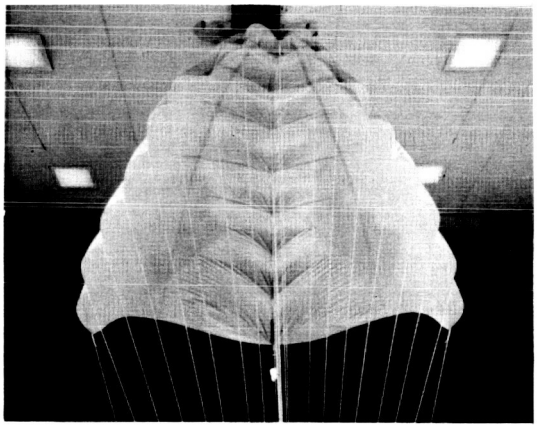

Front view

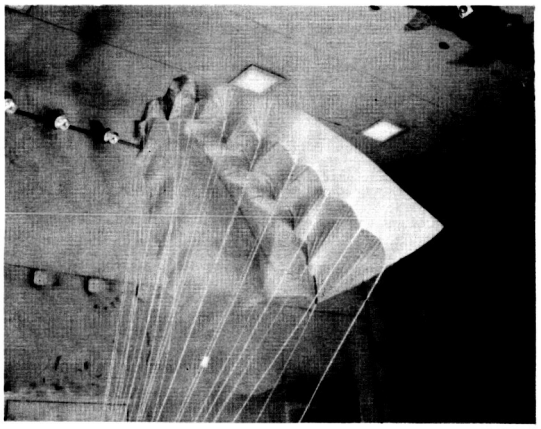

Front three-quarter view

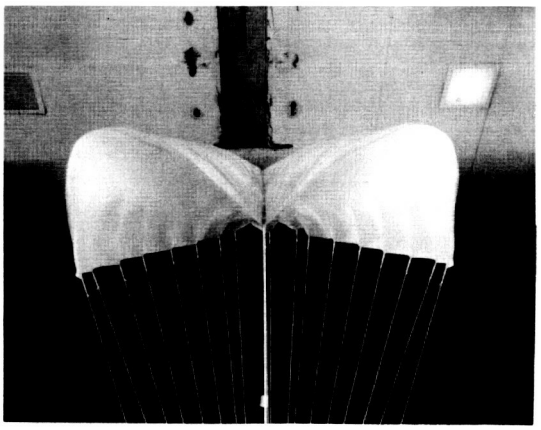

Rear view

(b) Photographs of model. L-67-943

Figure 43.- Concluded.

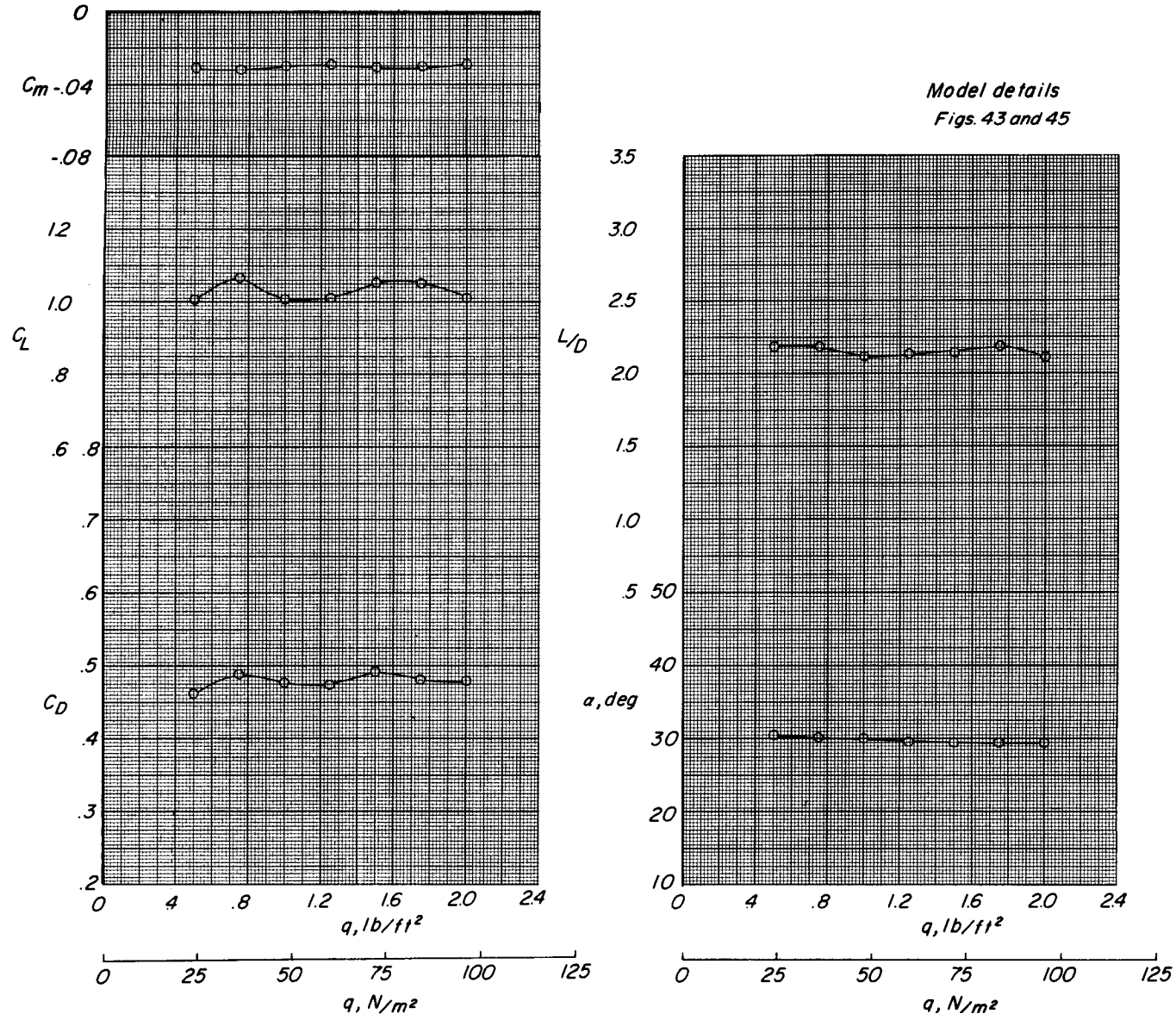

Figure 44.- Variation of the longitudinal aerodynamic characteristics with dynamic pressure for a parawing with 1.25 ℓ_k curved leading-edge planform, 1.00 ℓ_k curved trailing-edge planform, and theoretical $\Lambda_0 = 45^0$.

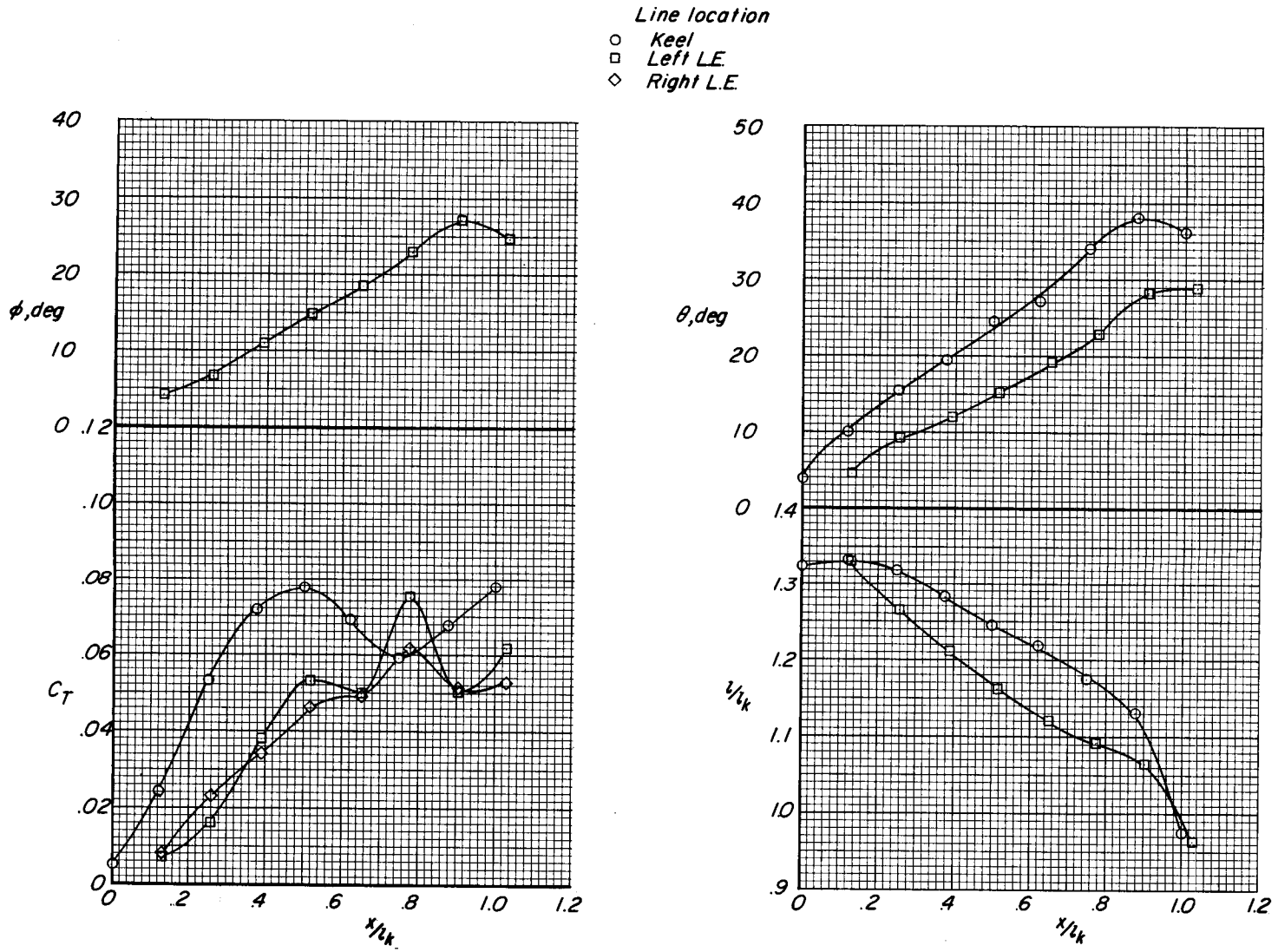

(a) q = 1.0.

Figure 45.- Tension coefficients, line angles, and line lengths for a parawing with 1.25 l_k curved leading-edge planform, 1.00 l_k curved trailing-edge planform, and theoretical $\Lambda_0 = 45^0$.

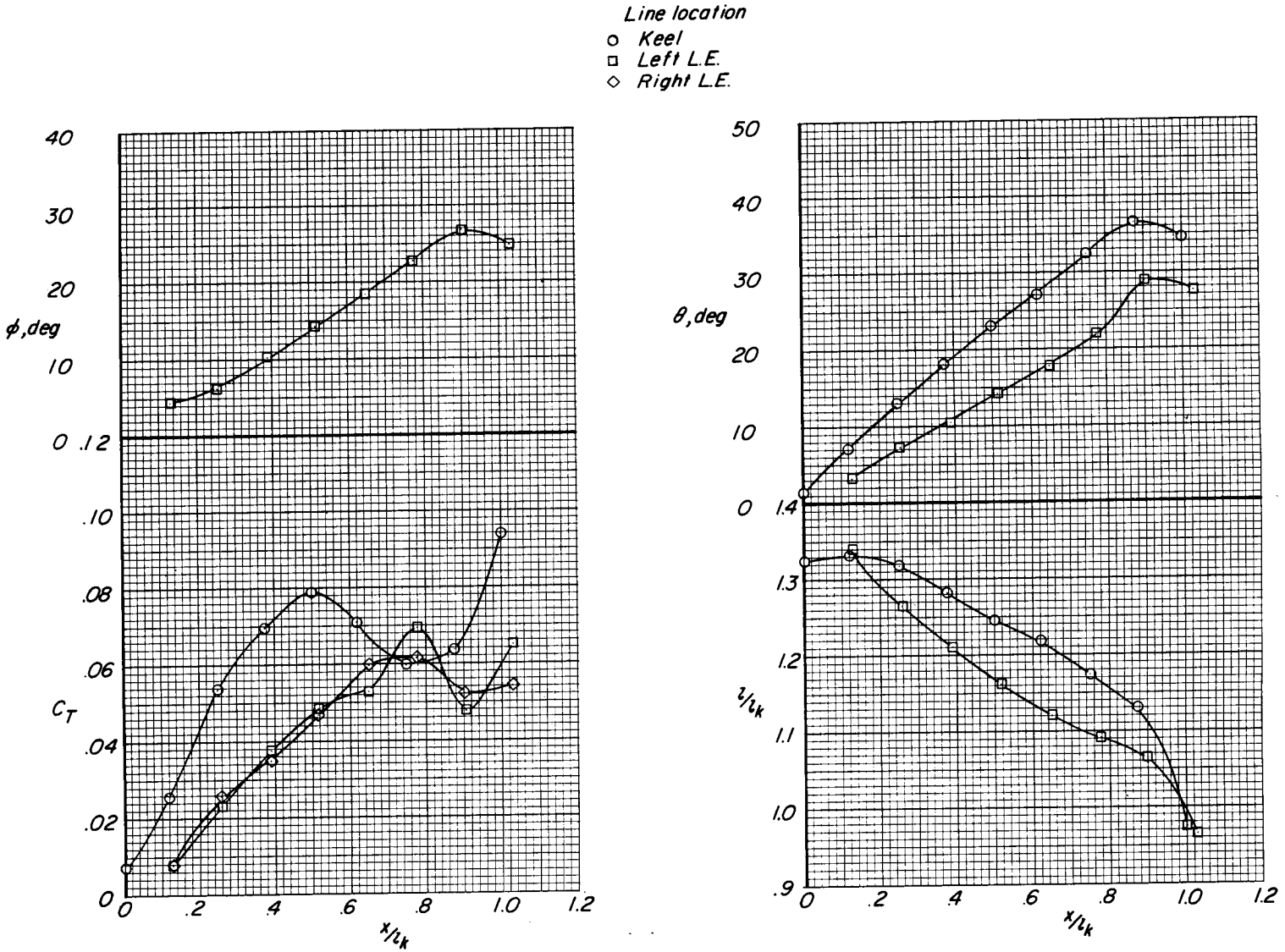

(b) q = 2.0.

Figure 45.- Concluded.

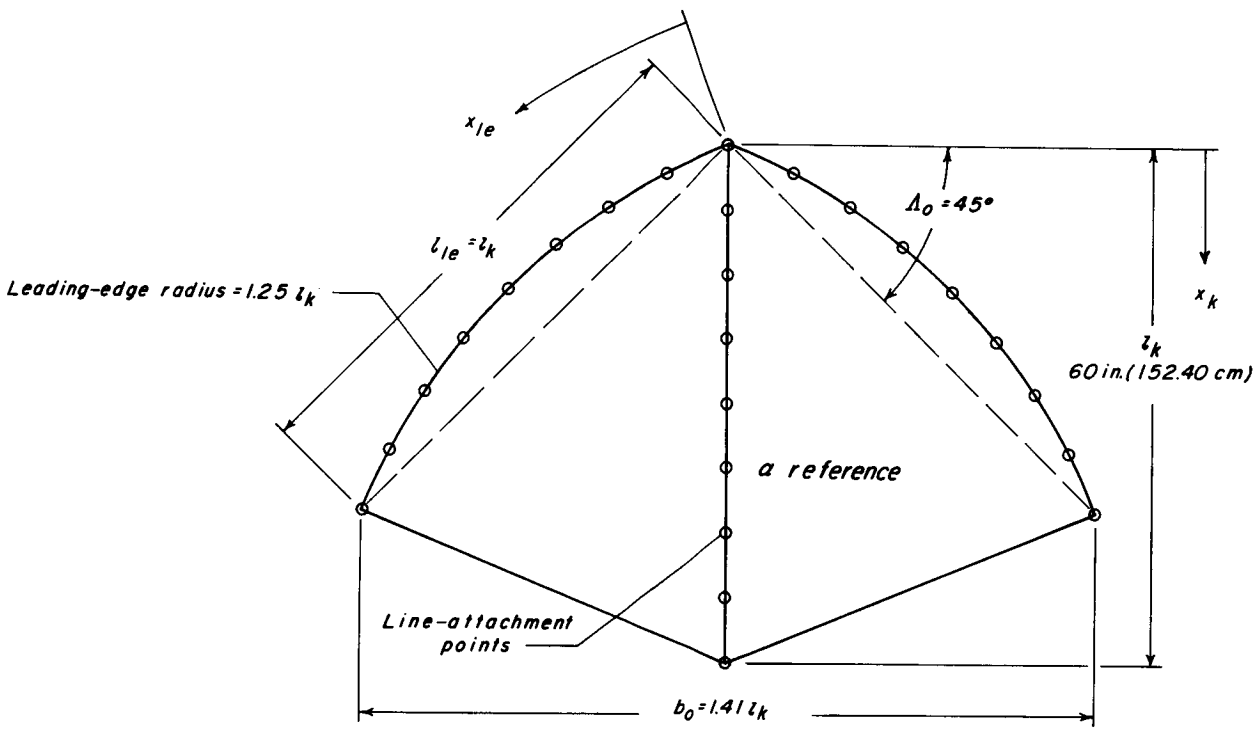

x/l_k	
Keel	Leading edge
0	0
.125	.129
.250	.259
.375	.389
.500	.518
.625	.647
.750	.776
.875	.905
1.000	1.034

Line-attachment location

(a) Flat-pattern details.

Figure 46.- Model of a parawing with curved leading-edge planform and theoretical $\Lambda_0 = 45^0$.

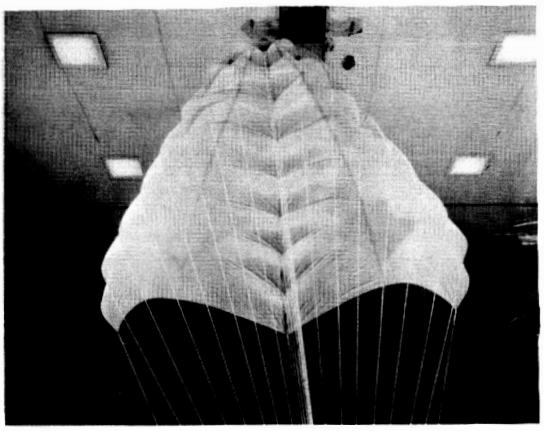

Front view

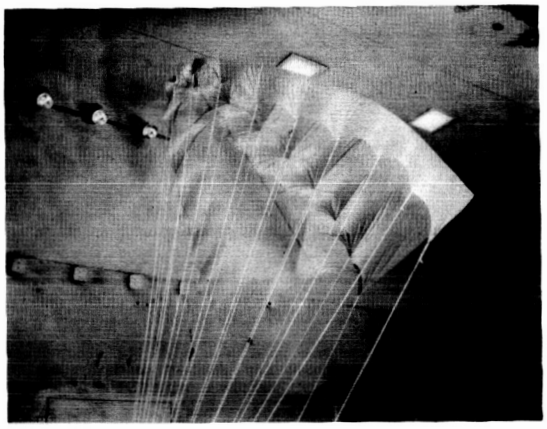

Front three-quarter view

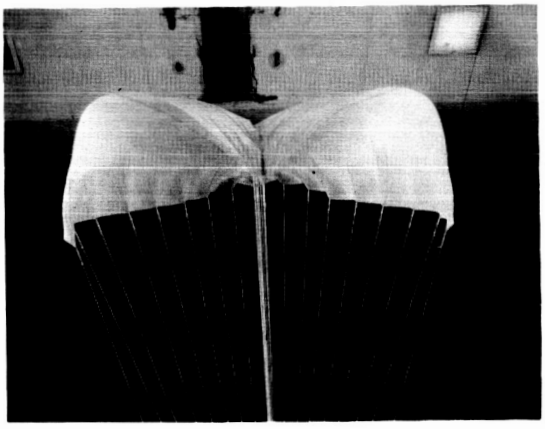

Rear view

(b) Photographs of model. L-67-944

Figure 46.- Concluded.

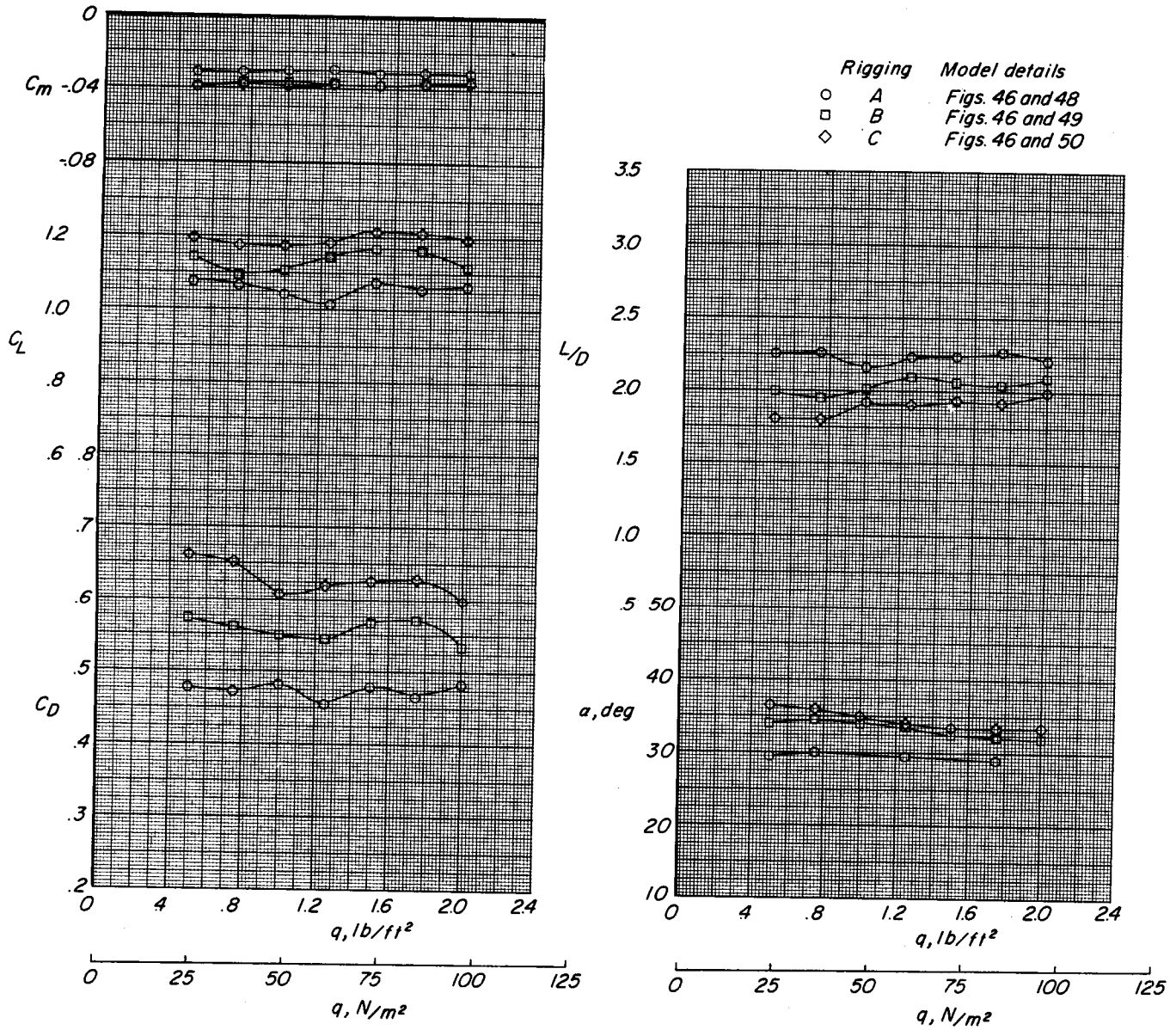

Figure 47.- Effect of changes in rigging on the variation of the wing longitudinal aerodynamic characteristics with dynamic pressure for a parawing with 1.25 ℓ_k radius leading-edge planform and theoretical $\Lambda_0 = 45^0$.

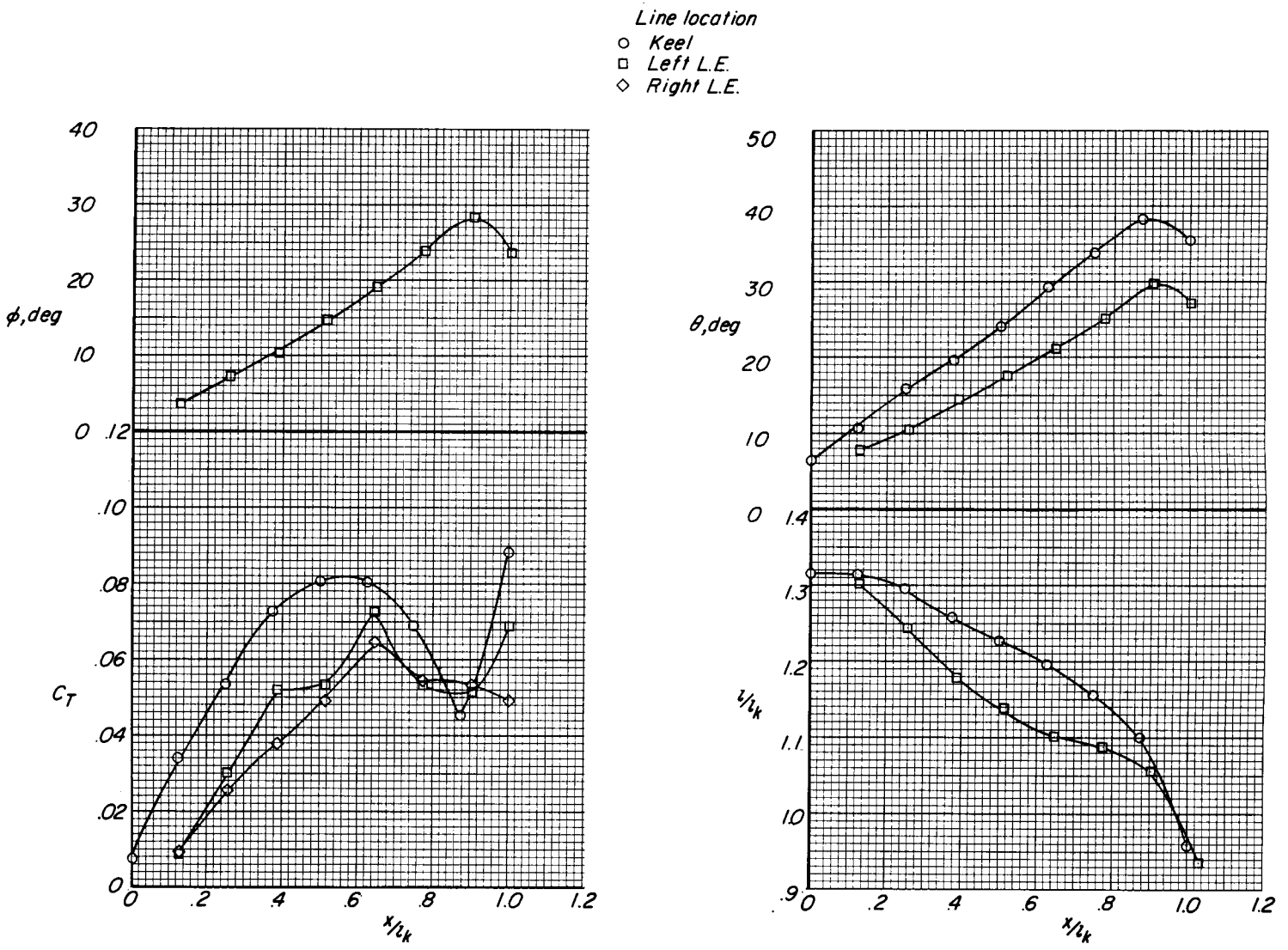

(a) Rigging A; q = 1.0.

Figure 48.- Tension coefficients, line angles, and line lengths for a parawing with a 1.25 l_k radius leading-edge planform and theoretical $\Lambda_0 = 45^0$.

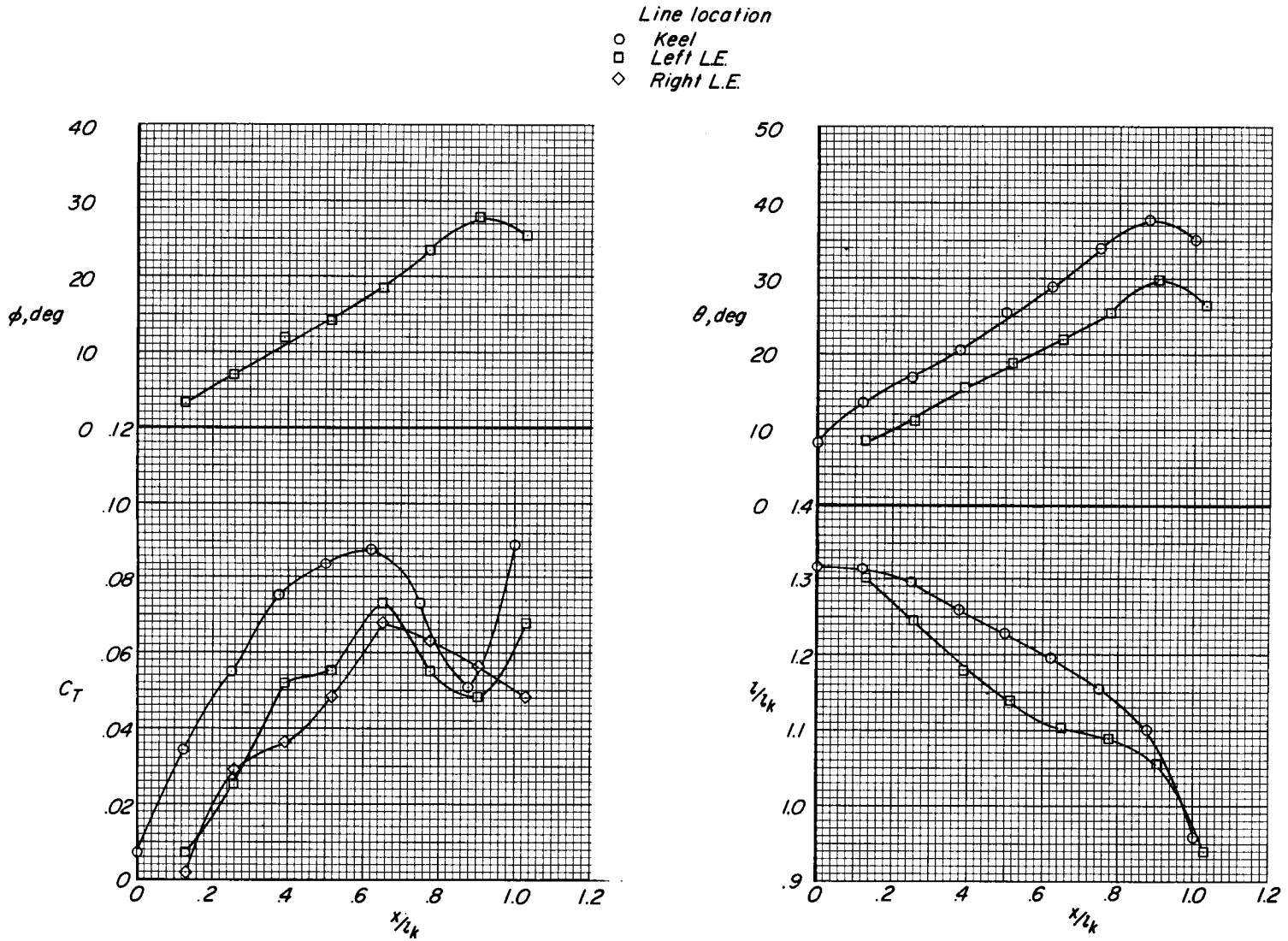

(b) Rigging A; q = 2.0.

Figure 48.- Concluded.

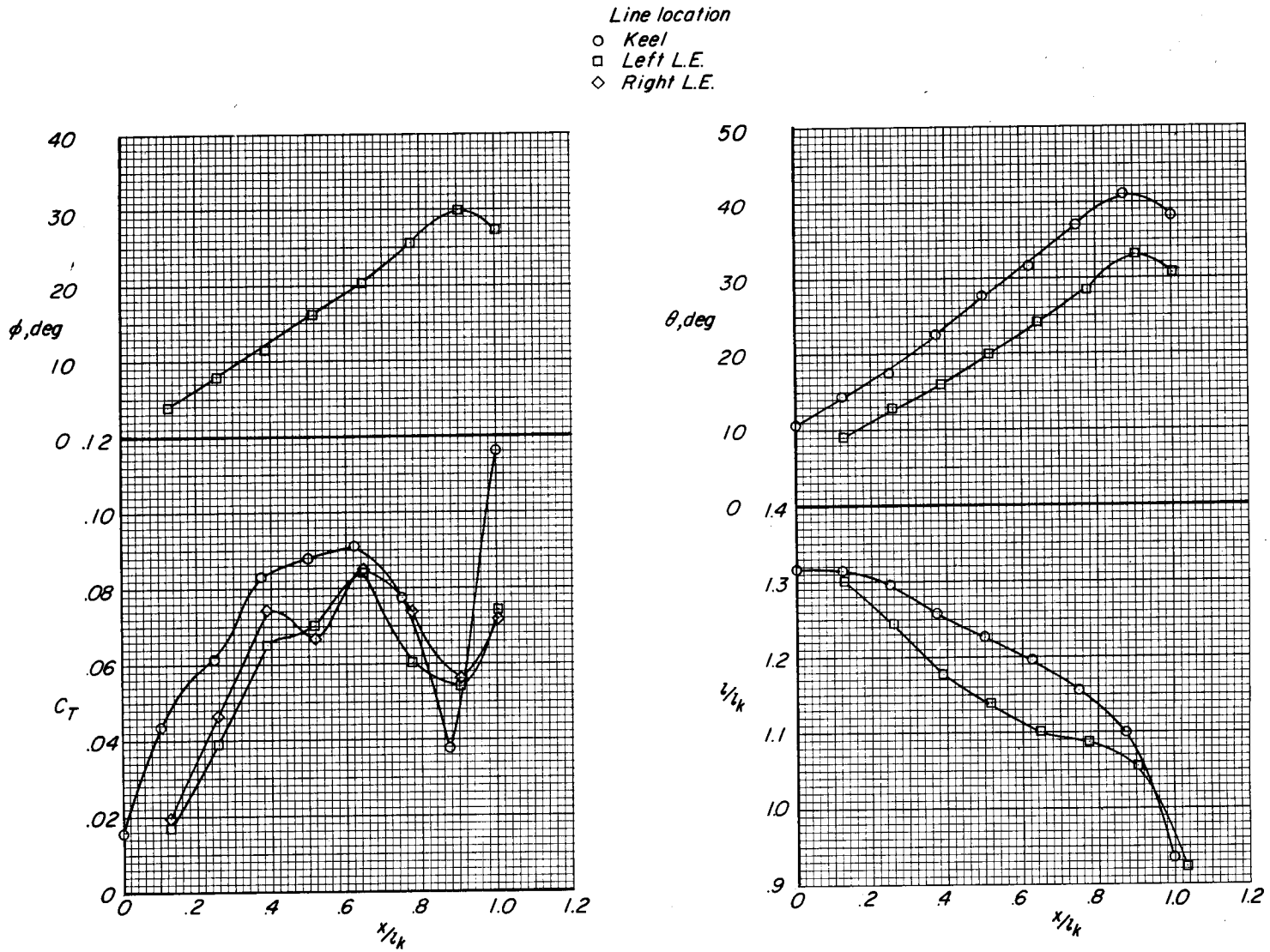

(a) Rigging B; q = 1.0.

Figure 49.- Tension coefficients, line angles, and line lengths for a parawing with a 1.25 l_k radius leading-edge planform and theoretical $\Lambda_0 = 45^0$.

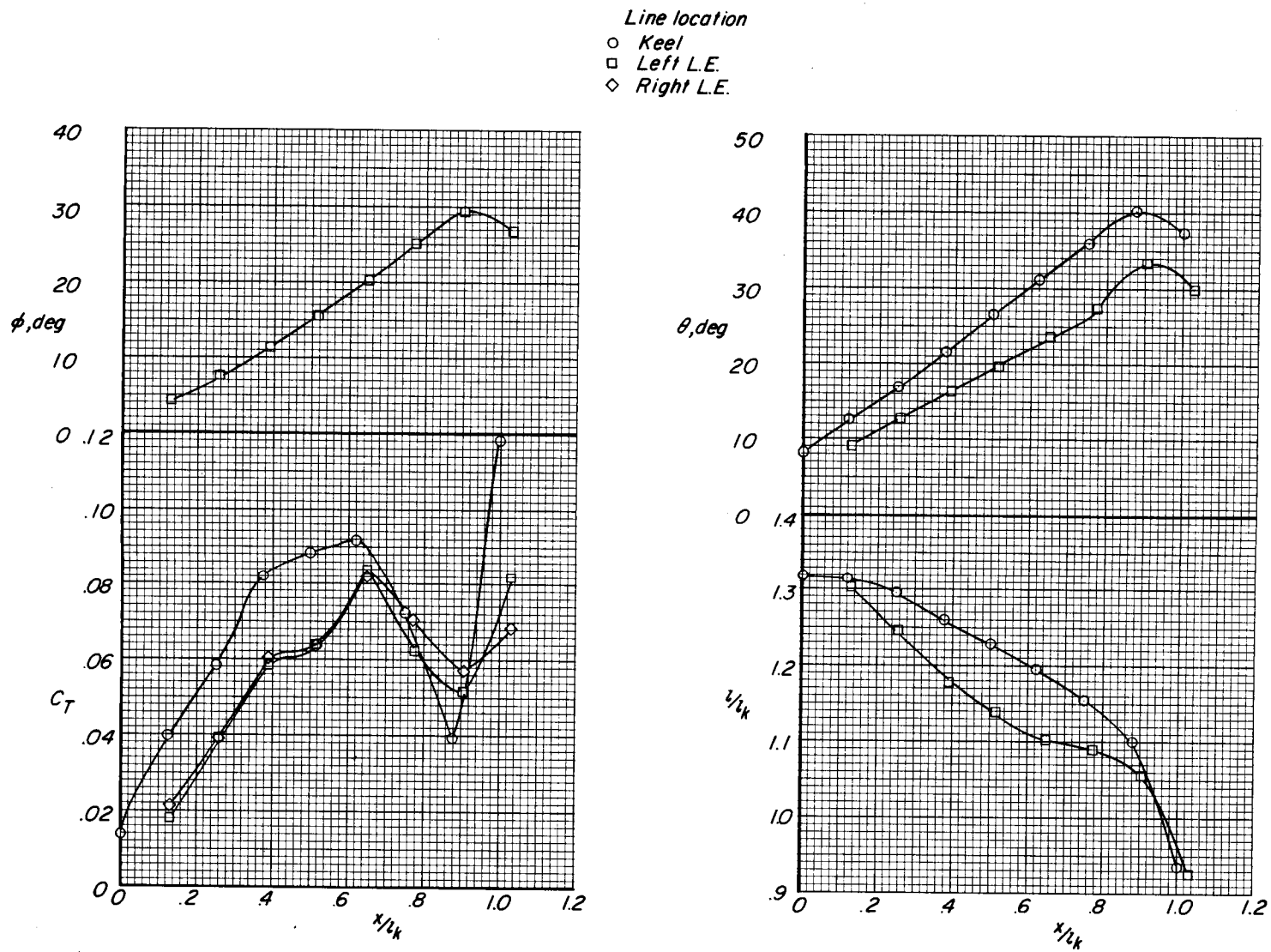

(b) Rigging B; q = 2.0.

Figure 49.- Concluded.

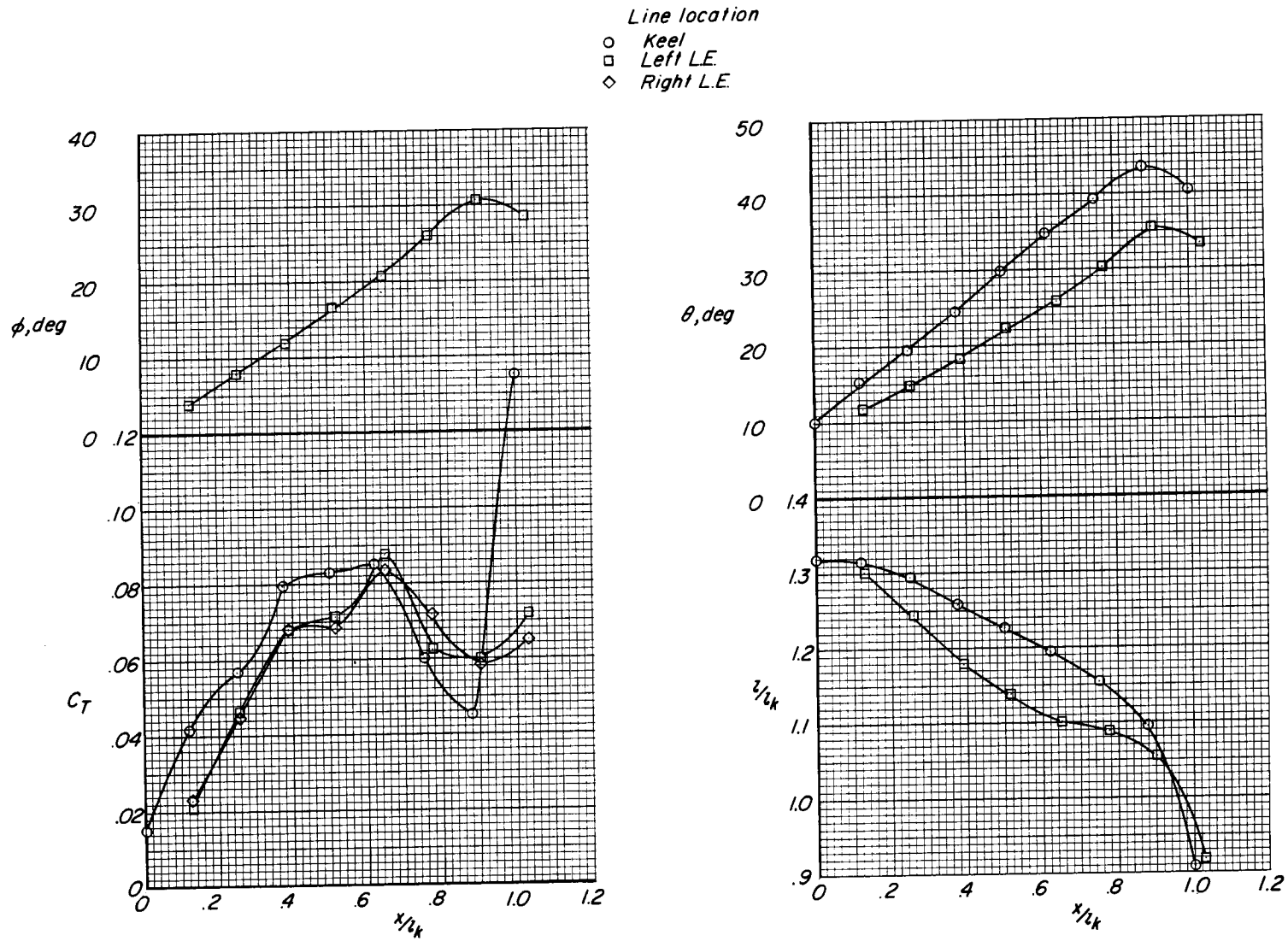

(a) Rigging C; q = 1.0.

Figure 50.- Tension coefficients, line angles, and line lengths for a parawing with a 1.25 l_k radius leading-edge planform and theoretical $\Lambda_0 = 45^0$.

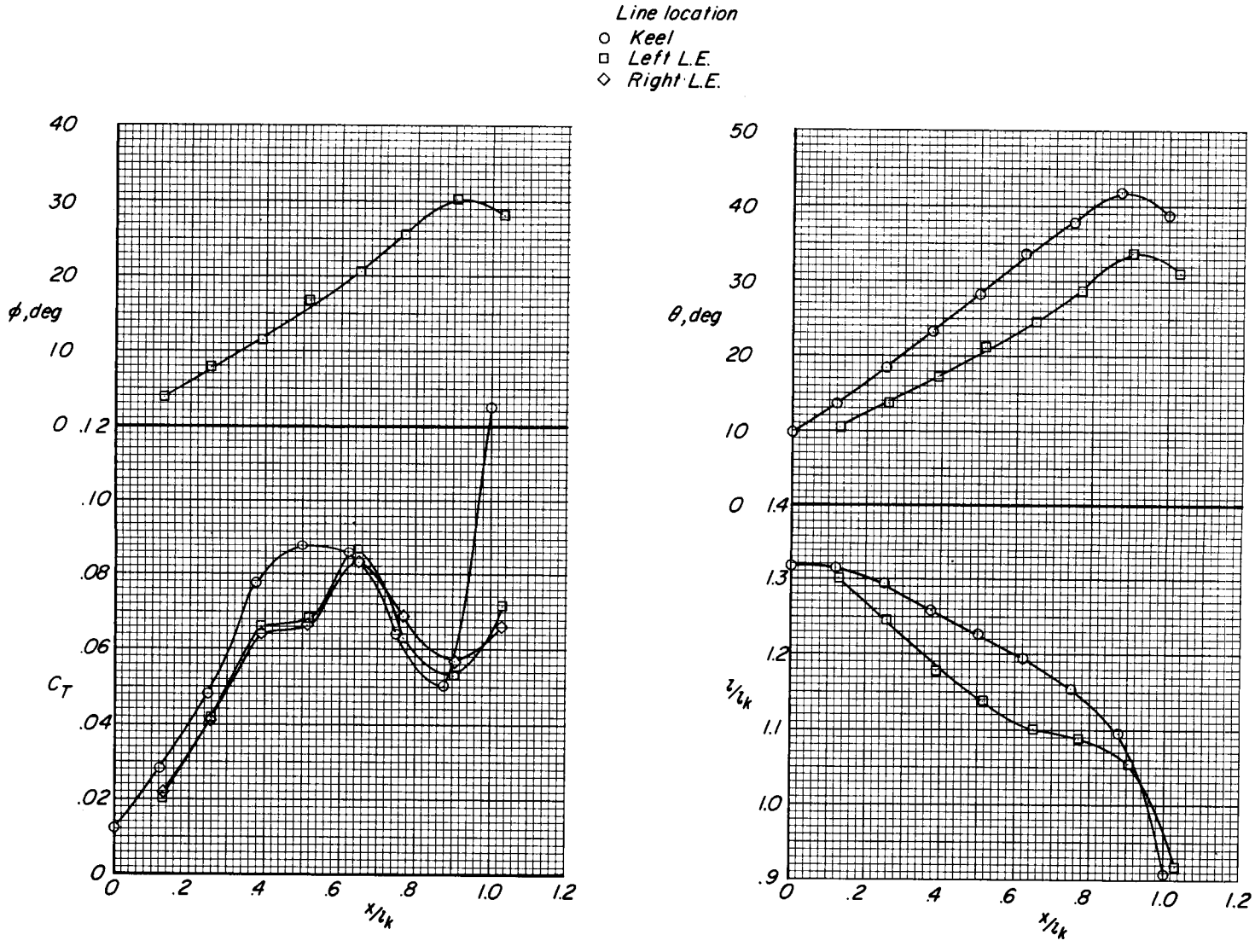

(b) Rigging C; q = 2.0.

Figure 50.- Concluded.

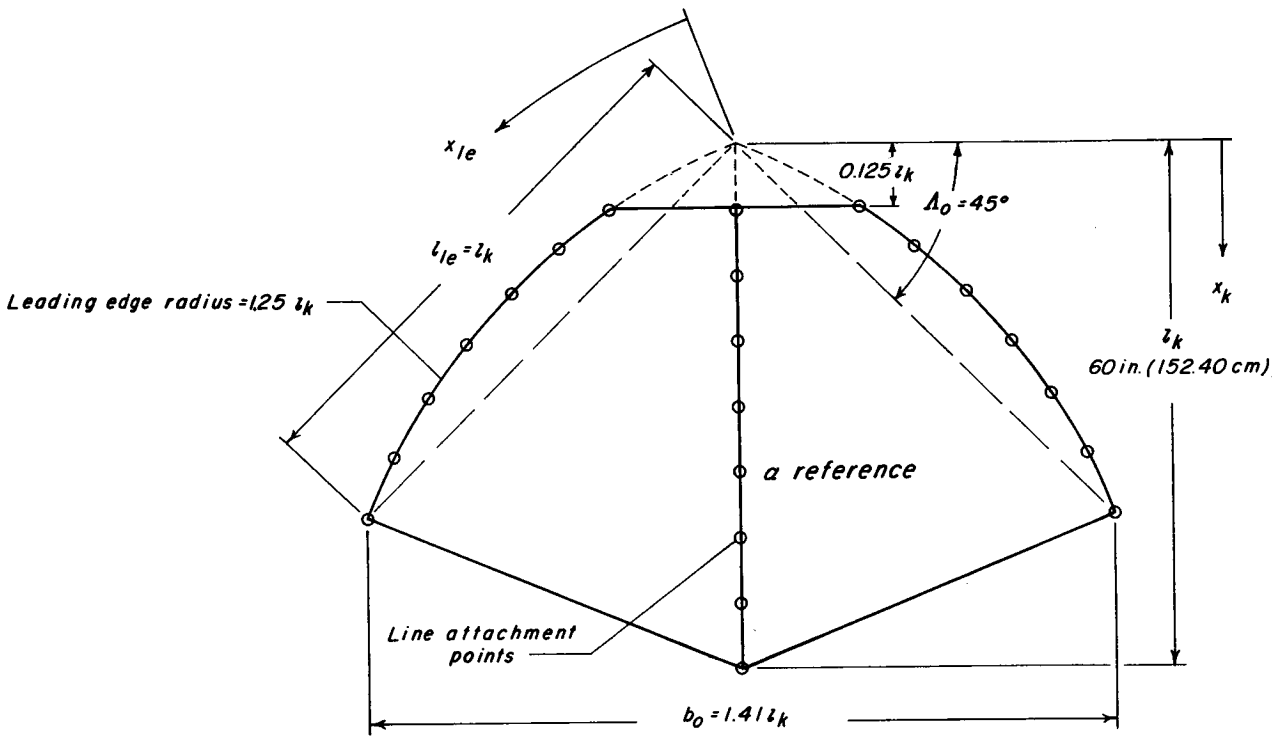

x/l_k	
Keel	Leading edge
.125	.259
.250	.389
.375	.518
.500	.647
.625	.776
.750	.905
.875	1.034
1.000	

Line attachment location

(a) Flat-pattern details.

Figure 51.- Model of a parawing with curved leading-edge planform, theoretical $\Lambda_0 = 45^0$, and $1/8\ l_k$ nose cut off.

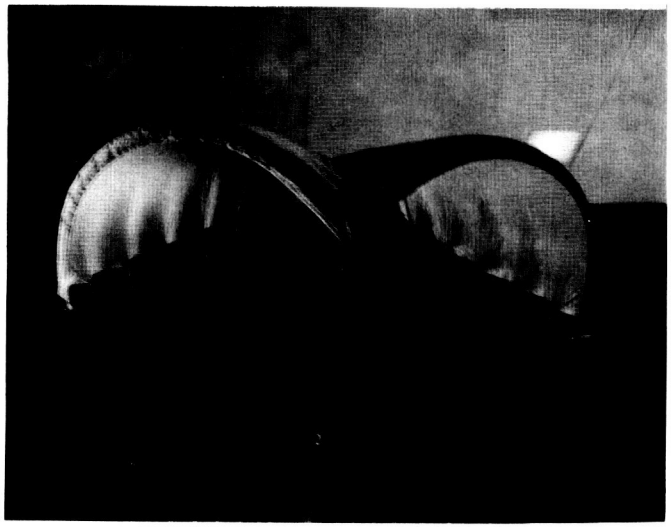

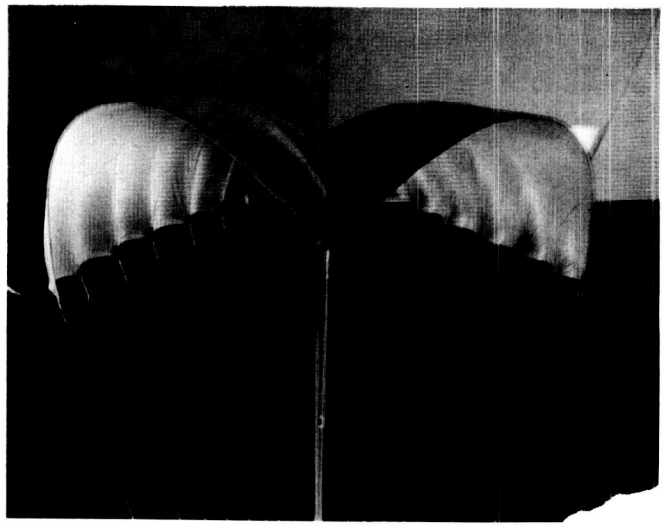

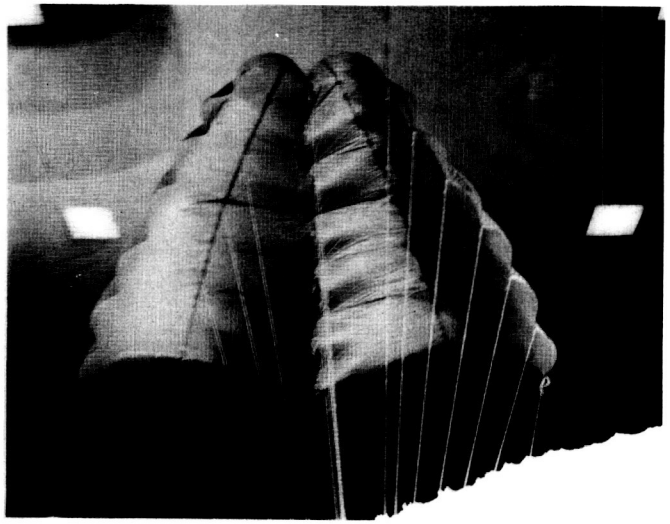

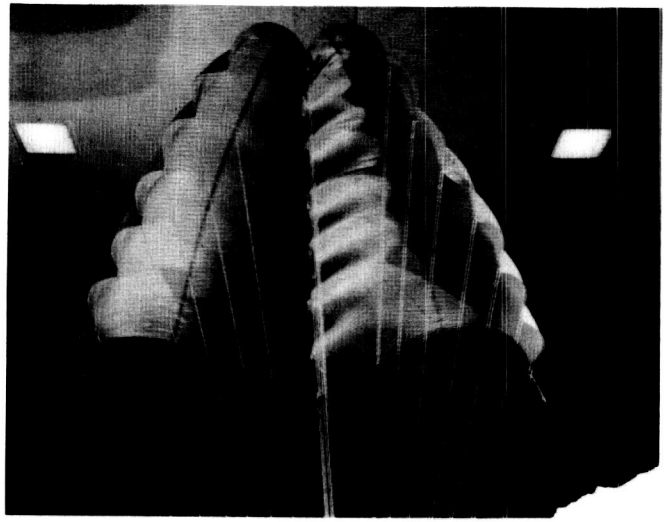

7.5-percent boltrope

0-percent boltrope

(b) Photographs of model.

L-67-945

Figure 51.- Concluded.

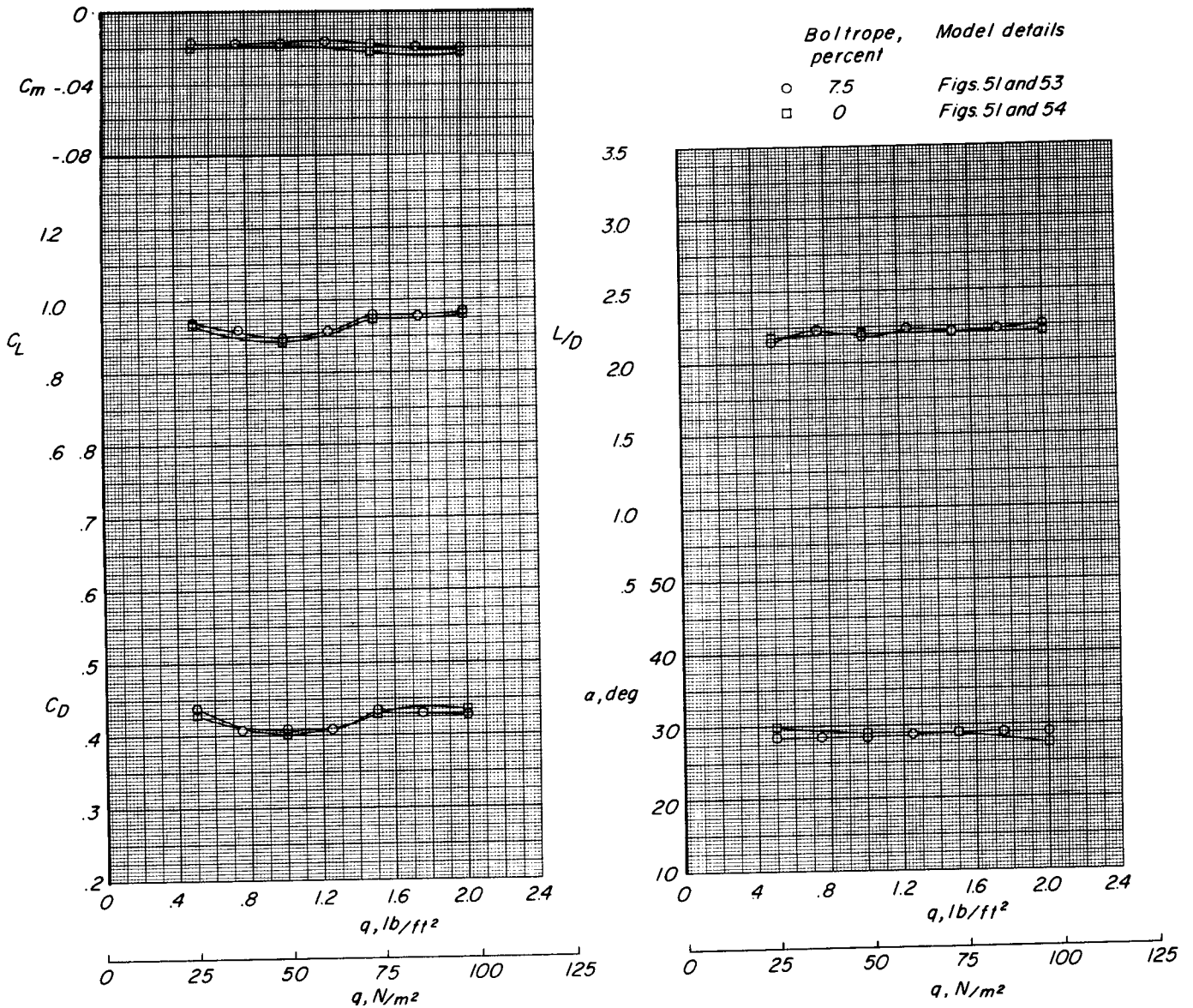

Figure 52.- Effect of boltrope on the variation of the longitudinal aerodynamic characteristics with dynamic pressure for a parawing with 1.25 l_k radius leading-edge planform, theoretical $\Lambda_0 = 45^0$, and 1/8 l_k nose cut off.

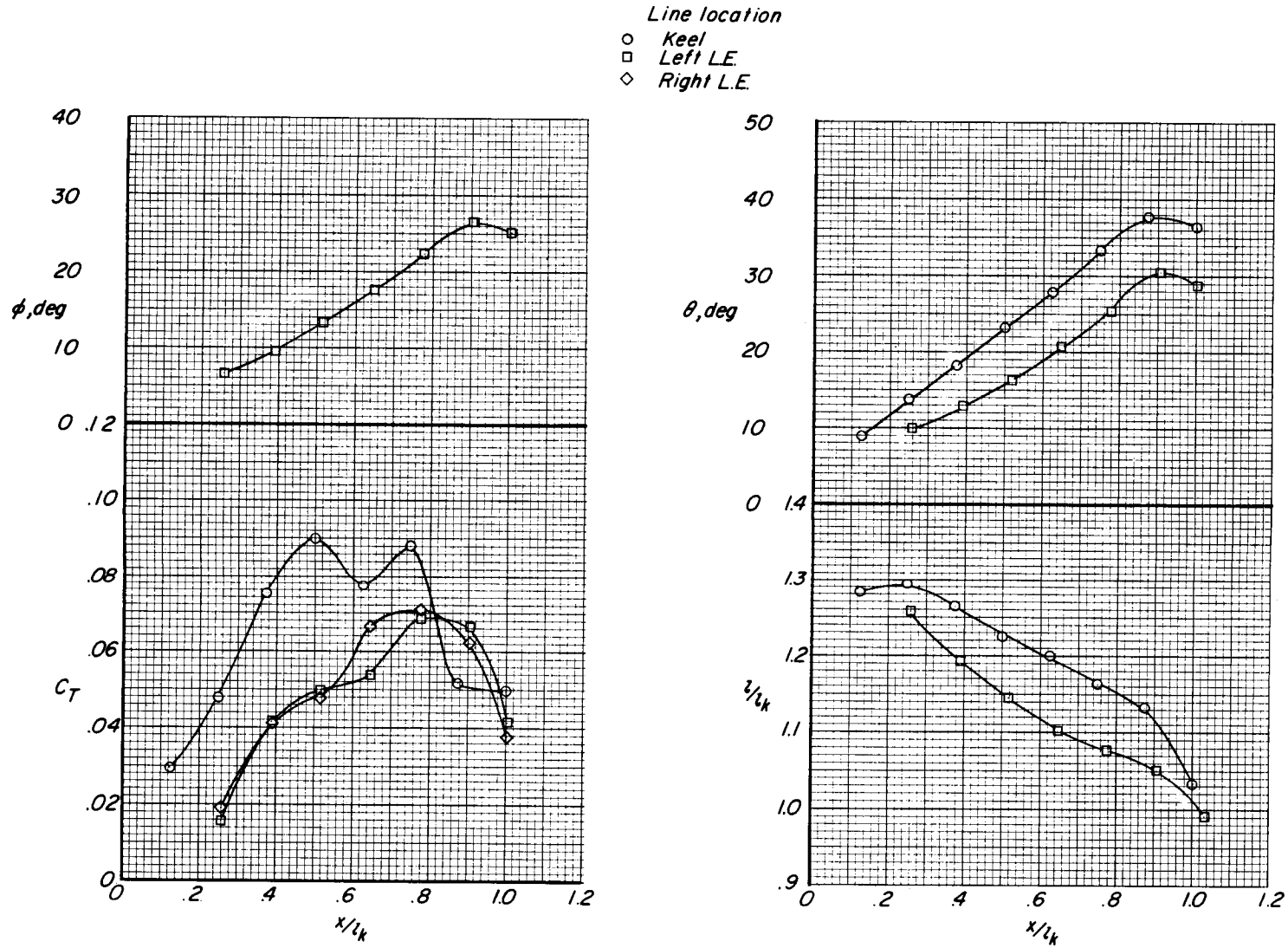

(a) q = 1.0.

Figure 53.- Tension coefficients, line angle, and line lengths for a parawing with 1.25 l_k radius leading-edge planform, theoretical $\Lambda_0 = 45^0$, 1/8 l_k nose cut off, and 7.5 percent boltrope.

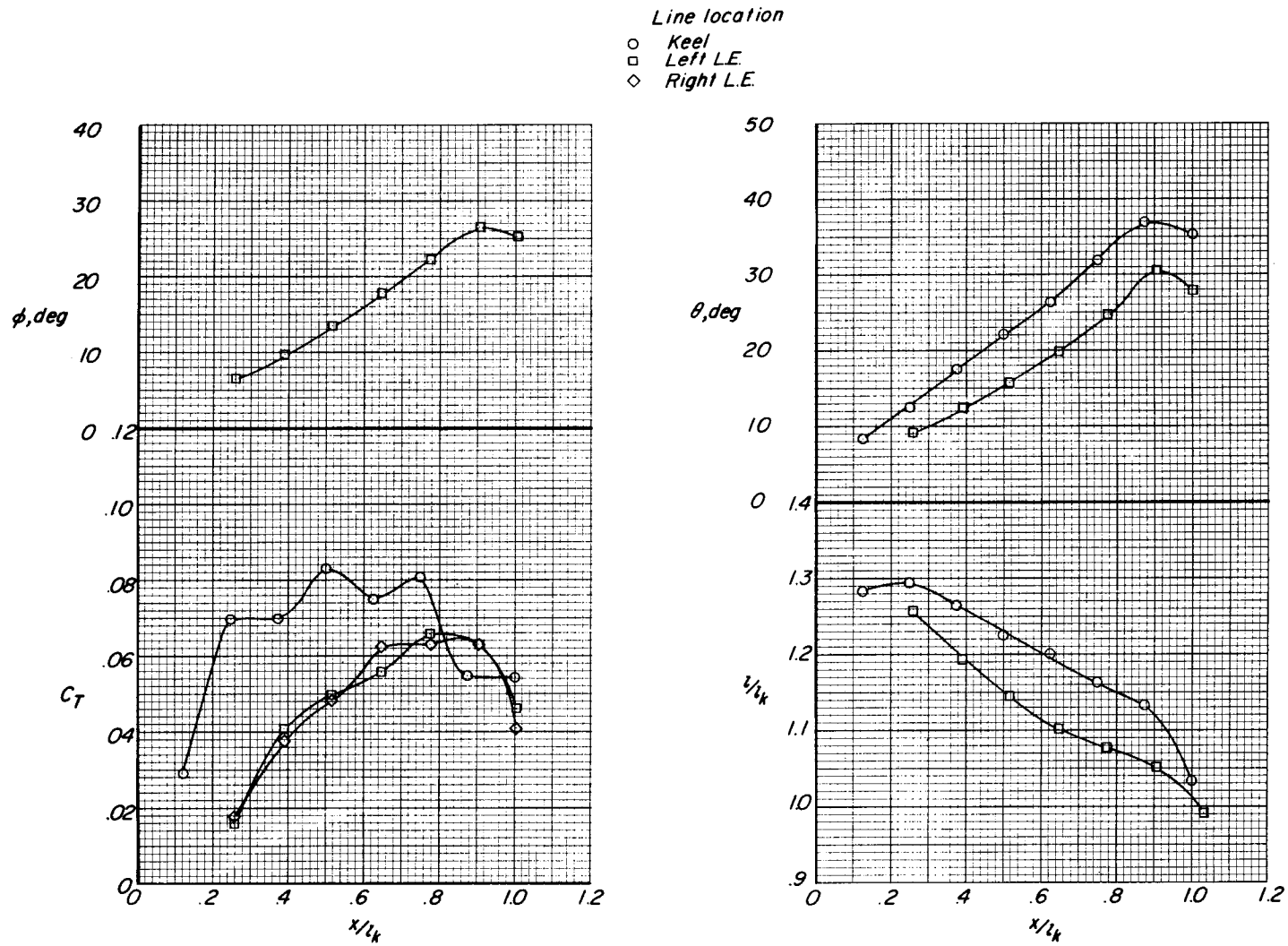

(b) q = 2.0.

Figure 53.- Concluded.

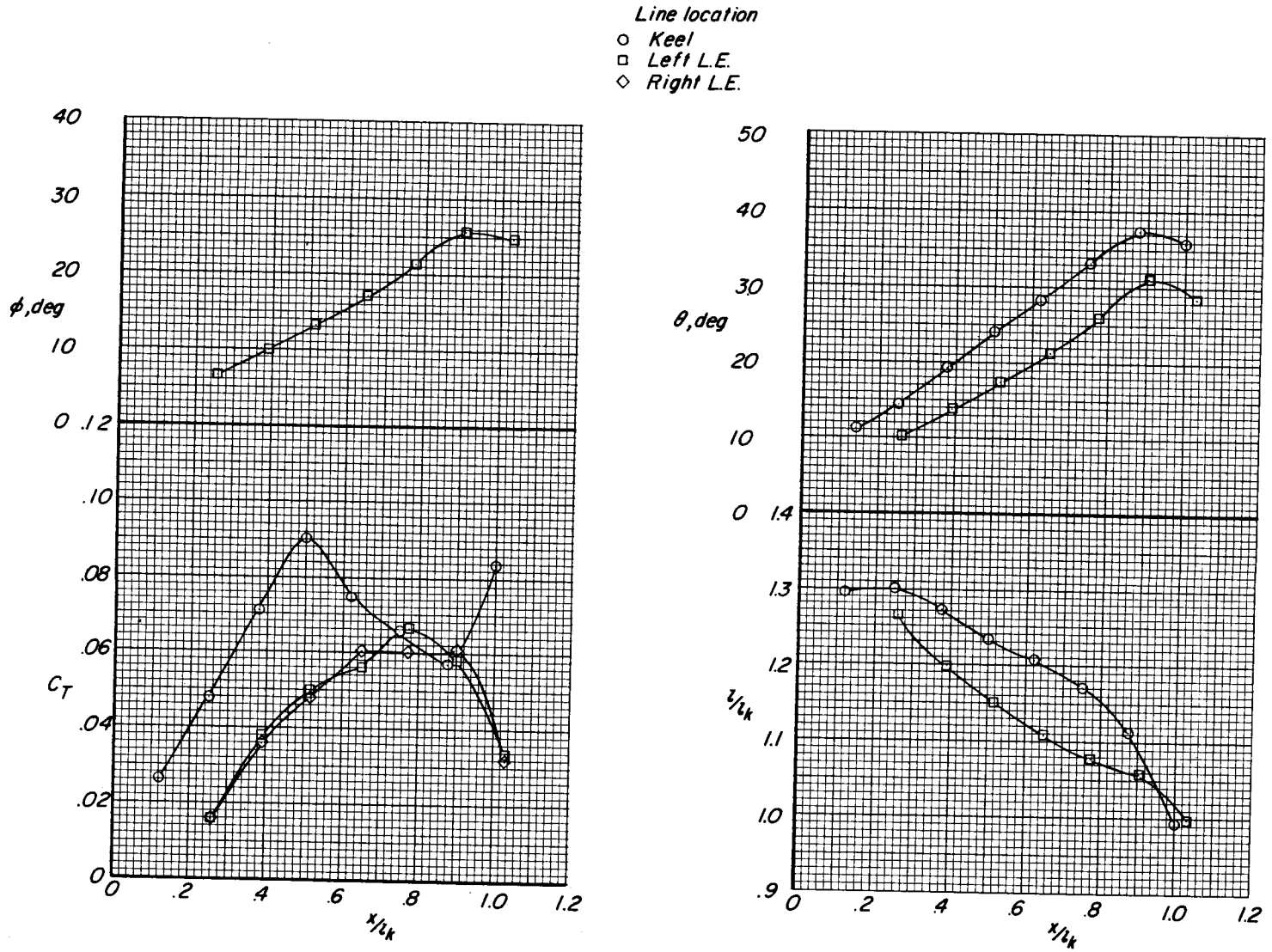

(a) q = 1.0.

Figure 54.- Tension coefficients, line angles, and line lengths for a parawing with 1.25 l_k radius leading-edge planform, theoretical $\Lambda_0 = 45^0$, 1/8 l_k nose cut off, and zero boltrope.

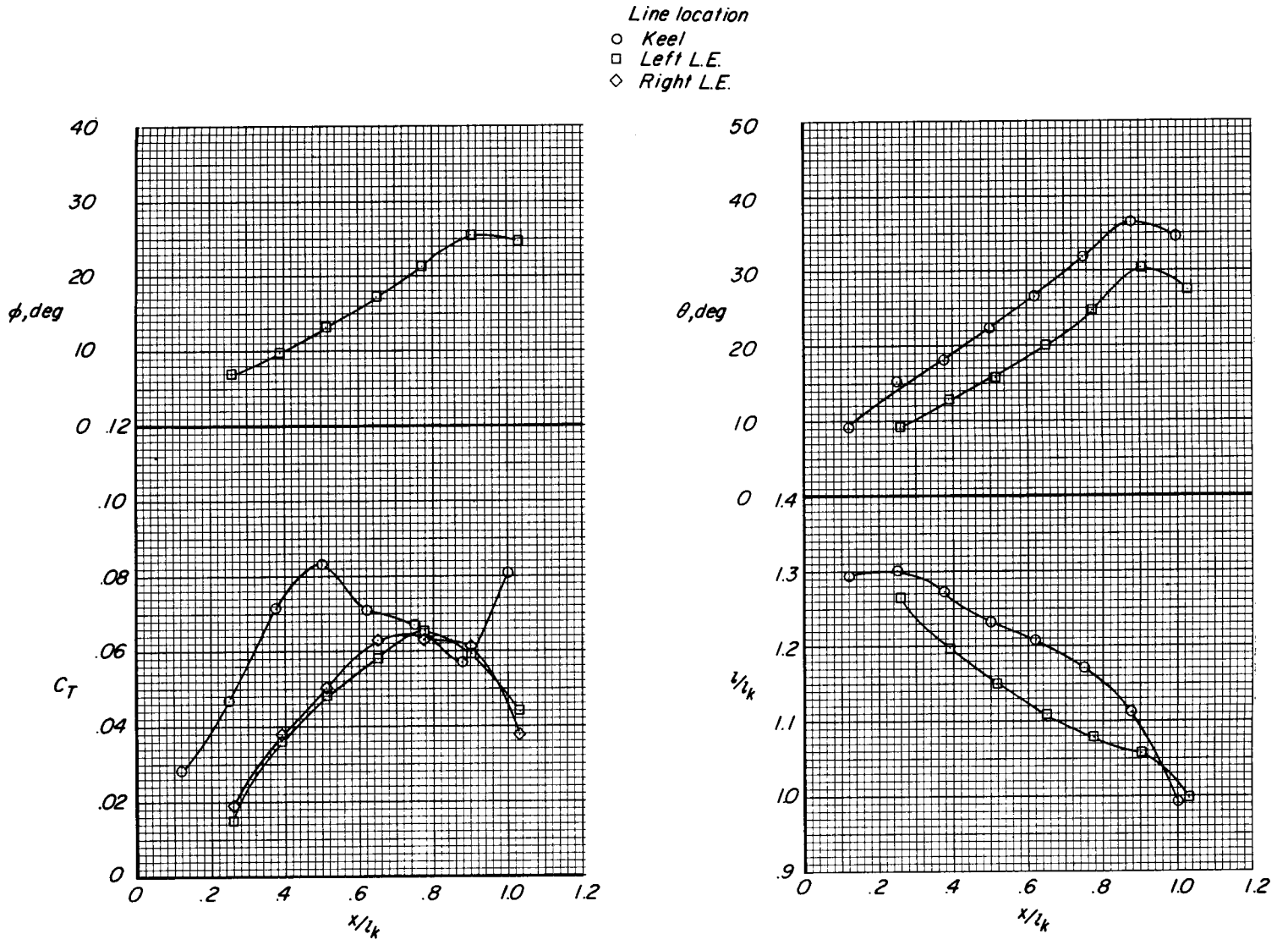

(b) q = 2.0.

Figure 54.- Concluded.

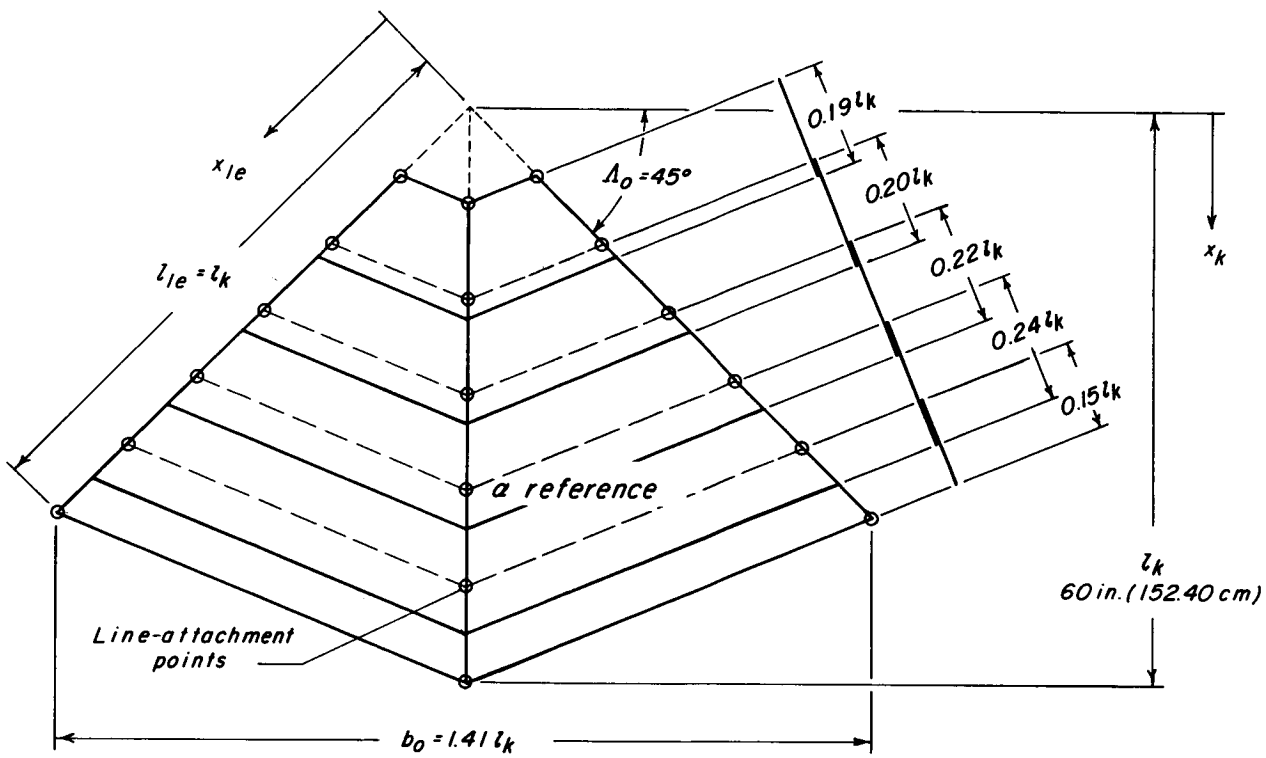

x/l_k	
Keel	Leading edge
0	0
.167	.167
.333	.333
.500	.500
.667	.667
.833	.833
1.000	1.000

Line-attachment location

(a) Flat-planform details.

Figure 55.- Model of a slotted parawing with $\Lambda_o = 45^0$ and 1/6 l_k nose cut off.

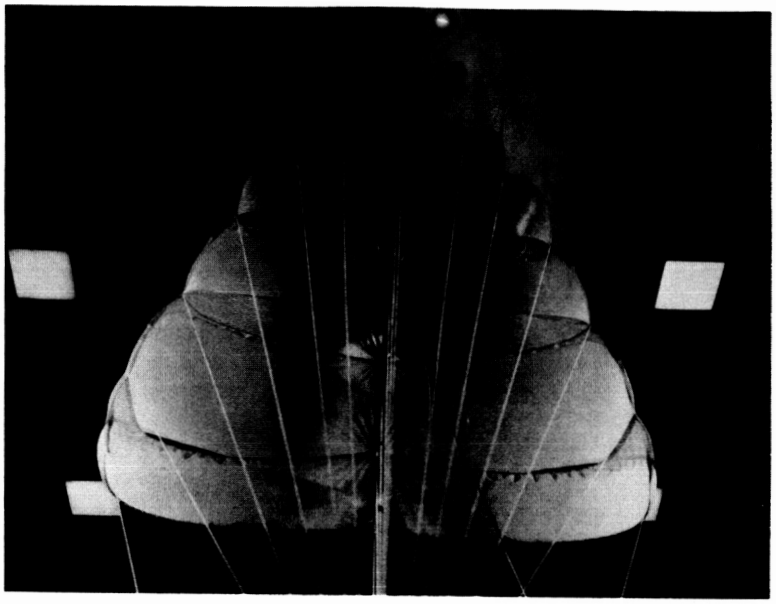

Lower plan view

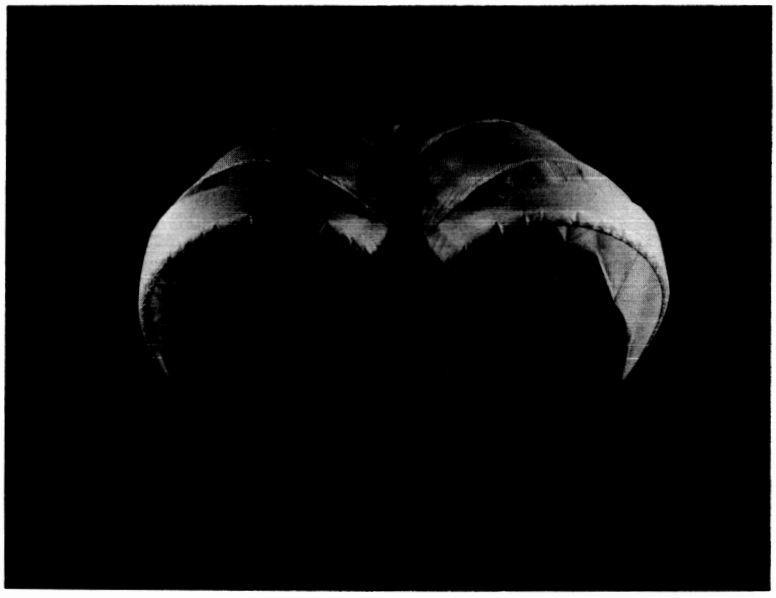

Rear view

(b) Photographs of the model. L-67-946

Figure 55.- Concluded.

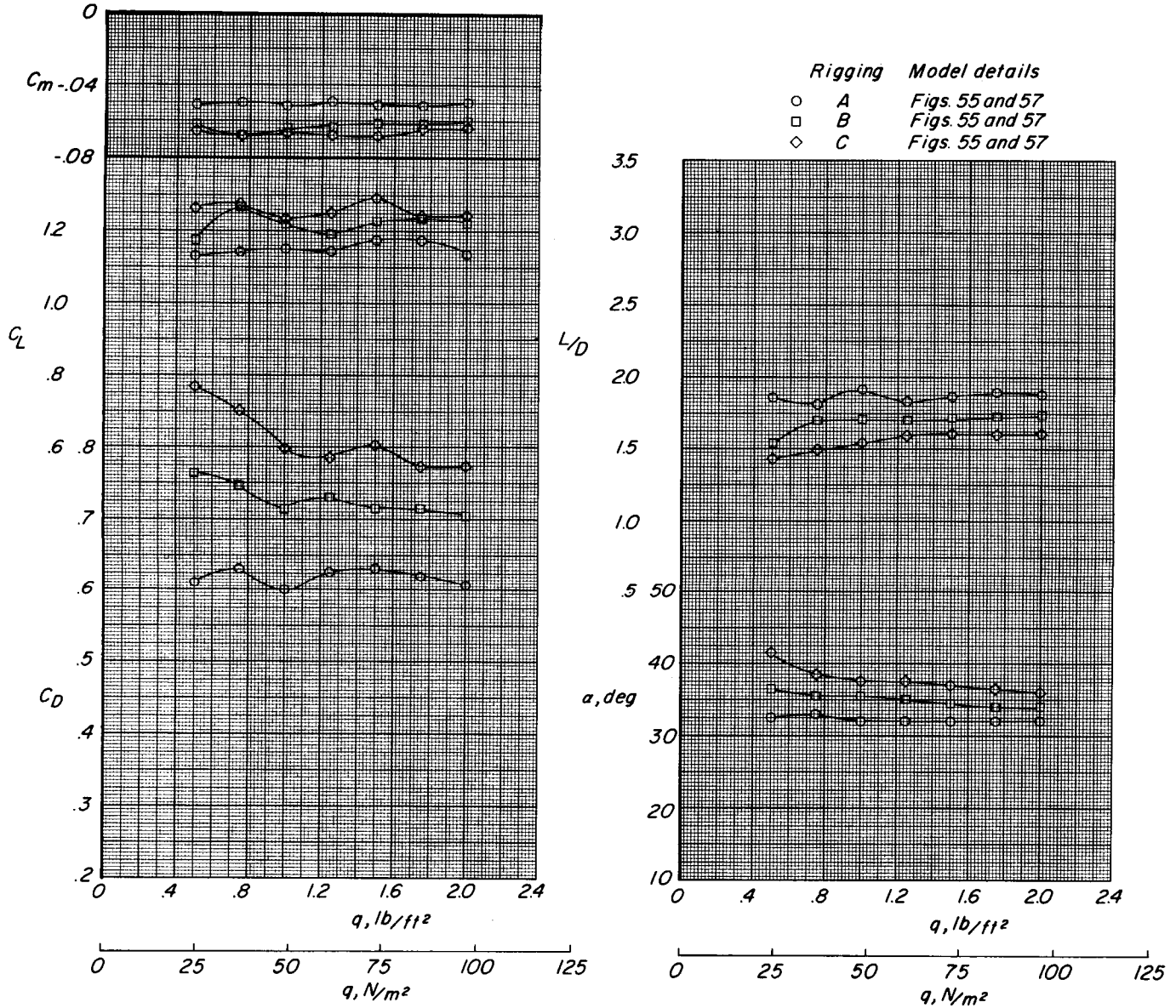

Figure 56.- Effect of changes in rigging on the variation of the wing longitudinal aerodynamic characteristics with dynamic pressure for a slotted parawing with $\Lambda_0 = 45^0$ and 1/6 l_k nose cut off.

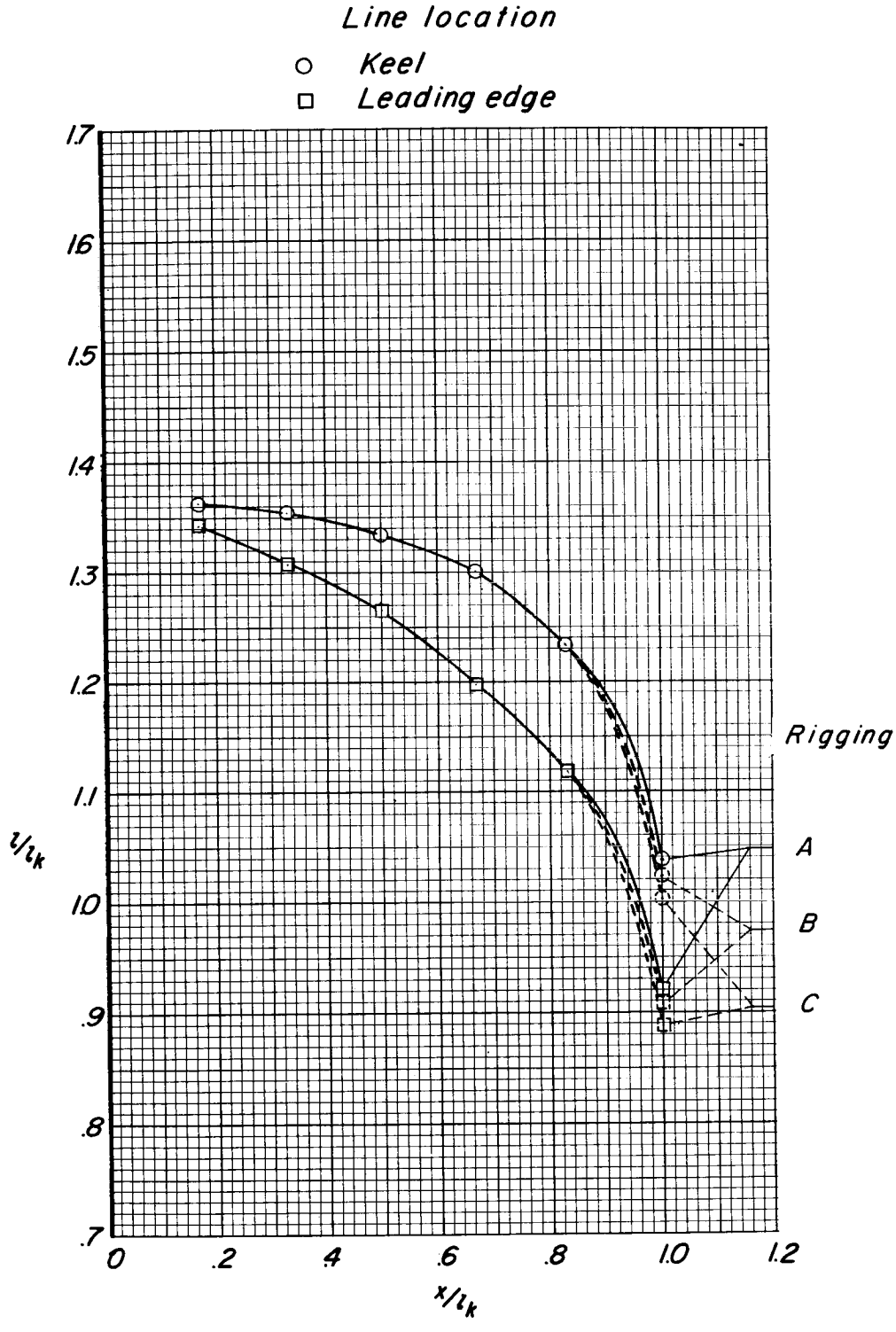

Figure 57.- Line lengths of a slotted parawing with $\Lambda_0 = 45^0$ and 1/6 l_k nose cut off.

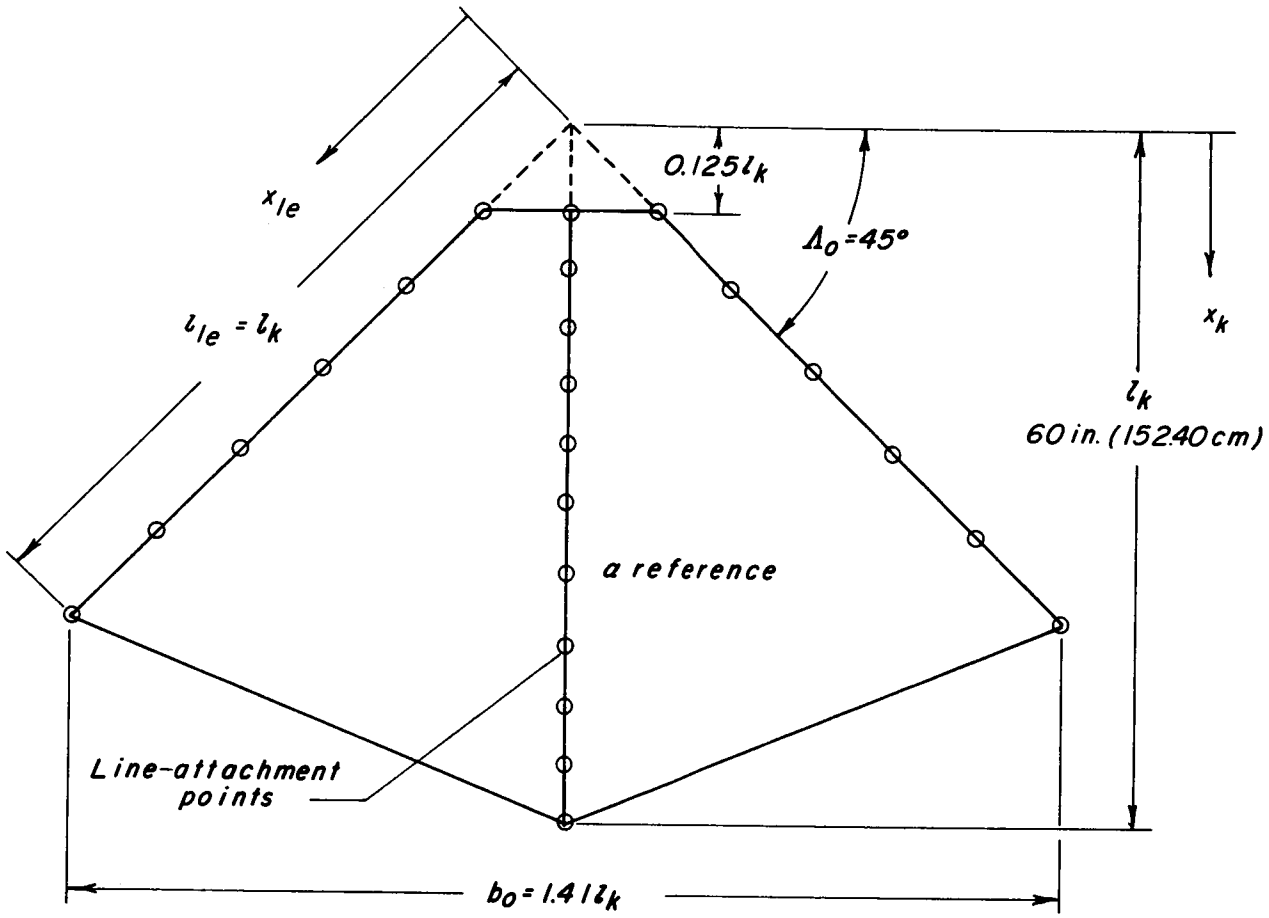

x/l_k	
Keel	Leading edge
.125	.177
.208	.333
.292	.500
.375	.667
.459	.833
.542	1.000
.645	
.750	
.833	
.917	
1.000	

Line-attachment location

Figure 58.- Details of the flat pattern of a parawing with $\Lambda_o = 45^o$ and 1/8 l_k nose cut off.

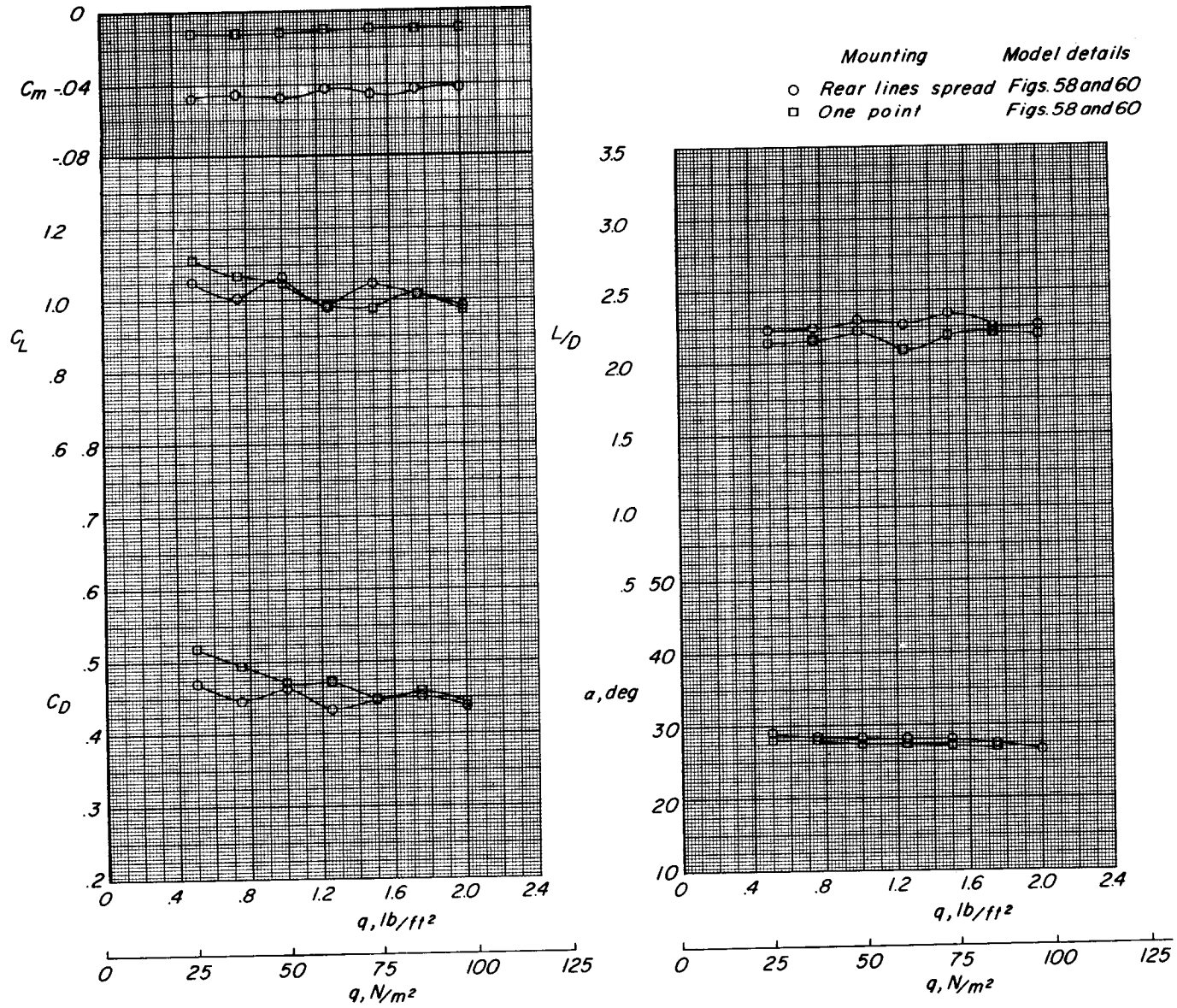

Figure 59.- Effect of moving control lines away from confluence point of lines on the variation of longitudinal aerodynamic characteristics with dynamic pressure for a parawing with $\Lambda_0 = 45^0$ and 1/8 l_k nose cut off.

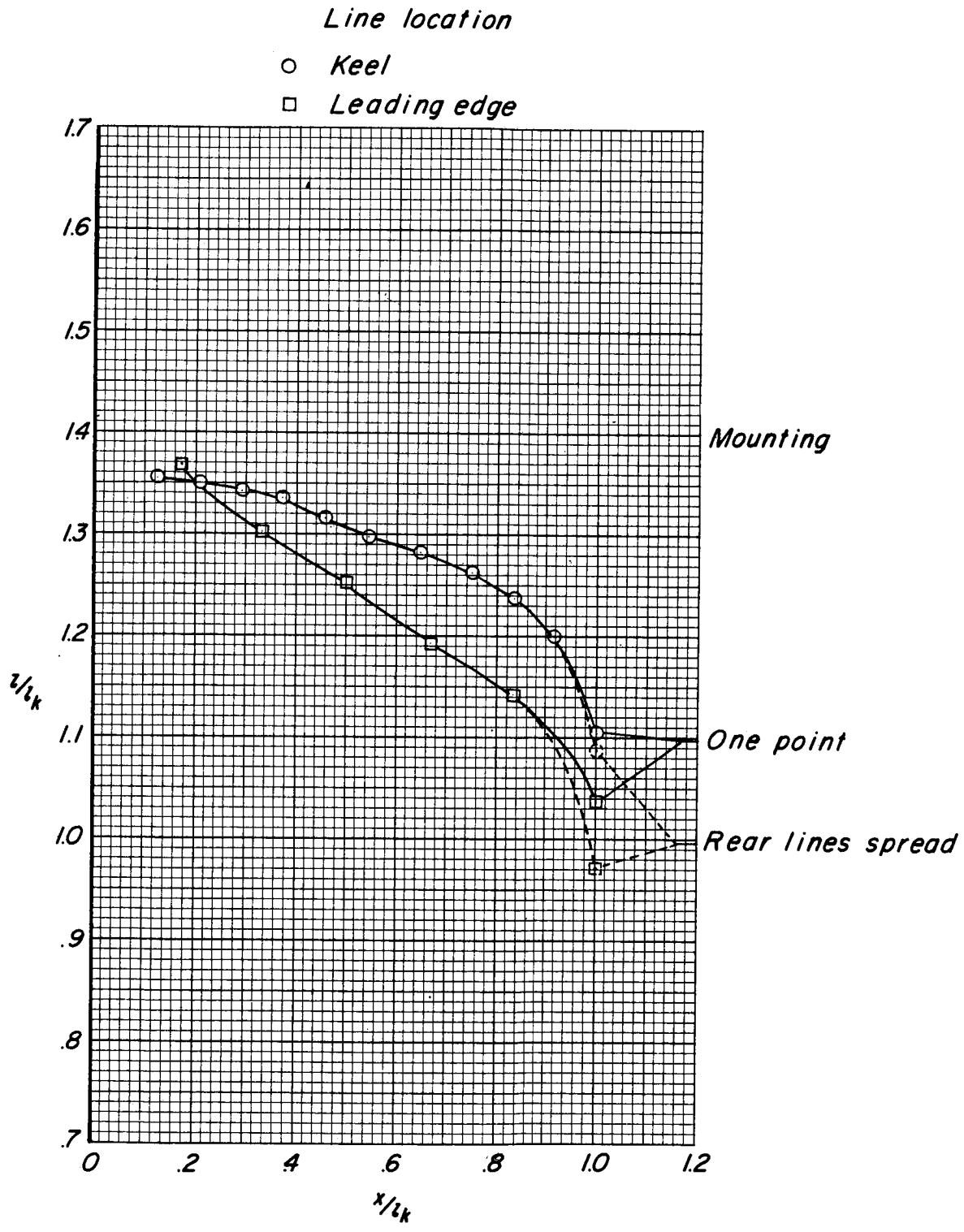

Figure 60.- Line lengths for a parawing with $\Lambda_0 = 45^0$ and 1/8 l_k nose cut off.

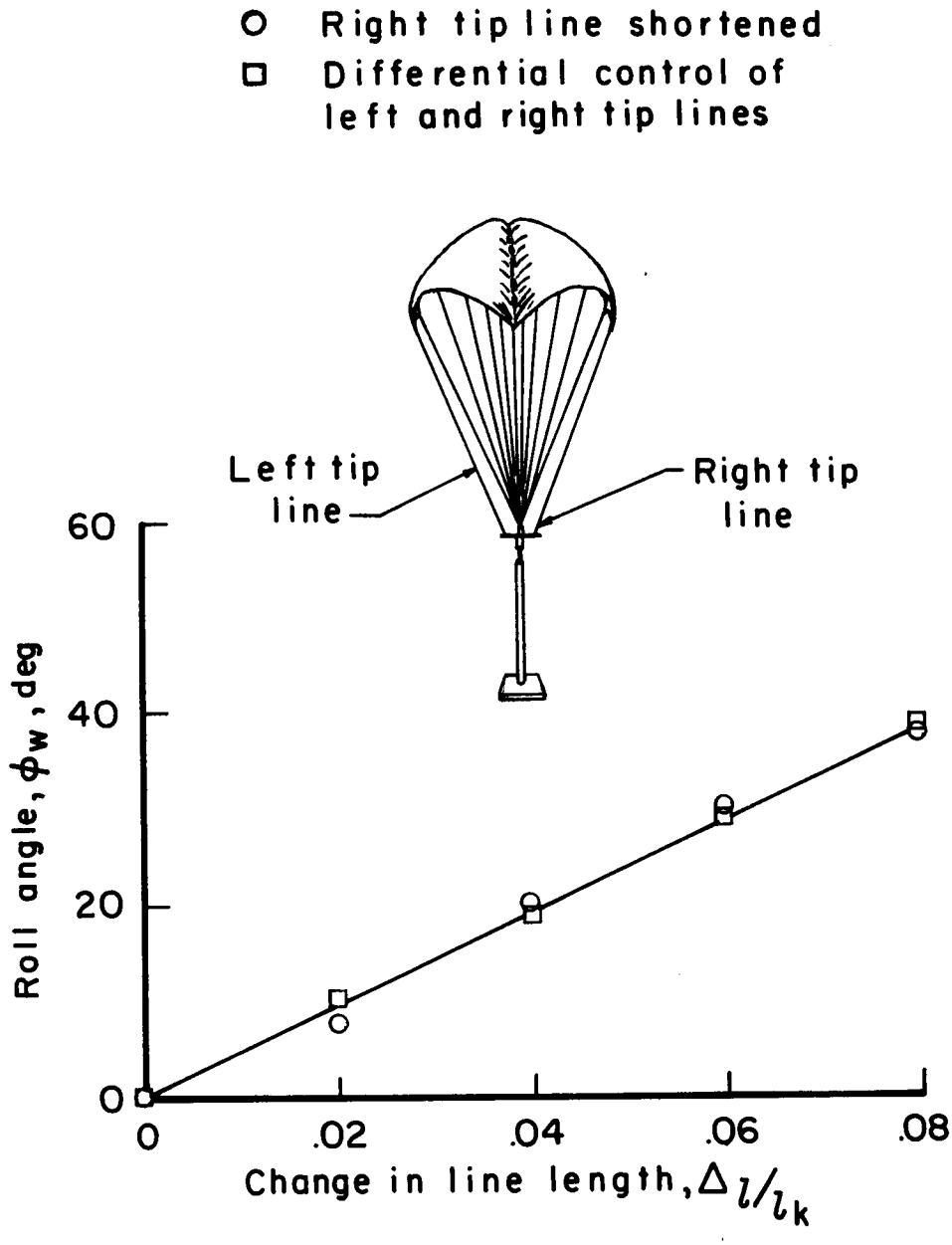

Figure 61.- Roll control by changing the length of the tip lines on a parawing with $\Lambda_0 = 45^0$ and 1/8 l_k nose cut off.

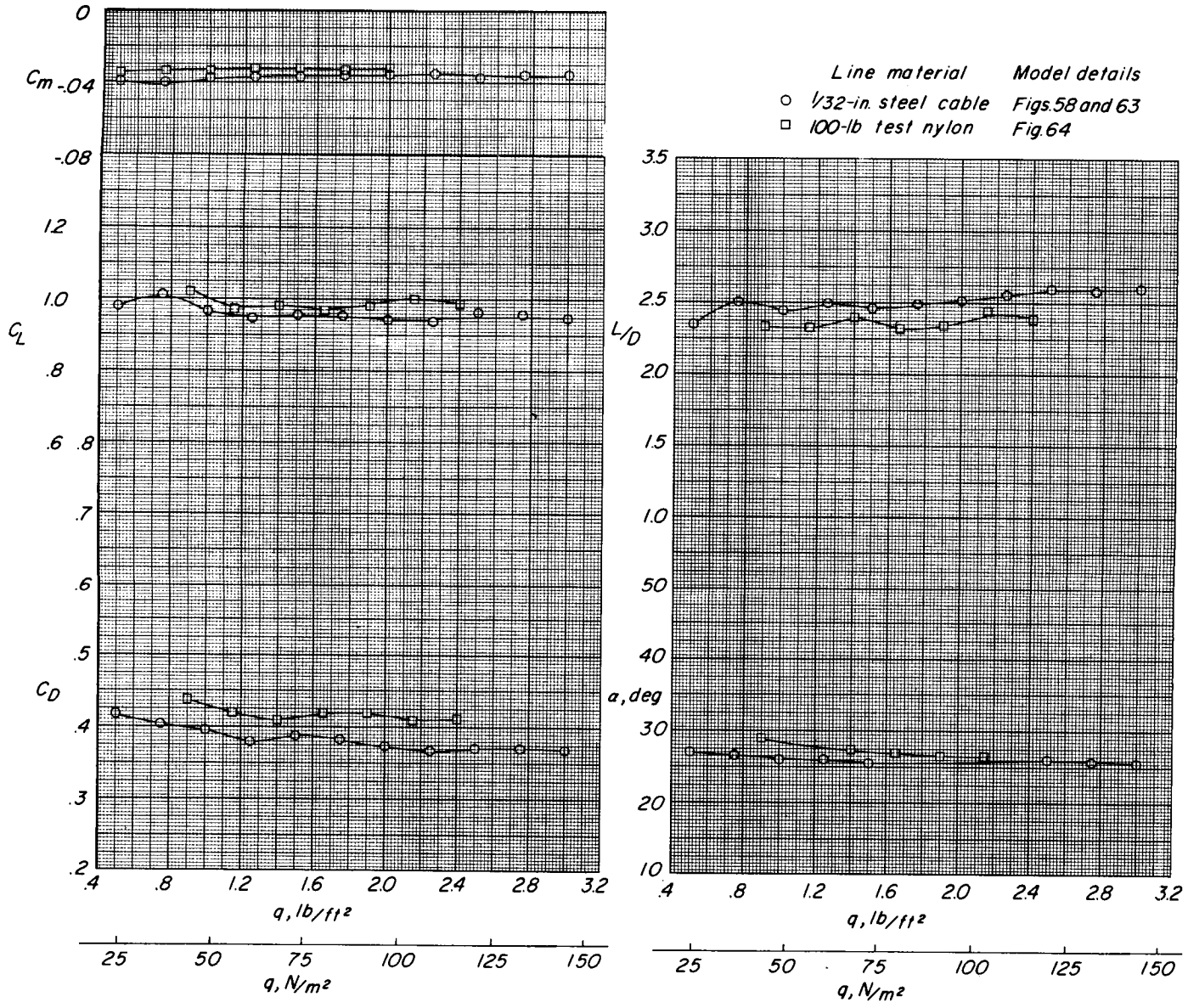

Figure 62.- Effect of line material on the variation of the longitudinal aerodynamic characteristics with dynamic pressure for a parawing with $\Lambda_0 = 45^0$ and 1/8 l_k nose cut off.

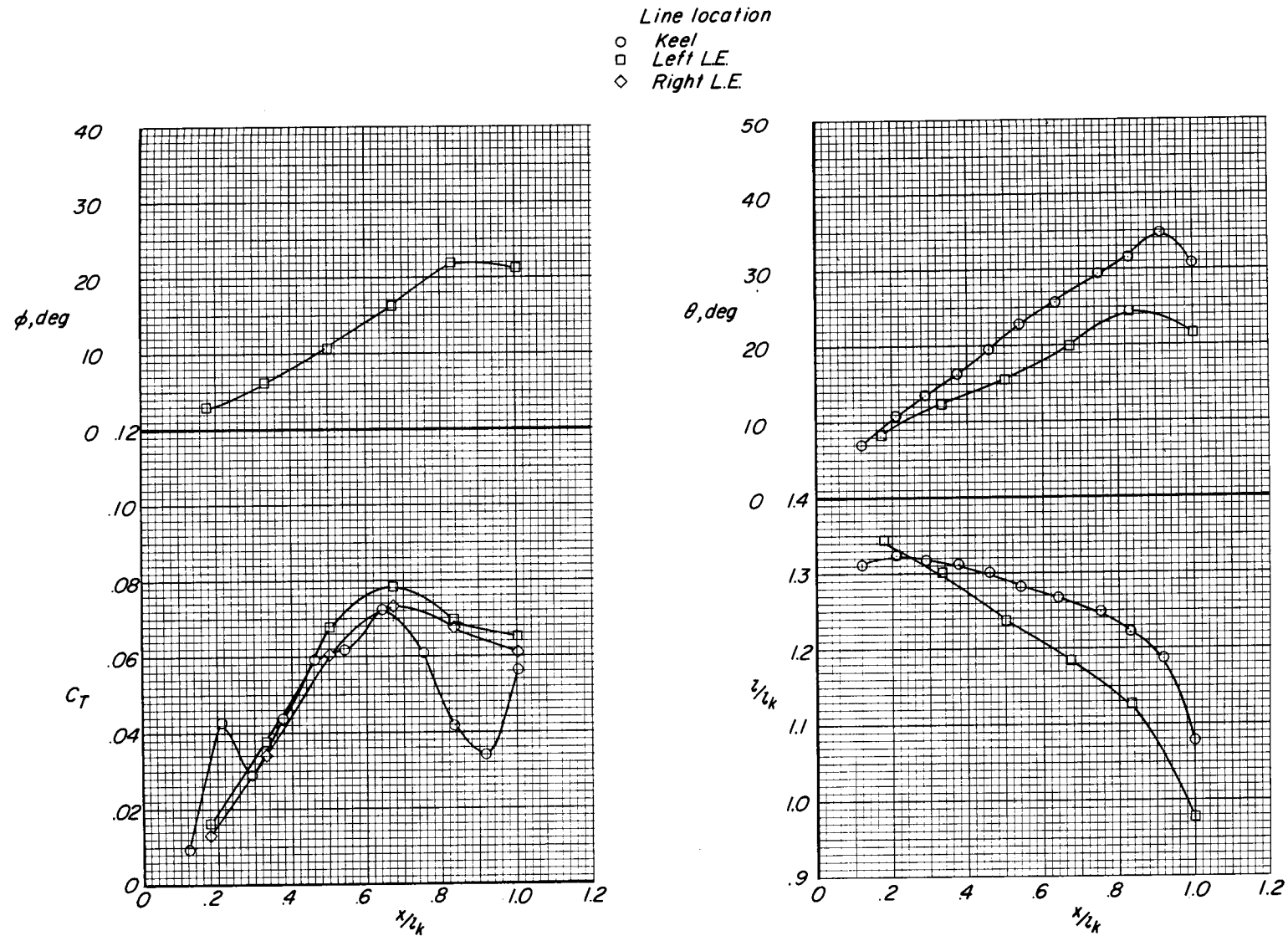

(a) q = 1.0.

Figure 63.- Tension coefficients, line angles, and line lengths for a parawing with $\Lambda_0 = 45^0$ and 1/8 l_k nose cut off. Steel lines.

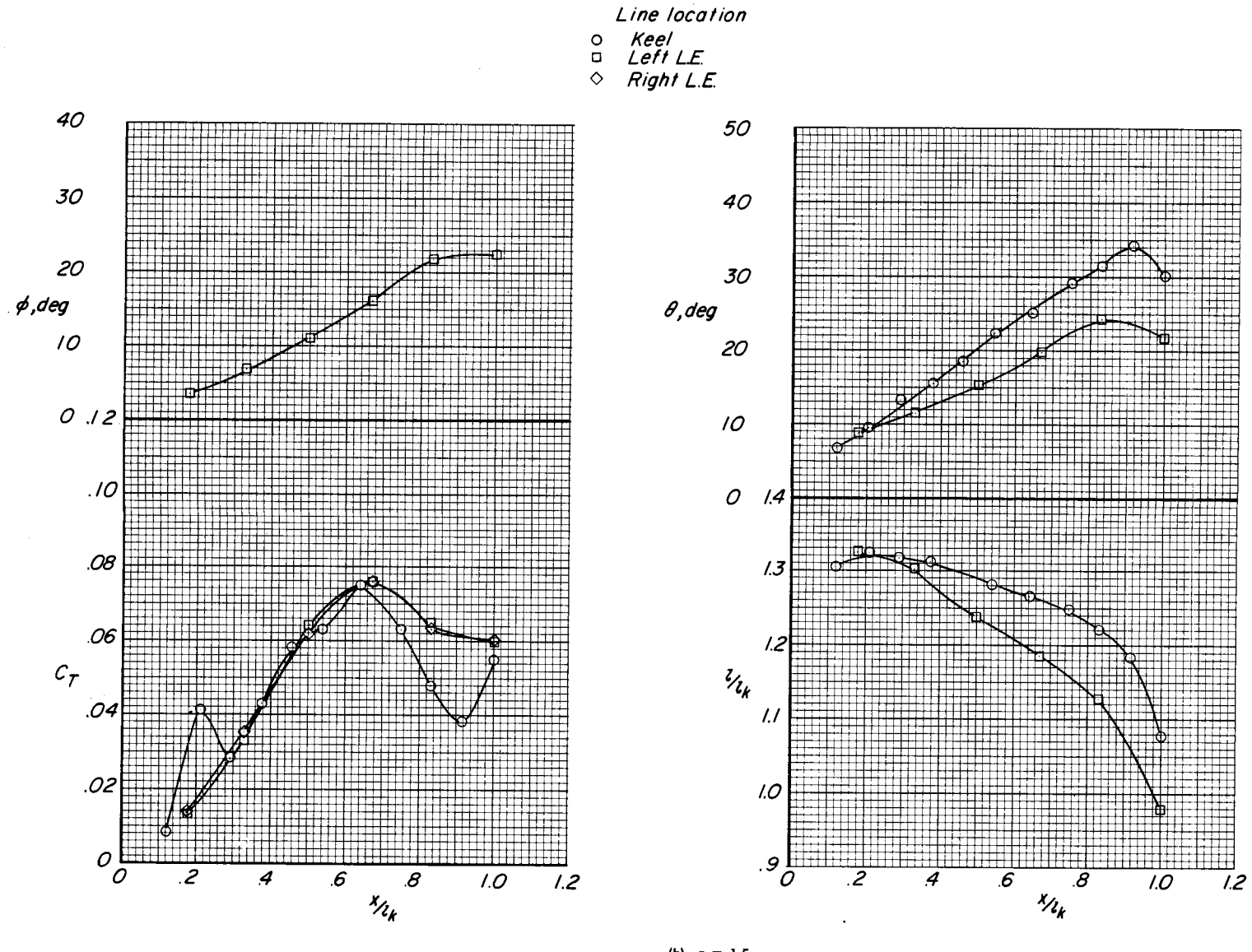

(b) q = 1.5.

Figure 63.- Concluded.

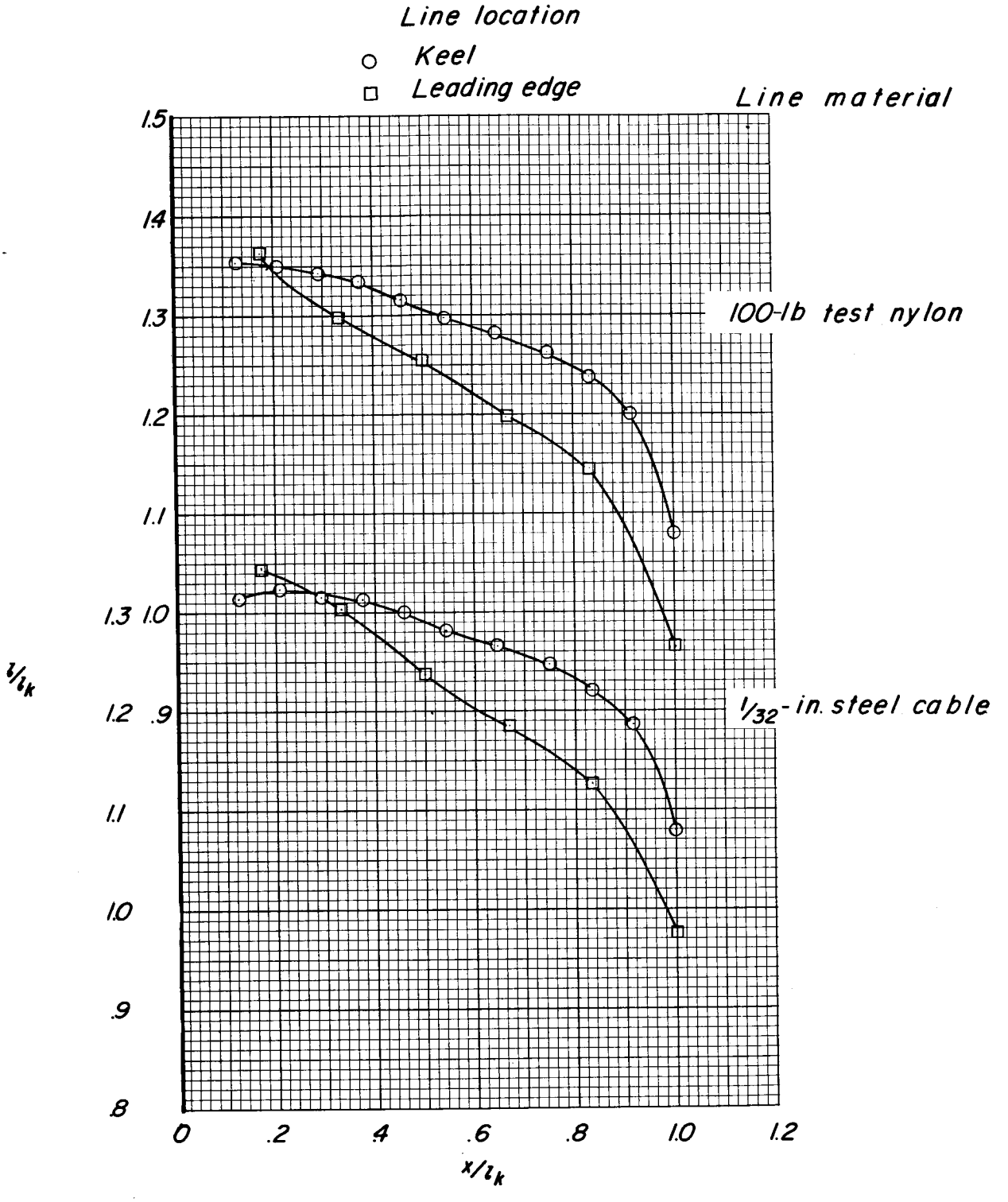

Figure 64.- Line lengths of a parawing with $\Lambda_0 = 45^0$ and 1/8 l_k nose cut off.

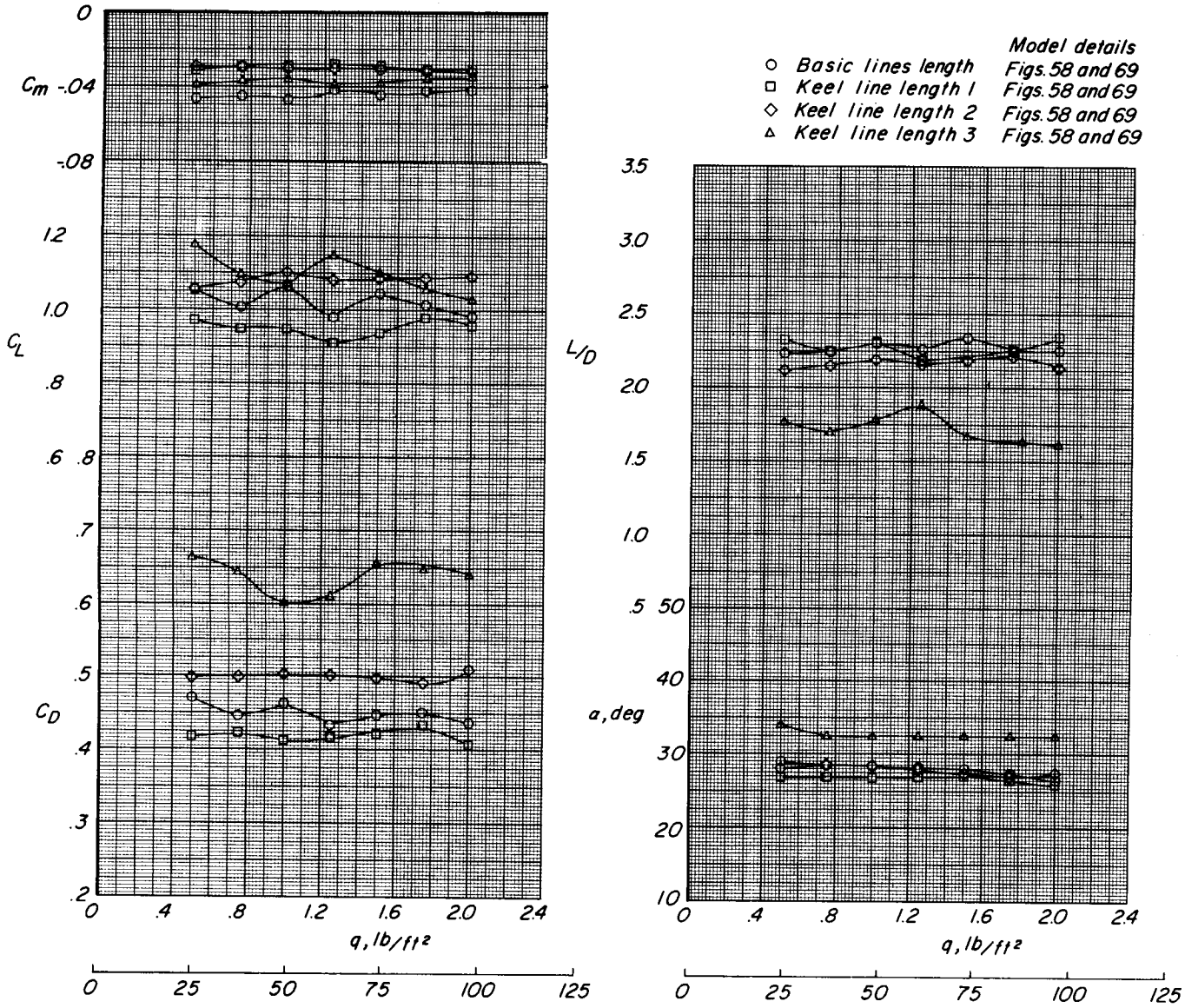

Figure 65.- Effect of keel-line shortening on the variation of the longitudinal aerodynamic characteristics with dynamic pressure for a parawing with $\Lambda_0 = 45^0$ and 1/8 ℓ_k nose cut off.

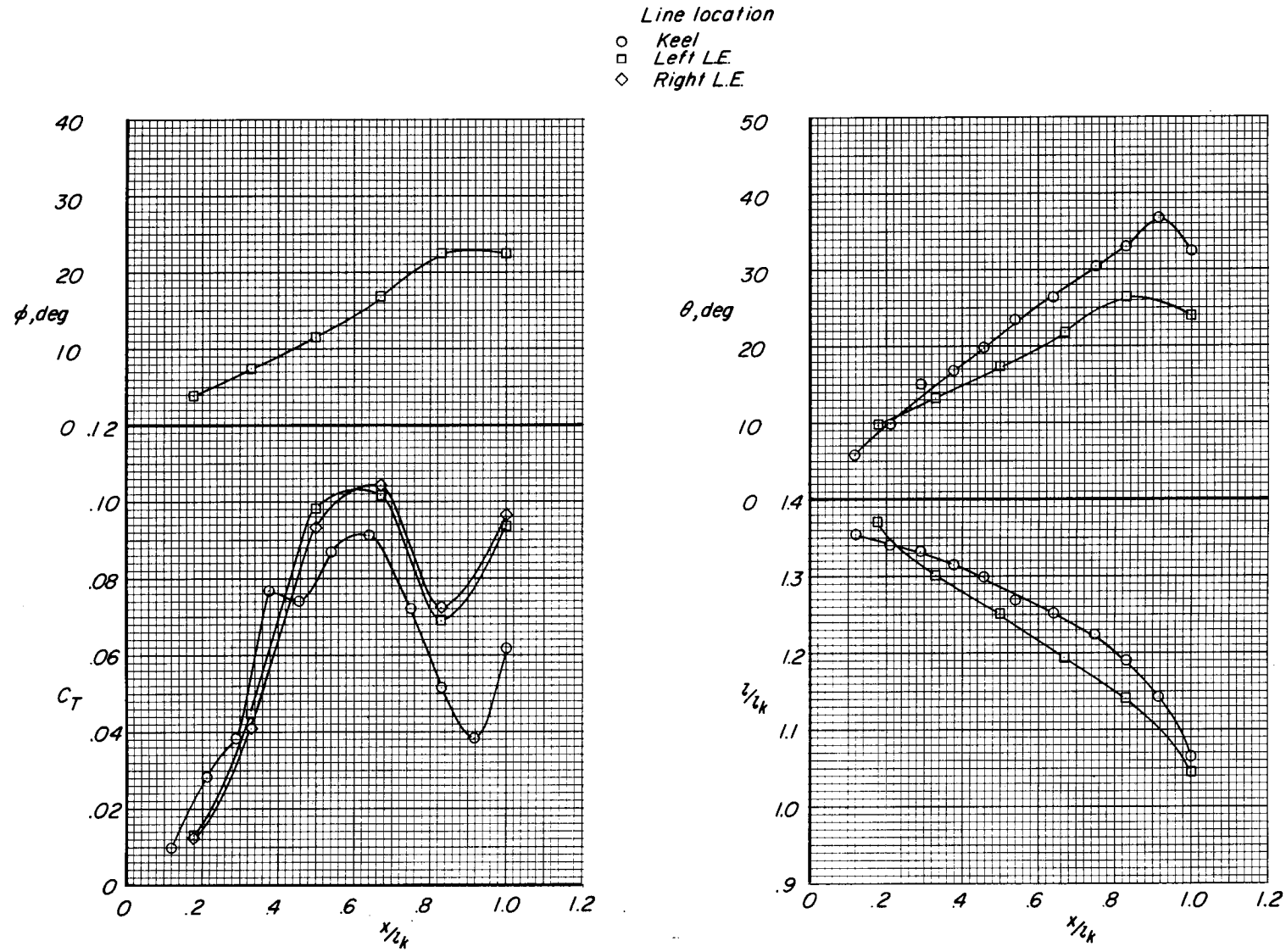

(a) q = 1.0.

Figure 66.- Tension coefficients, line angles, and line lengths for a parawing with $\Lambda_0 = 45^0$ and 1/8 l_K nose cut off. Keel-line length 1.

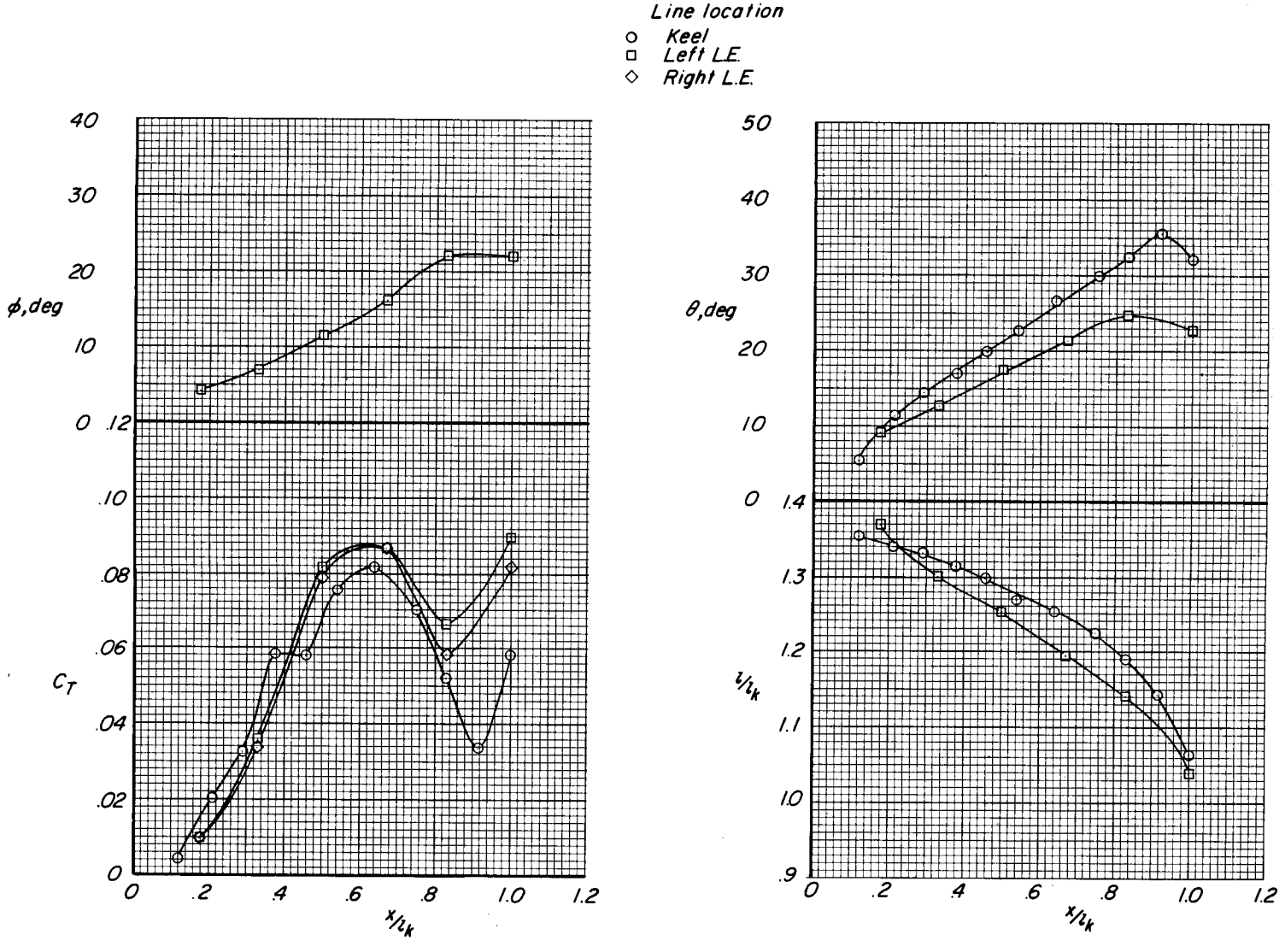

(b) q = 2.0.

Figure 66.- Concluded.

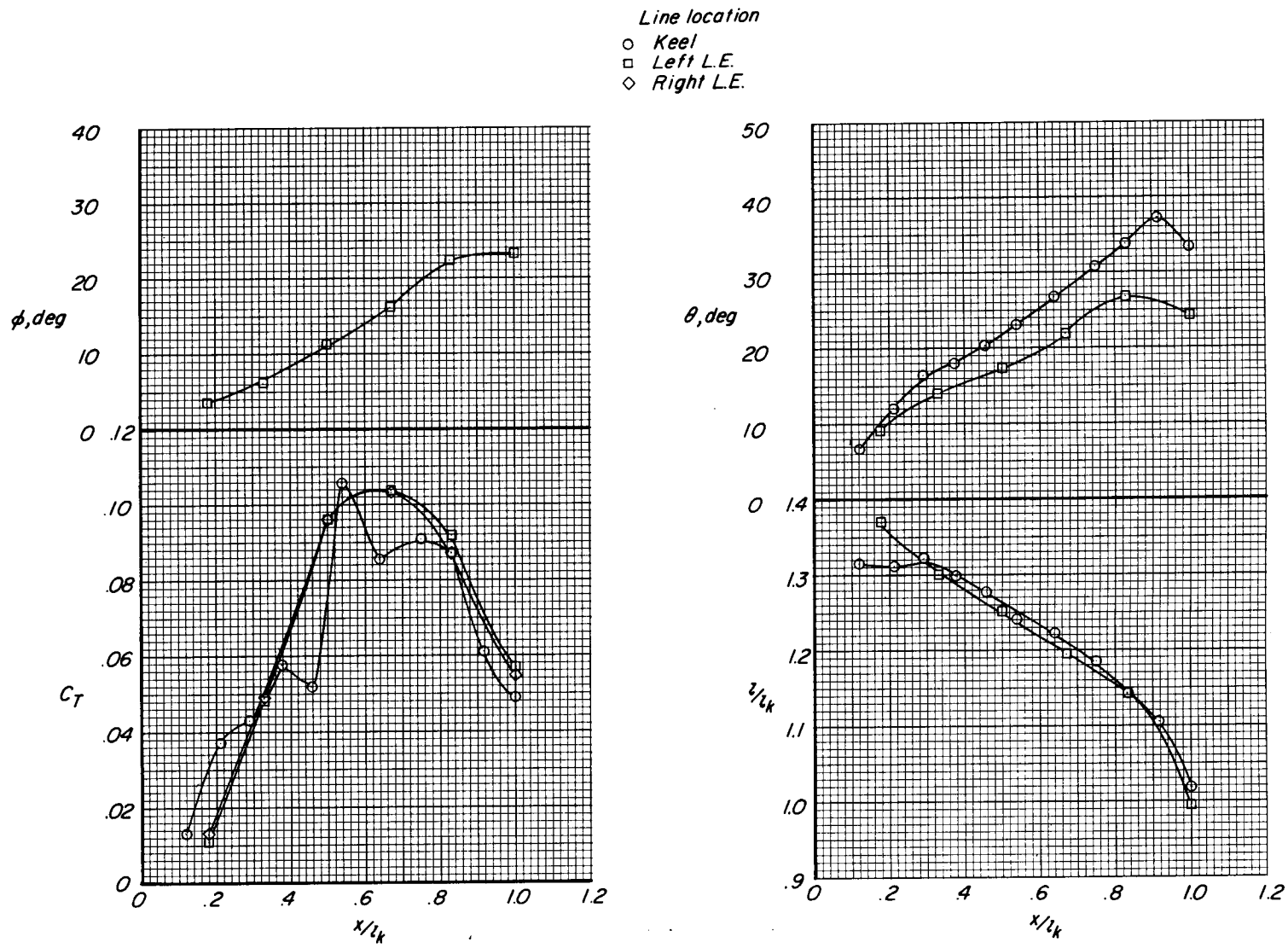

(a) q = 1.0.

Figure 67.- Tension coefficients, line angles, and line lengths for a parawing with $\Lambda_0 = 45^0$ and 1/8 l_k nose cut off. Keel-line length 2.

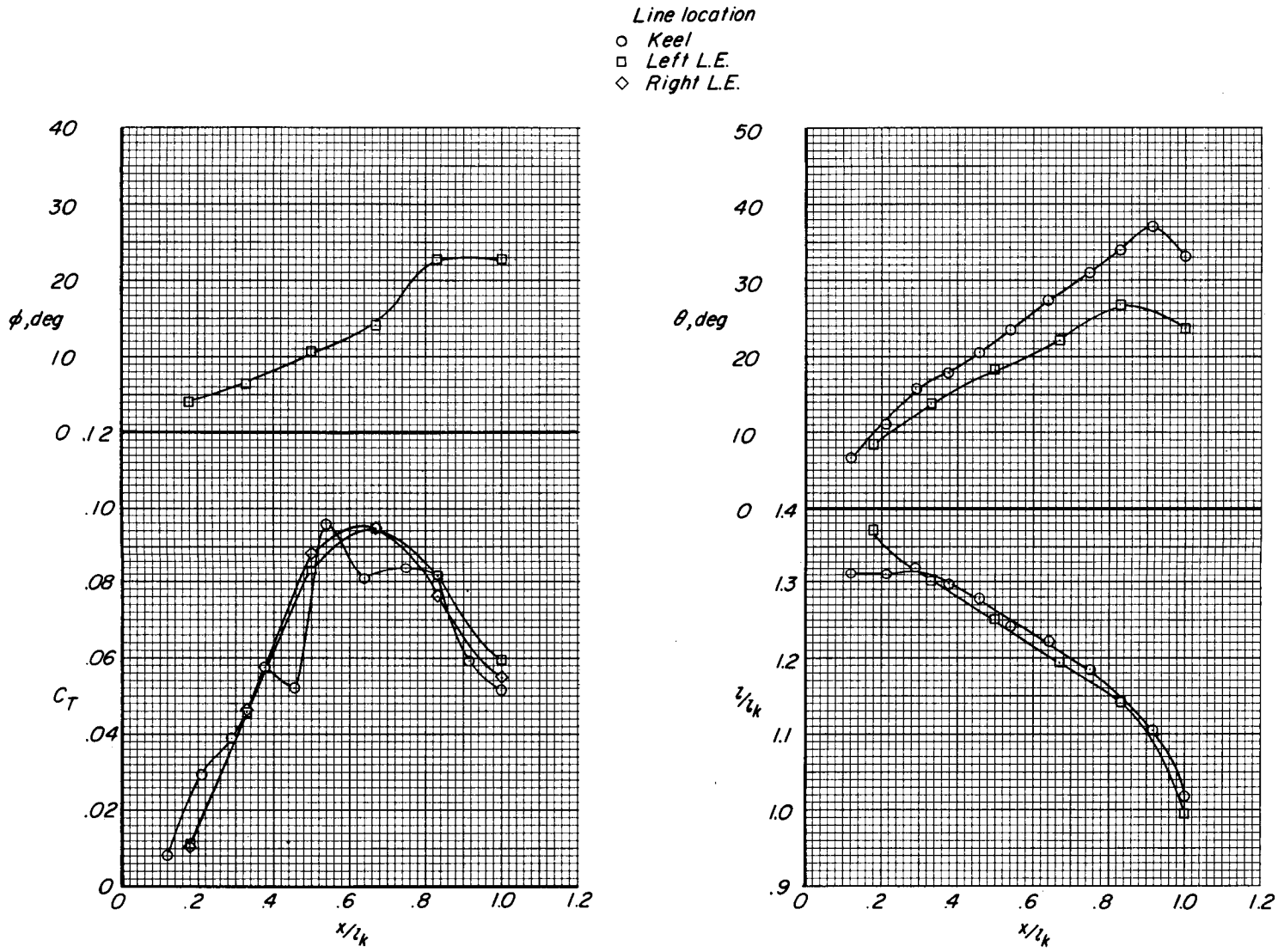

(b) q = 2.0.

Figure 67.- Concluded.

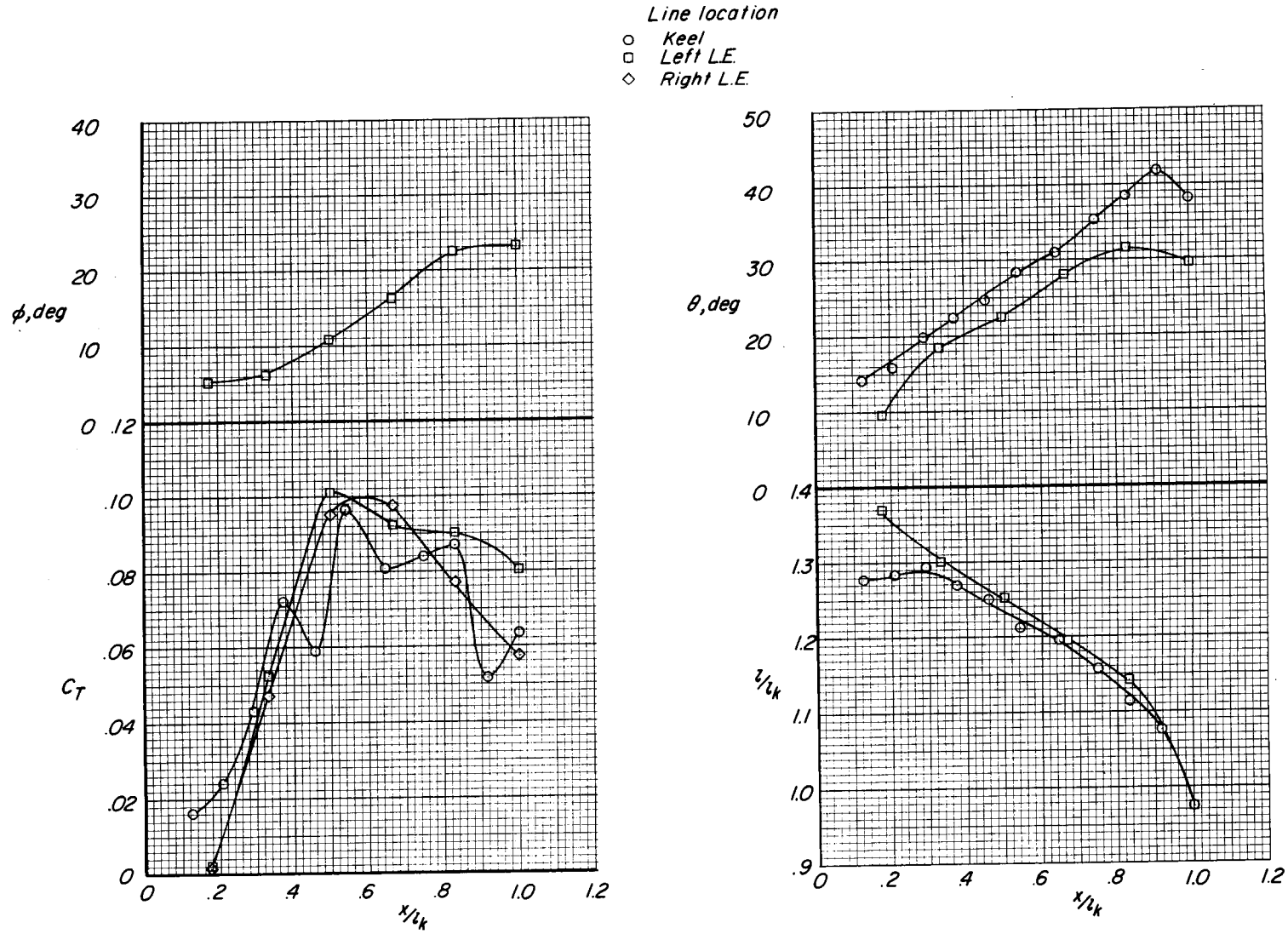

Figure 68.- Tension coefficients, line angles, and line lengths for a parawing with $\Lambda_0 = 45^0$ and 1/8 l_k nose cut off. Keel-line length 3; q = 2.0.

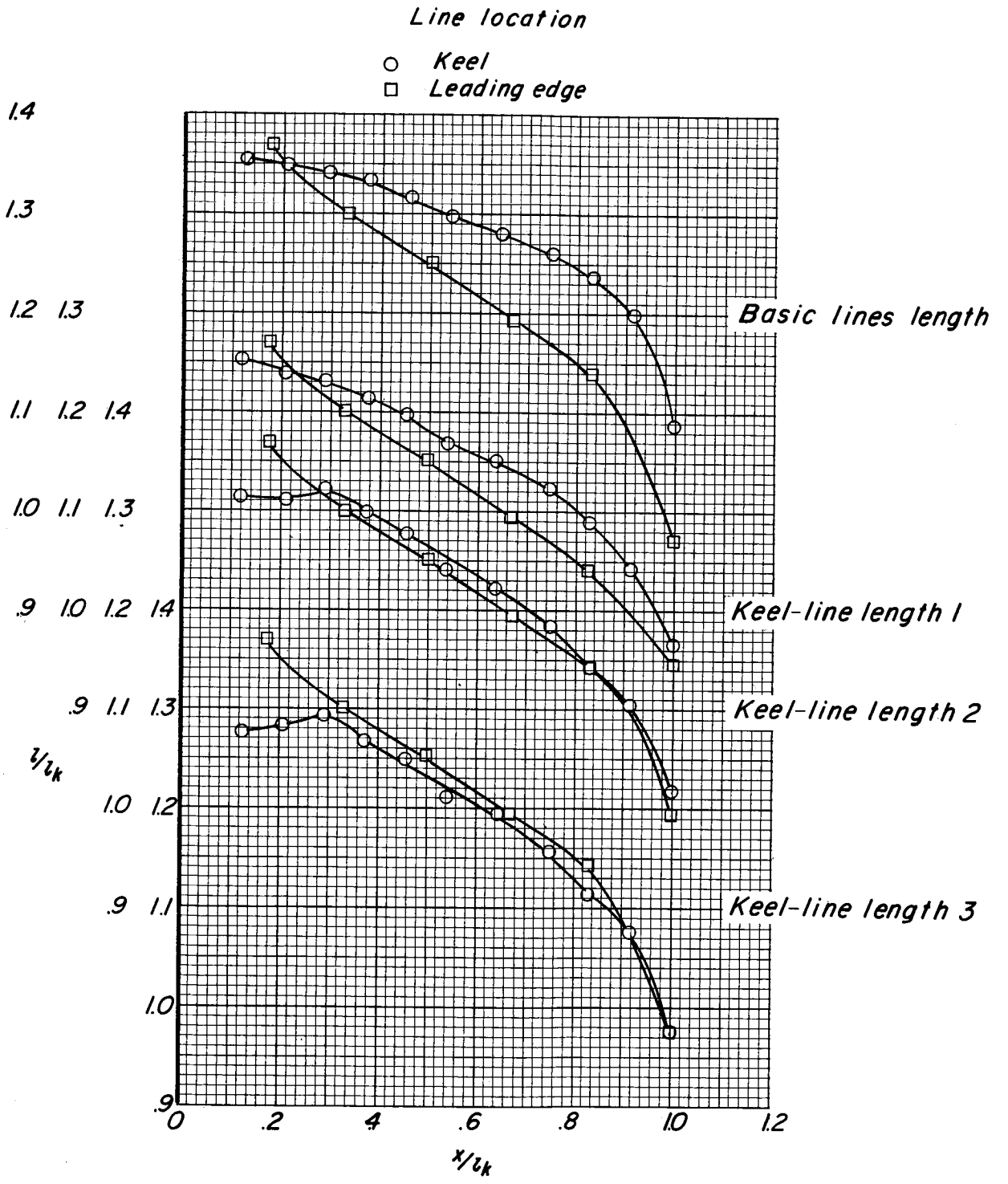

Figure 69.- Line lengths of a parawing with $\Lambda_0 = 45^0$ and 1/8 l_k nose cut off. Various keel-line lengths. The scales from left to right are to be read with the curves from top to bottom.

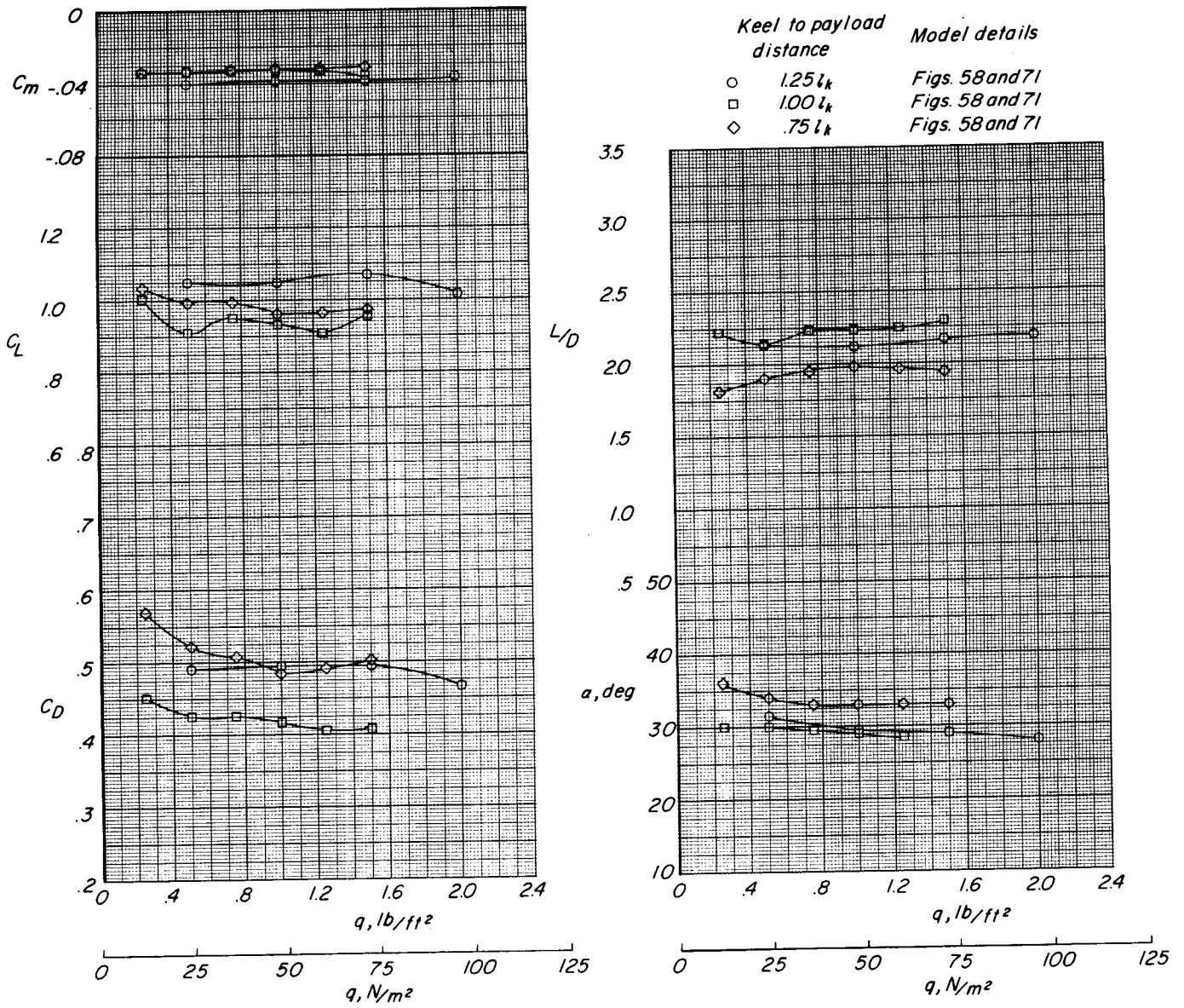

Figure 70.- Effect of keel-payload distance on the variation of the aerodynamic characteristics with dynamic pressure for a parawing with $\Lambda_0 = 45^0$ and 1/8 l_k nose cut off.

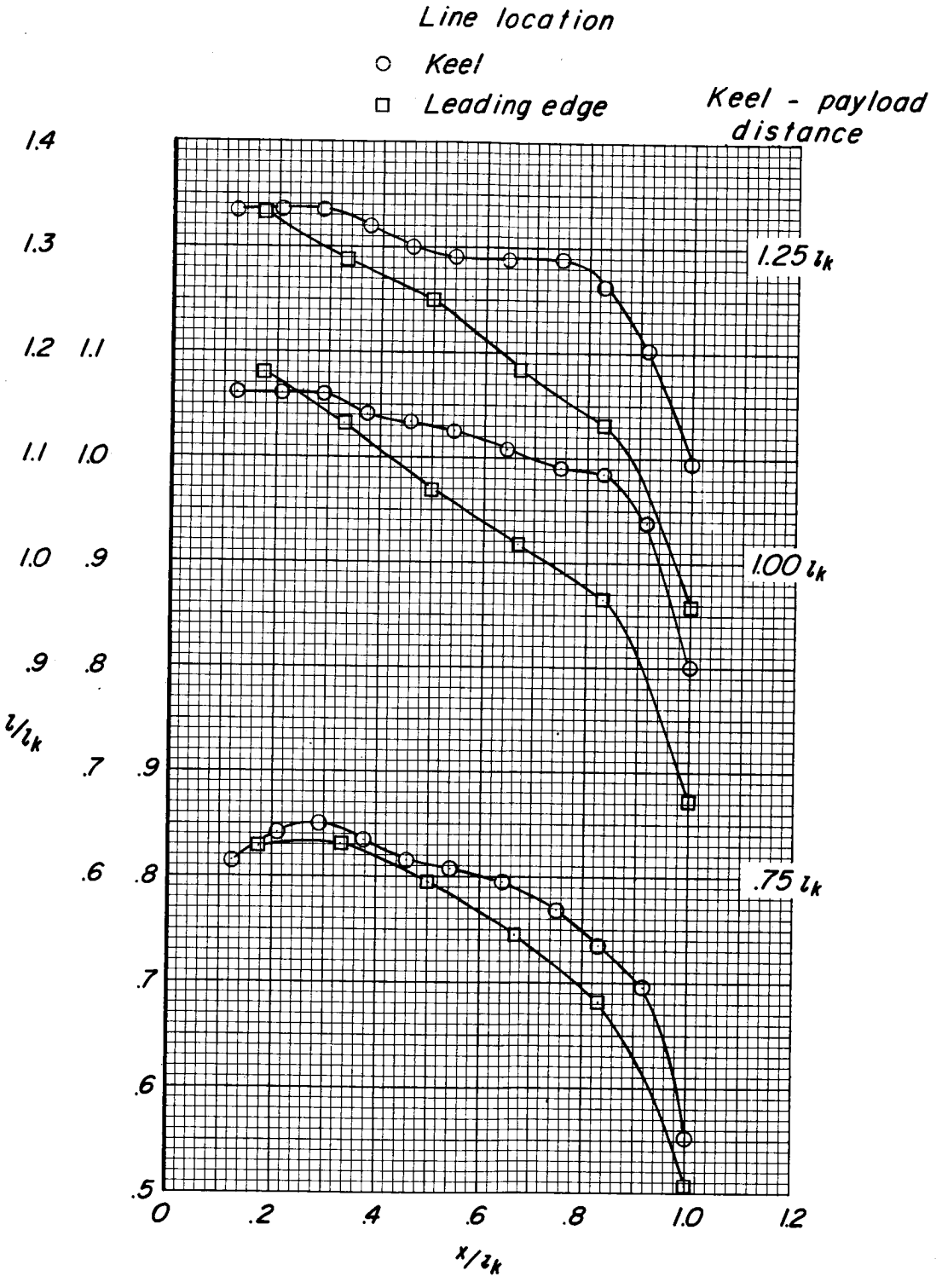

Figure 71.- Line lengths of a parawing with $\Lambda_0 = 45^0$, 1/8 l_k nose cut off, and keel-payload distances of 1.25 l_k, 1.00 l_k, and 0.75 l_k. The scales from left to right are to be read with the curves from top to bottom.

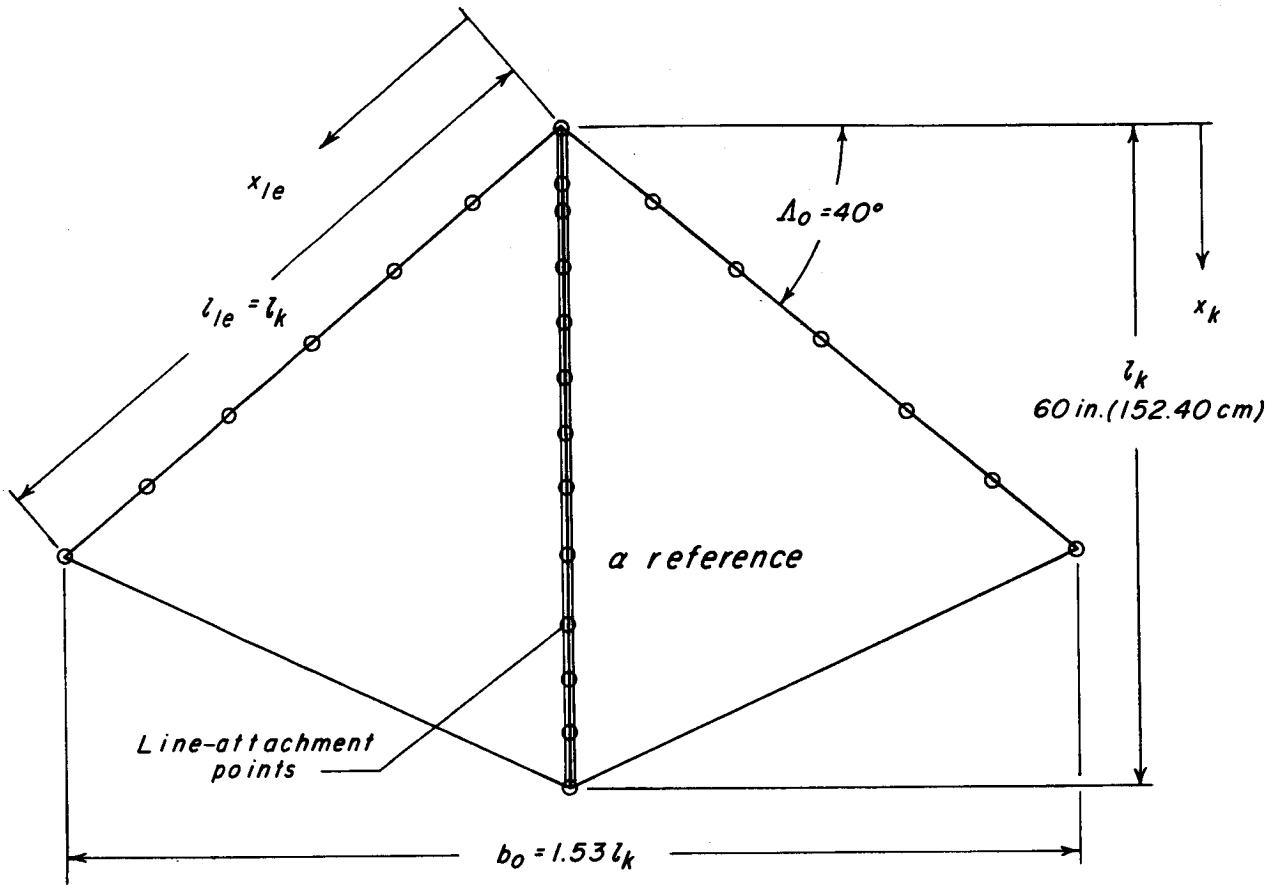

x/l_k	
Keel	Leading edge
0	0
.083	.177
.125	.333
.208	.500
.292	.667
.375	.833
.459	1.000
.542	
.645	
.750	
.833	
.917	
1.000	

Line-attachment location

(a) Flat-planform details; $\Lambda_0 = 40^0$.

Figure 72.- Models of a series of parawings with pointed nose and full-length keel batten.

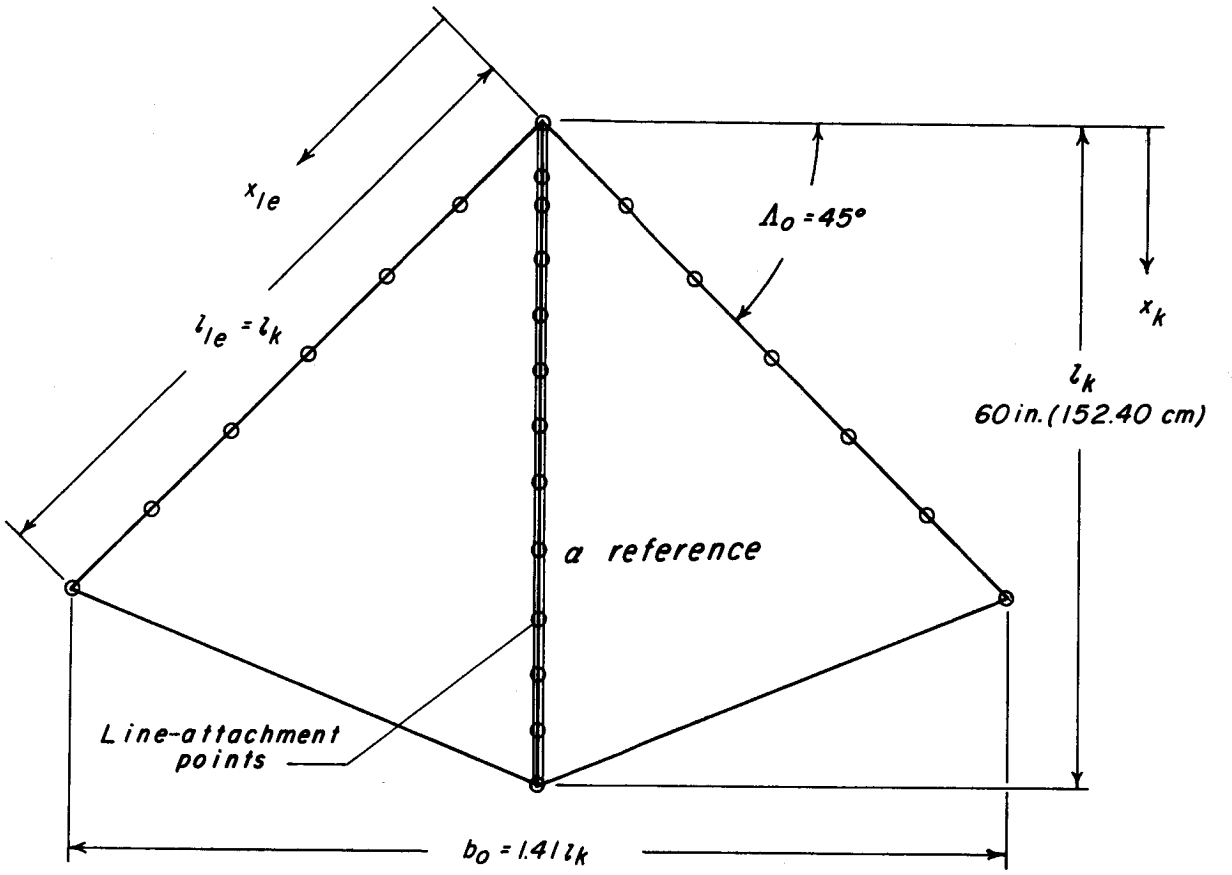

x/l_k	
Keel	Leading edge
0	0
.083	.177
.125	.333
.208	.500
.292	.667
.375	.833
.459	1.000
.542	
.645	
.750	
.833	
.917	
1.000	

Line-attachment location

(b) Flat-planform details; $\Lambda_0 = 45^0$.

Figure 72.- Continued.

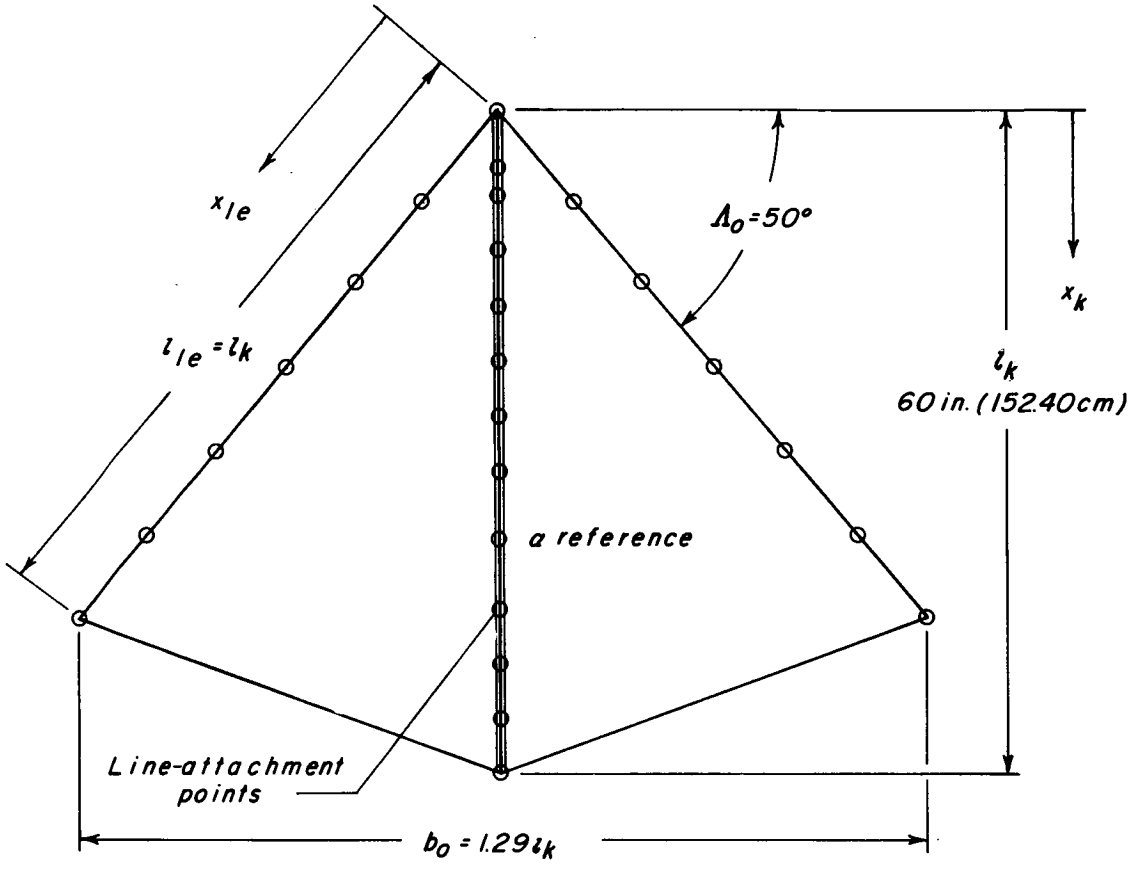

x/l_k	
Keel	Leading edge
0	0
.083	.177
.125	.333
.208	.500
.292	.667
.375	.833
.459	1.000
.542	
.645	
.750	
.833	
.917	
1.000	

Line-attachment location

(c) Flat-planform details; $\Lambda_0 = 50^0$.

Figure 72.- Continued.

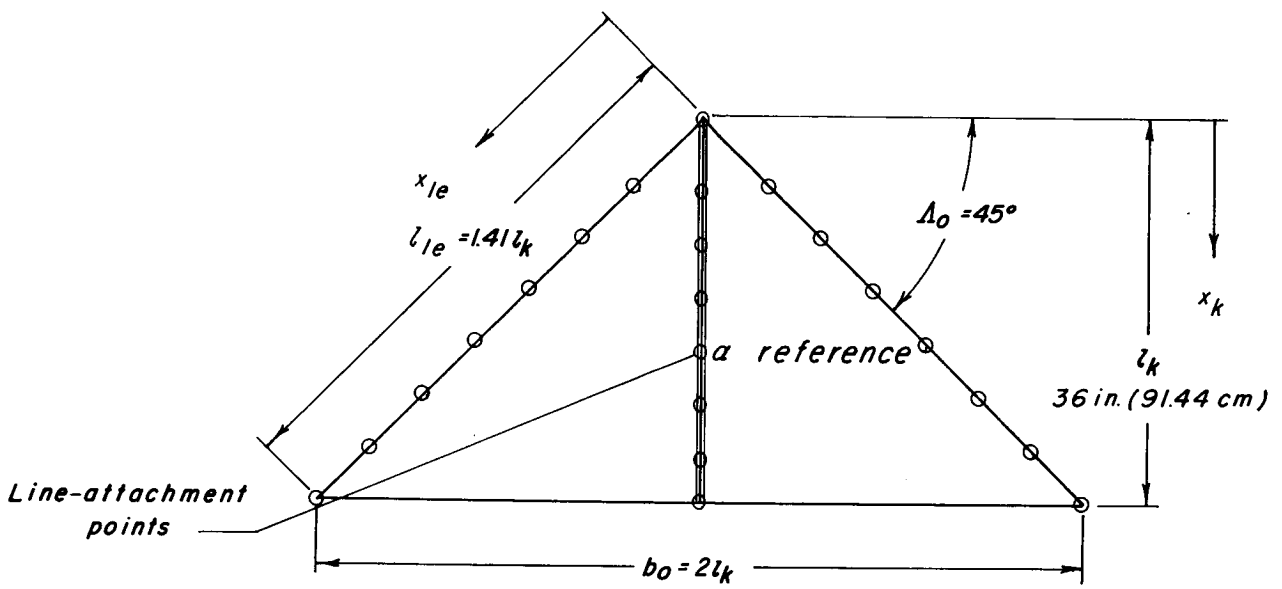

x/l_k	
Keel	Leading edge
0	0
.194	.250
.333	.444
.472	.639
.611	.833
.750	1.028
.889	1.222
1.000	1.413

Line-attachment location

(d) Flat-planform details; $\Lambda_0 = 45^0$ triangular.

Figure 72.- Continued.

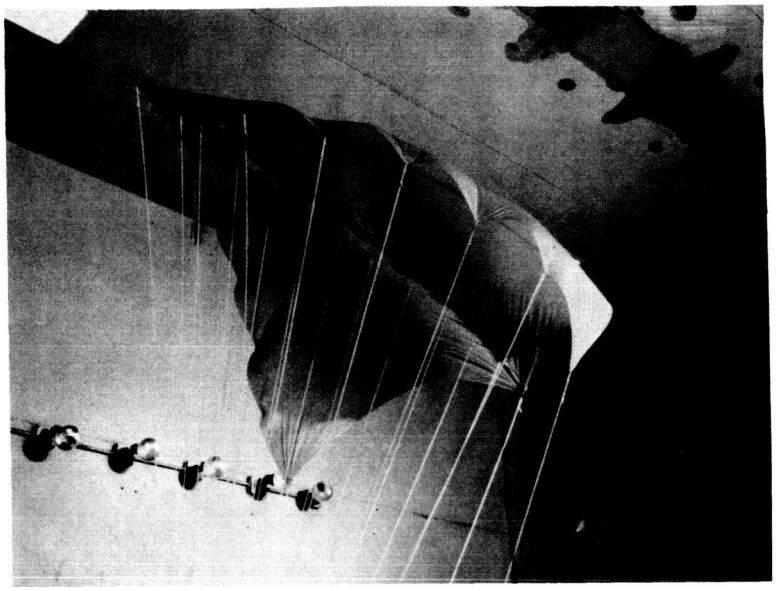

$\Lambda_o = 50°$

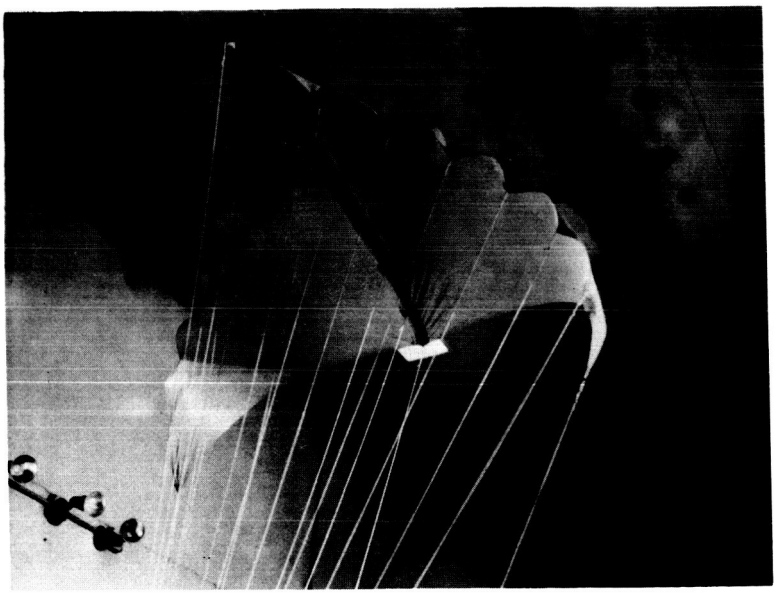

$\Lambda_o = 45°$ triangular wing

(e) Photographs of model. L-67-947

Figure 72.- Concluded.

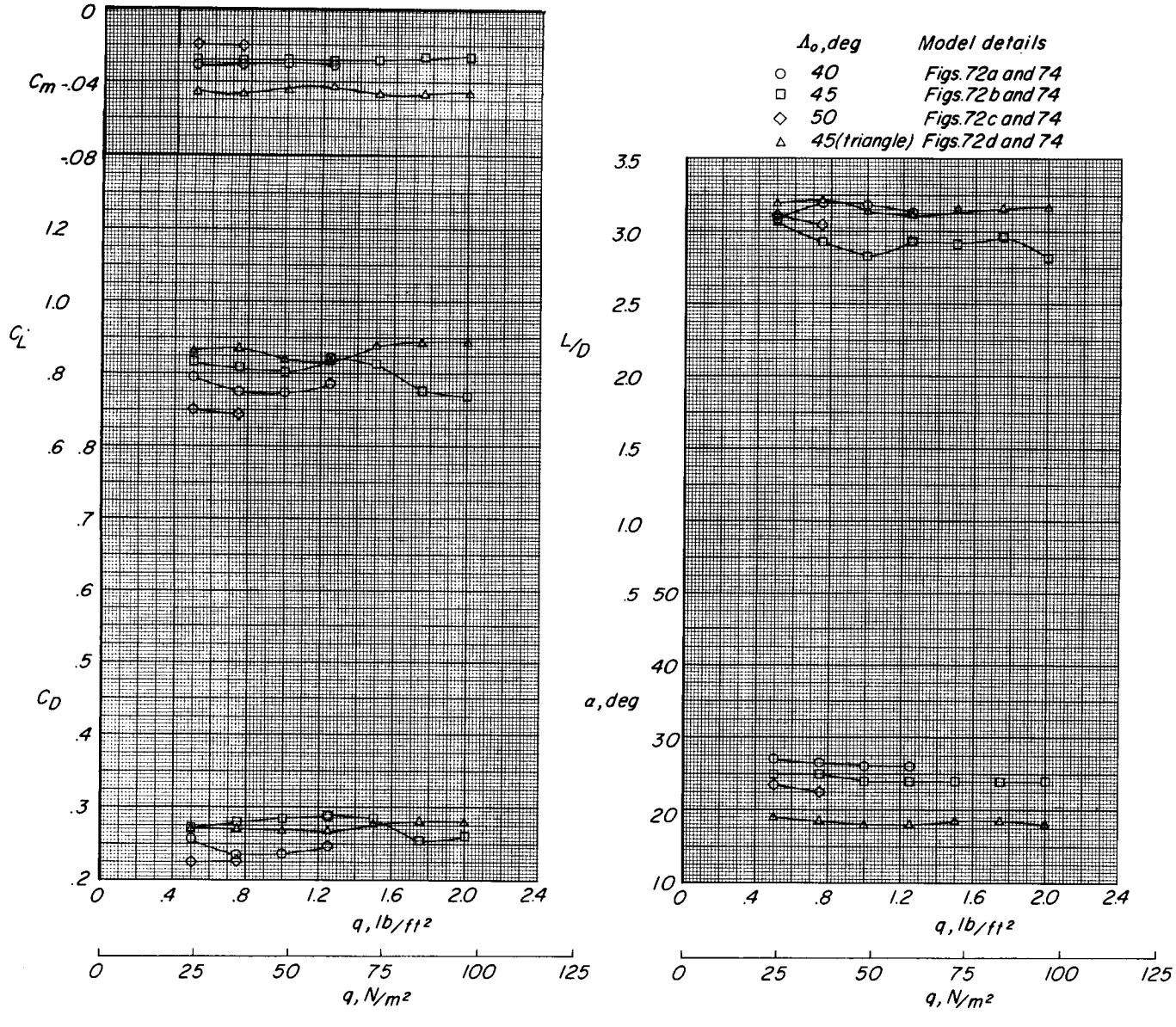

Figure 73.- Effect of sweep angle on the variation of the longitudinal aerodynamic characteristics with dynamic pressure for parawings with pointed noses and full-length keel battens.

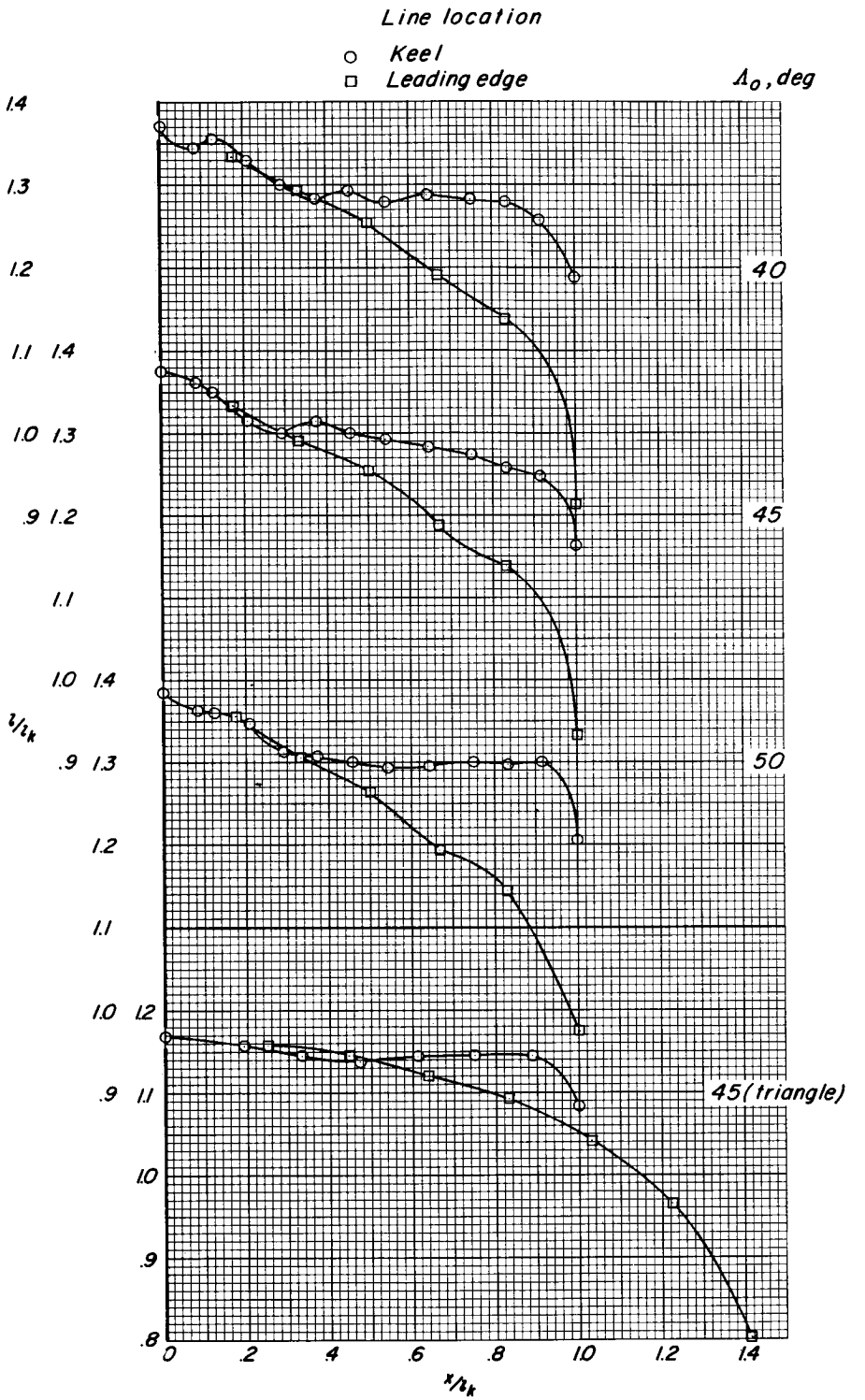

Figure 74.- Line lengths of parawings with pointed noses and full-length keel battens. The scales from left to right are to be read with the curves from top to bottom.

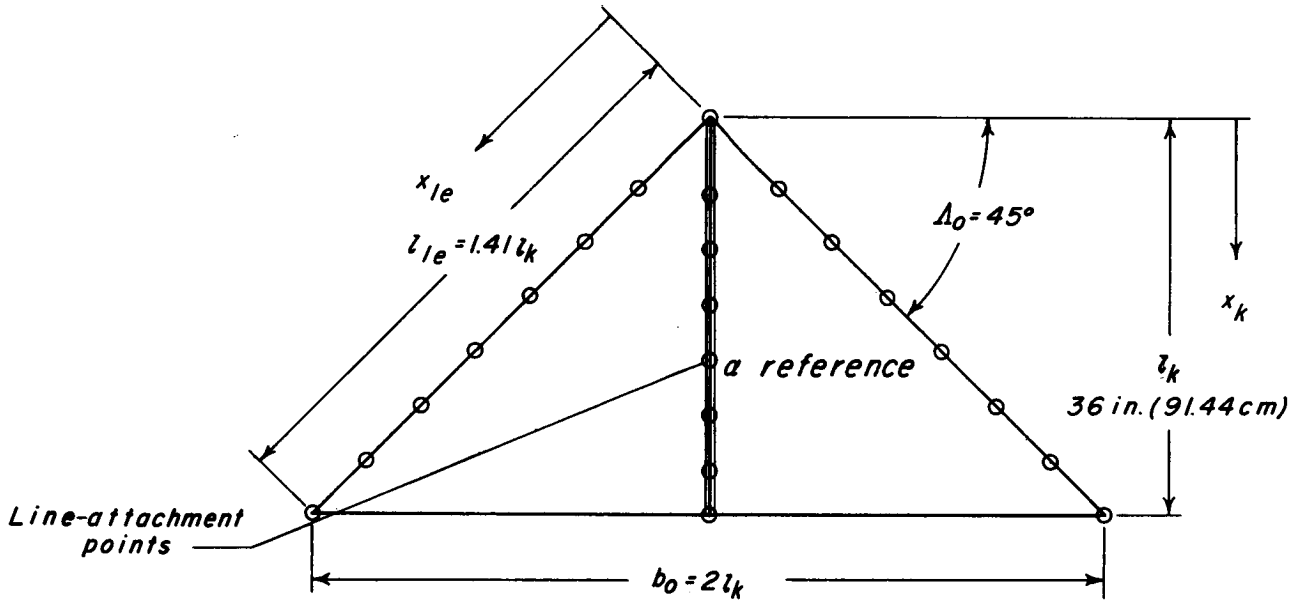

x/l_k	
Keel	Leading edge
0	0
.194	.250
.333	.444
.472	.639
.611	.833
.750	1.028
.889	1.222
1.000	1.413

Line-attachment location

Figure 75.- Details of the flat pattern of a triangular parawing with $\Lambda_0 = 45^0$, pointed nose, and full-length keel batten.

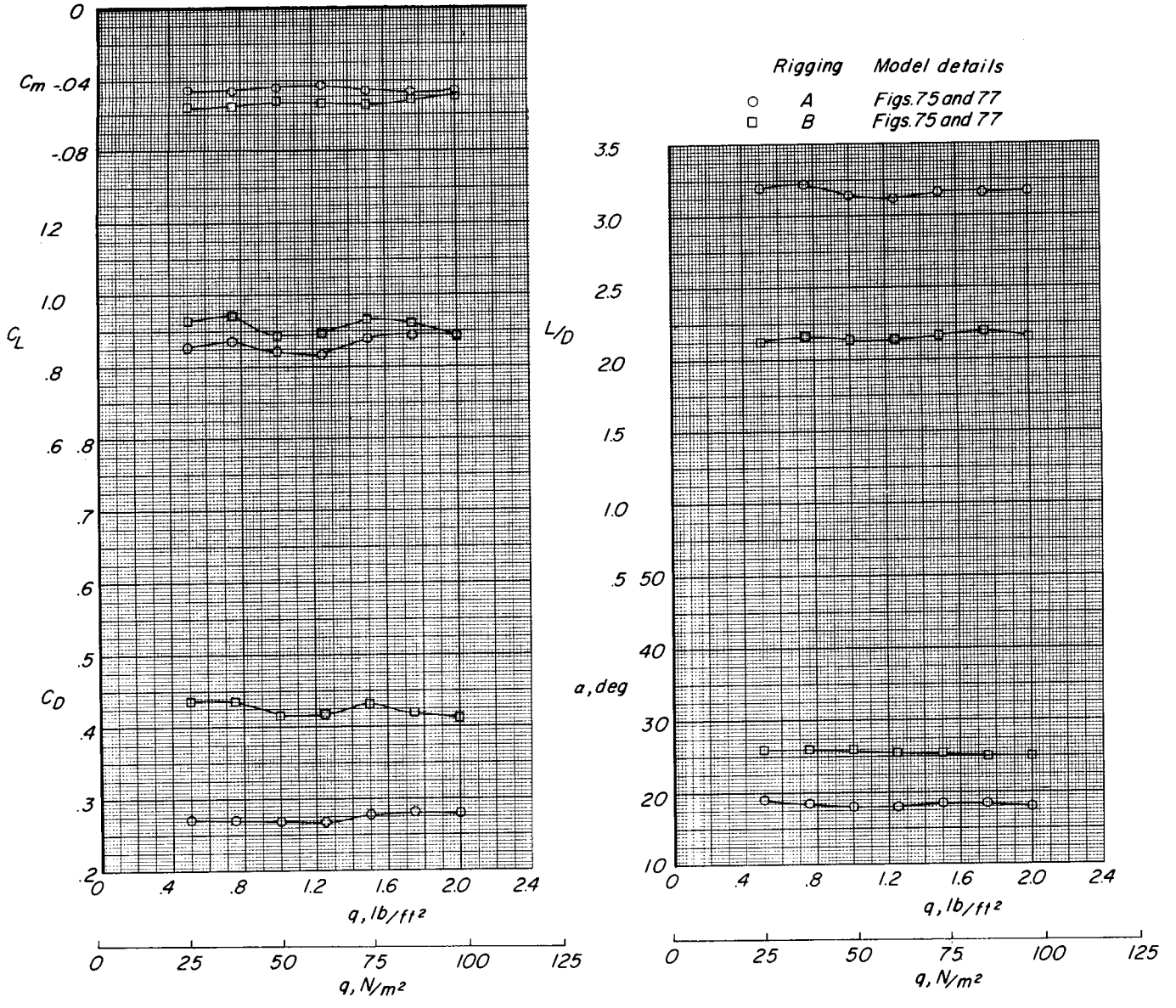

Figure 76.- Effect of changes in rigging on the variation of the longitudinal aerodynamic characteristics with dynamic pressure for a triangular parawing with $\Lambda_0 = 45^0$, pointed nose, and full-length keel batten.

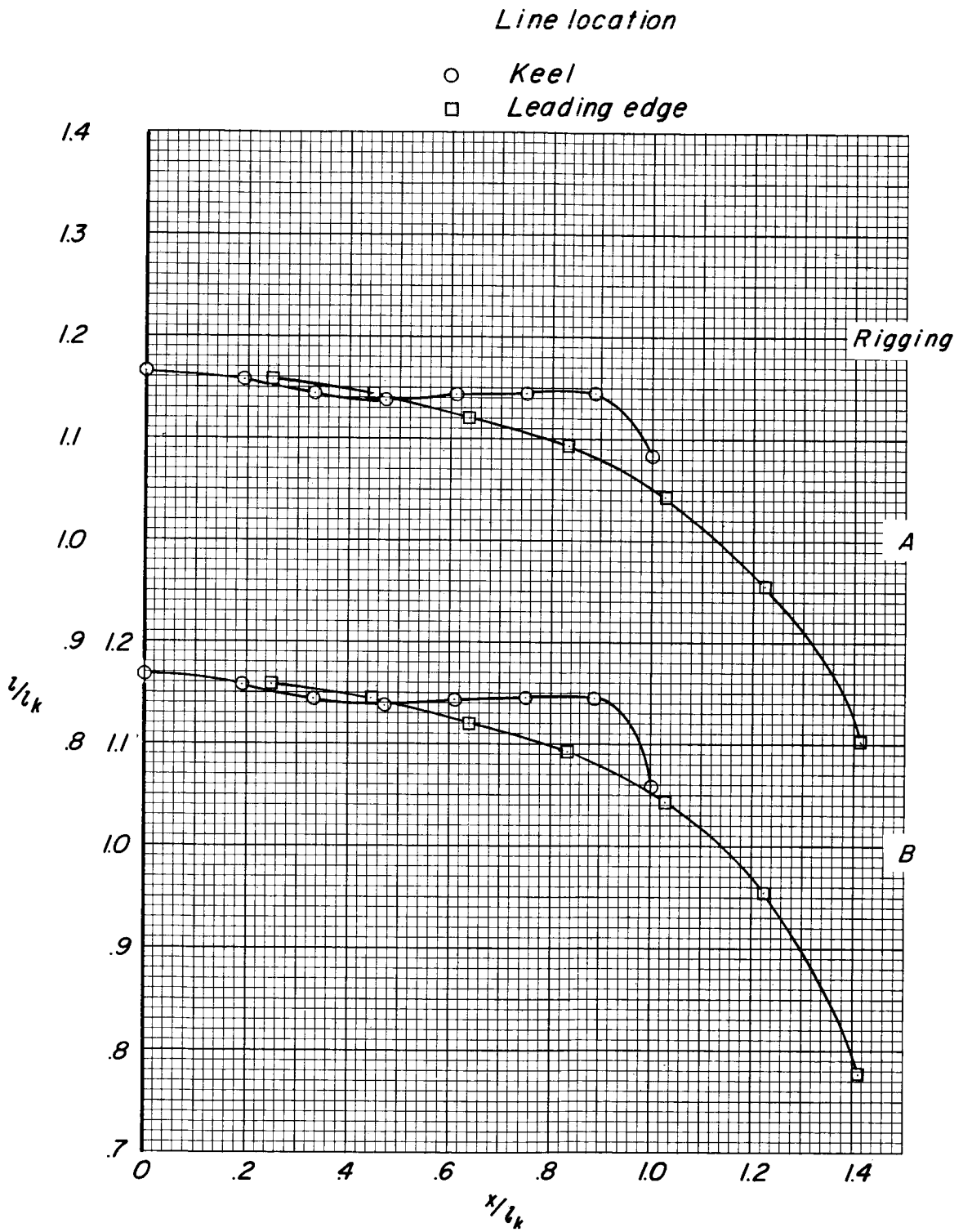

Figure 77.- Line length of a triangular parawing with $\Lambda_0 = 45^0$, pointed nose, and full-length keel batten.

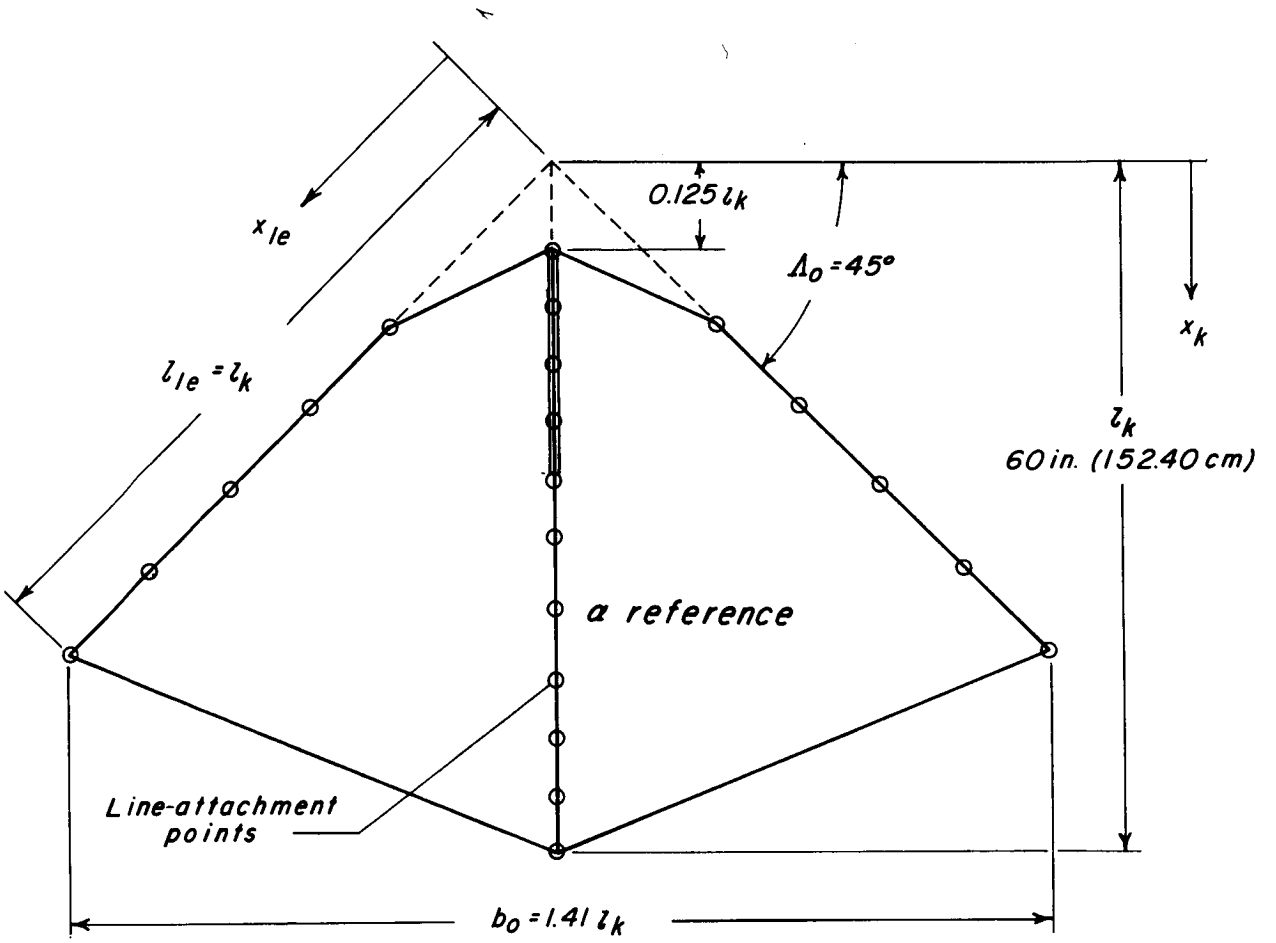

x/l_k	
Keel	Leading edge
.125	.333
.208	.500
.292	.667
.375	.833
.459	1.000
.542	
.645	
.750	
.833	
.917	
1.000	

Line-attachment location

Figure 78.- Details of the flat pattern of a parawing with $\Lambda_0 = 45^0$ and pointed nose stiffened with a keel batten extending 0.325 l_k back from the nose.

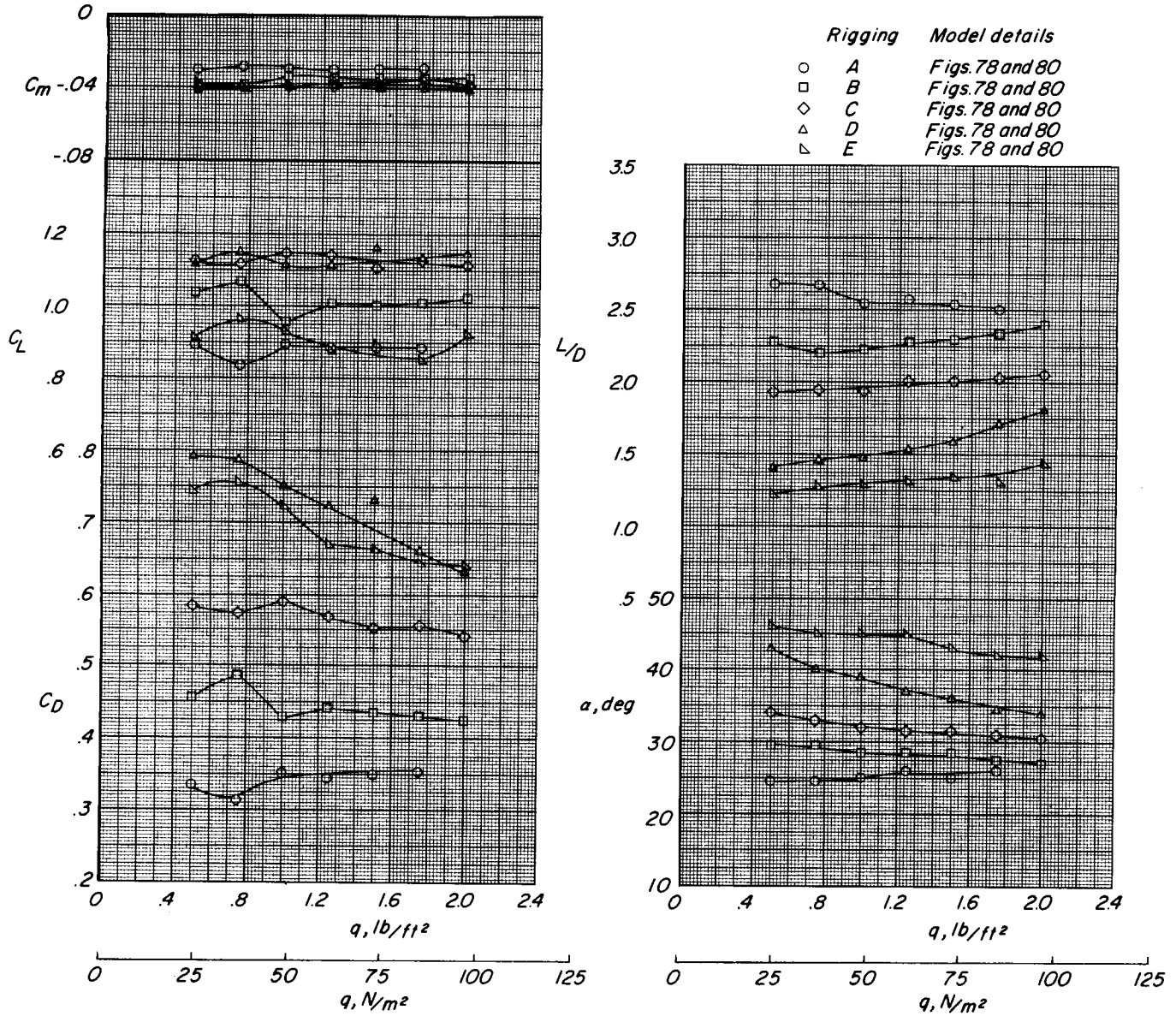

Figure 79.- Effect of changes in rigging on the variation of the longitudinal aerodynamic characteristics with dynamic pressure for a parawing with $\Lambda_0 = 45^0$ and pointed nose stiffened with 0.325 l_k keel batten.

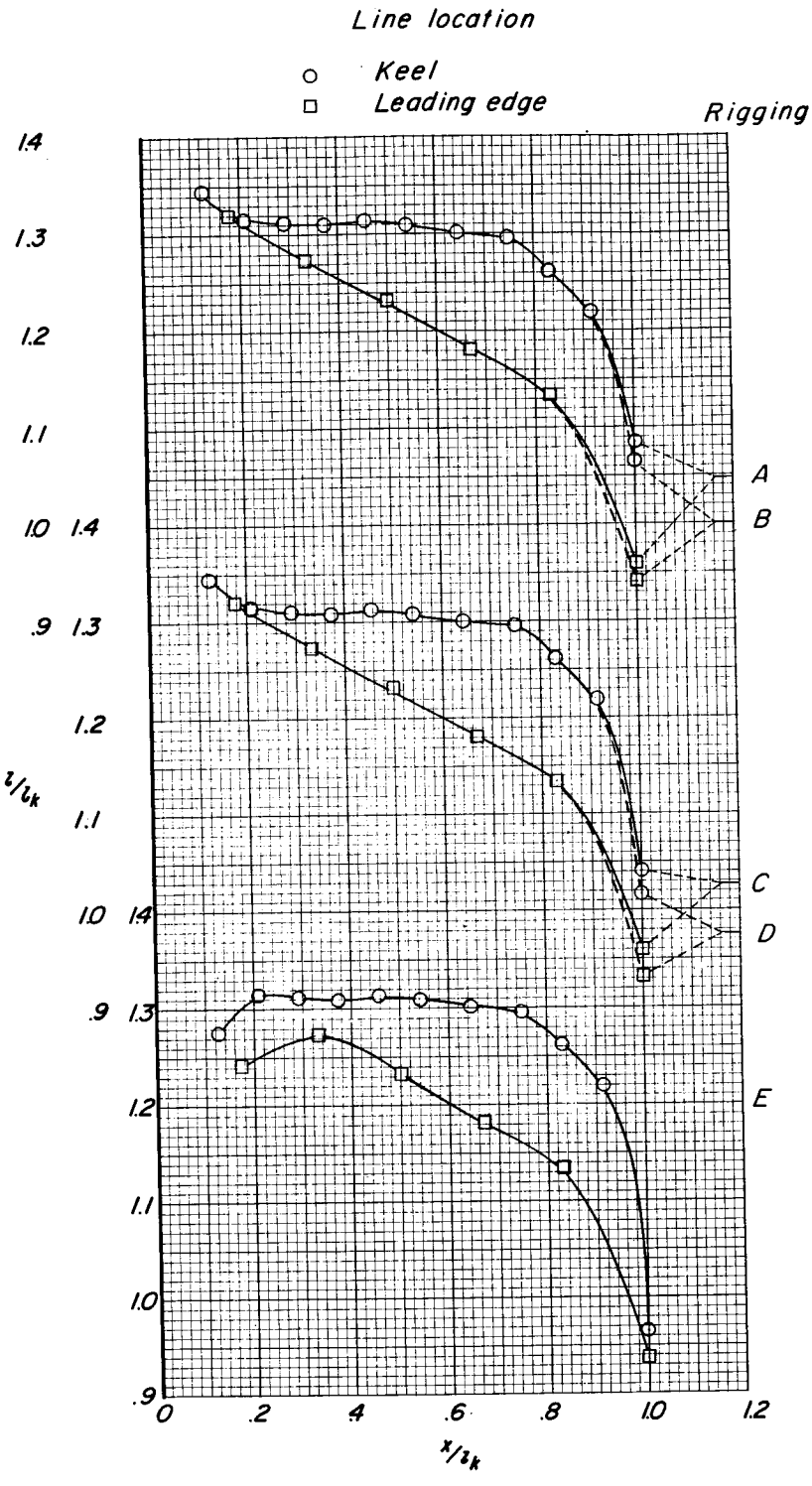

Figure 80.- Line lengths of a parawing with $\Lambda_0 = 45^0$ and pointed nose stiffened with 0.325 l_k keel batten. The scales from left to right are to be read with the curves from top to bottom.

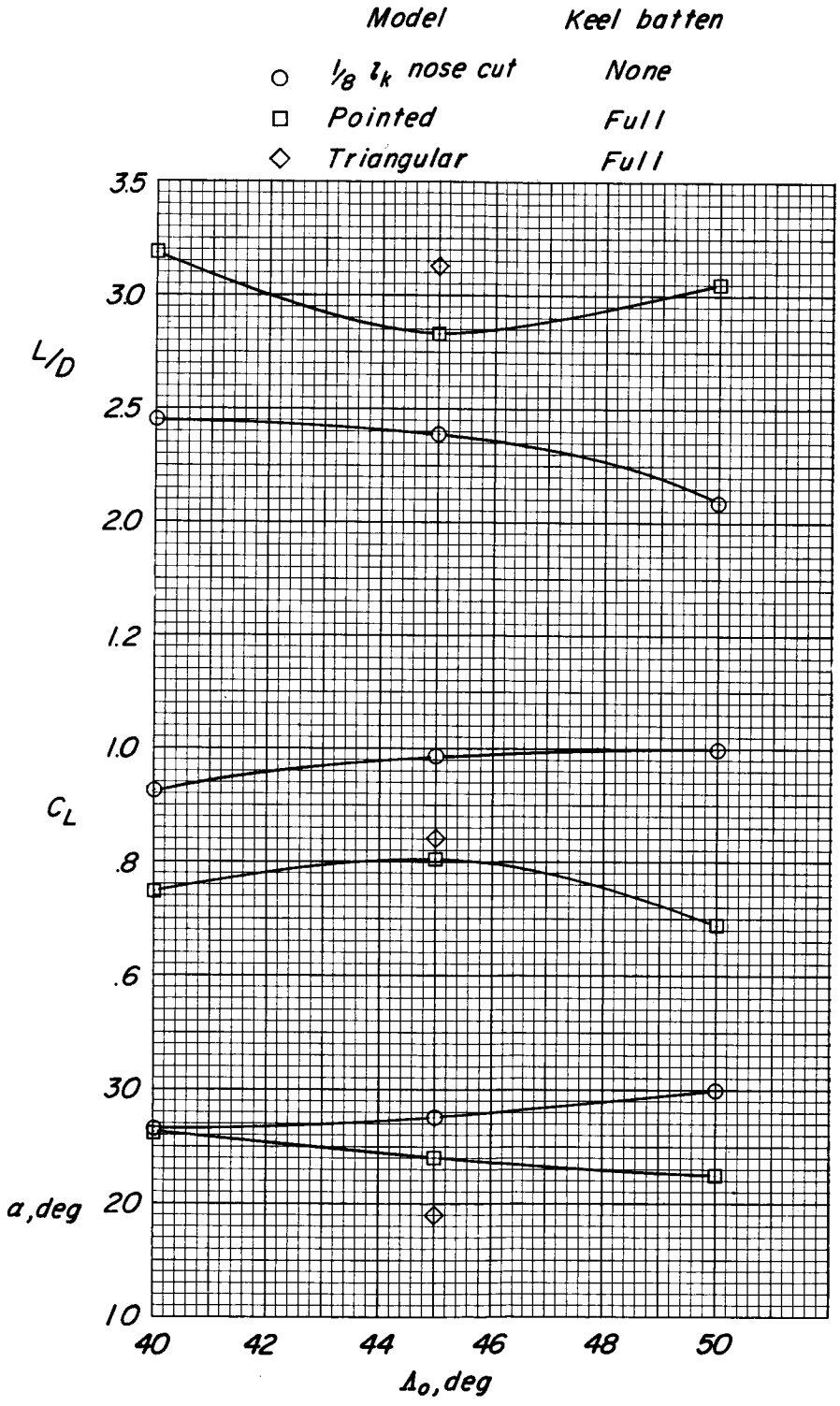

Figure 81.- Summary of results for nonstiffened and minimum-structure parawings. q = 1.0 lb/sq ft (47.9 N/sq m).

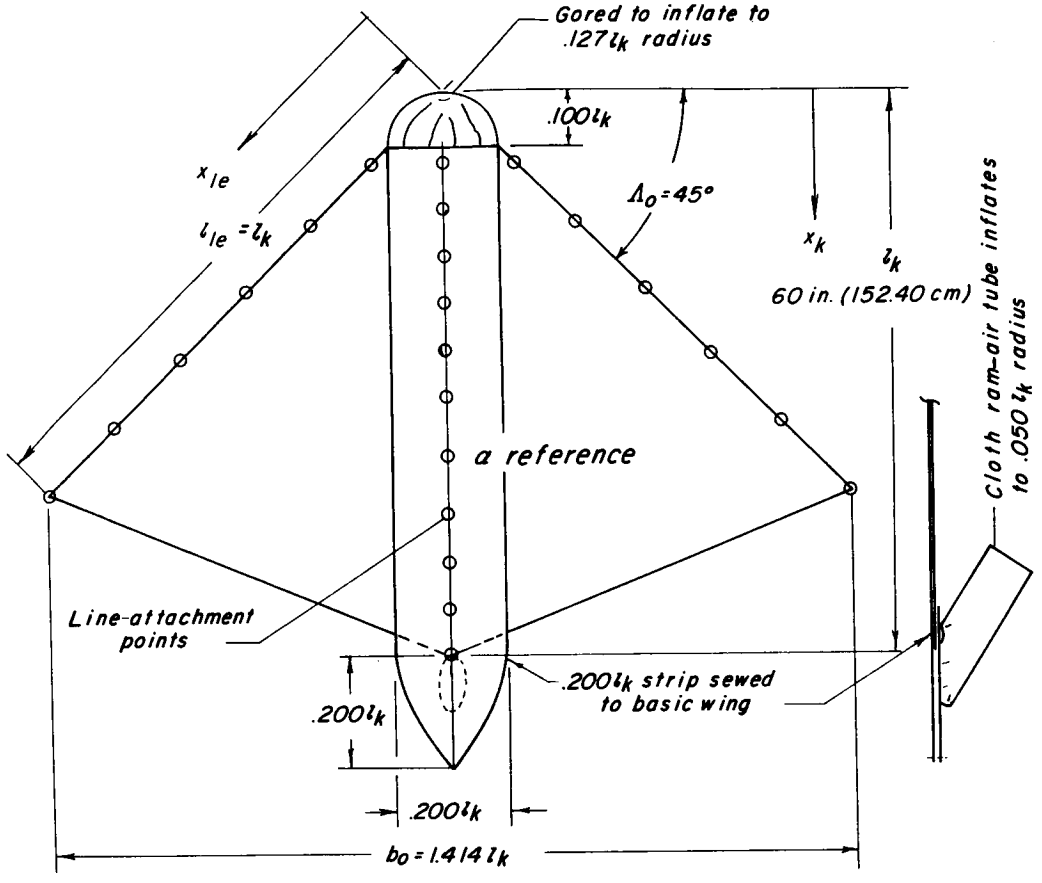

x/ℓ_k	
Keel	Leading edge
.125	.177
.208	.333
.292	.500
.375	.667
.459	.833
.542	1.000
.645	
.750	
.833	
.917	
1.000	

Line-attachment location

(a) Flat-pattern details.

Figure 82.- Model of a parawing with ram-air-inflated keel stiffener, aft-located inlet, $\Lambda_o = 45^0$, and 1/10 ℓ_k nose cut off.

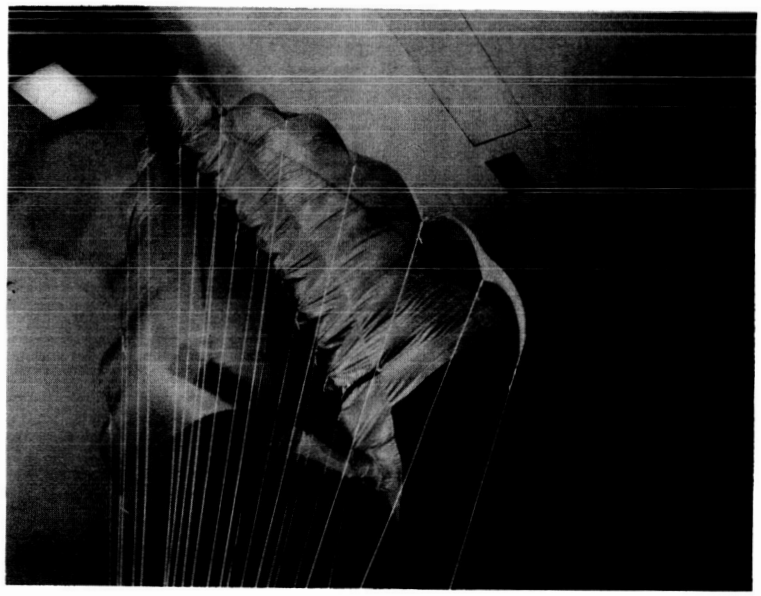

Three-quarter front view

Three-quarter rear view

(b) Photographs of model. L-67-948

Figure 82.- Concluded.

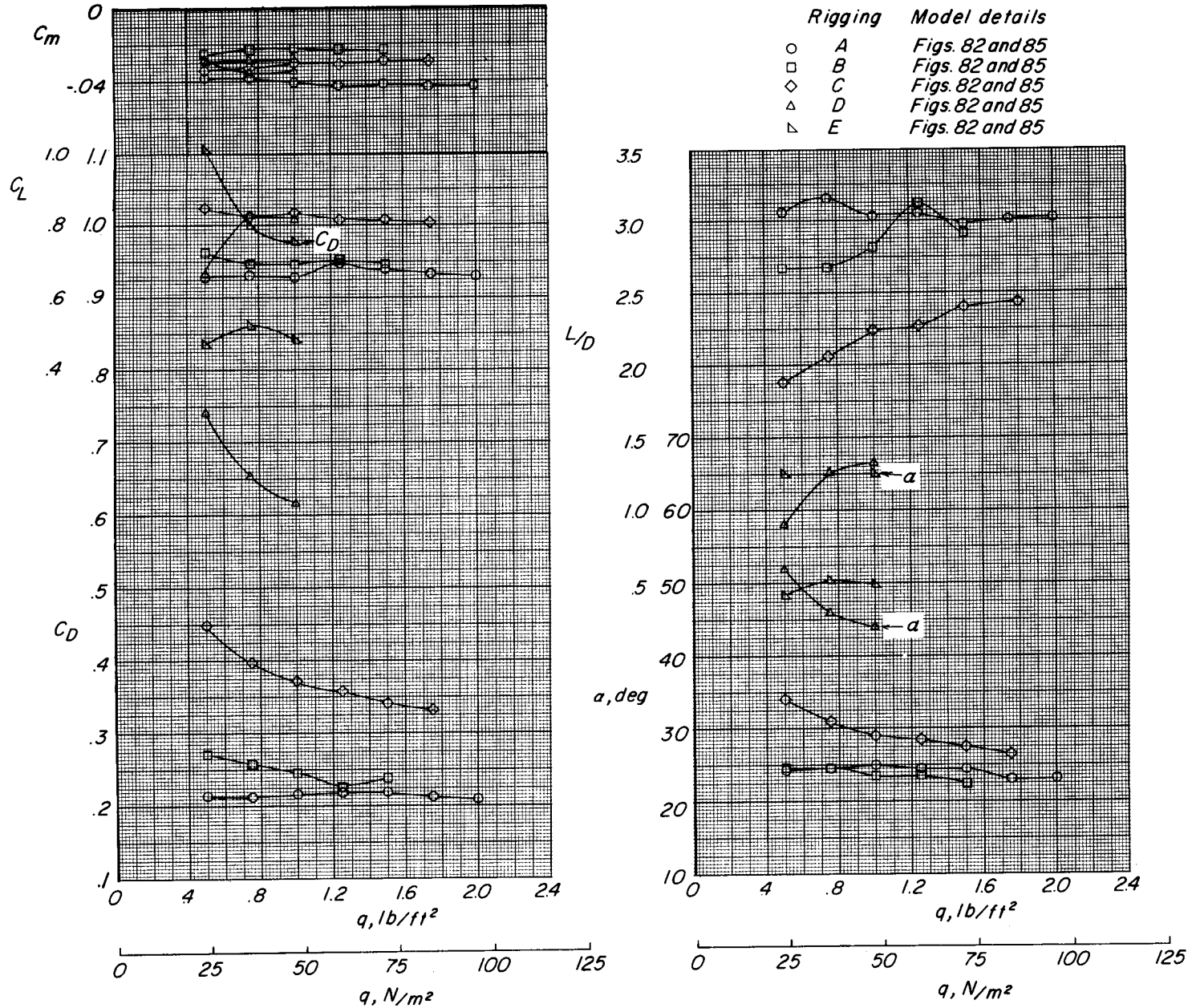

Figure 83.- Effect of changes in rigging on the variation of the wing longitudinal aerodynamic characteristics with dynamic pressure for a parawing with ram-air-inflated keel stiffener, aft-located inlet, $\Lambda_0 = 45^0$, and 1/10 l_k nose cut off.

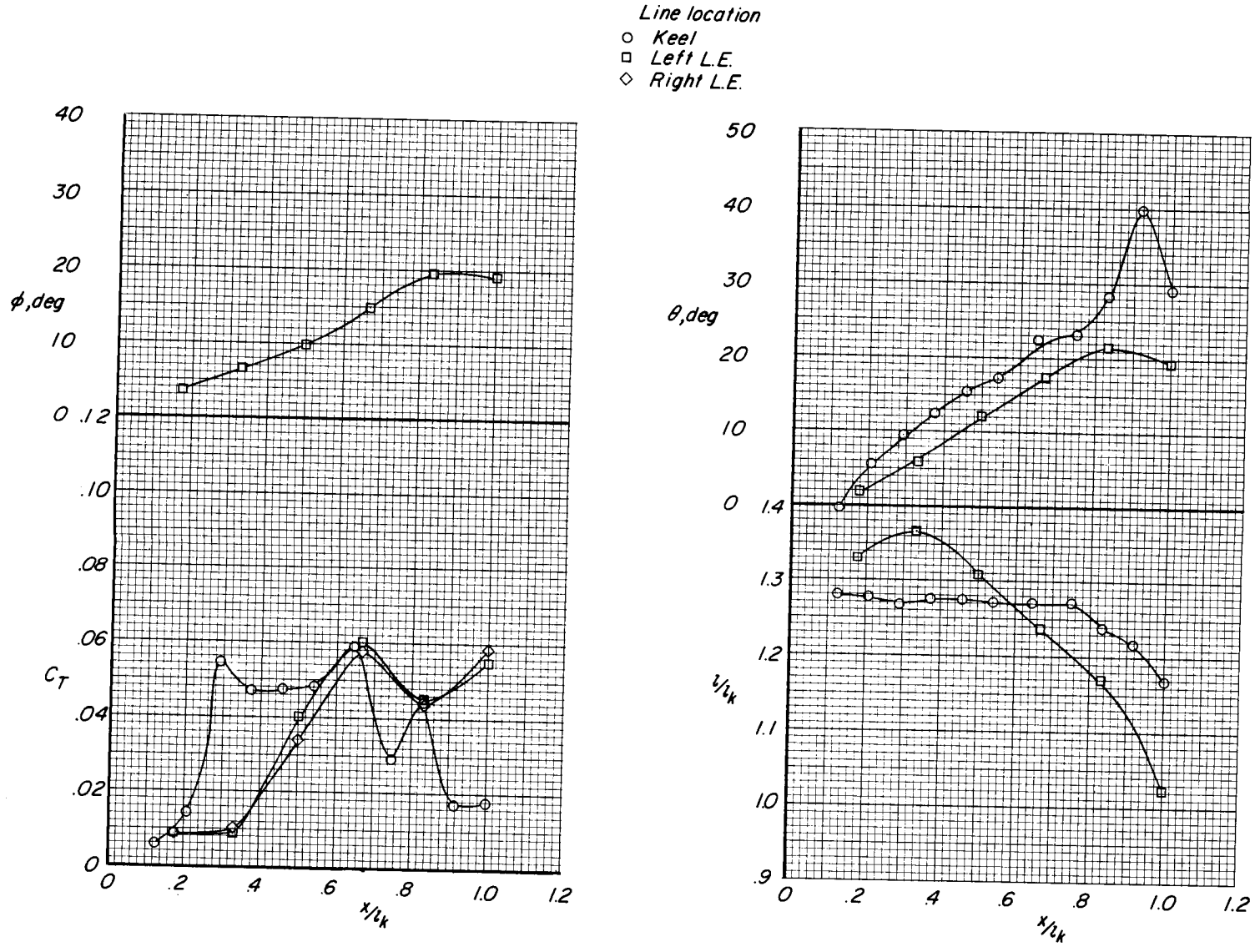

(a) Rigging A; q = 1.0.

Figure 84.- Tension coefficients, line angles, and line lengths for a parawing with ram-air-inflated keel stiffener, aft-located inlet, $\Lambda_0 = 45^0$, and 1/10 l_k nose cut off.

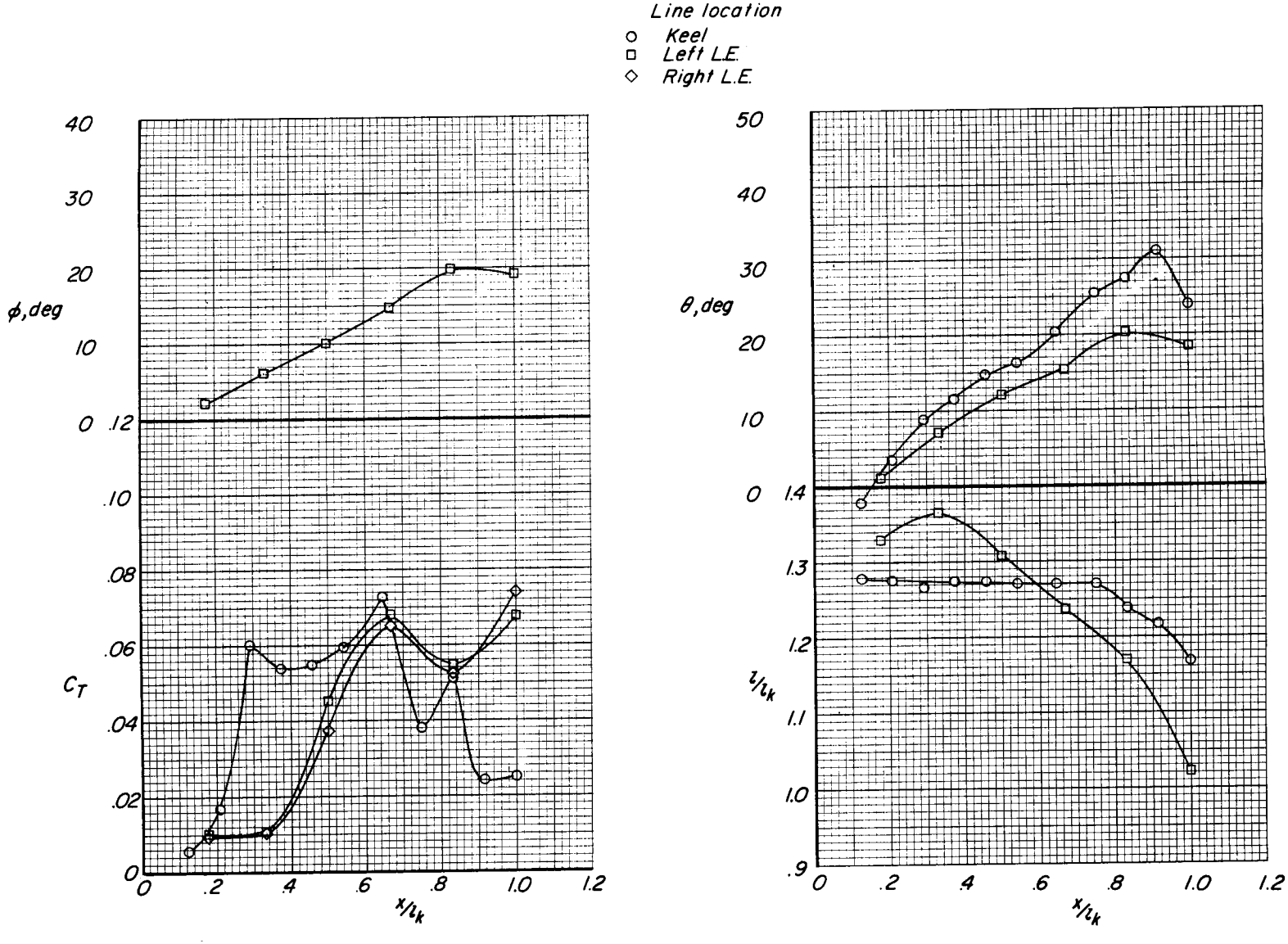

(b) Rigging A; q = 1.5.

Figure 84.- Concluded.

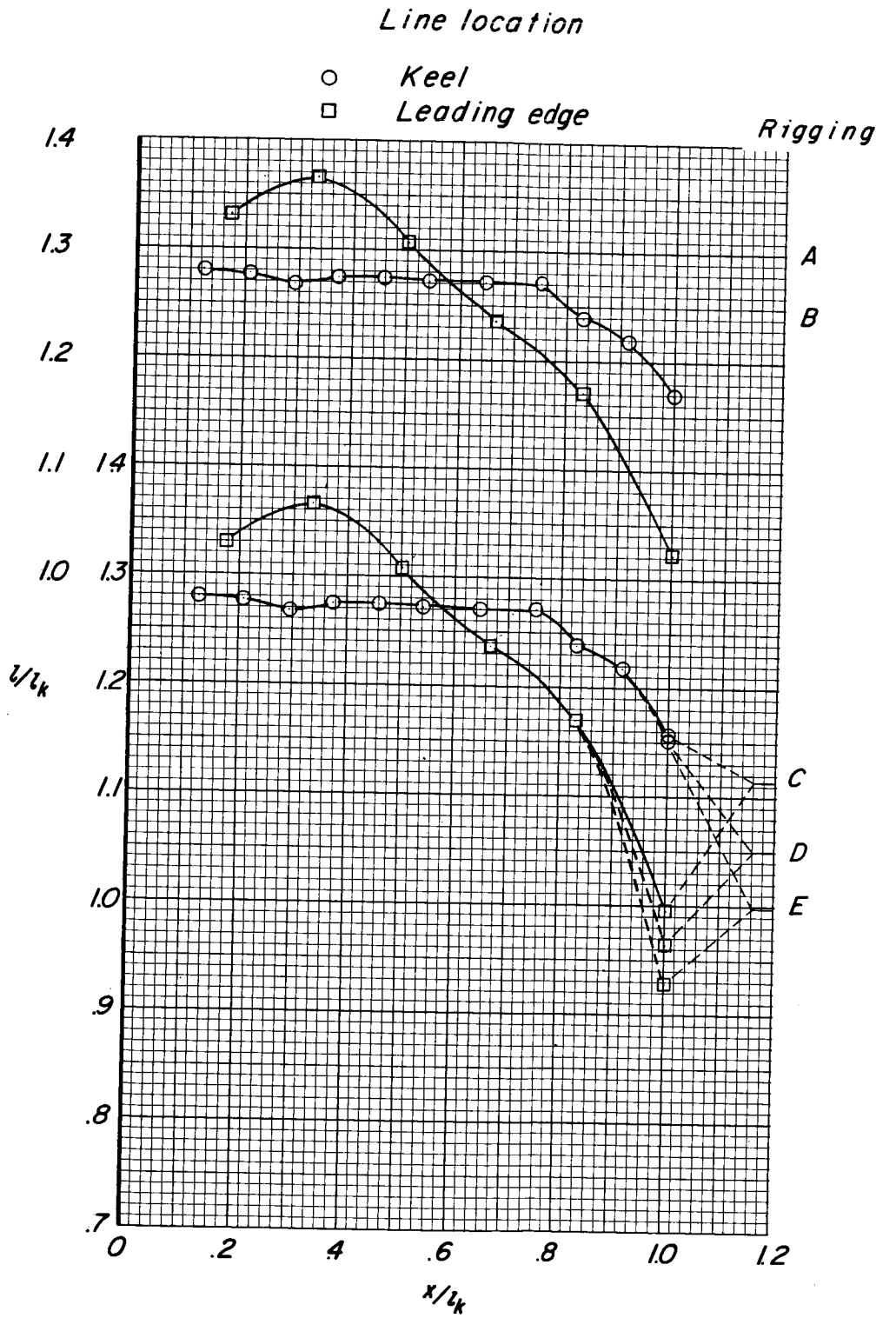

Figure 85.- Line lengths of a parawing with ram-air-inflated keel stiffener, aft-located inlet, $\Lambda_0 = 45^0$, and 1/10 l_k nose cut off.

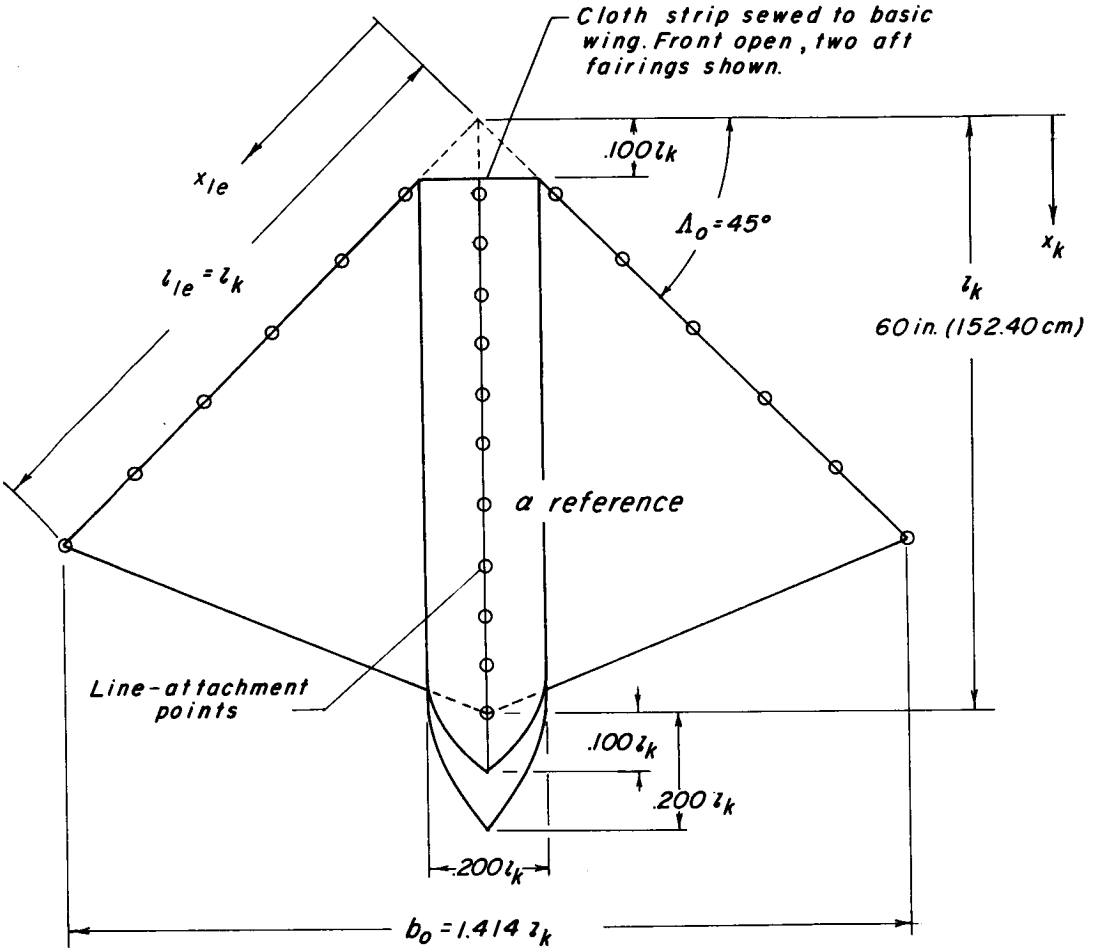

l/l_k	
Keel	Leading edge
.125	.177
.208	.333
.292	.500
.375	.667
.459	.833
.542	1.000
.645	
.750	
.833	
.917	
1.000	

Line-attachment location

(a) Flat-pattern details.

Figure 86.- Model of a parawing with ram-air-inflated keel stiffener, nose inlet, $\Lambda_0 = 45^0$, and 1/10 l_k nose cut off.

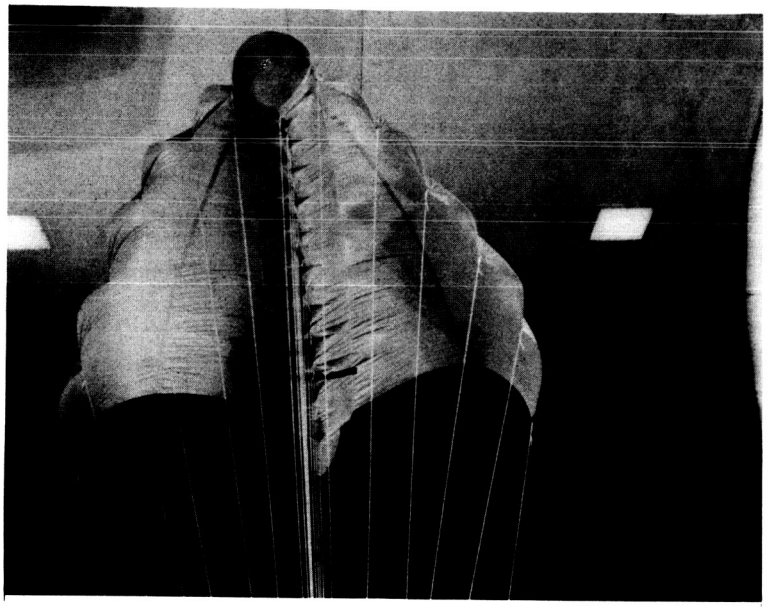

Front view

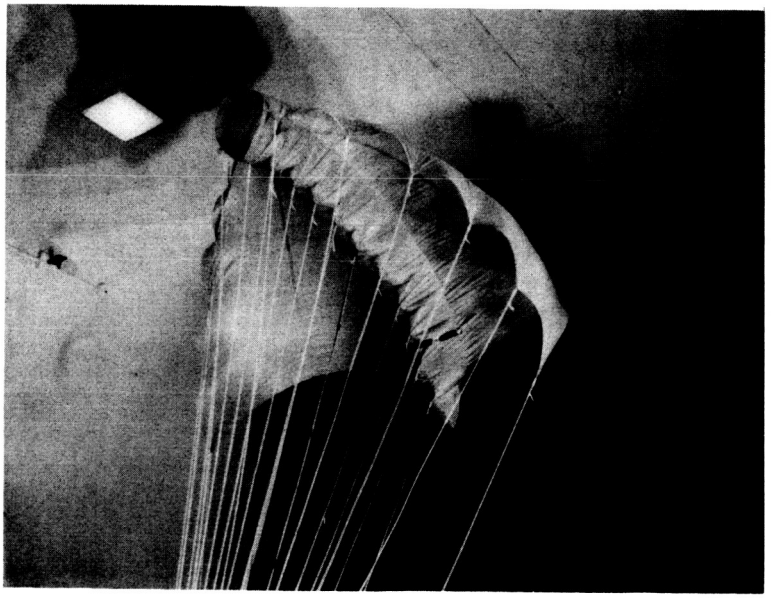

Three-quarter front view

(b) Photographs of models. L-67-949

Figure 86.- Concluded.

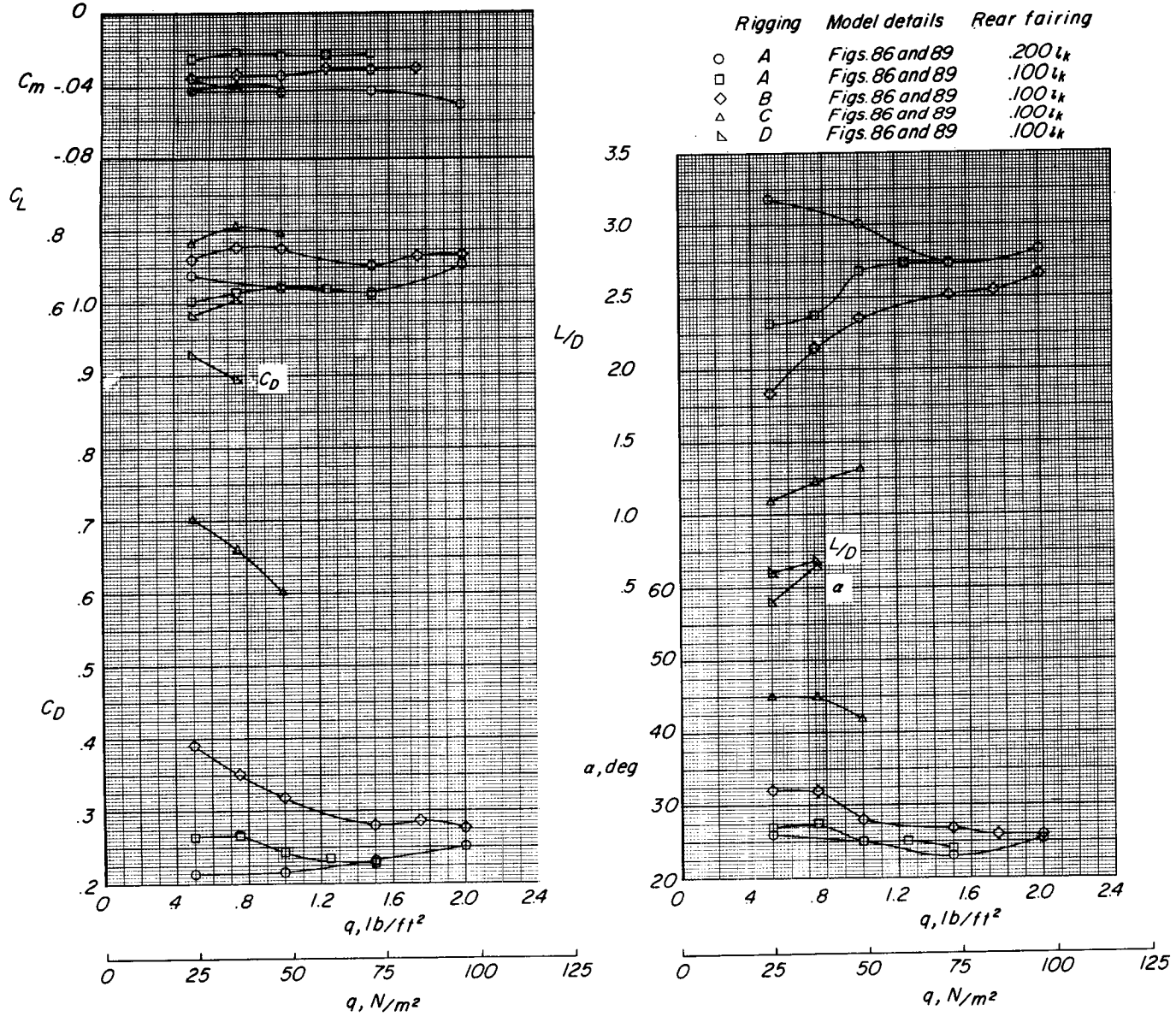

Figure 87.- Effect of changes in rigging on the variation of the wing longitudinal aerodynamic characteristics with dynamic pressure for a parawing with ram-air-inflated keel stiffener, aft-located inlet, $\Lambda_0 = 45^0$, and 1/10 l_k nose cut off.

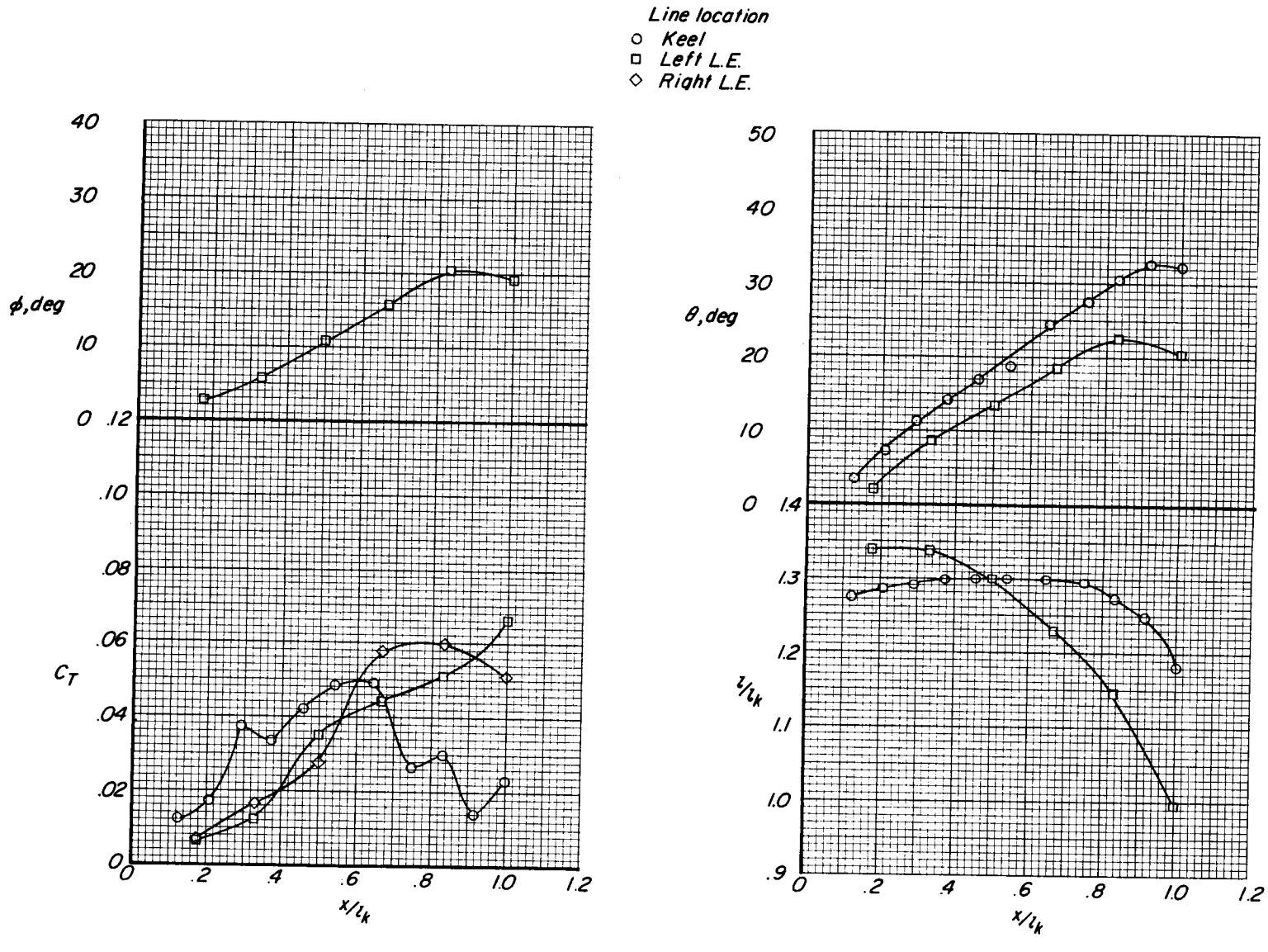

(a) Rigging A; q = 1.0.

Figure 88.- Tension coefficients, line angle, and line lengths for a parawing with ram-air-inflated keel stiffener, nose inlet, $\Lambda_0 = 45^0$, and 1/10 l_k nose cut off.

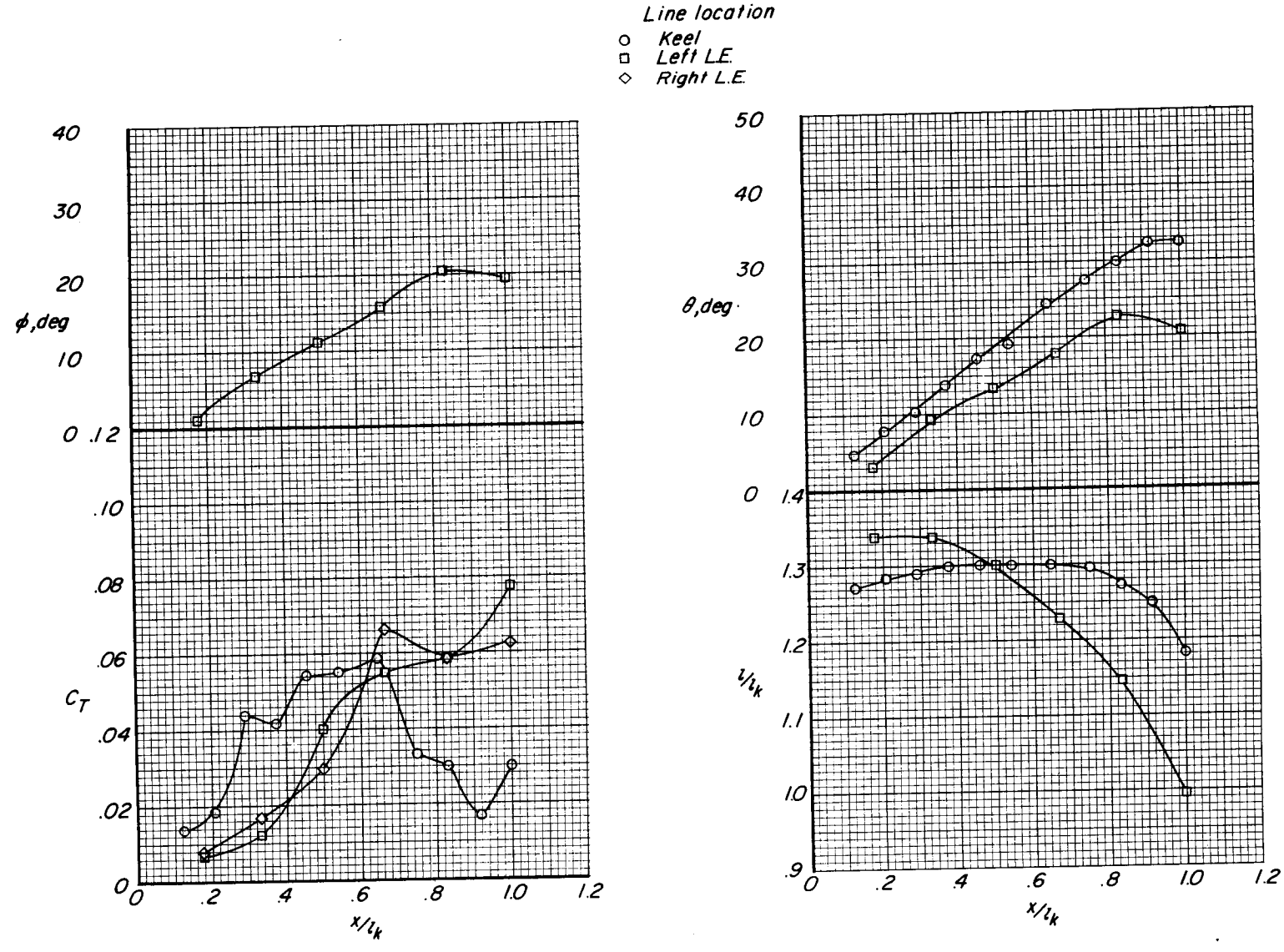

(b) Rigging A; q = 1.5.

Figure 88.- Concluded.

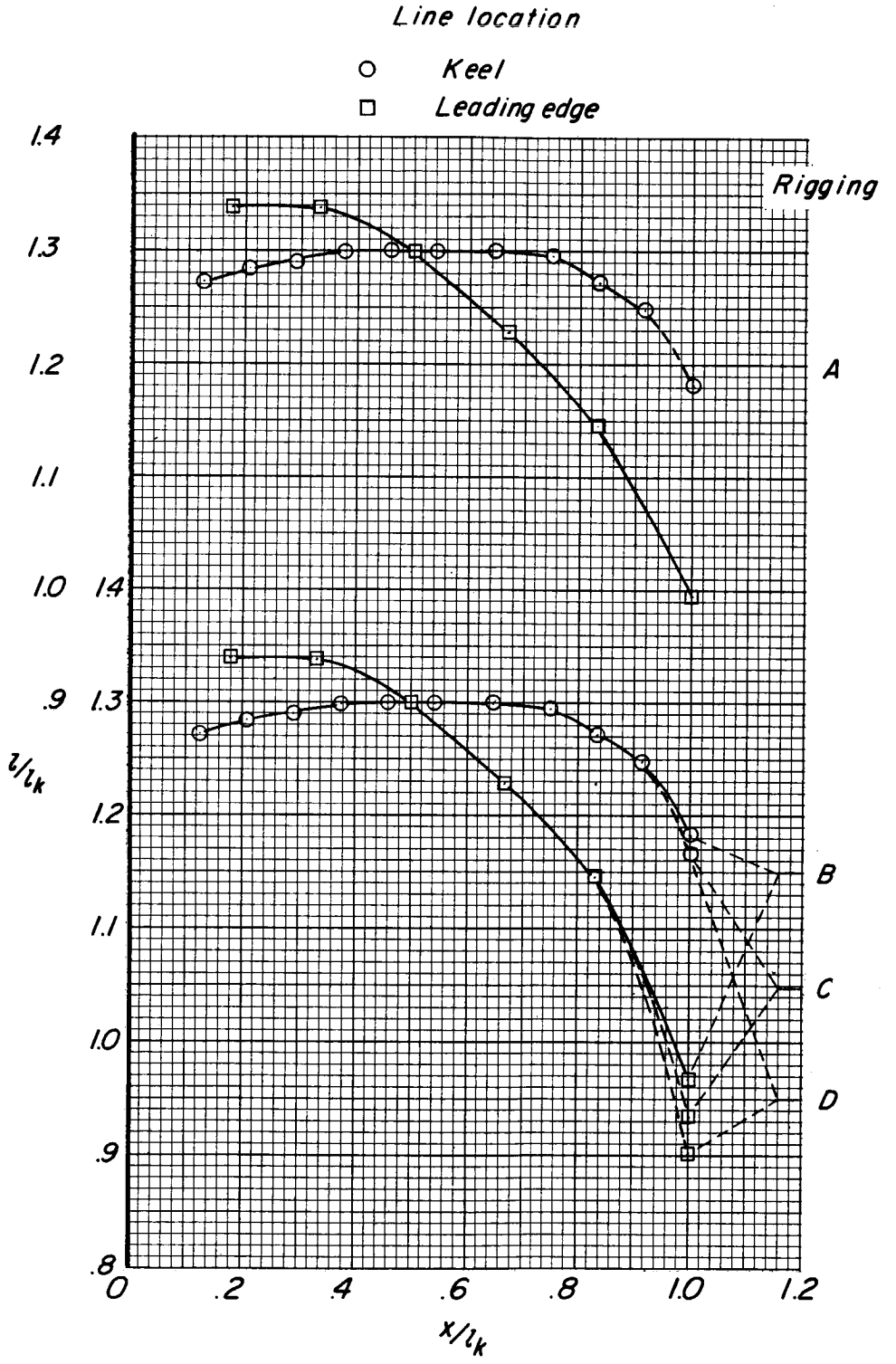

Figure 89.- Line lengths of a parawing with ram-air-inflated keel stiffener, nose inlet, $\Lambda_0 = 45^0$, and 1/10 l_k nose cut off.

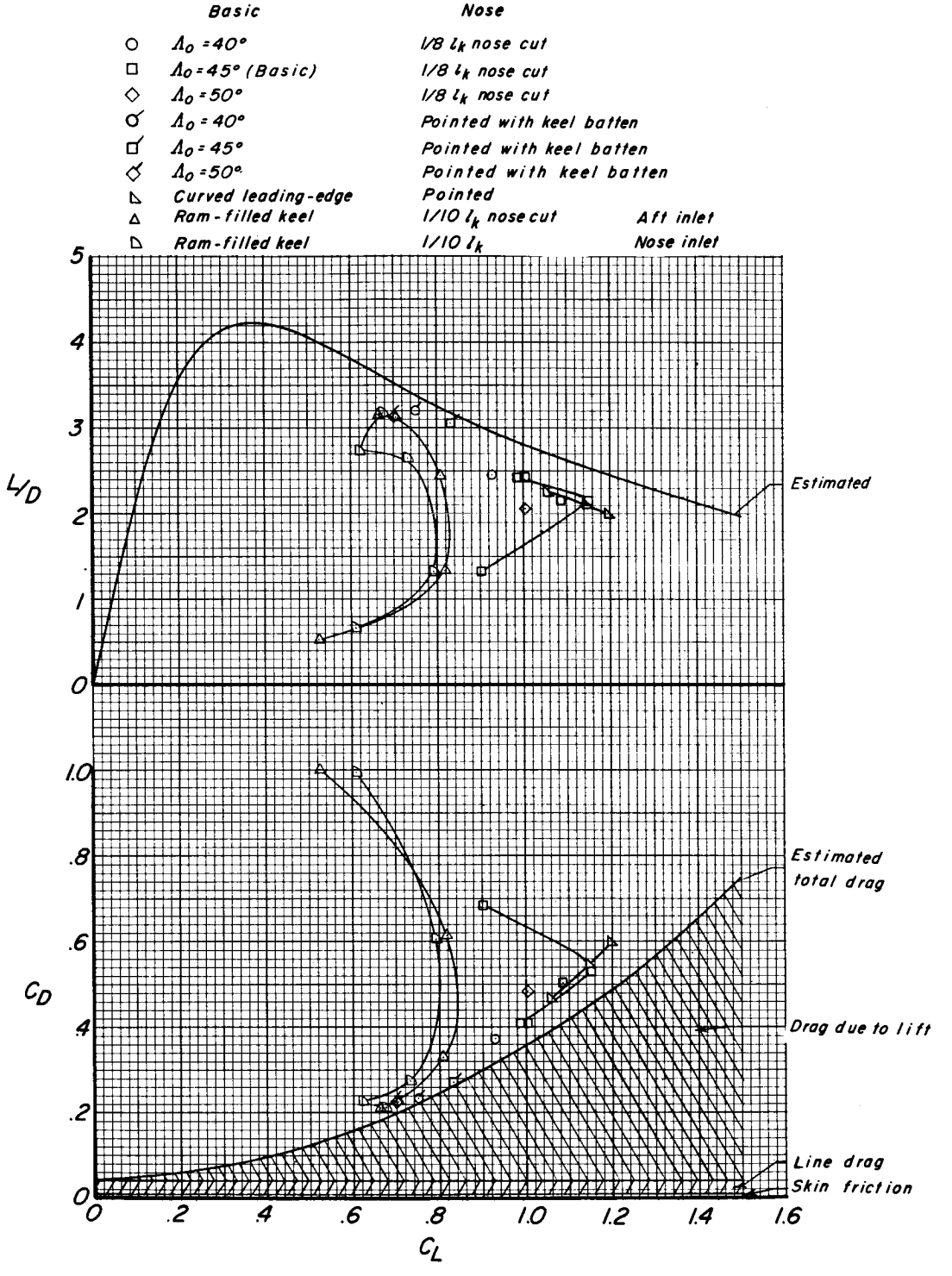

Figure 90.- Comparison of experimental and estimated drag and lift-drag ratios for 5-foot-long (1.5240-m) parawings.

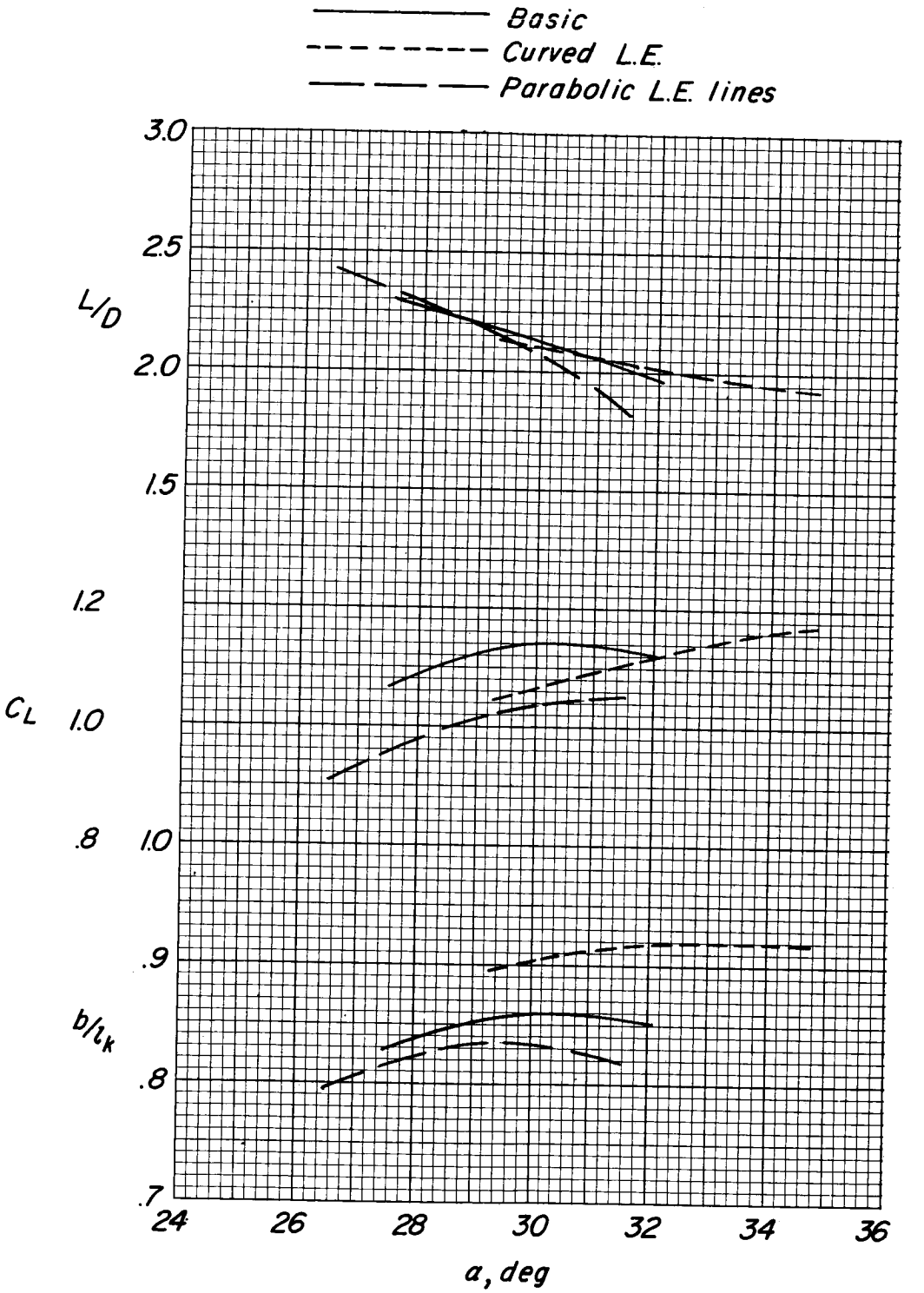

Figure 91.- Variation of lift-drag ratio, lift coefficient, and flight span with angle of attack for a parawing with $\Lambda_0 = 45^0$ and 1/8 l_k nose cut off. q = 1.0 lb/sq ft (47.9 N/sq m).

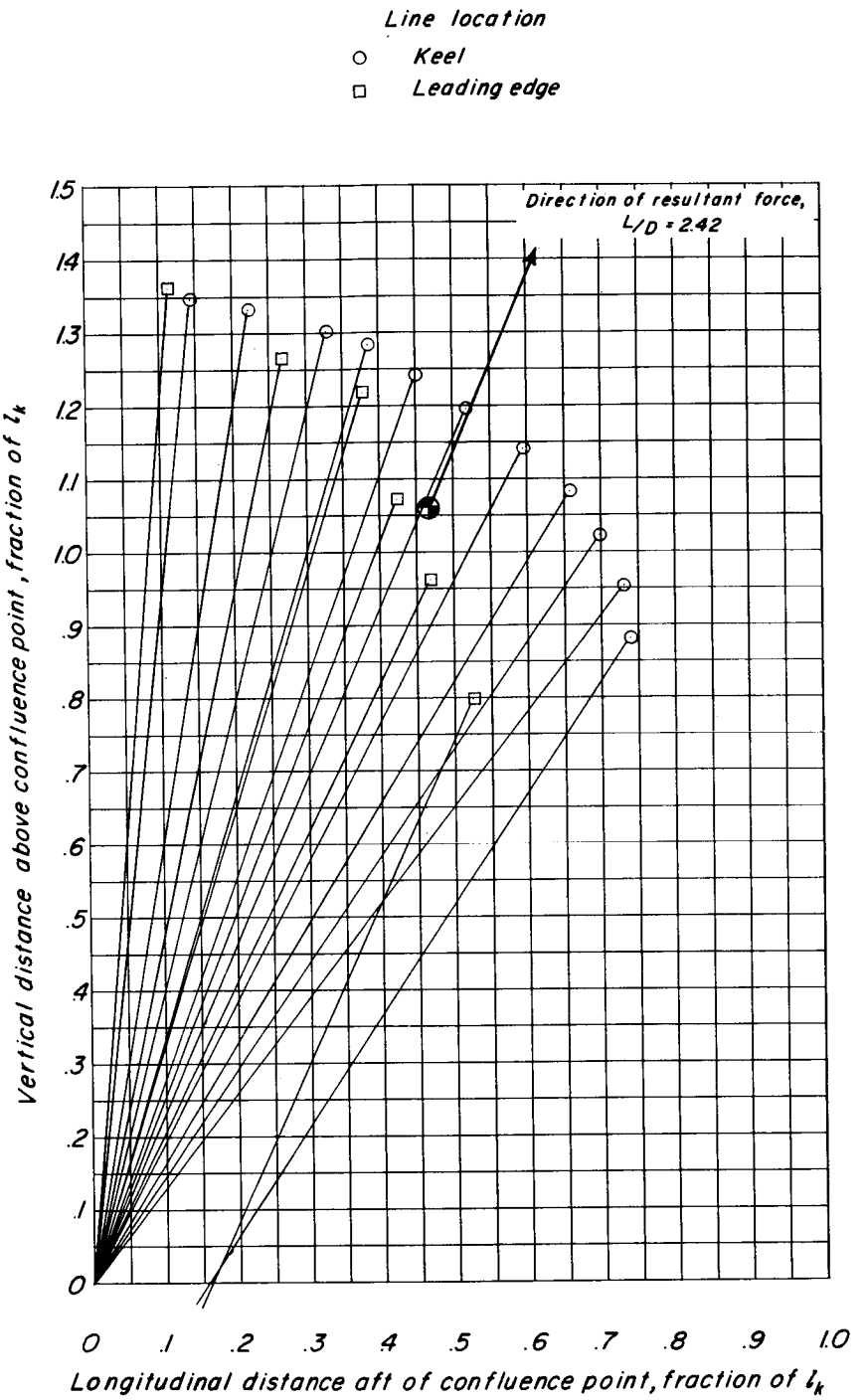

(a) $q = 1.0$; $\alpha = 27.5^0$.

Figure 92.- Center of pressure, lift-drag ratio, and direction of resultant force for a parawing with $\Lambda_0 = 45^0$ and 1/8 l_k nose cut off, computed from measured line angles, line lengths, and line tension.

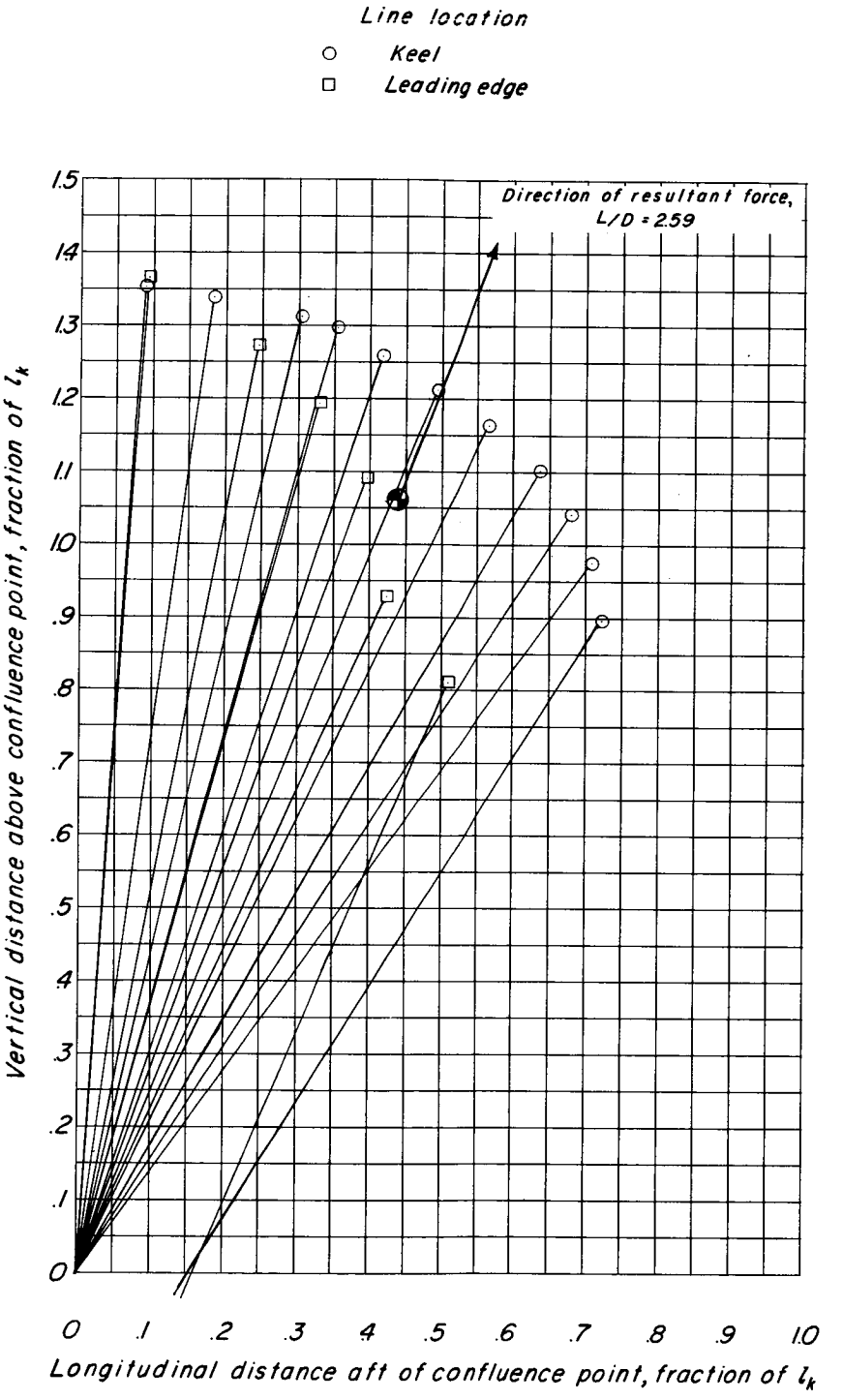

(b) $q = 2.0$; $\alpha = 25.8^0$.

Figure 92.- Continued.

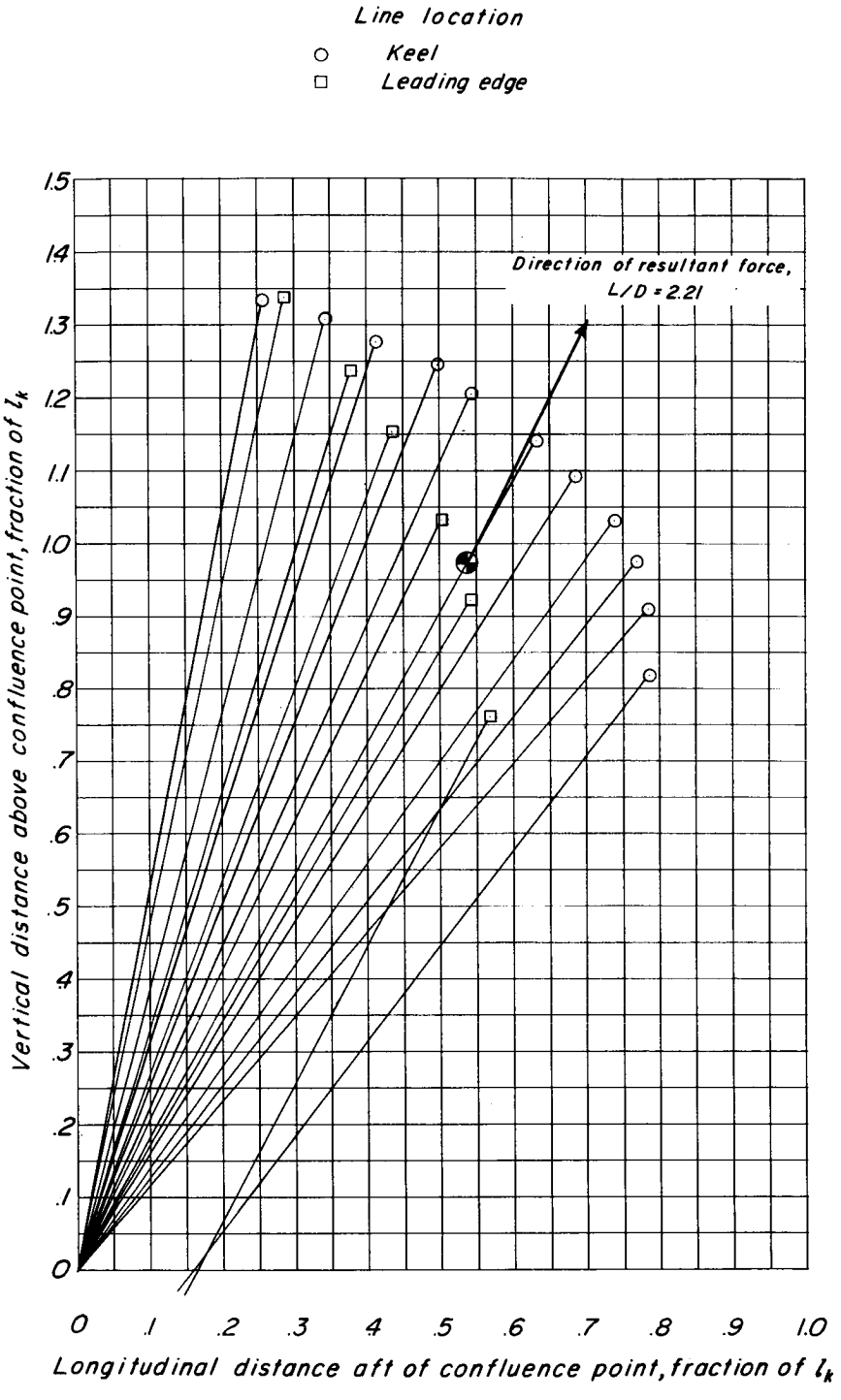

(c) q = 1.0; α = 32.0°.

Figure 92.- Continued.

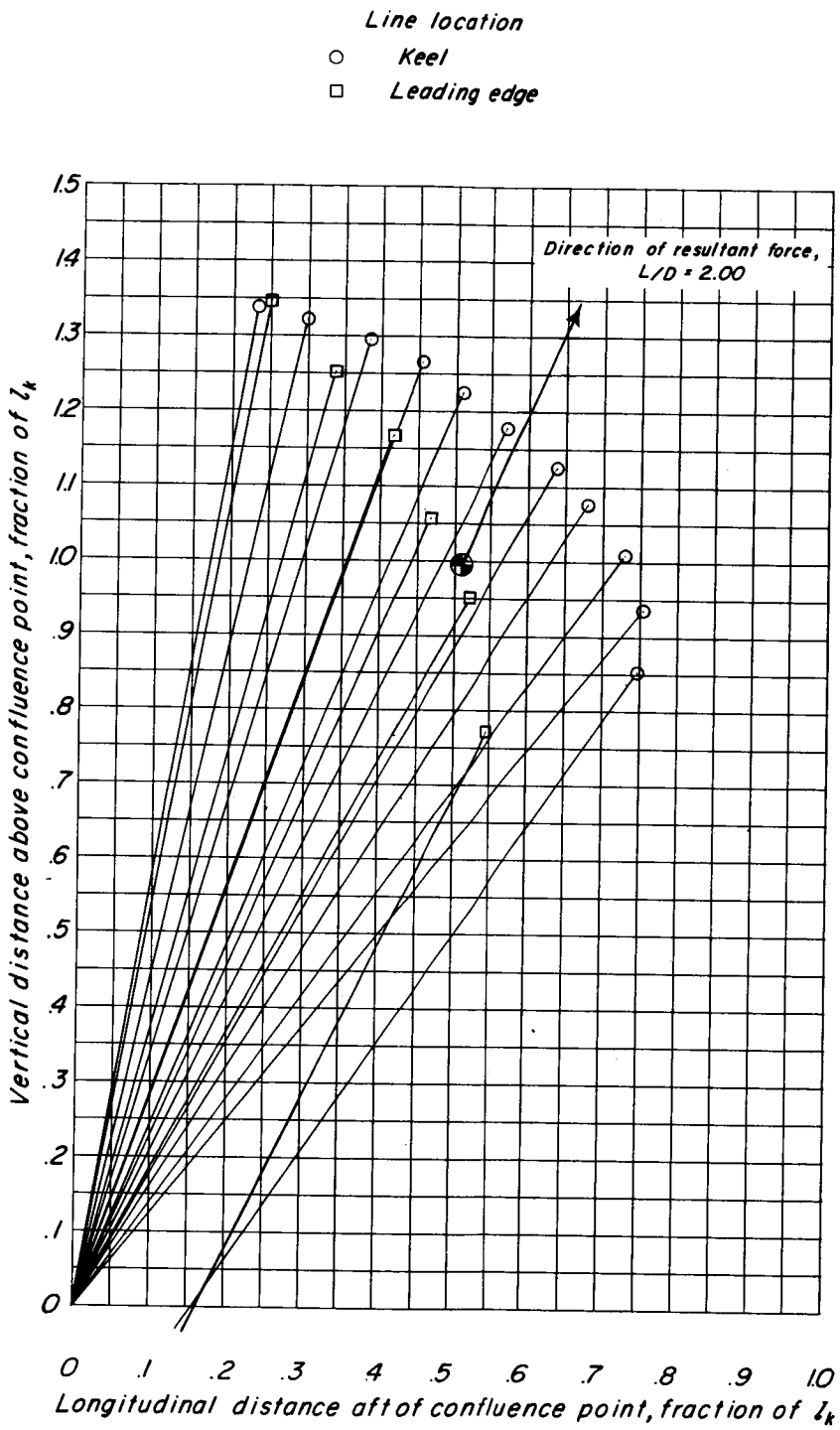

(d) $q = 2.0$; $\alpha = 29.5^0$.

Figure 92.- Concluded.

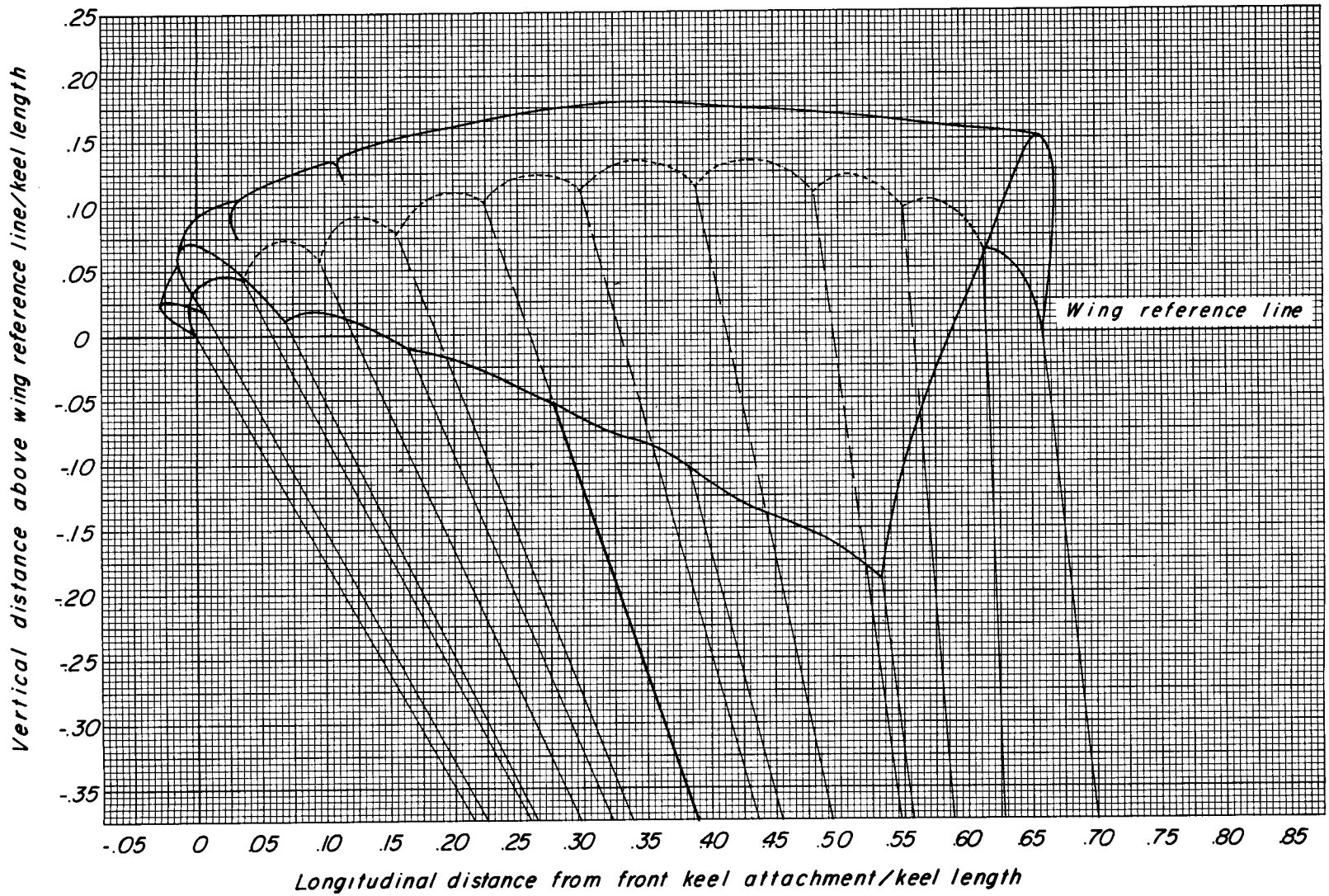

Figure 93.- Geometry measured during test.

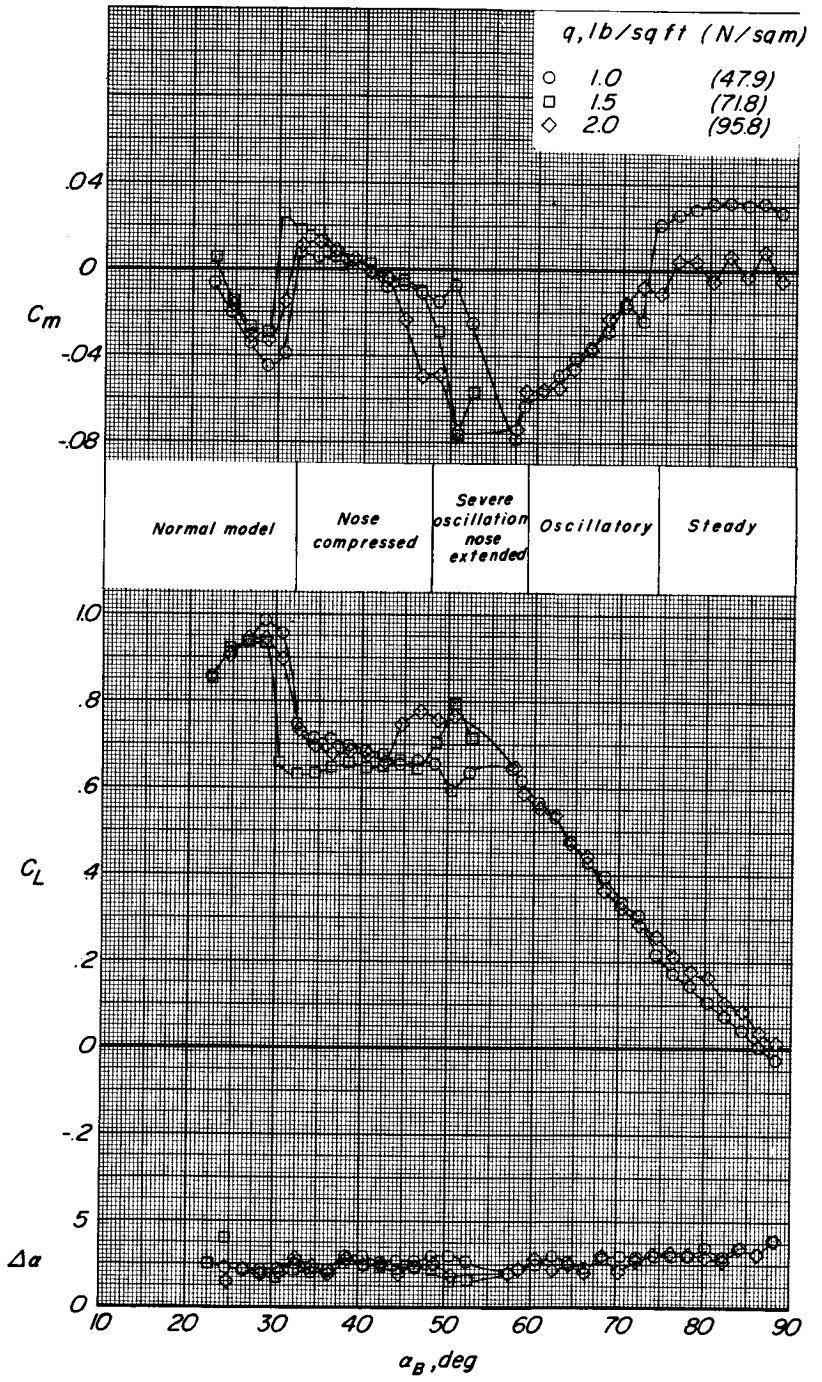

(a) C_m, C_L, $\Delta\alpha$ against α_B.

Figure 94.- Effect of dynamic pressure on the longitudinal aerodynamic characteristics of a parawing with $\Lambda_0 = 45^0$ and 1/8 l_k nose cut off. Aft-keel-line length, $l/l_k = 1.137$.

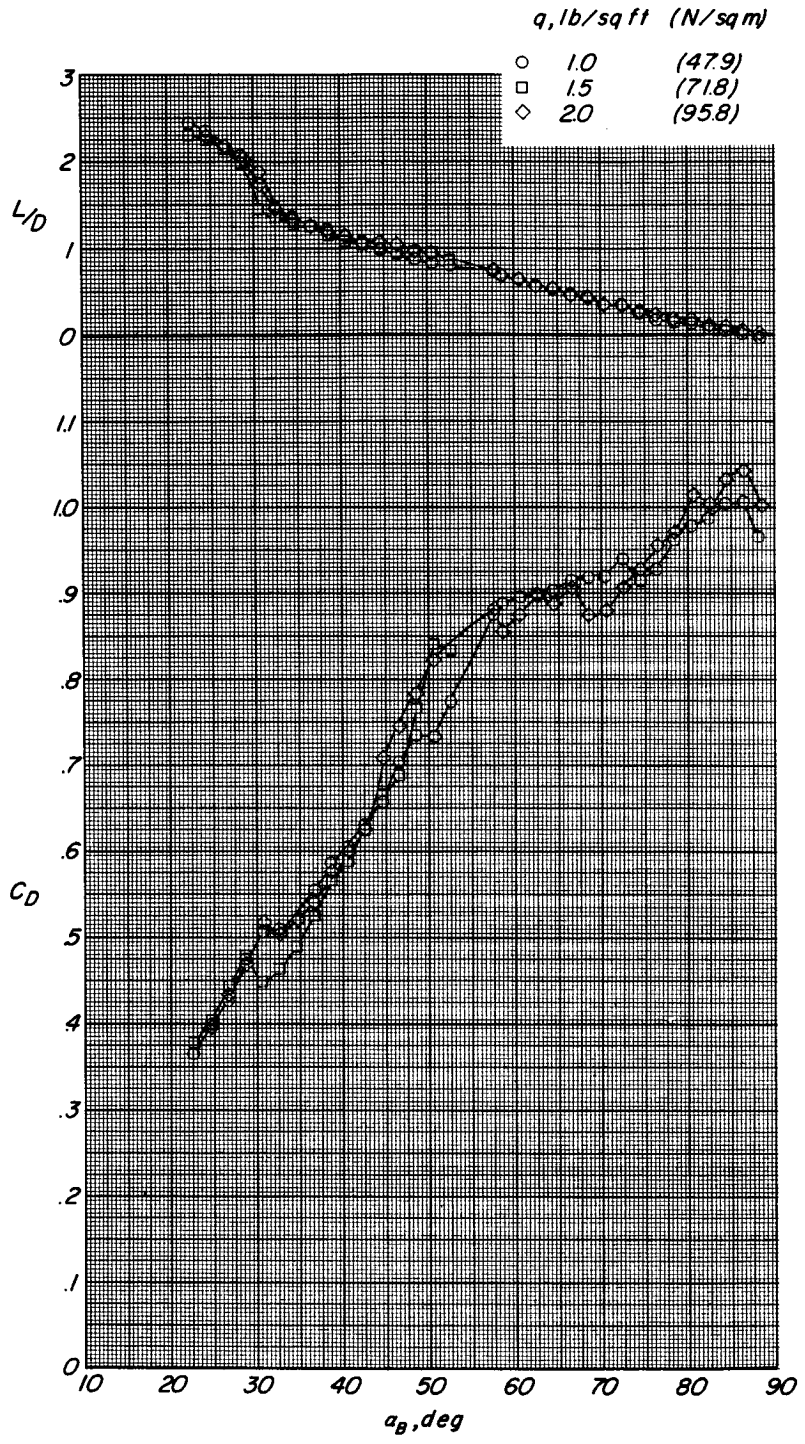

(b) L/D and C_D against α_B.

Figure 94.- Continued.

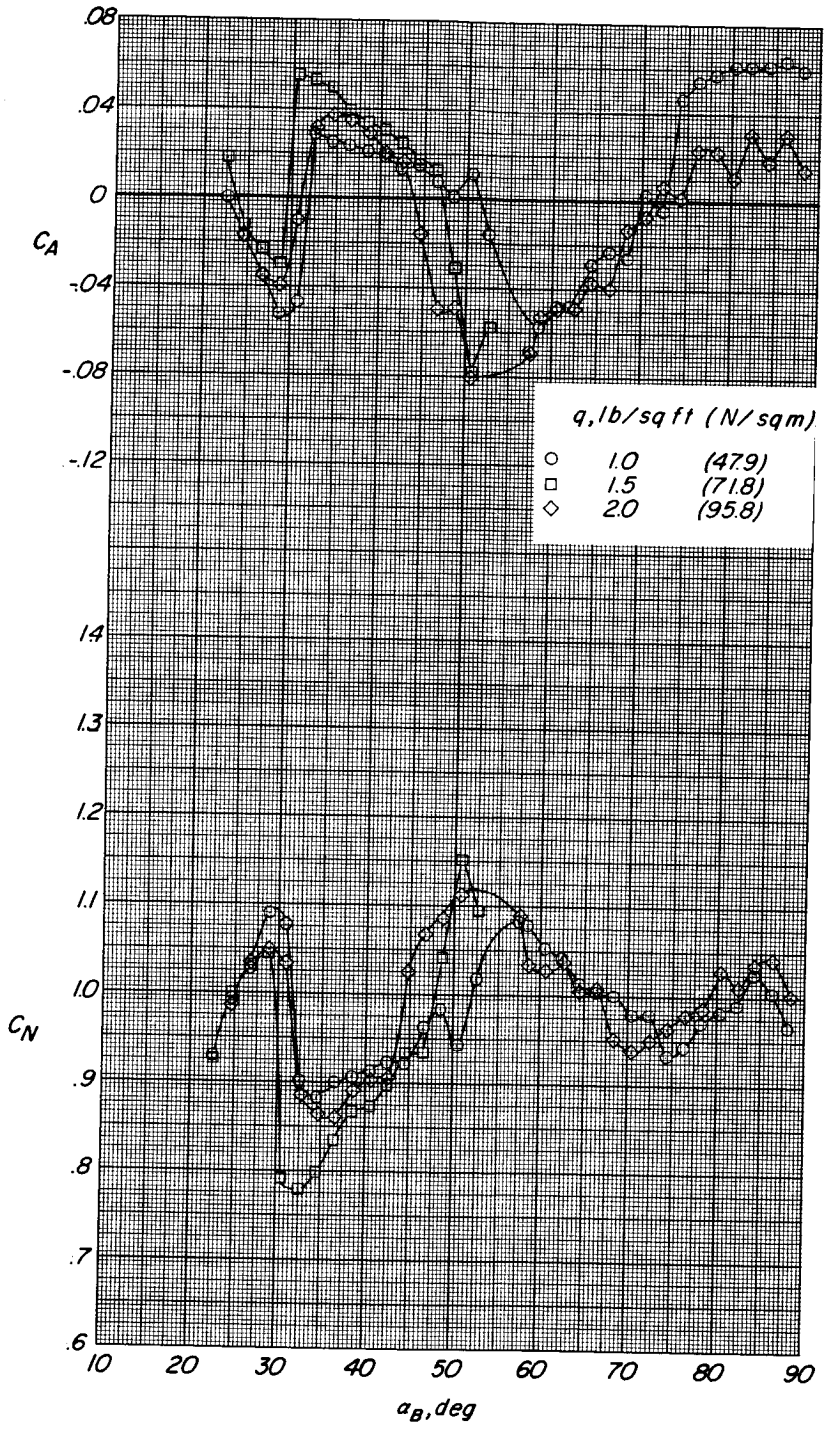

(c) C_A and C_N against α_B.

Figure 94.- Concluded.

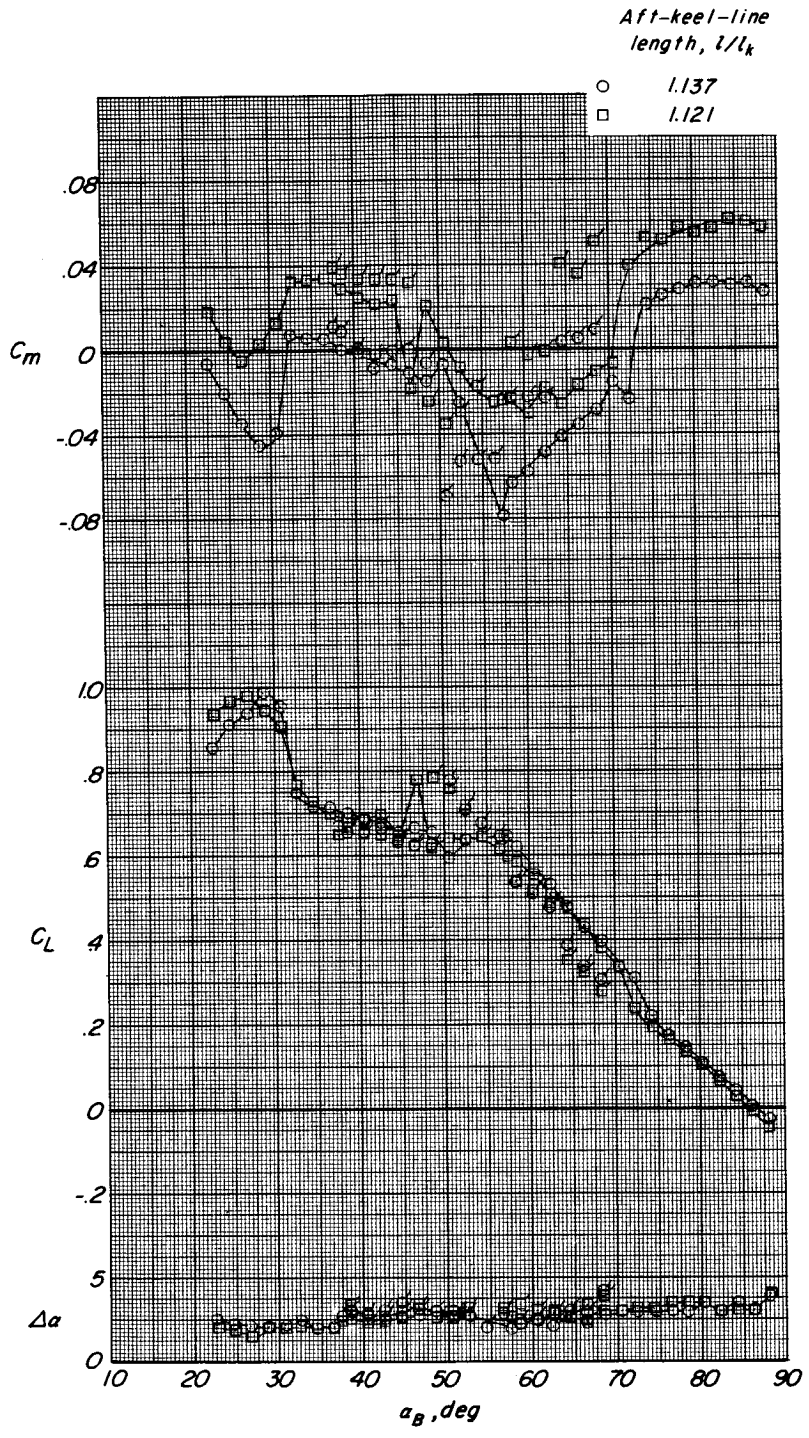

(a) C_m, C_L, and $\Delta\alpha$ against α_B.

Figure 95.- Variation of the longitudinal aerodynamic characteristics with overlapping angle-of-attack ranges for a parawing with $\Lambda_0 = 45^0$ and 1/8 l_k nose cut off. q = 1.0 lb/sq ft (47.9 N/sq m).

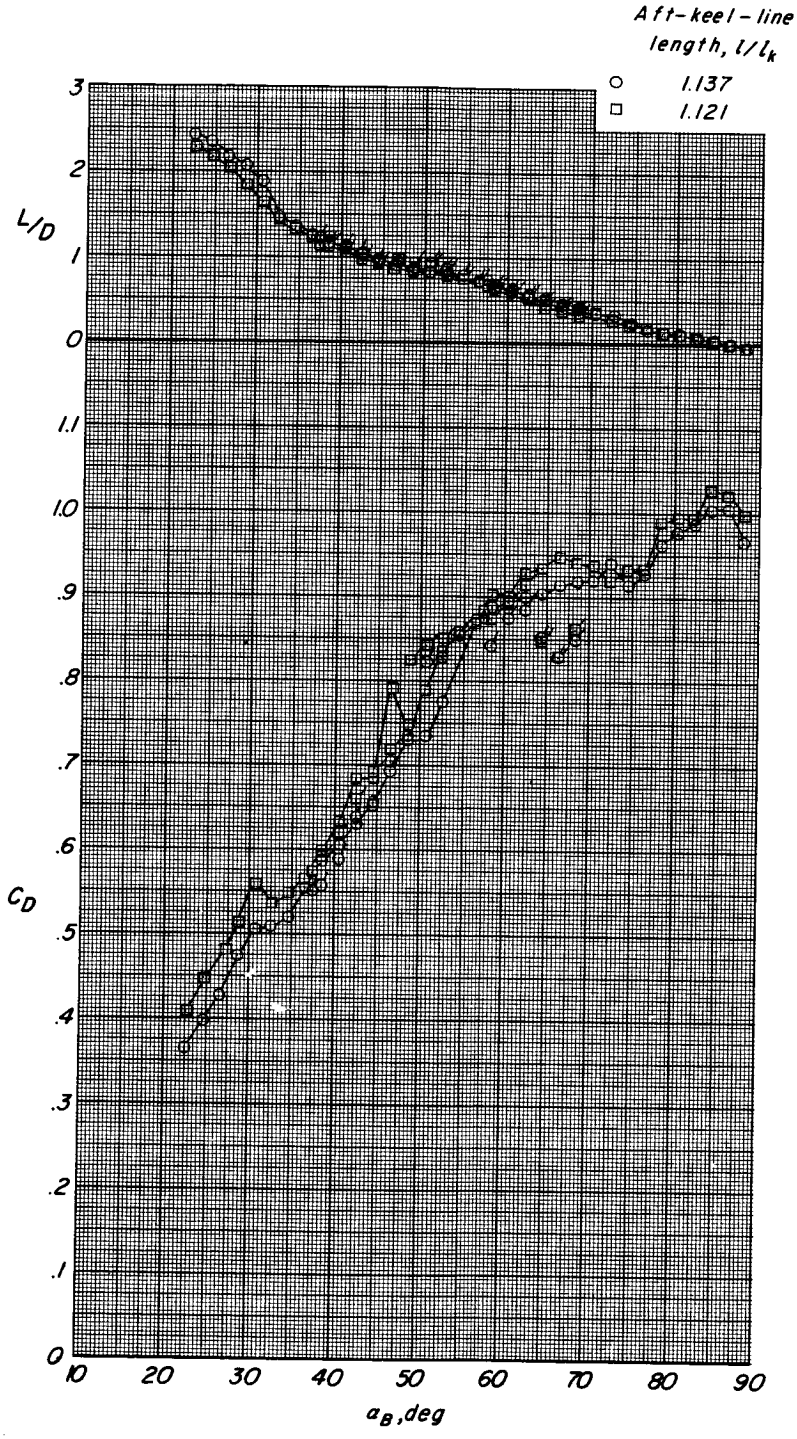

(b) L/D and C_D against α_B.

Figure 95.- Continued.

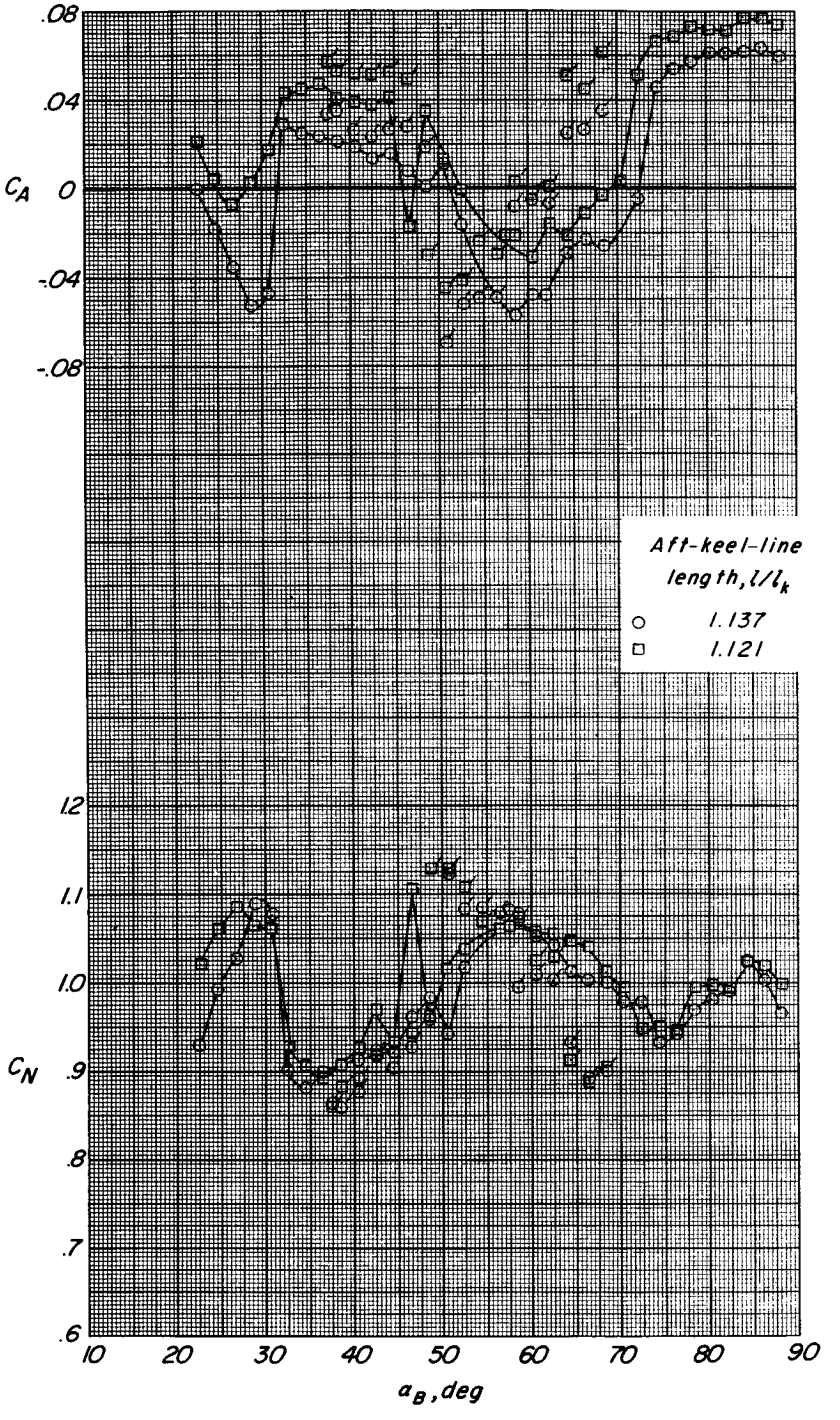

(c) C_A and C_N against α_B.

Figure 95.- Concluded.

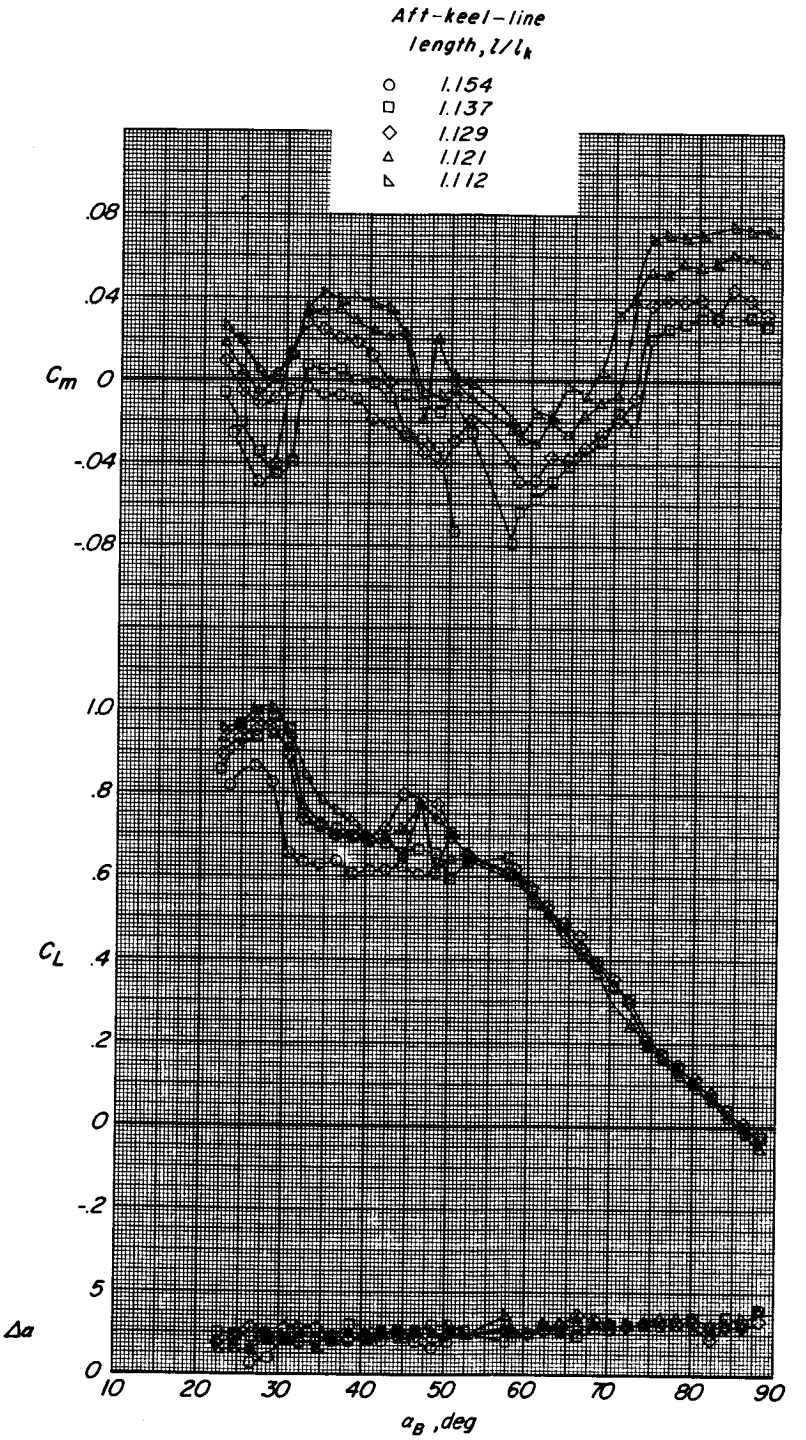

(a) C_m, C_L, and $\Delta\alpha$ against α_B.

Figure 96.- Longitudinal aerodynamic characteristics of the basic wing for various aft-keel-line control changes. q = 1.0 lb/sq ft (47.9 N/sq m).

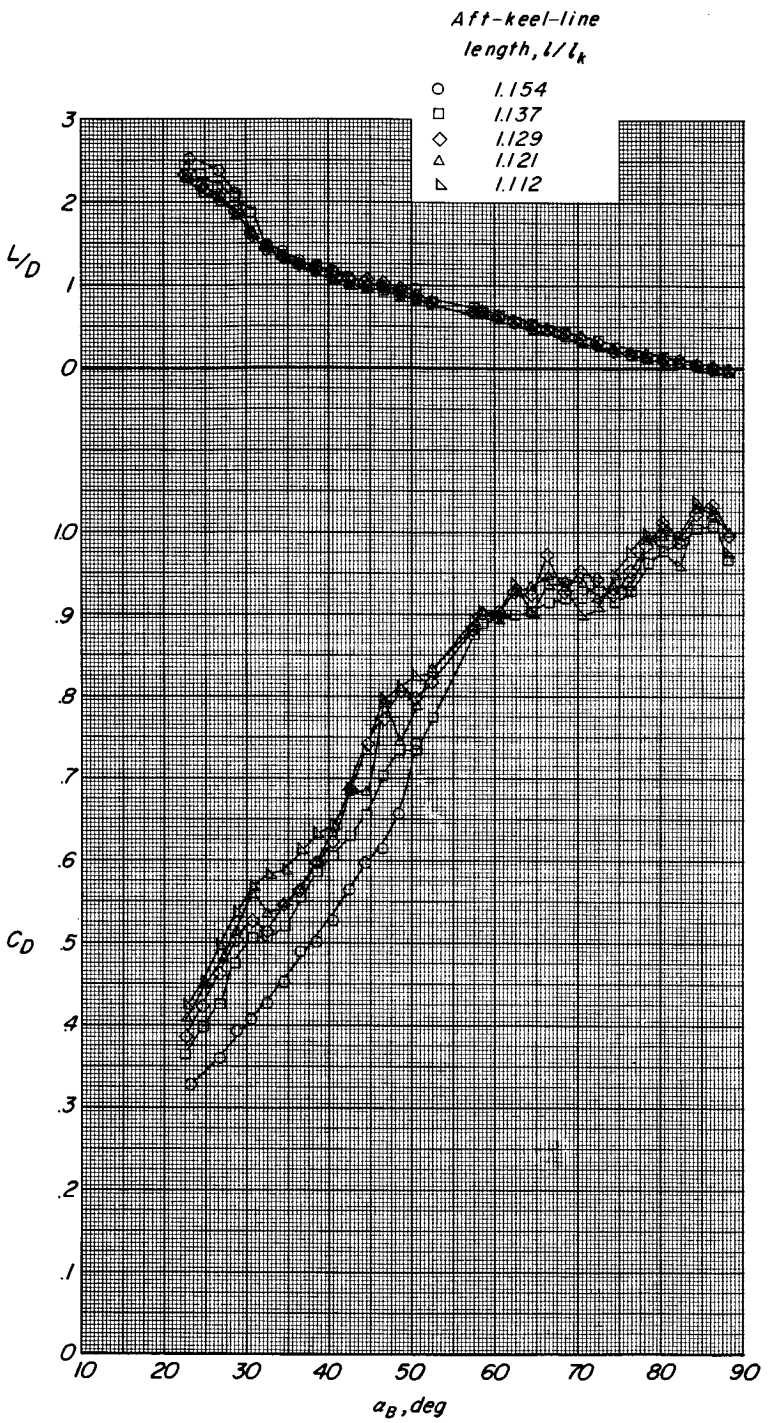

(b) L/D and C_D against α_B.

Figure 96.- Continued.

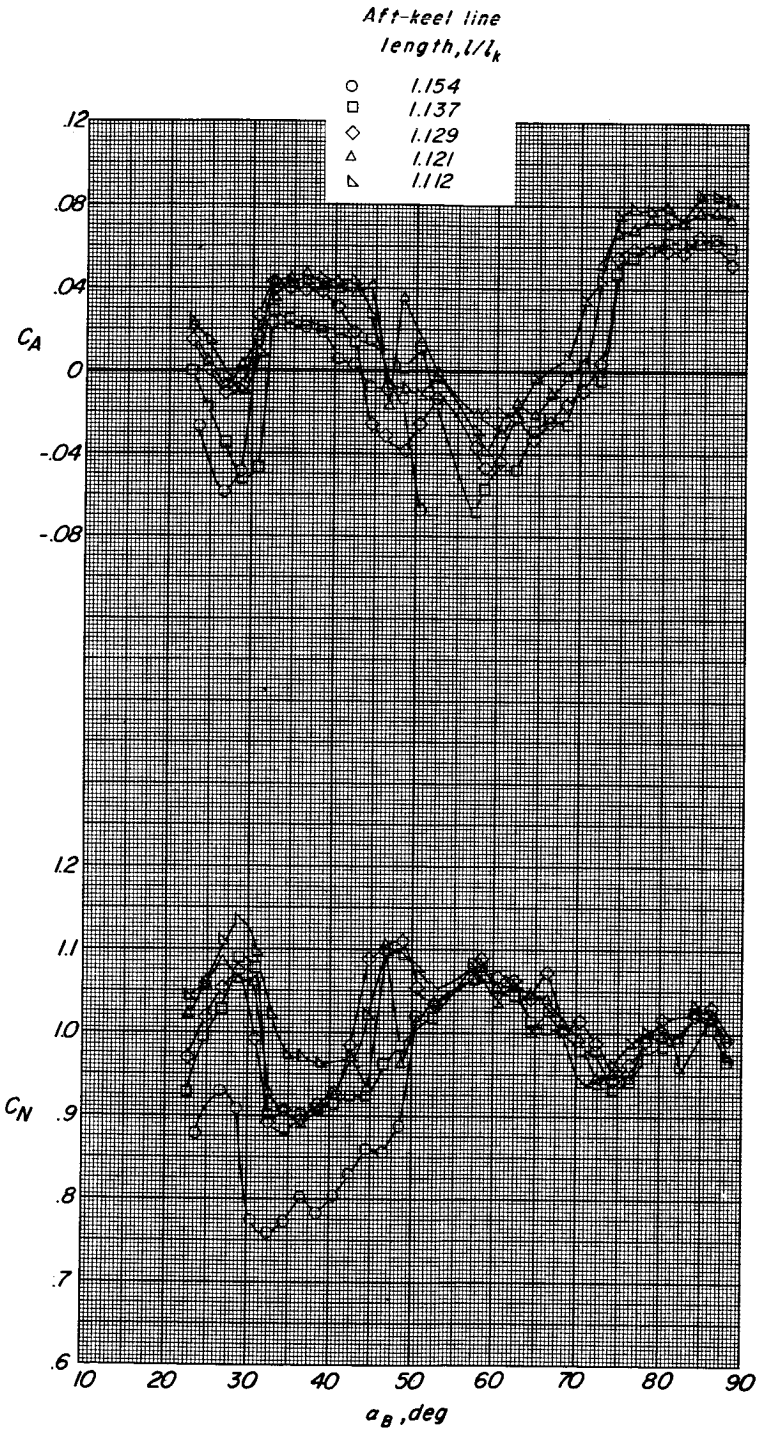

(c) C_A and C_N against α_B.

Figure 96.- Concluded.

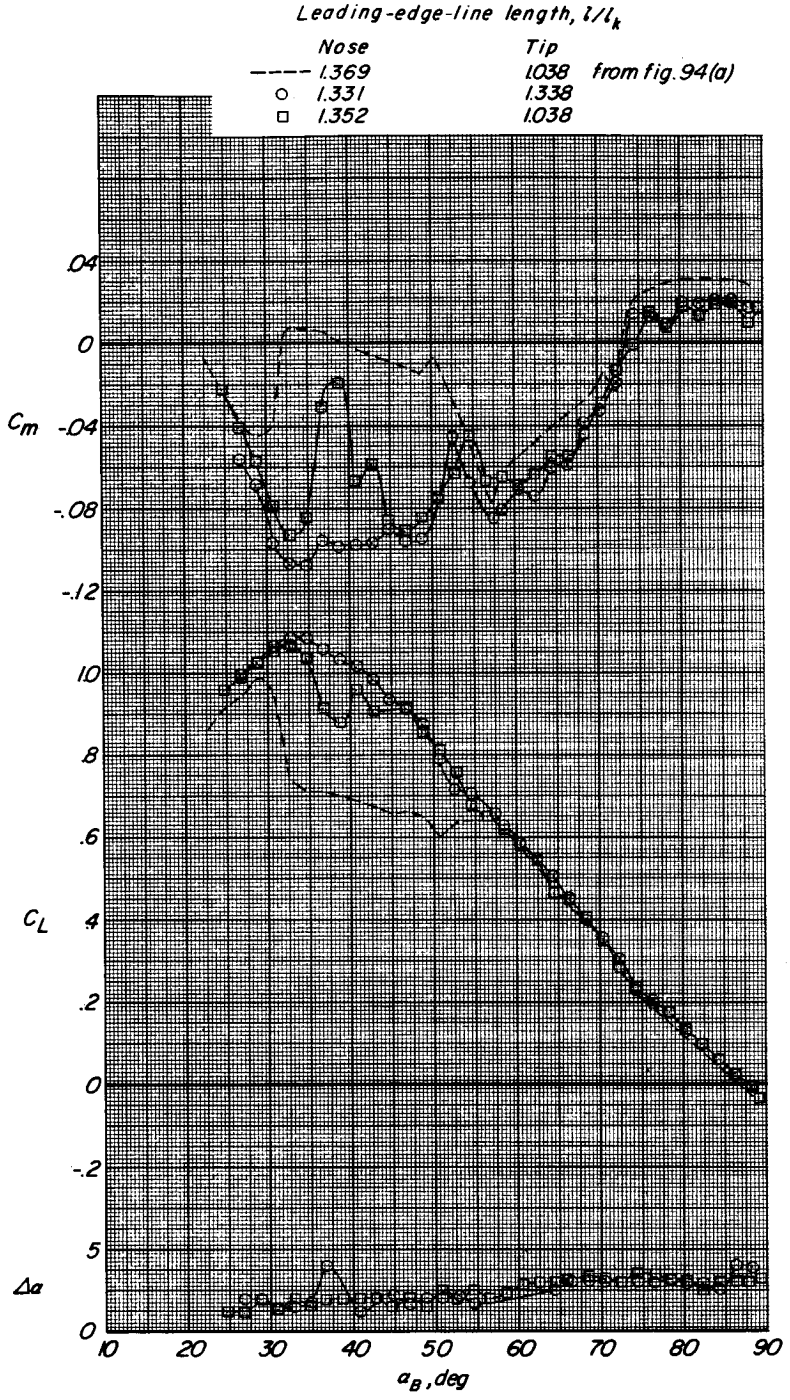

(a) C_m, C_L, and $\Delta\alpha$ against α_B.

Figure 97.- Longitudinal aerodynamic characteristics of basic wing for various control changes of the forward- and tip-leading-edge lines. Aft-keel-line length, l/l_k = 1.137; q = 1.0 lb/sq ft (47.9 N/sq m).

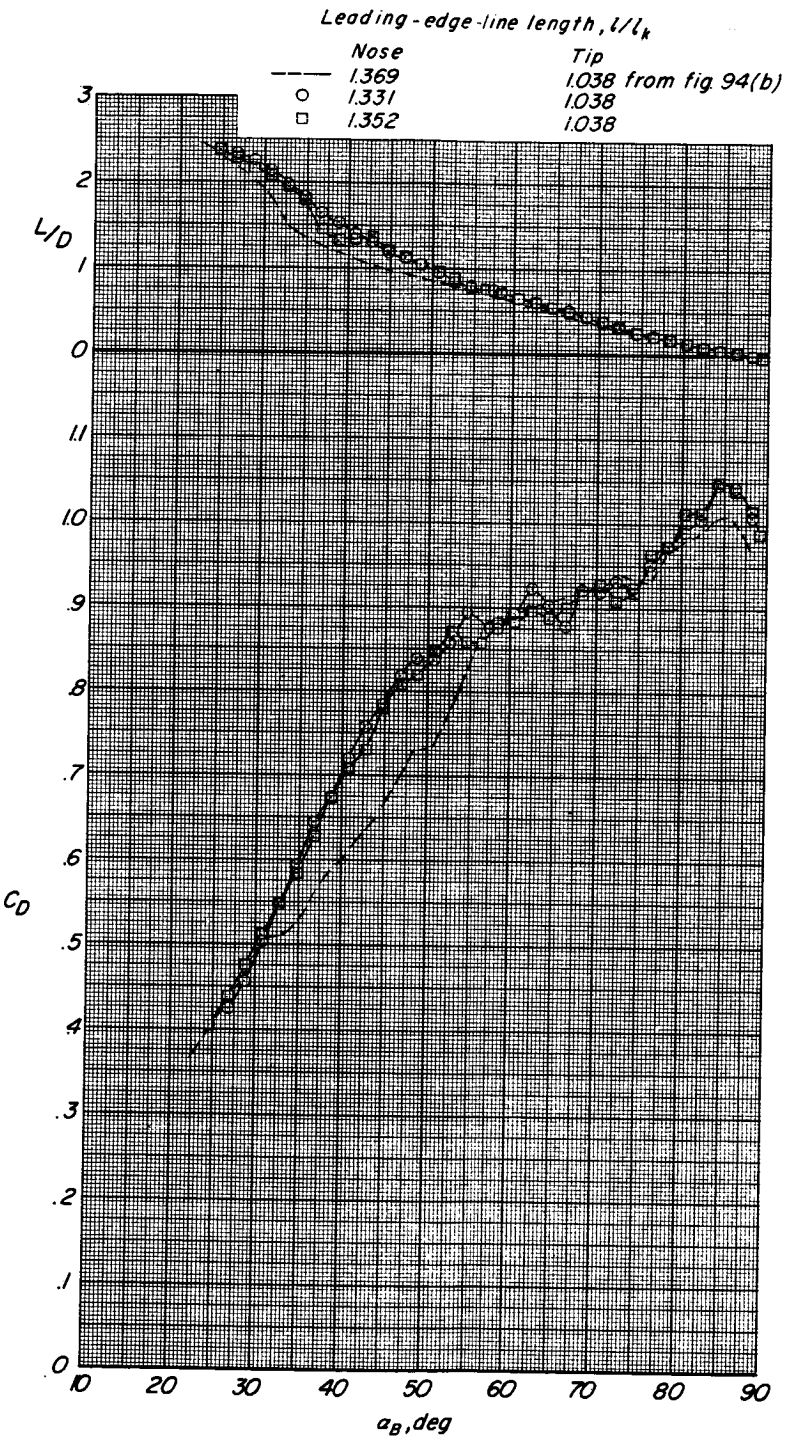

(b) L/D and C_D against α_B.

Figure 97.- Continued.

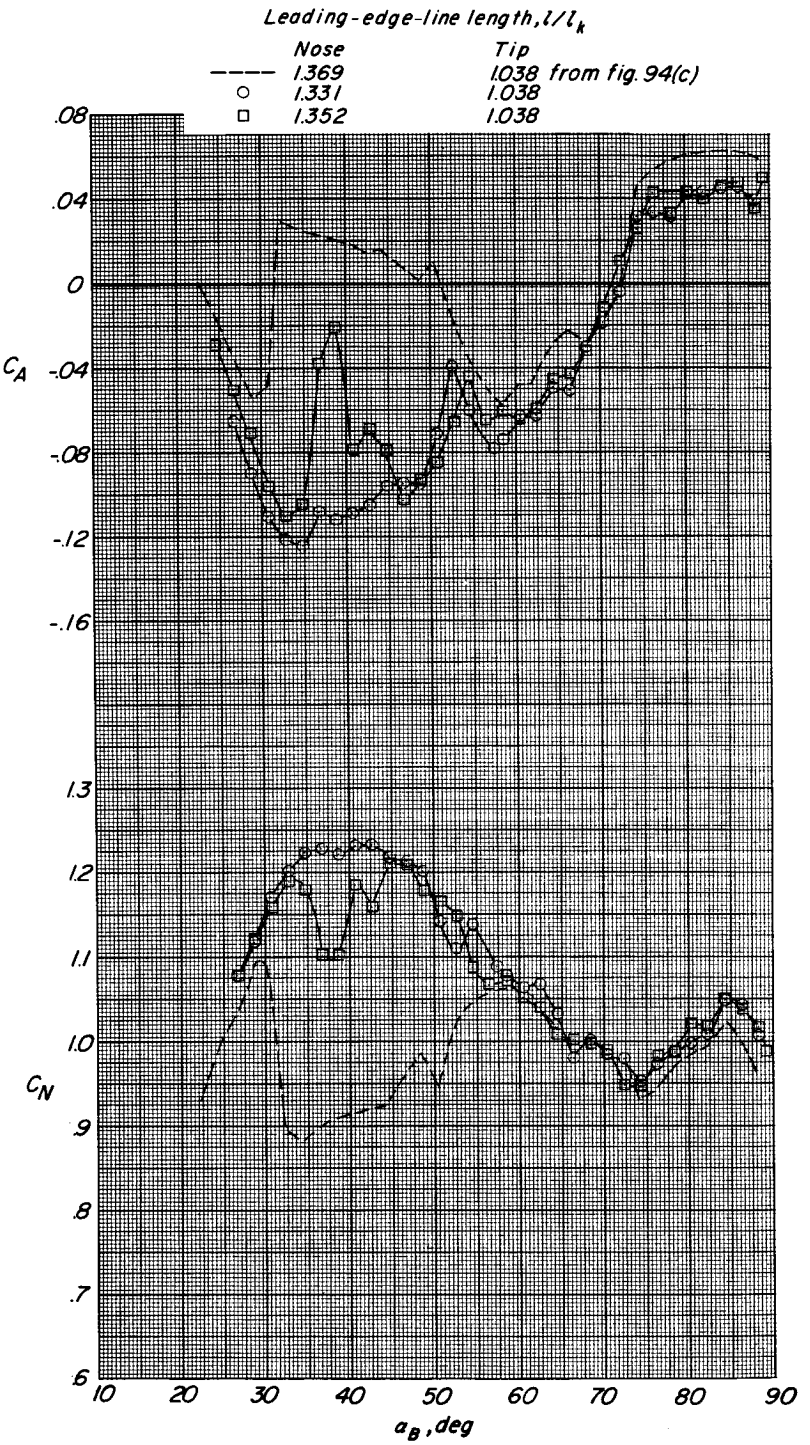

(c) C_A and C_N against α_B.

Figure 97.- Concluded.

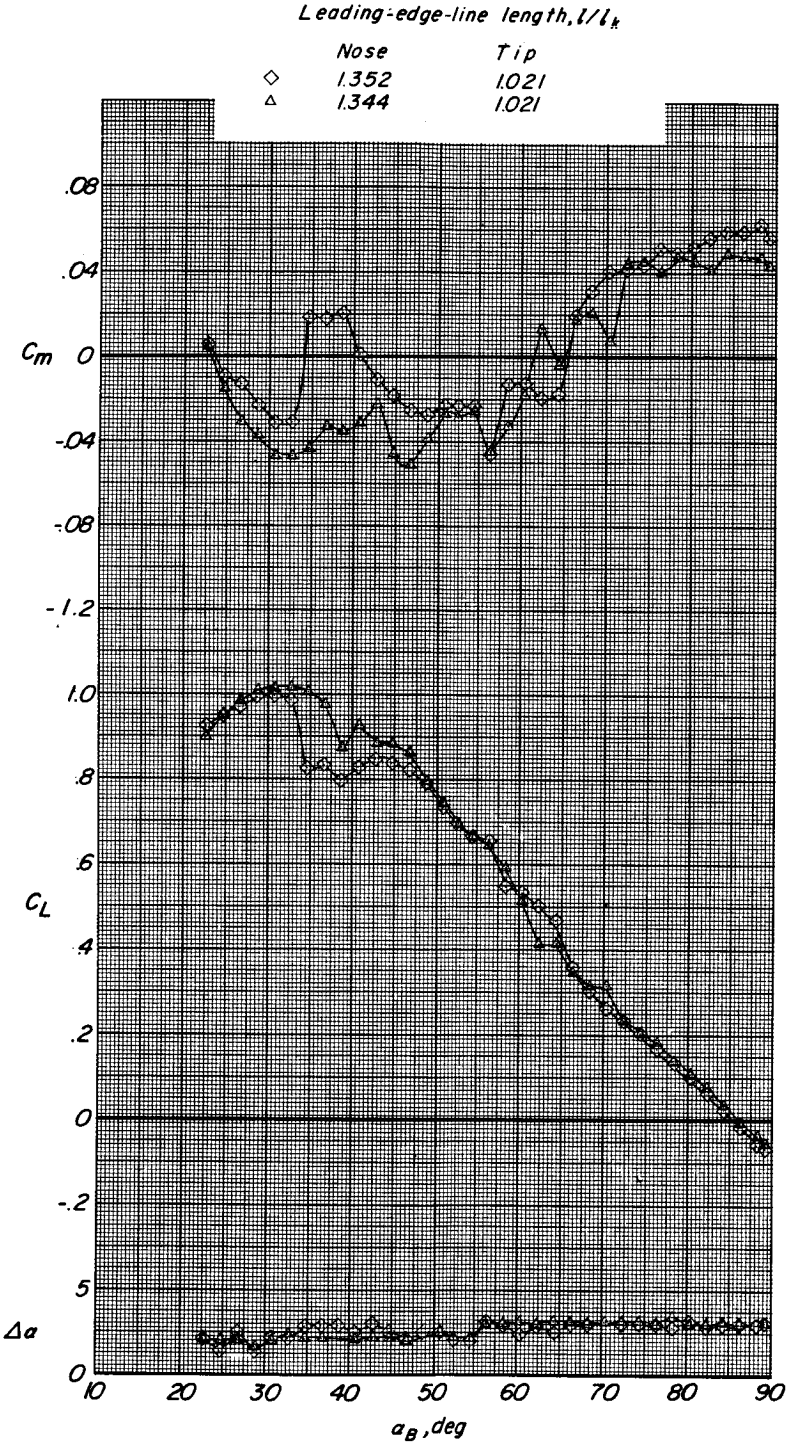

(a) C_m, C_L, and $\Delta\alpha$ against α_B.

Figure 98.- Longitudinal aerodynamic characteristics of the basic wing for various control changes of the forward- and tip-leading-edge lines. Aft-keel-line length, l/l_k = 1.137; q = 1.0 lb/sq ft (47.9 N/sq m).

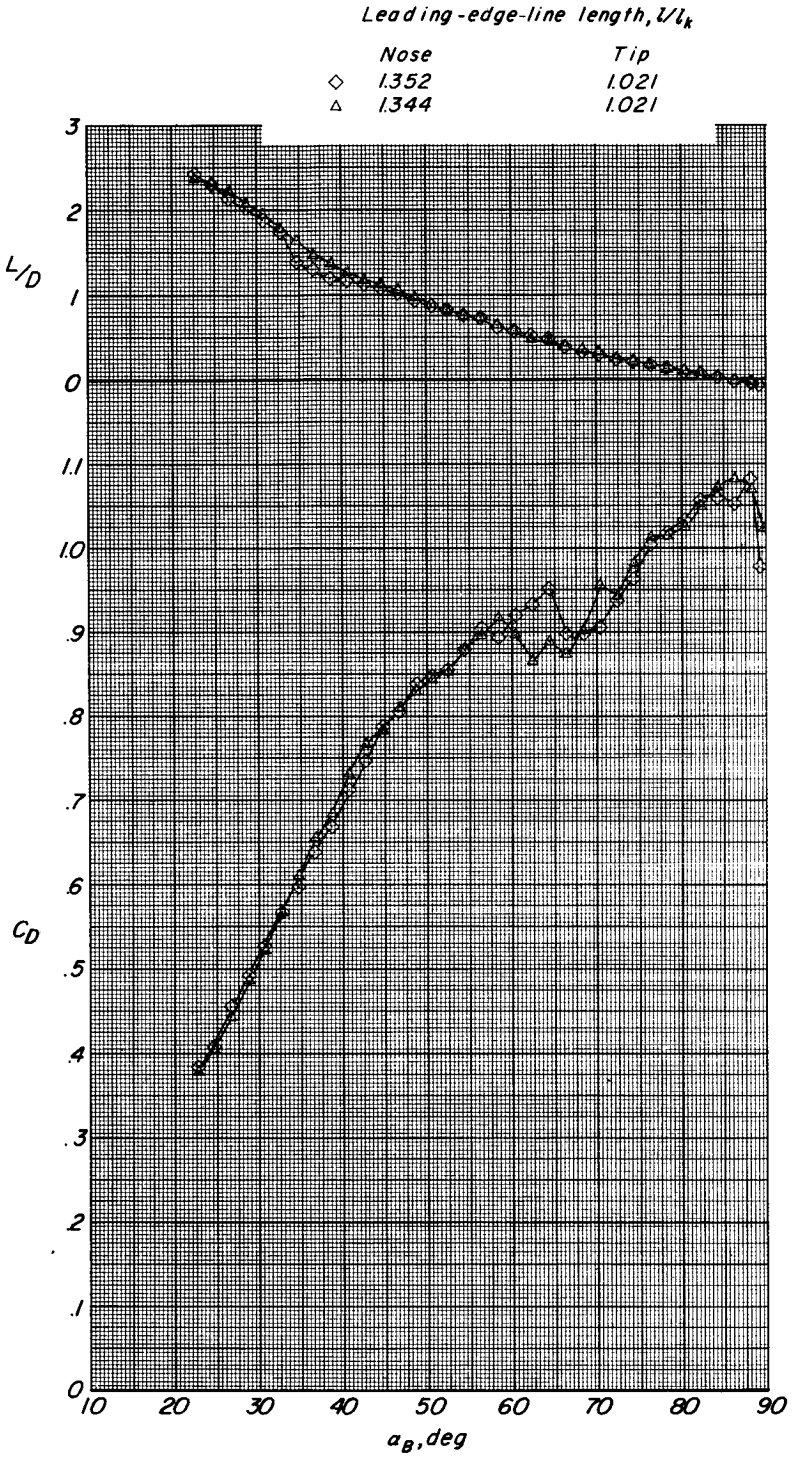

(b) L/D and C_D against α_B.

Figure 98.- Continued.

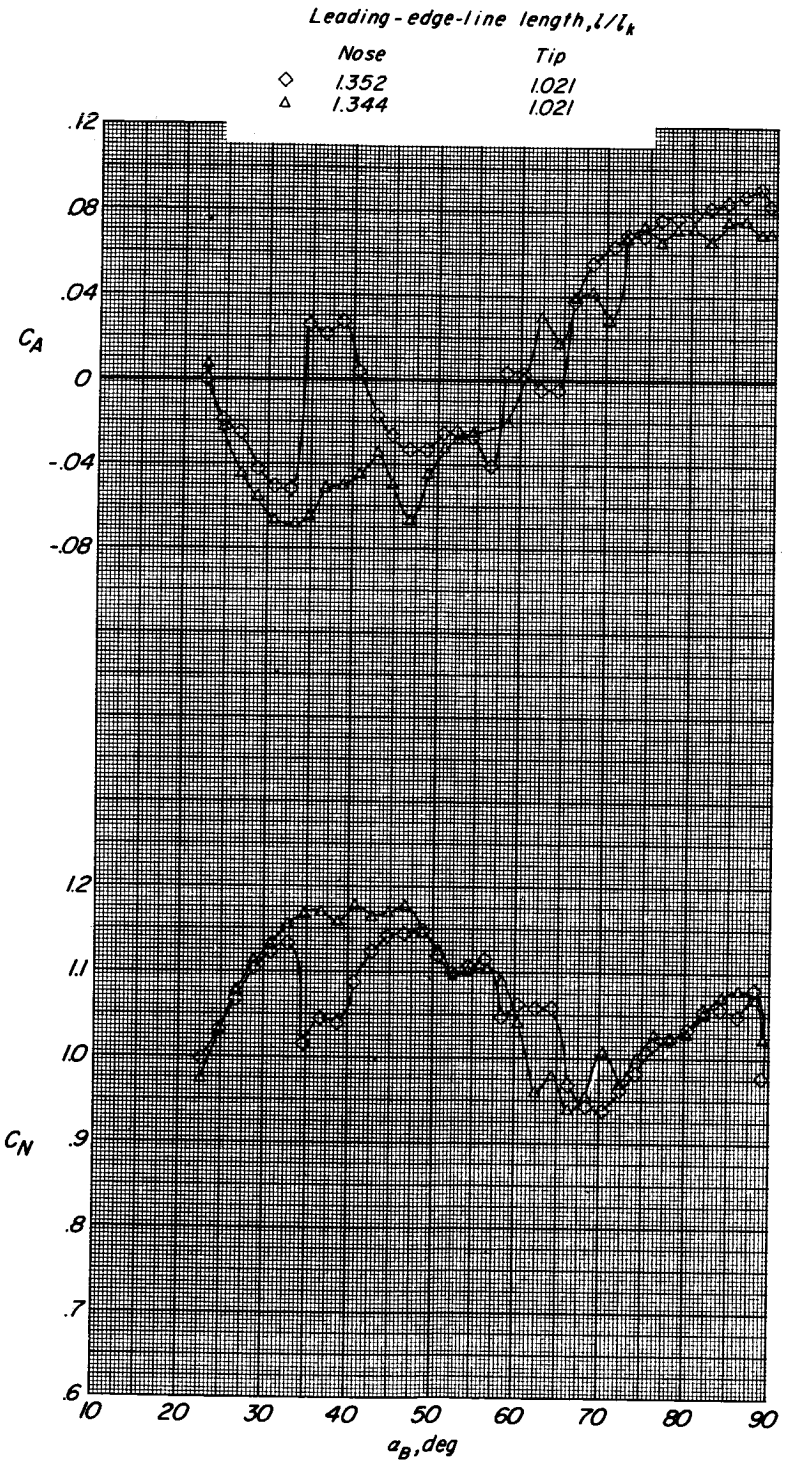

(c) C_A and C_N against α_B.

Figure 98.- Concluded.

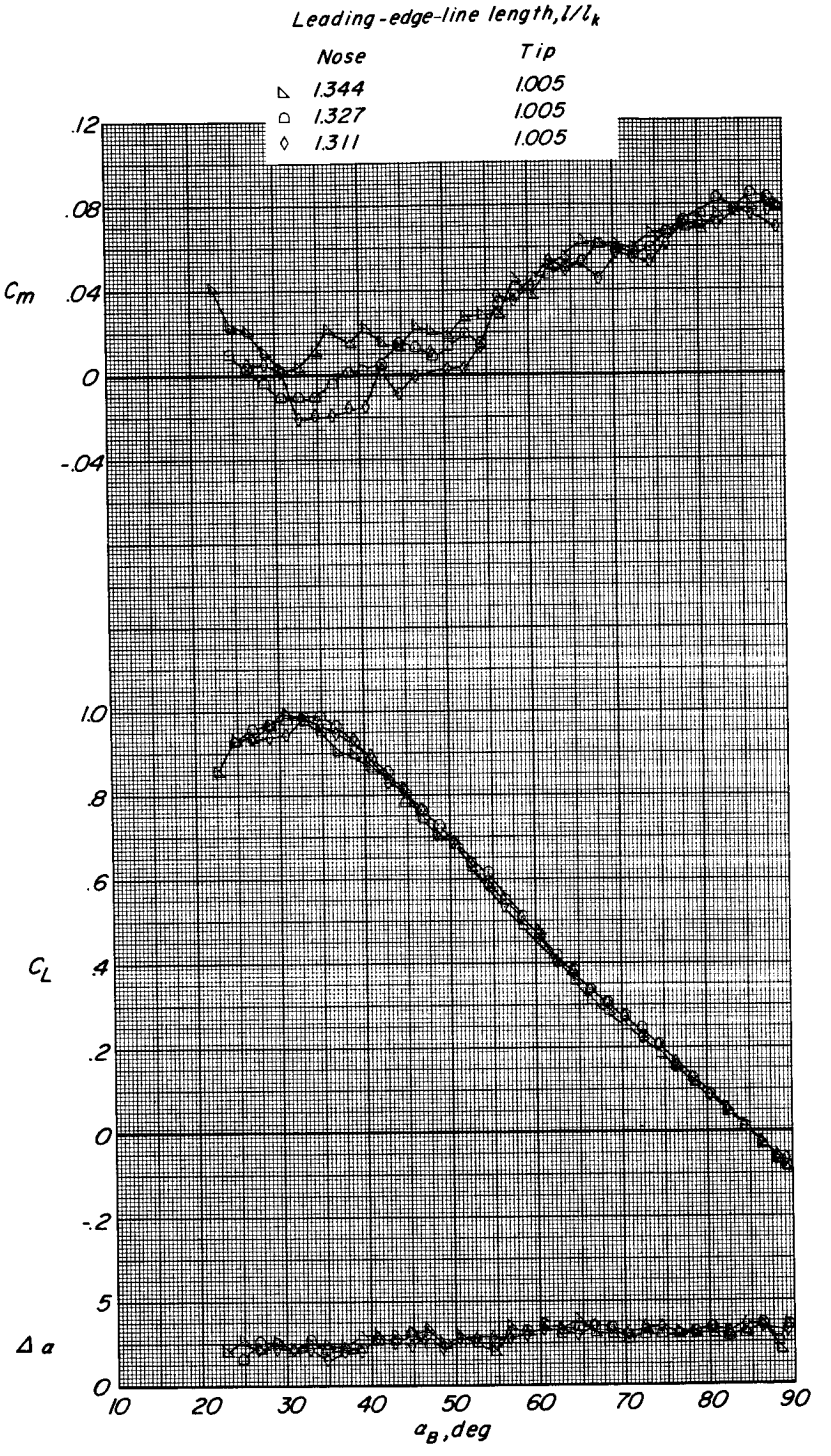

(a) C_m, C_L, and $\Delta\alpha$ against α_B.

Figure 99.- Longitudinal aerodynamic characteristics of the basic wing for various control changes of the forward- and tip-leading-edge lines. Aft-keel-line length, l/l_k = 1.137; q = 1.0 lb/sq ft (47.9 N/sq m).

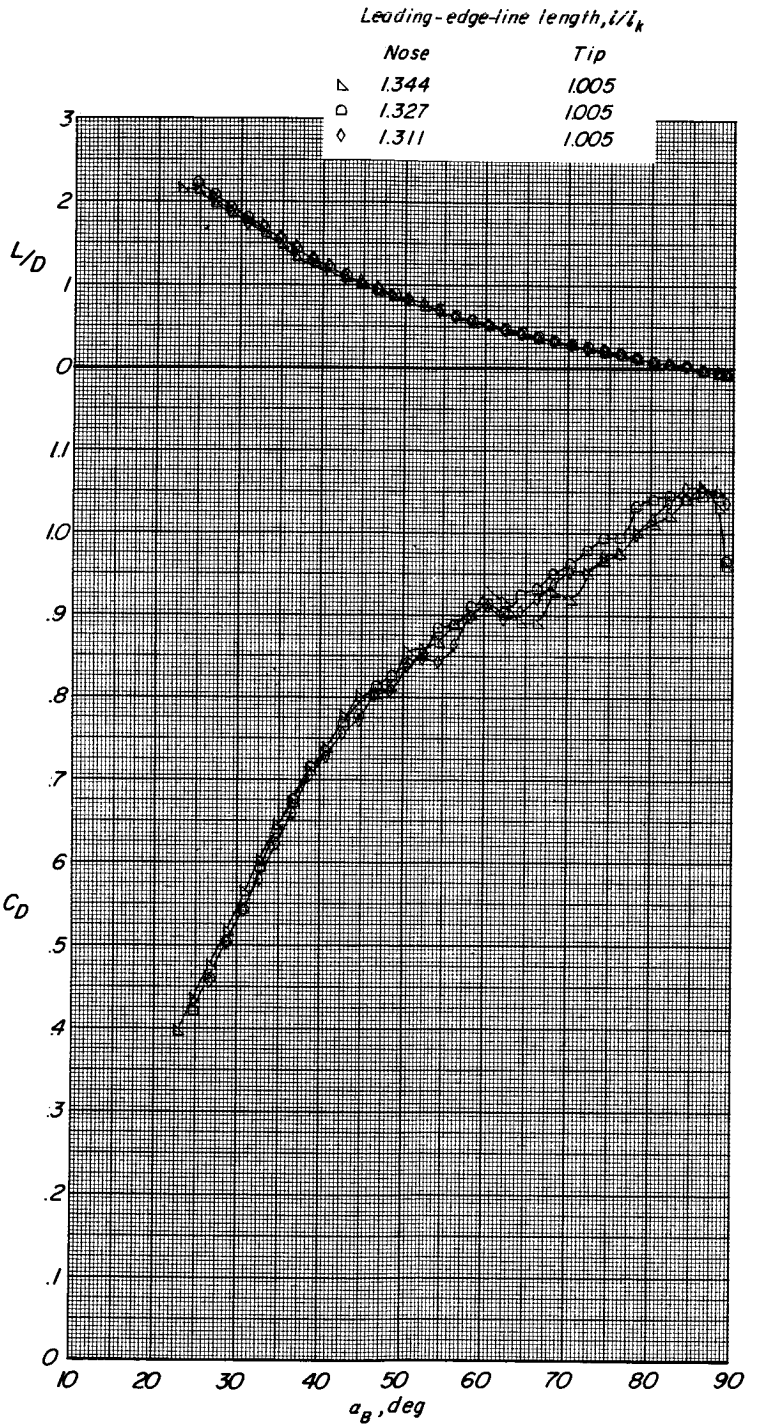

(b) L/D and C_D against α_B.

Figure 99.- Continued.

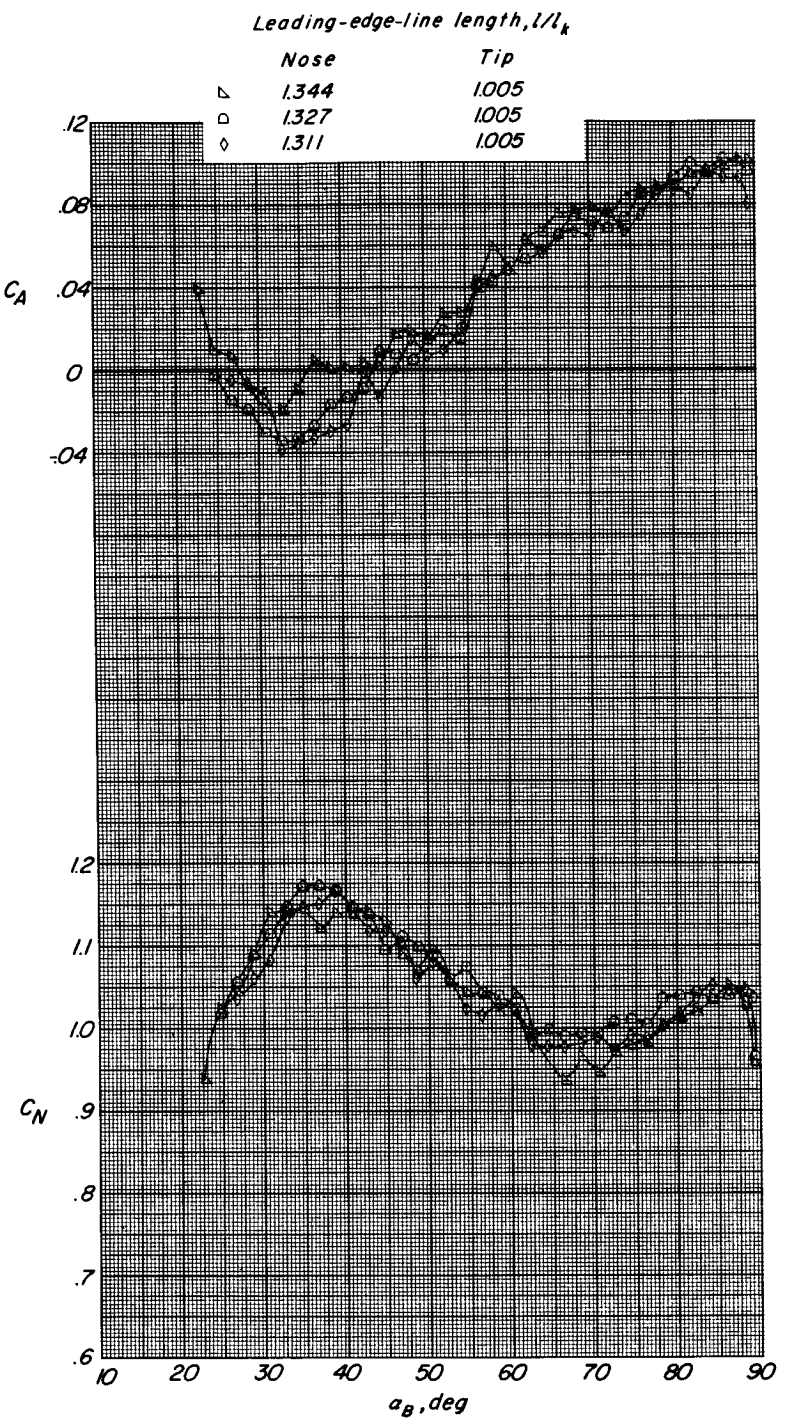

(c) C_A and C_N against α_B.

Figure 99.- Concluded.

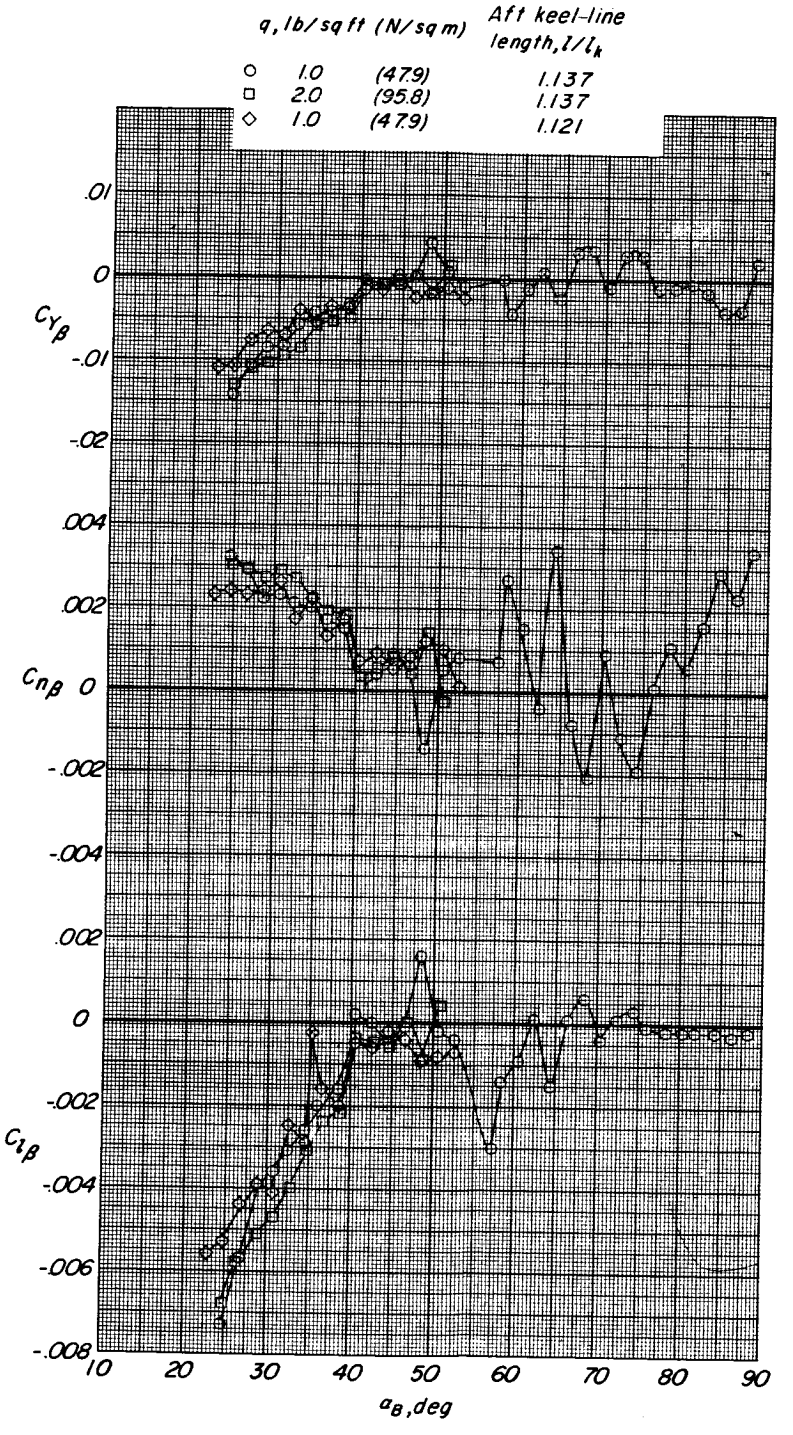

Figure 100.- Static lateral-stability parameters for a parawing with $\Lambda_0 = 45^0$ and 1/8 l_k nose cut off.

"The aeronautical and space activities of the United States shall be conducted so as to contribute . . . to the expansion of human knowledge of phenomena in the atmosphere and space. The Administration shall provide for the widest practicable and appropriate dissemination of information concerning its activities and the results thereof."

—NATIONAL AERONAUTICS AND SPACE ACT OF 1958

NASA SCIENTIFIC AND TECHNICAL PUBLICATIONS

TECHNICAL REPORTS: Scientific and technical information considered important, complete, and a lasting contribution to existing knowledge.

TECHNICAL NOTES: Information less broad in scope but nevertheless of importance as a contribution to existing knowledge.

TECHNICAL MEMORANDUMS: Information receiving limited distribution because of preliminary data, security classification, or other reasons.

CONTRACTOR REPORTS: Scientific and technical information generated under a NASA contract or grant and considered an important contribution to existing knowledge.

TECHNICAL TRANSLATIONS: Information published in a foreign language considered to merit NASA distribution in English.

SPECIAL PUBLICATIONS: Information derived from or of value to NASA activities. Publications include conference proceedings, monographs, data compilations, handbooks, sourcebooks, and special bibliographies.

TECHNOLOGY UTILIZATION PUBLICATIONS: Information on technology used by NASA that may be of particular interest in commercial and other non-aerospace applications. Publications include Tech Briefs, Technology Utilization Reports and Notes, and Technology Surveys.

Details on the availability of these publications may be obtained from:

SCIENTIFIC AND TECHNICAL INFORMATION DIVISION

NATIONAL AERONAUTICS AND SPACE ADMINISTRATION

Washington, D.C. 20546